

Ursel Fantz

Atomic and Molecular Emission Spectroscopy in Low Temperature Plasmas Containing Hydrogen and Deuterium

Atomic and Molecular Emission Spectroscopy in
Low Temperature Plasmas Containing
Hydrogen and Deuterium

Habilitationsschrift

Mathematisch-Naturwissenschaftliche Fakultät
Universität Augsburg
Germany

Ursel Fantz

June 2001

Contents

1	Introduction	1
2	Low Temperature Plasmas	5
2.1	Typical plasma parameters	5
2.1.1	Densities	6
2.1.2	Temperatures	6
2.1.3	Electron energy distribution function (EEDF)	6
2.2	Equilibrium and population models	7
2.2.1	Corona model	8
2.2.2	Collisional-radiative model	10
2.2.3	Effective rate coefficients	13
2.2.4	Radiation transfer and self-absorption	14
2.3	Modeling of plasma parameters	18
2.3.1	Particle balance and confinement times: particle densities	18
2.3.2	Ionization balance: electron temperature	22
2.3.3	Power balance or electrical conductivity: electron density	23
2.3.4	Boltzmann equation: EEDF	25
2.4	Experiments	27
2.4.1	Laboratory plasmas	28
2.4.2	Edge plasmas in fusion experiments	33
3	Diagnostic Methods	37
3.1	Emission spectroscopy	37
3.1.1	Absolute intensity calibration of the optical systems	38
3.1.2	Electron temperature, EEDF and particle densities	39
3.1.3	Population of electronic excited states	44
3.1.4	Rotational and vibrational populations of molecules	44
3.2	Absorption spectroscopy	47
3.3	Microwave interferometry	51
3.4	Langmuir probes	52
3.4.1	Electron density	54
3.4.2	Electron temperature and EEDF	55
3.4.3	Operation conditions	55
3.5	Mass spectrometry	56

3.5.1	Residual gas analyser	56
3.5.2	Energy resolved mass spectrometry	57
4	Helium and Argon Plasmas	59
4.1	Particle densities and gas temperature	59
4.2	Electron density	60
4.2.1	Spatial profiles in ICP sources	61
4.2.2	Measuring n_e in glow discharges	64
4.3	Electron temperature and EEDF	65
4.3.1	Glow discharge	65
4.3.2	ICP reactor	67
4.3.3	ECR and MW discharge	70
4.4	Metastable states and opacity	71
4.4.1	Energy level diagram	71
4.4.2	Population density of excited states	72
4.4.3	Boltzmann-plot of helium	76
4.4.4	Identification of preferred diagnostic lines	77
5	Hydrogen and Deuterium Plasmas	79
5.1	Collisional-radiative model	83
5.1.1	Population of excited states	85
5.1.2	Electron density dependence	88
5.1.3	Influence of vibrational population on rate coefficients	89
5.2	Laboratory plasmas	91
5.2.1	Interpretation of Balmer lines	92
5.2.2	Degree of dissociation	96
5.2.3	Atomic hydrogen fluxes	98
5.2.4	Reflection coefficients	101
5.2.5	Particle densities and molecular radiation	102
5.2.6	Vibrational population in the ground state	105
5.2.7	Continuum radiation	110
5.2.8	Formation of HD molecules	113
5.3	Divertor plasmas	116
5.3.1	Atomic hydrogen fluxes from S/XB	116
5.3.2	Balmer line ratios	117
5.3.3	Molecular fluxes from $(S + D)/XB$	119
5.3.4	Electron temperature diagnostics using molecular radiation	123
5.3.5	Molecular assisted recombination (MAR)	128
5.4	Chemical erosion of carbon	135
5.4.1	Determination of erosion yields	136
5.4.2	Parameter range and diagnostics	138
5.4.3	Formation of methane and higher hydrocarbons	139
5.4.4	Erosion yields at low temperatures and low ion energies . .	144

6	Other Molecular Plasmas: Methane, Silane, Nitrogen, Oxygen	149
6.1	Methane and silane plasmas	149
6.1.1	Dissociation channels	150
6.1.2	Formation of higher hydrocarbons and silanes	150
6.1.3	Particle densities	151
6.2	Degree of dissociation	157
6.2.1	Nitrogen and nitrogen/hydrogen plasmas	158
6.2.2	Oxygen plasmas	159
6.2.3	Comparison of N ₂ , O ₂ , H ₂ and D ₂ plasmas	160
7	Summary and Conclusions	163
	References	171
	List of Symbols	183
	List of Tables	187
	List of Figures	189

Chapter 1

Introduction

Low temperature plasmas are commonly used in industrial applications for such surface modifications as cleaning, etching and the formation of thin films, such as diamond coatings or amorphous silicon films [Gri94, Rot95, Jan92]. As a working gas or dissociation product hydrogen is present in most of these plasmas. Typical processing plasmas are direct current, radio-frequency or microwave discharges, which can operate over a wide range of adjustable parameters [CS00]. In order to optimize and control the processes, simple and easily handled plasma diagnostic methods have to be applied as standard [Hut87, AF89]. Furthermore, model calculations which predict plasma parameters in a wide range of applications have to be checked with results obtained using plasmas diagnostic methods. Here, emission spectroscopy is a powerful tool providing a wealth of information about plasma parameters [Gri64, TLJ99].

In controlled fusion experiments [Wes87, Sch93] hydrogen and its isotopes are the fundamental gases. Here it is distinguished between the plasma core and the plasma edge. The edge plasma is in contact with surfaces and plasma wall interaction takes place [PB86]. To reduce the heat load to the surfaces plasma particles can be forced to flow into the so-called divertor, where they recycle [Sta00a]. Here, the plasma is characterized by parameters which are comparable to those of low temperature plasmas. Atoms recombine at the target plates of the divertor and produce hydrogen molecules. Chemical erosion of carbon, commonly used as wall material, by hydrogen atoms and ions leads to the formation of hydrocarbons which then penetrate into the plasma [Rot01]. In order to quantify the products (H_2 and hydrocarbons) and to study their influence on plasma dynamics, diagnostic methods have to be used. Since emission spectroscopy is one of the standard diagnostics in fusion experiments, the methods of analysis developed and proved in laboratory experiments can also be applied here.

This work focuses on the application of emission spectroscopy to typical processing plasmas (laboratory experiments at the Universität Augsburg) and to the plasma edge of fusion experiments (divertor plasmas at the Max-Planck-Institut für Plasmaphysik, Garching). Emission spectroscopy is an easily handled diagnostic method of plasmas, preferably in the visible spectral range and is frequently

used for detecting impurities in the plasma and for monitoring processing plasmas. Here, relative dependencies of line radiation of atoms and molecular bands can be observed readily. However, to derive plasma parameters from the measured radiation, the interpretation of spectra can be complex due to the amount of information included.

The objective of the underlying investigations is to derive as many as possible plasma parameters from measurements of absolute line radiation of atoms and of molecules, particularly in hydrogen and deuterium plasmas. Special emphasis is given to a detailed analysis to provide reliable results. The interpretation of radiation is supported by population models, which are generally applied in low pressure, low temperature plasmas and are typical models for these non-equilibrium plasmas: corona model and collisional-radiative model. In particular, in molecular plasmas with low degree of dissociation and a variety of dissociation products, the radiation of atoms and molecules originates from various excitation processes: direct excitation and dissociative excitation from different species in the plasma.

Emission spectroscopy in the visible range gives information of the population of excited states which is related to ground state densities by applying the population model. However, results of calculations depend on plasma parameters as electron temperature and electron density but metastable states and self-absorption of resonance lines may also influence population of the higher excited states. Here, laboratory experiments are advantageous because, in comparison to inhomogeneous divertor plasmas, they have well defined parameters along a line of sight. Therefore, emission spectroscopy is applied first to helium and argon laboratory plasmas where the densities of metastable states are measured by using white-light absorption spectroscopy. Furthermore, self-absorption of resonance lines is checked by a comparison of measured and calculated population densities applying the population escape factor method. This method is then simplified for direct applications by introducing correction factors for absorption. Helium and argon are generally used as diagnostic and buffer gases in the laboratory experiments. In particular, a emission line of helium is identified to be preferred for sensitive measurements of electron temperatures in mixtures of hydrogen and helium.

Other diagnostics techniques are applied also in order to determine as many plasma parameters as possible. These results are used to support and confirm interpretation of emission spectroscopy measurements. Spatial profiles of plasma parameters are measured by Langmuir probes in particular the electron density. Line integrated electron densities are determined by microwave interferometry. Neutral particle densities in the plasma chamber, either of gas components or of particles produced in the plasma are measured by a residual gas analyser. Furthermore, some basic balance equations are used to either compare measurements of plasma parameters with calculations or to predict parameters which are not accessible directly by the diagnostic techniques. Here, particle densities of radicals are of main interest.

Collisional-radiative models and modeling of plasma parameters need reliable

input data such as cross sections and rate coefficients for excitation, ionization and dissociation. Therefore, data necessary for the investigations are compiled from literature, critically reviewed and selected if necessary. Since rate coefficients for electron impact are calculated by a convolution of the cross section and the electron energy distribution function, the latter must be determined. For this purpose, calculations of electron energy distribution functions are compared with results from a spectroscopic diagnostic method.

On the basis of the detailed analysis of pure rare gas plasmas, mixtures with hydrogen and deuterium are investigated in laboratory experiments. Here, emission spectroscopy is applied to determine particle densities of atoms and molecules whereas in the plasma edge of fusion experiments flux measurements are preferred. Again special emphasis is given to the interpretation of atomic and molecular hydrogen radiation. Isotope effects are highlighted. Furthermore, a new diagnostic method for the determination of the vibrational population of molecules in technical plasmas is described and established in a variety of experiments. The method is supported by a collisional-radiative model and offers a sensitive diagnostics of electron temperature in cold divertor plasmas of fusion experiments. Results are given which prove the diagnostic method to be complementary to other techniques. In addition, the role of hydrogen molecules in divertor plasmas is investigated in detail, in particular the role of the vibrational population on the recycling regime.

A further important issue in fusion experiments is the plasma wall interaction, which is investigated in laboratory plasmas. Here the interaction of hydrogen plasmas and carbon surfaces is studied, with special respect to the effect of hydrogen isotopes. The diagnostic methods, emission spectroscopy, residual gas analyser and weight loss measurements methods are described briefly and results for chemical erosion of carbon at low temperatures and low ion energies are presented and compared with an established semi-empirical model.

Since hydrogen is also present in methane and silane plasmas, similar diagnostics are applied to methane and silane laboratory plasmas. Furthermore diagnostics of hydrocarbons in methane plasmas contribute to an improved understanding of chemical erosion processes as discussed in the paragraph before. The investigations focus on a comparison of the dissociation channels and on the measurement of the dissociation products. Nitrogen and oxygen plasmas, commonly used for the nitriding and cleaning of films respectively, are also investigated by emission spectroscopy, and the degree of dissociation is determined and compared with those of hydrogen plasmas.

In summary, atomic and molecular emission spectroscopy is shown to be a powerful tool for the diagnostics of low temperature plasmas containing hydrogen and deuterium. Special emphasis is given to the interpretation of measured radiation in particular for molecules. Investigations are carried out in both types of plasmas (laboratory and divertor plasmas) in hydrogen and deuterium in order to obtain scaling laws to other isotopes such as HD, DT or tritium, which are important for future fusion plants.

The report is organized as follows: first typical properties of low pressure,

low temperature plasmas are described together with equilibrium models and some balance equations useful for theoretical predictions. Then the basic experiments are introduced. The next chapter gives an overview over the diagnostic methods, starting with emission spectroscopy which is followed by the diagnostic technique of absorption measurements. Microwave interferometry, Langmuir probes and mass spectroscopy are described as well. Chapter four gives results of helium and argon plasmas in laboratory experiments whereas chapter five deals with results of hydrogen and deuterium plasmas in laboratory discharges as well as in divertor experiments. Results of diagnostics of plasma wall interaction of hydrogen plasmas with carbon surfaces are also presented in this chapter. Investigations of methane and silane plasmas are given in chapter six, which also presents dissociation degrees of various (diatomic) molecular plasmas. The last section summarizes and concludes.

Chapter 2

Low Temperature Plasmas

A useful definition of a plasma is the following [Che74]:

“A plasma is a quasineutral gas of charged and neutral particles which exhibits collective behaviour.”

Plasmas can be characterized by two parameters, density n and temperature T , which cover a wide range of values: 18 and seven orders of magnitude, respectively. In nature, low density (10^6 m^{-3}) and low temperature (0.01 eV) plasmas dominate the interstellar space, whereas inertial confinement fusion plasmas are dense and hot (10^{27} m^{-3} and 10^4 eV). Other plasmas cover the range between. In plasma physics, temperature is frequently measured in electron volts (eV) where 1 eV corresponds to 11605 K. In thermal equilibrium the particle motion is given by a Maxwellian distribution and the average kinetic energy $\langle E \rangle$ is related to temperature by: $\langle E \rangle = 3/2 k T$ ($1/2 k T$ per degree of freedom). In most cases, plasmas are not fully ionized and are described by densities and temperatures for the species separately neutrals, ions and electrons. Quasineutrality of a plasma ensures that the ion density is equal to the electron density ($n_i = n_e$), whereas because of their similar masses the ion temperature is closely coupled with the temperature of neutral particles (atoms or molecules) and is usually lower than the electron temperature ($T_n \approx T_i < T_e$). This is especially true for low temperature plasmas, which are not in thermal equilibrium.

2.1 Typical plasma parameters

Low temperature plasmas are frequently used for technical applications and can be generated by various frequencies of power supplies: DC (direct current), RF (radio-frequency, 1 – 100 MHz) and MW (microwave, 1 – 100 GHz). Due to the small mass of the electrons and their fast mobility these particles are heated preferentially in discharges. Depending on the frequency applied and the generator input power, the plasma discharges operate in a wide pressure range, typically

between 0.01 and 10000 Pa. These plasmas are often called low pressure plasmas. Typical plasma parameters are $n_e = 10^{15} - 10^{18} \text{ m}^{-3}$ and $T_e = 1 - 10 \text{ eV}$. The manifold of processing plasmas, i.e. technical plasmas, and their applications are described, e.g., in [Gri94, Rot95, Jan92].

In the following the characterization of low temperature plasmas is restricted to the fraction of low pressure plasmas which are used for industrial applications and as laboratory experiments, in particular in case of this work, for diagnostic purposes. Therefore, typical glow discharges (DC plasmas), RF discharges at 13.56 and 27.12 MHz, and MW plasmas at 2.45 GHz in the pressure range of 0.1 – 1000 Pa are illustrated.

2.1.1 Densities

In the pressure range of some Pa electrons accelerated by the electric field collide with neutral particles and produce ionization. Since the collision frequency ν_c is high, the mean energy of the electrons remains lower than the ionization energy of the neutrals. As a consequence, low pressure plasmas are mostly singly ionized plasmas with a low degree of ionization $\alpha = n_i/(n_n + n_i) \approx n_e/n_n = 10^{-3} - 10^{-6}$. Electron densities are in the range of $n_e = 10^{15} - 10^{18} \text{ m}^{-3}$. Typically, DC and RF discharges belong to the lower density range whereas MW discharges belong to the higher end of n_e .

2.1.2 Temperatures

The heavy particle temperature of these plasmas is in most cases slightly higher than room temperature ($T_n, T_i : \approx 300 - 1000 \text{ K}$) whereas electron temperature is considerably higher: $T_e = 1 - 10 \text{ eV}$. Since the density of electrons is much lower than the neutral particle density, the heat transfer to surfaces or chamber walls is low and is dominated by the neutral particles. As a consequence, surfaces inserted into such a plasma will not be heated by electrons and remain at the neutral particle temperature which is an advantage for surface processing. For the heavy particles a Maxwell energy distribution function can be used and a temperature is defined for these particles. However, the energy distribution of the electrons can deviate from a Maxwellian distribution, since the electrons make inelastic collisions. Thus, an assignment of a temperature to the electrons may not be justified and has to be checked for each discharge separately.

2.1.3 Electron energy distribution function (EEDF)

The velocity distribution of particles is described by a Maxwell distribution function if elastic collisions are dominant. In a plasma, each species (neutrals, ions and electrons) may have his own temperature, i.e. Maxwellian distribution function. Due to high density the neutrals thermalize among themselves by elastic collisions. In addition, the heavy particle temperature is low in comparison with

the electrons temperature, which means that the high velocity (or energy) tail is not relevant for inelastic collisions. For electrons the situation is different. In terms of particle energies the Maxwell energy distribution is given by:

$$f(E) dE = \frac{2}{\sqrt{\pi}} \frac{\sqrt{E}}{(kT_e)^{3/2}} \exp(-E/kT_e) dE. \quad (2.1)$$

The distribution function $f(E)$ depends on the energy of the electrons E and is characterized by the electron temperature T_e . If the electrons make inelastic collisions, deviations from a Maxwellian distribution occur, especially in the energy region above the first energy threshold of the inelastic process. Examples are excitation of an atom from the ground state which needs the threshold energy E_{thr} or ionization requiring the ionization energy E_{ion} . Since the electrons lose their energy, the low energy part of the distribution function is enhanced and the high energy part is depleted. A special kind of such a shape of the energy distribution function is described by a Druyvesteyn distribution [Dru30]:

$$f(E) dE = \frac{2}{\Gamma(3/4)} \left(\frac{2\Gamma(5/4)}{3\Gamma(3/2)} \right)^{3/2} \frac{\sqrt{E}}{(kT_e)^{3/2}} \exp \left(- \left(\frac{2\Gamma(5/4)}{3\Gamma(3/4)} \right)^2 (E/kT_e)^2 \right) dE \quad (2.2)$$

where $\Gamma(x)$ is the Gamma-function. The distribution function is normalized so that

$$\int_0^\infty f(E) dE = 1 \quad (2.3)$$

is fulfilled. In detail, the electron energy distribution function (EEDF) depends mainly on the neutral species and their densities, on the applied electric field and also on the generator frequency leading to individual distribution functions for the particular discharge in question. Such functions have been calculated by many authors for a variety of gases and discharge conditions (see e.g. [CGL93] for a general overview). A useful general statement for the applicability of a Maxwellian distribution is given in [FL84] which correlates the ionization degree with the type of distribution, i.e. a Maxwellian distribution is given for $\alpha \gtrsim 10^{-4}$. Therefore it can be expected that typical DC and RF discharges have EEDFs which are non-Maxwellian and tend to a Druyvesteyn distribution (due to operating at higher pressure), whereas in MW plasmas EEDFs are close to a Maxwellian distribution.

2.2 Equilibrium and population models

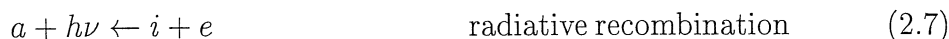
Due to the collective behaviour of particles the plasma can be described by statistical mechanics. In thermodynamic equilibrium (TE) only one temperature exists and the following four equilibrium distributions are valid:

- Planck blackbody function for radiation energy
- Saha equation relating the number densities of atoms, ions and electrons
- Boltzmann distribution of population among excited states
- Maxwell distribution of particle velocities for all types of particle

TE requires that every collision and radiation process is in equilibrium with the corresponding inverse process. Most plasmas are not in thermal equilibrium and equilibrium equations are only partly fulfilled. If the radiation density is below the blackbody level but the three other distributions are still valid, then this is called the local thermodynamic equilibrium (LTE). This is a collision dominated regime. Partly local thermodynamic equilibrium (PLTE) is a further classification: LTE holds down to a definite excited level called the thermal limit. Typical applications for LTE and PLTE plasmas are stabilized arcs at atmospheric pressure. Details of these equilibrium equations and their limitations can be found in, e.g., [TLJ99, LH68, Gri64]. For the variety of laboratory plasmas further restrictions have to be made which follow the order of the four equilibrium equations given above, i.e. Maxwell distribution of each particle species alone is valid longest. Frequently these plasmas are described by corona equilibrium or the collisional-radiative model until they reach Boltzmann equilibrium. Low temperature, low pressure plasmas are of this type.

2.2.1 Corona model

In low temperature plasmas where electron densities and ionization degrees are low and each particle species is defined by its own temperature (if this is possible), equilibrium can be described by the corona model. Corona equilibrium is applicable to the corona of the sun where electron temperature is high (≈ 100 eV) and electron density low ($\approx 10^{12} \text{ m}^{-3}$). The radiation density is also low and it is assumed that upward transitions are due to electron collisions while downward transitions occur by radiative decay. The balance equations concerning population and ionization are given as follows:



a and i denote the atom and the ion in its ground state, a^* is an electronically excited atom, $h\nu$ describe the radiation and e_f , e_s denote the fast and slow electron. The inverse processes of (2.4) and (2.6), which are electron impact de-excitation and three-body recombination, are not relevant because electron density, excited state population and ionization degree are all low. Since radiation density is also low, self-absorption, which is the inverse of processes (2.5) and (2.7)

is not important either. In its simplest form the corona equation for excitation is:

$$n_1 n_e X_{1,p}^{exc}(T_e) = n(p) \sum_k A_{p,k}, \quad (2.8)$$

where $n(p)$ is the population density in the electronically excited level p . $A_{p,k}$ denotes the Einstein A coefficient (transition probability). Equation (2.8) requires that level p is populated by electron impact excitation from the ground state and depopulation occurs only by spontaneous emission. Since populations of excited levels are orders of magnitude lower than the population of the ground state n_1 , the latter can be replaced by the neutral particle density n_n . $X_{1,p}^{exc}(T_e)$ is the rate coefficient for electron impact excitation which depends on electron temperature T_e and is given by integrating the excitation cross section $\sigma_{1,p}(E)$ over the EEDF:

$$X_{1,p}^{exc}(T_e) = \langle \sigma_{1,p}(v) v \rangle = \int_{E_{thr}}^{\infty} \sigma_{1,p}(E) \sqrt{\frac{2E}{m_e}} f(E) dE. \quad (2.9)$$

Electrons below the energy threshold of the process in question do not contribute to the excitation. Since in most cases T_e is lower than E_{thr} only electrons in the high energy part of the EEDF lead to excitation and the cross section around the energy threshold has to be known precisely.

The corona model gives the following balance for ionization:

$$n_Z n_e S_{Z,Z+1}(T_e) = n_{Z+1} n_e \alpha(T_e). \quad (2.10)$$

n_Z and n_{Z+1} denote the particle density in the ionization stage Z and $Z + 1$ respectively. $S_{Z,Z+1}(T_e)$ is the rate coefficient for electron impact ionization which is again given by Eq. (2.9) using the corresponding ionization cross section. The radiative recombination coefficient $\alpha(T_e)$ depends also on T_e . The ionization degree is independent of electron density:

$$\alpha = \frac{n_i}{n_n} = \frac{S(T_e)}{\alpha(T_e)}. \quad (2.11)$$

Often the corona equations (2.8) and (2.10) have to be extended by including electron impact excitation from metastable levels since their population is considerable and cross sections from these states into higher excited states are orders of magnitude higher than cross sections for ground state excitation. Other processes, such as self absorption of resonance lines or dissociative excitation of atoms from molecules, will be discussed later but can be implemented easily in the balance equations.

If each process of (2.4) – (2.7) is in equilibrium with the inverse process (detailed balance) one would get a Boltzmann distribution (Eq. (2.12)) among the excited states and the Saha equation (Eq. (2.13)) would be valid, which means the plasma is in thermal equilibrium (or LTE or PLTE). For the relative population of level p to the ground state the Boltzmann distribution yields:

$$\frac{n(p)}{n_1} = \frac{g_p}{g_1} \exp\left(-\frac{E_p}{kT_e}\right) \quad (2.12)$$

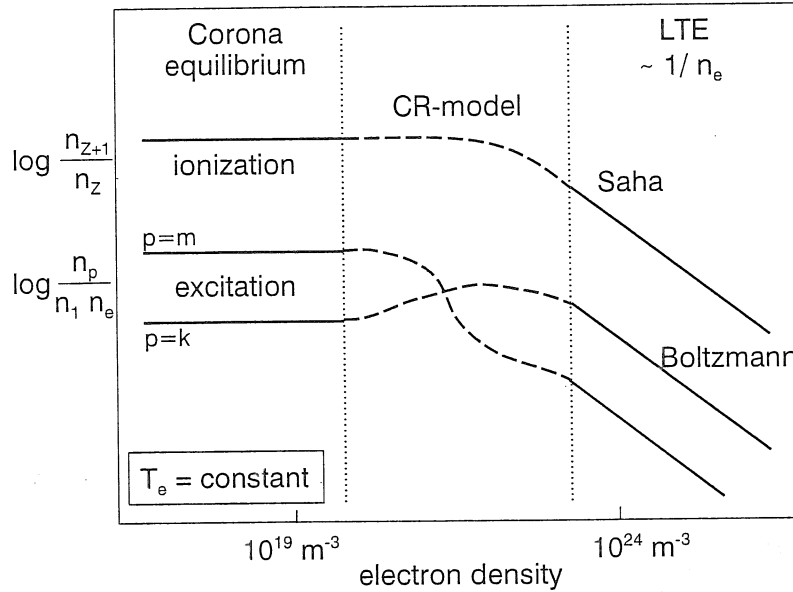


Figure 2.1: Dependence of the ionization and excitation balance on electron density in corona equilibrium and LTE. The intermediate range can be described by collisional–radiative models.

with the statistical weights g_p and g_1 of the levels involved and the energy E_p of level p . The ionization balance is given by the Saha distribution:

$$n_e \frac{n_{z+1}}{n_z} = \frac{g_{z+1}}{g_z} 2 \frac{(2\pi m_e kT_e)^{3/2}}{h^3} \exp\left(-\frac{E_{ion}}{kT_e}\right). \quad (2.13)$$

Assuming single charged ions the left hand side of the equation is equal to n_e^2/n_1 and the ionization degree increases with decreasing electron density.

Figure 2.1 summarizes, schematically, how the corona equations, the Boltzmann and Saha equation depend on electron density. Rough electron density limits for application of these two types of equilibrium are given. In the range between, so-called collisional–radiative models (CR-model) have to be applied, in which a balance of collisional and radiative processes for each level of an atom or molecule is considered. They depend on more parameters than electron density and electron temperature particularly they also depend on properties of the atoms or molecules themselves and bridge the region between corona and Boltzmann, Saha equilibrium in a complex manner.

2.2.2 Collisional–radiative model

The corona model can be extended by taking into account population and depopulation processes amongst a set of relevant levels so that the time development

of the population density of state p in a CR-model is given by:

$$\begin{aligned}
 \frac{dn(p)}{dt} = & \sum_{k < p} n(k) n_e X_{k,p}^{exc} + \sum_{k > p} n(k) n_e X_{k,p}^{de-exc} \\
 & - \sum_{k < p} n(p) n_e X_{p,k}^{de-exc} - \sum_{k > p} n(p) n_e X_{p,k}^{exc} \\
 & - \sum_{k < p} n(p) A_{p,k} + \sum_{k > p} n(k) A_{k,p} \\
 & - n(p) n_e S_p + n_e n_e n_i \beta_p + n_e n_i \alpha_p .
 \end{aligned} \tag{2.14}$$

The first two terms of Eq. (2.14) are populating processes by electron impact from all levels $k \neq p$. The inverse depopulating processes with the corresponding rate coefficients are described by the next two terms. Following these, the fifth and sixth terms describe spontaneous emission from and into state p . The last three terms take into account ionization from the specific level and recombination processes into this state, i.e. three-body and radiative recombination. Furthermore, opacity, i.e self absorption of emission lines, may be important and can be included in the equation by reducing the transition probability by the population escape factor (Sec. 2.2.4). In most cases the time derivative can be assumed to be negligible (quasi-stationary states)

$$\frac{dn(p)}{dt} = 0 , \tag{2.15}$$

except for the ground state and metastable states (if they exist). For these, particle transport may be important and one then has rate equations for each species. According to the quasi-steady-state solution the set of coupled differential equations (2.14) is transformed into a set of coupled linear equations which depend on the ground state density and ion density. These equations are readily solved in the form:

$$n(p) = R_0(p) n_i n_e + R_1(p) n_1 n_e . \tag{2.16}$$

$R_0(p)$ and $R_1(p)$ are the so-called collisional-radiative coupling coefficients describing ionic and ground state population and depopulation processes, respectively. They are functions of n_e and T_e , the latter arising from temperature dependence of the rate coefficients.

The population density is also often expressed in terms of the Saha-Boltzmann equilibrium using a normalized population density, i.e. the Saha decrement:

$$\rho(p) = \frac{n(p)}{n_E(p)} \quad \text{with} \quad n_E(p) = Z(p) n_i n_e . \tag{2.17}$$

$Z(p)$ is the reciprocal value of the right hand side of the Saha equation (2.13) applied to state p . This leads to the following expression for the population density:

$$\rho(p) = r_0(p) + r_1(p) \rho(1) , \tag{2.18}$$

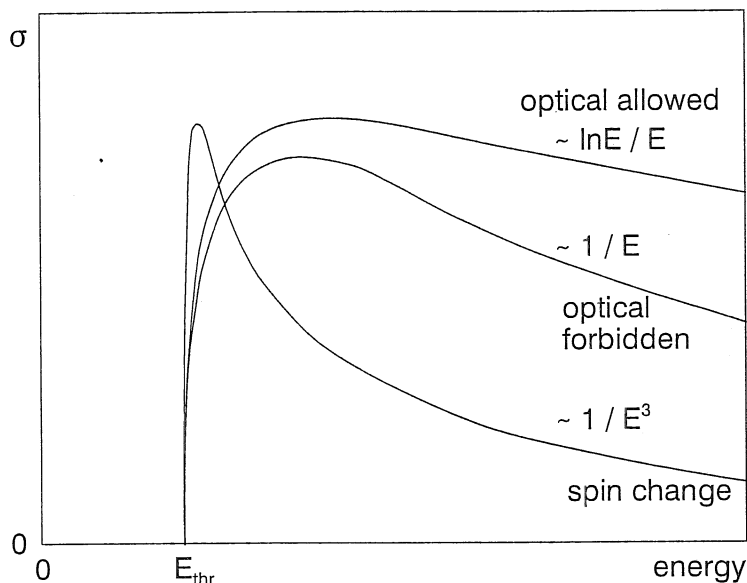


Figure 2.2: Typical shapes of electron impact cross sections for three types of transitions.

where $r_0(p)$ and $r_1(p)$ are called the (reduced) population coefficients.

For atoms with simple and clear energy level structure such as hydrogen and helium a variety of CR-models exist, namely the models of Drawin [Dra69] or Johnson&Hinnov [JH73] for hydrogen and Drawin&Emard [DEK73, DE73] for helium. These tabulate the (reduced) population coefficients for several plasma conditions. Fujimoto has CR-models for atomic hydrogen [Fuj79b, Fuj79c] and helium [Fuj79a] which includes metastable states. Because of the increasing number of levels with atomic number, CR-models are rare for other elements.

A common issue arising in the construction of CR-models is the data base needed for cross sections or rate coefficients. Since, for a specific element, not all cross sections for the manifold of transitions are known, simplifications or extrapolations have to be made, especially for higher excited levels. Cross sections or rate coefficients can be calculated by various methods, e.g. Coulomb-Born or Born-Bethe approximation for excitation or Lotz formula for ionization, which are in particular valid for high energies $E \gg E_{thr}$. A summary of the various methods is given, for example, in [SVY81] or [She81]. Many cross sections have been measured by different methods, mostly electron beam experiments. They have to be compiled from literature and critically reviewed. Unfortunately, in many cases data points are measured at high energies. For many applications a Maxwellian distribution of collision partner velocities is assumed and rate coefficients are implemented as polynomial fits in a computer code. Since low temperature plasmas are characterized by low ionization degree and $T_e < E_{thr}$, the EEDF have to be known, and accurate cross section data near threshold energy are necessary to get reliable rate coefficients.

Cross sections for excitation can be divided into three groups: cross sections

for optical allowed transitions, optical forbidden transitions and transitions with spin change (intercombination). Their characteristic dependence on energy is sketched in Fig. 2.2. For optical allowed transitions the cross section decreases asymptotically with $\ln E/E$ and in the optical forbidden case with $1/E$. Transitions changing the multiplet system show typically a $1/E^3$ behaviour.

Cross sections for electron impact de-excitation can be calculated by using detailed balancing:

$$n_k n_e X_{k,p}^{exc} = n_p n_e X_{p,k}^{de-exc} \Rightarrow X_{p,k}^{de-exc} = X_{k,p}^{exc} \frac{n_k}{n_p} \bigg|_{TE} = X_{k,p}^{exc} \frac{g_k}{g_p} \exp\left(\frac{\Delta E}{kT_e}\right). \quad (2.19)$$

This assumes population of level p by electron impact from level k and depopulation by the inverse process without any competing processes, i.e. population densities of these levels are in thermal equilibrium (TE) among each other. ΔE is the energy difference between the two levels.

2.2.3 Effective rate coefficients

The emitted power of a transition from level p to level j per unit volume and solid angle is given by the line emission coefficient $\varepsilon_{p,k}$:

$$\varepsilon_{p,k} = \frac{h\nu}{4\pi} n(p) A_{p,j}. \quad (2.20)$$

The number of emitted photons per unit volume and time $\dot{N}_{p,j}$ is then written as follows:

$$\dot{N}_{p,j} = n(p) A_{p,j}, \quad (2.21)$$

which means that emission spectroscopy yields the population density in the upper state of the measured transition. On the other hand population densities can be calculated by the corona equilibrium (2.8) resulting in:

$$\dot{N}_{p,j} = n_1 n_e X_{1,p}^{exc}(T_e) \frac{A_{p,j}}{\sum_k A_{p,k}} = n_1 n_e X_{p,j}^{em}(T_e), \quad (2.22)$$

with the emission rate coefficient $X_{p,j}^{em}(T_e)$ given by the excitation rate coefficient times the branching ratio:

$$b_{p,j} = \frac{A_{p,j}}{\sum_k A_{p,k}}. \quad (2.23)$$

If the corona equation for excitation has to be extended by other processes, e.g. excitation out of metastable states, or if a CR-model has to be applied for the plasma in question, effective rate coefficients can be calculated from the predicted population densities by combining Eq. (2.21) and Eq. (2.22):

$$X_{p,j}^{eff}(T_e, \dots) = \frac{n(p)}{n_i n_e} A_{p,j}, \quad (2.24)$$

which gives $X_{p,j}^{em}(T_e)$ in the simplest corona case. As a consequence all populating and depopulating processes which are not included in Eq. (2.22) are now represented by the effective rate coefficient. Due to the manifold of processes included in a CR-model this rate coefficient no longer depends only on T_e but also on n_e and other plasma parameters. For evaluation of spectroscopic data, i.e. \dot{N} , the corona model can be applied together with the effective rate coefficient calculated by using a CR-model.

2.2.4 Radiation transfer and self-absorption

Plasmas in which self-absorption of radiation can be neglected are called optically thin. Since low temperature plasmas are collisional-dominated plasmas they can be treated as optical thin in a first approximation. However, due to high population density in the ground state in comparison with excited states, reabsorption of the strong resonance lines may occur, in particular in plasmas with large dimensions. Then, the effect of radiation trapping must be taken into account and the influence of the radiation field on the population density of the atomic levels must be considered. Furthermore, the intensity measured at any wavelength is no longer the emission coefficient itself and the line shape is influenced too. Due to the complexity of reabsorption a general solution does not exist and the problem has been treated in different approximations. A general overview of optical thick plasmas and their description is given in [LH68, TLJ99, Hut87].

The following summarizes the essential definitions and formulae necessary to introduce a method frequently used for considering opacity in CR-models — the population escape factor method. For simplicity it is assumed that the plasma is homogeneous over its whole length l , i.e. T_e , n_e and n_1 are uniform.

The passage of radiation through a plasma has to be described by the radiative transport equation:

$$\frac{dI_\nu}{dl} = \varepsilon_\nu - \kappa(\nu) I_\nu . \quad (2.25)$$

The change of intensity I_ν when passing a unit path length dl is given by the emission within this layer and by the decrease of the intensity due to absorption along dl . ε_ν is the spectral emission coefficient and $\kappa(\nu)$ the absorption coefficient per m, both depending on frequency ν . It has to be mentioned that $\kappa_{k,p}(\nu)$, the spectral line absorption coefficient is the effective absorption coefficient, i.e. absorption minus stimulated emission. Since the latter is not of importance for the plasmas considered here, stimulated emission is neglected. By introducing the so-called source function $S_\nu = \varepsilon_\nu / \kappa(\nu)$ the radiative transport equation (2.25) can be written as

$$\frac{dI_\nu}{d\tau} = S_\nu - I_\nu \quad \text{with} \quad d\tau = \kappa(\nu) dl . \quad (2.26)$$

$d\tau$ is the optical depth and $\tau(\nu)$ describes the optical thickness at frequency ν , of a plasma with length l :

$$\tau(\nu) = \kappa(\nu) l . \quad (2.27)$$

For homogeneous plasmas, Eq. (2.26) can be readily integrated ($I_\nu(0) = 0$):

$$I_\nu = \frac{\varepsilon_\nu}{\kappa(\nu)} (1 - \exp(-\kappa(\nu) l)) = S_\nu (1 - \exp(-\tau(\nu))) . \quad (2.28)$$

One definition of optical thin is that $\kappa(\nu) l = \tau(\nu) \ll 1$, since in this case the exponential function in Eq. (2.28) can be approximated by using its linear expansion and I_ν is correlate only to the spectral emission coefficient.

The total area under the absorption coefficient is related to Einstein's transition probability for absorption $B_{k,p}$ or with the oscillator strength f (f-value) by:

$$\int_{line} \kappa_{k,p}(\nu) d\nu = n_k B_{k,p} \frac{h \nu_0}{c} = n_k f \frac{e^2}{4 \varepsilon_0 m_e c} = n_k A_{p,k} \frac{g_p}{g_k} \frac{c^2}{\nu^2 8 \pi} . \quad (2.29)$$

ν_0 is the frequency of the line centre, c the velocity of light and ε_0 the permittivity of free space. in comparison to the reabsorption of atomic lines, the reabsorption of molecular bands is rare because of the distribution of the absorption coefficient over the variety of rotational lines in the resolved rotational structure.

The spectral emission coefficient and the transition probability are related by:

$$\int_{line} \varepsilon_\nu(\nu) d\nu = \varepsilon_{p,k} = n_p A_{p,k} \frac{h \nu_0}{4 \pi} , \quad (2.30)$$

using the line emission coefficient. The emission and absorption line profiles are usually assumed to be equal. It has to be kept in mind that to convert frequencies into wavelengths c/λ has to be used whereas c/λ^2 holds for converting spectral coefficients.

The equation for the population balance in a CR-model, Eq. (2.14), can now be extended by an expression for the absorption from all lower levels, which is a populating process so that:

$$\frac{dn(p)}{dt} = \dots - \sum_{k < p} n(p) A_{p,k} + \sum_{k < p} \int_{line} \frac{4 \pi}{h \nu} \kappa_{k,p}(\lambda) L_\lambda(\lambda) d\lambda + \dots \quad (2.31)$$

The frequency dependence has been changed to a wavelength dependence and the spectral radiance $L_\lambda(\lambda)$ is used instead of the spectral intensity. Furthermore, isotropic radiation in the plasma volume is assumed. The first term represents the losses by spontaneous emission and is already included in Eq. (2.14). To combine spontaneous emission and absorption, the latter is subtracted to give:

$$\begin{aligned} \frac{dn(p)}{dt} &= \dots - n(p) \sum_{k < p} A_{p,k} \left(1 - \frac{4 \pi}{n_p A_{p,k} h \nu} \int_{line} \kappa_{k,p}(\lambda) L_\lambda(\lambda) d\lambda \right) + \dots \\ &= \dots - n(p) \sum_{k < p} A_{p,k} \Theta_{p,k} + \dots \end{aligned} \quad (2.32)$$

Thus optically thin transition probabilities are reduced by the population escape factors $\Theta_{p,k}$ which can be expressed as the ratio of absorbed to emitted radiation power. The population escape factors describe the influence of the radiation field in the plasma volume on the population of the electronic states. They may not be mixed up with escape factors which represent calculations of the radiation transfer along a line of sight through the plasma, and which are necessary for analysing measured line radiation influenced by self-absorption. As can be seen from Eq. (2.32) the population escape factor is smaller than 1 and depends on the absorption coefficient, the line shape and the plasma geometry.

The escape factor method was first introduced by Holstein [Hol47, Hol51] who also derived an approximation for a plasma of large optical thickness:

$$\Theta(\tau_0) \approx \frac{1}{\tau_0 \sqrt{\pi \ln \tau_0}} \quad \text{with} \quad \tau_0 = \kappa(\nu_0) b. \quad (2.33)$$

b is the characteristic length of about half the shortest dimension in the plasma and $\kappa(\nu_0)$ is the absorption coefficient in the line centre. There are many authors who have developed approximate formulae for the dependence of the escape factor on the optical thickness of the plasma, usually under the assumption of a Doppler line profile and cylindrical plasma geometry.

To calculate escape factors the definition of Θ implied in Eq. (2.32) can be converted as follows:

$$\begin{aligned} \Theta_{p,k} &= 1 - \frac{4\pi}{n_p A_{p,k} h \nu} \int_{line} \kappa_{k,p}(\lambda) L_\lambda(\lambda) d\lambda \\ &= 1 - \frac{1}{\varepsilon_{k,p}} \int_{line} \varepsilon_\lambda (1 - \exp(-\kappa_{k,p}(\lambda) b)) d\lambda \end{aligned} \quad (2.34)$$

using the solution of the radiative transport equation (2.28). The population escape factor is then given by:

$$\Theta_{p,k} = \int_{line} P_\lambda \exp(-\kappa_{k,p}(\lambda) b) d\lambda \quad \text{with} \quad \int_{line} P_\lambda d\lambda = 1, \quad (2.35)$$

in terms of spectral line profile P_λ . Examples of escape factors for various plasma profiles and plasma geometries in low temperature plasmas are given in [Beh98] together with a detailed derivation of the formulae. Figure 2.3 shows escape factors for hydrogen as a function of the optical thickness in the line centre $\kappa(\lambda_0)$ assuming a Doppler profile, cylindrical plasma geometry and homogeneous plasma. The position of the escape factors of the Lyman series are indicated for an atomic hydrogen density of $n_H = 10^{20} \text{ m}^{-3}$ with a gas temperature $T_g = 1 \text{ eV}$ (corresponding to a Doppler width of $\Delta\lambda_D \approx 0.01 \text{ nm}$ for L_α) and a radius of the plasma cylinder of 5 cm. $\kappa(\lambda_0)$ is proportional to the number density of the lower state, in this case n_1 , the oscillator strength f and the Doppler width:

$$\kappa(\lambda_0) = n_1 \frac{\lambda_0}{c} \frac{f e^2}{4 \varepsilon_0 m_e} \sqrt{\frac{\mu m_p}{2 \pi k T_g}}. \quad (2.36)$$

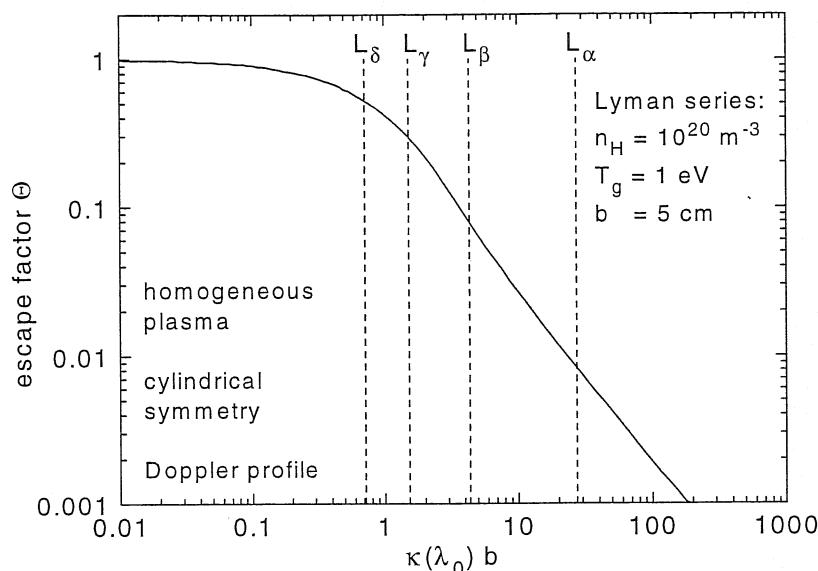


Figure 2.3: Escape factors for a hydrogen plasma with radius b . The positions of the first four Lyman lines are indicated.

where μ is the atomic mass number. It is obvious from Fig. 2.3 that the first lines of the Lyman series are optically thick (in particular L_α) for typical parameters of low density plasmas. This may have consequences for population densities of higher levels too. For a quantification CR-modeling is required.

As discussed in Sec. 2.2.3 the consequences of repopulating processes can be taken into account by introducing effective rate coefficients, and this can be done for reabsorption as well. Correction factors K_{abs} will be introduced here to correct the optically thin effective emission rate coefficients for the influence of opacity. These factors depend on the specific emission line, T_e , n_e , n_1 , T_g i.e. the set of parameters described in this section.

For convenience, important radiative quantities are summarized in Tab. 2.1.

name	symbol	unit
radiant flux	Φ	W
intensity	I	W / sr
radiance	L	W / m ² / sr
spectral radiance	$L_\lambda(\lambda)$	W / m ² / nm / sr
	$L_\nu(\nu)$	W / m ² / Hz / sr
radiation density	$u_\nu = 4\pi L_\nu / c$	W s / m ³ / Hz
line emission coefficient	$\varepsilon_{p,k} = \dot{N}_{p,k} h\nu / 4\pi$	W / m ³ / sr
line radiation	$\dot{N}_{p,k}$	photons / m ³ / s

Table 2.1: Compilation of radiative quantities frequently used.

2.3 Modeling of plasma parameters

To calculate plasma parameters several approaches can be used: plasmas can be described as fluids (fluid theory) or plasma as particles (kinetic theory); pure hydrodynamic models or hybrid models can be used. The choice depends on the type of plasma, on the parameters which are to be predicted and on whether or not a self-consistent solution is required. The following sections describe briefly some useful balance equations which are applicable to low pressure, low temperature plasmas (technical plasmas) and which complement experimental diagnostics.

2.3.1 Particle balance and confinement times: particle densities

Plasma processing often requires a specified particle density for optimizing films. Since, in most cases direct measurements of radical densities produced by electron impact dissociation or heavy particle collisions is not trivial, the densities of dissociation products are calculated and then compared with selected densities accessible to measurements. Prominent examples are methane plasmas producing diamond-like coatings or silane plasmas for amorphous or crystalline silicon films. Here, the important point is the question of the dominant species: are the CH_3 or CH_2 densities substantial for film growing? Density calculations can give an answer for most species in these plasmas under various conditions but do not describe, in the first step, the surface physics, in particular the interaction of plasmas with the surface produced.

Particle densities in a plasma can be obtained from a particle balance assuming a stationary state in which the production of particles must be equal to the integral losses. Volume losses are assumed to be negligible. Furthermore, it is assumed that the shape of spatial profiles does not change. Losses of particle species k with density n_k can be characterized by an average confinement time τ_k , which represents the mean residence time of particles in the plasma volume and is described in detail in the next paragraphs. Each particle species, i.e. the volume averaged density, is then given by a balance equation of the form:

$$\begin{aligned}
 j_k + n_e \sum_p R_{p;kr} n_p + \sum_{\substack{p,q \\ p < q}} R_{pq;kr} n_p n_q \\
 - n_e n_k \sum_{\substack{r,s \\ r < s}} R_{k;rs} - n_k \sum_{\substack{p,r,s \\ p < r < s}} R_{kp;rs} n_p \\
 - \frac{n_k}{\tau_k} = 0 .
 \end{aligned} \tag{2.37}$$

The first source term is the gas flow j_k of species k per unit volume. Particles of species k are produced by electron impact processes from the educt species p with rate coefficient $R_{p;kr}$ and by heavy particle collisions of species p and q with rate coefficient $R_{pq;kr}$. Particles are lost by electron impact reactions of

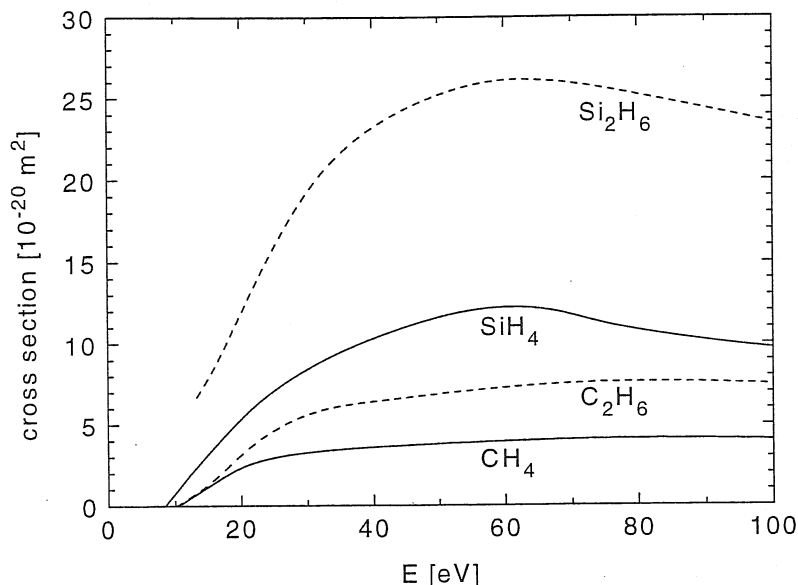


Figure 2.4: Electron impact dissociation cross sections for CH_4 , SiH_4 and C_2H_6 , Si_2H_6 [PSR⁺ 82].

species k producing particles of species r and s (rate coefficient $R_{k;rs}$) and by heavy particle collisions of species k with species p (rate coefficient $R_{kp;rs}$). Rate coefficients for electron impact processes depend on electron temperature, whereas gas temperature is relevant for heavy particle collisions.

The number of equations depends on the number of radicals resulting from dissociation or formation. The reaction chains and, in particular, the rate coefficients of each process have to be known. Because of the large number of reactions, especially in the case of reactive species, data have to be compiled, critically reviewed and, completed by scaling laws. The selection criteria for considering a specific reaction in the model are the absolute value of the number densities of the species involved and the values of the reaction rates. Additionally, if metastable states are involved, e.g. in mixtures with noble gases He or Ar, their densities have to be treated individually and Penning reactions have to be considered, increasing ionization or dissociation. Figure 2.4 gives an example for total dissociation cross section of CH_4 , SiH_4 and C_2H_6 , Si_2H_6 by electron impact. Higher hydrocarbons or silanes are produced in methane or silane plasmas, respectively. A comparison of methane and silane plasmas on the basis of the dissociation cross sections gives higher dissociation of silane plasmas than methane plasmas at comparable densities and temperatures. Since rate coefficients are based on cross sections, the knowledge of the EEDF is essential; it is normally assumed to be Maxwellian. Further input data are T_e , n_e , τ_k which can be either calculated by additional formulae (described in the next paragraphs) or are known from measurements as is usually the case for T_g and j_k .

In addition, the plasma quasineutrality yields that the sum over all ion densi-

ties is equal to the electron density. In some plasmas the production of negative ions may play a role, e.g. $H_2 \rightarrow H^-$ or $CF_4 \rightarrow C_xF_y^-$, and has to be considered in the calculations.

The relation between the pressure in the plasma chamber and the neutral particle densities is given by Dalton's law:

$$p = n_n k T_g \quad \text{and} \quad n_n = \sum_k n_k. \quad (2.38)$$

The partial pressure of ions and electrons can be neglected in low temperature plasmas because of their low densities.

Collision and diffusion parameters

Random collisions of particles, e.g. electrons with neutrals, are expressed by the collision parameter, i.e. the mean free path:

$$\lambda_m = \frac{1}{n_n \sigma}. \quad (2.39)$$

The cross section σ describes the probability of momentum loss. The mean time between collisions τ_m for particles of velocity v is given by:

$$\tau_m = \frac{\lambda_m}{v}. \quad (2.40)$$

Now, assuming a Maxwell velocity distribution the collision frequency ν is then $\nu = n_n \bar{\sigma} \bar{v}$, whereas the mean frequency of collisions is given by $\tau^{-1} = n_n \sigma v$.

The motion of particles in a plasma caused by a density gradient is described by diffusion, i.e. Fick's law, in which the net flux from dense plasma regions to less dense regions (e.g. the wall of a reactor chamber) occurs because more particles starts in the dense region. The transport coefficient is the diffusion coefficient D_k . It is assumed that there is no additional electrical and magnetic field and plasma waves are also neglected.

The confinement time is the mean residence time of particles in the plasma volume and is given by the diffusion length Λ and the diffusion coefficient:

$$\tau_k = \frac{\Lambda_k^2}{D_k}. \quad (2.41)$$

The diffusion length is a characteristic of the plasma geometry. In case of diffusion in a cylinder of radius R and length H one finds:

$$\frac{1}{\Lambda^2} = \left(\frac{2.405}{R} \right)^2 + \left(\frac{\pi}{H} \right)^2, \quad (2.42)$$

which contains the first zero of the zero order Bessel function, which occurs in the solution of the differential equation for diffusion in a infinitely long cylinder. Particles leaving the plasma by diffusion will be adsorbed at the surfaces which

means the sticking coefficient is $s = 1$. Calculations of confinement times or diffusion lengths depending also on plasma geometry have been carried out by [Möl93] and [Cha87] including formulae for $s < 1$. A simple approach is carried out by introducing a extrapolation length l_α scaled with the characteristic length of the plasma chamber l_d (volume to surface ratio):

$$(\Lambda_s)^2 = \Lambda^2 + l_\alpha l_d \quad \text{and} \quad l_\alpha = \frac{2}{3} \lambda_m \frac{2-s}{s}. \quad (2.43)$$

The overall confinement time is calculated from the diffusion time of the particles and the confinement time due to the pumping gas flow τ_p :

$$\frac{1}{\tau} = \frac{1}{\tau_{diff}} + \frac{1}{\tau_p}. \quad (2.44)$$

Strictly speaking, one has to distinguish between the type of particle flow, which depends on the pressure. Diffusion is characterized by $\lambda_m \ll l_d$, i.e. particle collisions dominate and one has a laminar flow. Molecular flow occurs if $\lambda_m \gg l_d$, i.e. wall collisions dominate. This condition is especially fulfilled at very low pressures. The range between is described by the Knudsen number. A simple approximation for the range between is an interpolation: $1/\tau = 1/\tau_{lam} + 1/\tau_{mol}$.

Confinement times of neutral particles

The diffusion coefficient of neutral particles D_n (diffusion of species 1 in species 2) can be calculated by applying the hard-sphere model [HCB64] which gives:

$$D_n = \frac{3\pi}{8} \frac{1}{(n_1 + n_2) \sigma_{1,2}} \sqrt{k T_g \frac{m_1 + m_2}{2 m_1 m_2}}, \quad (2.45)$$

using the averaged cross section of the two species with diameter d_1 and d_2 : $\sigma_{1,2} = \pi/2 (d_1 + d_2)$. The confinement time is then given by Eq. (2.41). Each particle species has its own confinement time depending on the background gas. Additionally, sticking coefficients for the individual species can be taken into account. They vary in a wide range between 10^{-6} and 1.

In case of molecular flow the confinement time is given by:

$$\tau = \frac{l_d}{v_{th}} \quad \text{with} \quad v_{th} = \sqrt{\frac{8 k T_g}{\pi m_n}}, \quad (2.46)$$

which is the ratio of the characteristic length to the mean velocity of the particles.

Confinement times of charged particles

Due to the quasineutrality of the plasma the diffusion rates for electrons and ions should be equal. Since electrons are much faster than ions they cause a electrical field which accelerates the ions until the flux is ambipolar. In weakly ionized plasmas with $T_e \gg T_i (= T_g)$, the diffusion coefficient for ambipolar diffusion D_a is dominated by the diffusion of the slower ions and the temperature ratio [TL29]:

$$D_a = \frac{T_e}{T_g} D_i = \frac{3\pi}{8} \frac{T_e}{T_g} \frac{1}{n_n \sigma_{i,n}} \sqrt{k T_g \frac{m_i + m_n}{2 m_i m_n}}. \quad (2.47)$$

$\sigma_{i,n}$ is the cross section of the ions for diffusion against the neutral particles and may be influenced by resonant charge exchange. Therefore, data from mobility measurements, which include this effect, have to be used. Furthermore, the composition of the ion species has to be taken into account.

The sticking coefficient of charged particles is unity, because of recombination at the chamber walls.

If collisions are negligible, τ can be calculated as follows:

$$\tau = \frac{\Lambda_i}{v_i} \quad \text{with} \quad v_i = \sqrt{\frac{2 k T_e}{m_i}}. \quad (2.48)$$

The ion loss length Λ_i again depends on plasma geometry [TL29, Möl93].

For completeness, some restrictions concerning the confinement times must be mentioned. First, the requirement of quasineutrality is not fulfilled within the length of the Debye shield. If the dimensions of a system are much larger than the Debye length ($\lambda_D = \sqrt{\epsilon_0 k T_e / (n_e e^2)}$) the ions are shielded by the electrons. In low temperature plasmas the typical Debye lengths are between 1 μm and 1 mm and are smaller than reactor dimensions. Next, the sheath near the wall should be considered. Since the walls of the reactor chamber are negatively charged with respect to the plasma, a space charge develops in front of them with a sheath potential of the order of $3 k T_e$. The dimension of the sheath is characterized by the sheath length. The formulae introduced above neglect the sheath potential and its dependence on, e.g. the excitation frequency. If magnetic fields are present, electrons and ions follow the field lines by cyclotron gyration. As a consequence drifts occur, depending on the direction with respect to the field lines.

Comparing confinement times of neutrals with those of charged particles in low pressure plasmas one finds typically that electron confinement times are three orders of magnitude lower and in the range of some μs .

2.3.2 Ionization balance: electron temperature

A simplification of the complete particle balance equation can be made in order to obtain the electron temperature. It is assumed that ions are produced by electron impact from the ground state of the neutral gas and that they are lost by diffusion:

$$n_1 n_e S(T_e) = \frac{n_i}{\tau_i}. \quad (2.49)$$

In order to consider ionization from excited states, effective ionization rate coefficients can be used instead of the ionization rate of the ground state only. As discussed above, this can be taken from results of a CR-model. Recombination is neglected as loss process for the ions because of the assumption of low radiation density and low electron density (justified for most of the low temperature plasmas) but can be implemented easily. In gas mixtures each species has to be

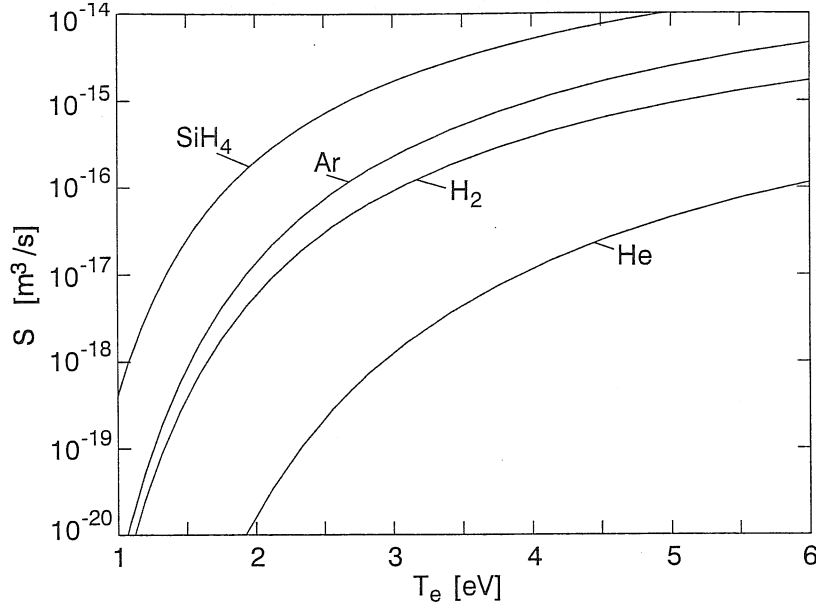


Figure 2.5: Electron impact ionization rate coefficients for He, Ar, H₂ and SiH₄ assuming a Maxwellian EEDF.

taken into account. In the case of singly ionized plasmas the ion and electron densities cancel in Eq. (2.49) and $S(T_e)$ (and thus T_e) is related to the confinement time of the charged particles. As a consequence, increasing the pressure in a discharge would decrease the electron temperature due to the higher confinement time, i.e. lower ion losses. Furthermore, comparing ionization rates, one would expect lower T_e for gases with higher ionization rates which are related to lower ionization energies.

Figure 2.5 gives examples for ionization rates of He, Ar, H₂ and SiH₄ under the assumption of a Maxwellian EEDF. The first three are calculated using the Lotz formulae ([Lot67]) whereas the total ionization rate of silane is taken from [CHRG84]. The highest T_e is expected for a pure helium plasma with decreasing values for the other gases in the same order as the ionization rates increase. Furthermore, it can be estimated that mixtures of hydrogen and helium have a higher T_e in comparison to pure hydrogen plasmas, whereas mixtures of hydrogen and silane will have a lower T_e . Precise calculations for T_e in plasmas can either be compared with measurements or used as input data for self-consistent modeling, e.g. to calculate particle densities from a particle balance.

2.3.3 Power balance or electrical conductivity: electron density

In general the electron density can be calculated by a power balance. For this purpose the power absorbed in the plasma has to be known. Depending on the type of power supply the absorbed plasma power is not the generator output

power because of power losses at coils etc.. Therefore, power measurements or calculations have to be carried out and are not trivial for, e.g., RF discharges. One of the advantages of DC plasmas is an easy accessibility to the discharge current and voltage so that Ohm's law can be used to get electron densities.

Power balance

If the power absorbed within the plasma is known, the electron density can be calculated from a power balance. For simplification, sheaths before electrodes will be neglected in the following. In the bulk plasma the majority of power is consumed by inelastic collisions, i.e. excitation, ionization and dissociation. Losses transferred to the neutrals by elastic collisions (and therefore increasing the gas temperature) or losses to the walls play a minor role. The balance is then given by:

$$P_{abs} = n_e V_{plasma} \sum_k n_k \left(S_k E_i + \sum_p X_{p,k} E_{p,k} + \sum_r Y_{r,k} E_{r,k} \right). \quad (2.50)$$

n_e represents in this case the mean electron energy in the bulk plasma with the plasma volume V_{plasma} . The first term describes the energy losses due to ionization of species k with ionization energy E_i , the next term describes excitation for the different excitation possibilities with excitation energy $E_{p,k}$ and the last term is the energy loss due to dissociation in species r with energy $E_{r,k}$ each with its corresponding rate coefficient. In molecular gases vibrational excitation occurs and may dominate the whole energy balance. Because of the low energy threshold for vibrational excitation these rate coefficients are almost independent of T_e whereas electronic excitation or ionization show steep dependencies of T_e in temperature range of one to several eV which is considered here.

The relation between electron density and absorbed power Eq. (2.50) shows a proportional increase of n_e with the power absorbed in the plasma and a decrease with an increase of particle density, i.e. discharge pressure. If the plasma volume is smaller than the reactor chamber an increase of input power may lead to a plasma expansion whereas n_e remains constant. A further parameter in the energy balance is T_e implied in the rate coefficients. Finally, it should be mentioned that the set of reactions which contribute to the energy balance is complex, in particular in molecular gas mixtures.

Electrical conductivity

The electrical current density j in a plasma can be derived from the drift velocity v_d of the charged particles:

$$j = j_i + j_e = e n_i v_{d_i} - e n_e v_{d_e} \approx -e n_e v_{d_e} \quad (2.51)$$

Since $v_{d_i} \ll v_{d_e}$ the current is dominated by the electrons. The ions are treated as fixed particles in space in comparison to the electrons. Using the relation between drift velocity and electron mobility $v_{d_e} = b_e E_{el}$ together with Ohm's law one gets:

$$j = \sigma_{el} E_{el} = e n_e b_e E_{el} = \frac{e^2 n_e}{m_e \nu_e} E_{el}, \quad (2.52)$$

where the electrical field strength is E_{el} and the electrical conductivity of the plasma is σ_{el} . The electron mobility is correlated to the mean collision frequency by $b_e = e/m_e/\nu_e$. In fully ionized plasmas the collision frequency is determined by collisions between ions and electrons and Spitzer's formula has to be used. In weakly ionized plasmas, which will be considered here, collisions between electrons and neutrals are dominant. Therefore, the Ramsauer cross section should be used. The book of Brown [Bro61] compiles data for these cross sections and electron mobilities for a variety of gases.

In case of DC discharges the formula can be used for the determination of electron density by measuring the electrical current and voltage. Since sheath effect have been neglected, Eq. (2.52) holds for the positive column of a glow discharge, which means the electrical field strength without electrode falls has to be known. Increasing the current of a discharge would enhance the electron density, whereas an increase of pressure leads to decrease of n_e . In general, one obtains a mean electron density but by assuming a density profile, for instance cylindrical symmetry, the density on the axis of the cylinder can be calculated using Bessel functions.

2.3.4 Boltzmann equation: EEDF

The electron energy distribution function (EEDF) can be theoretically determined by using the kinetic theory of plasmas. Detailed analysis of kinetic theory can be found in many textbooks, e.g [Che74] gives an introduction, whereas [SJB66] or [GZS80] are an advanced level. Applications to low temperature plasmas are given in [KT98, FL00] together with a short summary of the theory. In the following, the basic equations and assumptions necessary for calculating EEDF in low temperature plasmas will be sketched very briefly.

In plasma kinetics the distribution of each species satisfies, in general, the Boltzmann equation. Since low temperature plasmas are collisional plasmas with a low degree of ionization, binary collisions between electrons and heavy particles are the dominant mechanism for particle-particle interactions. The electron distribution function $F(\mathbf{r}, \mathbf{v}, t)$ describes the density of electrons in the six-dimensional phase space \mathbf{r}, \mathbf{v} , i.e. $\int F d^3v = n_e(\mathbf{r}, t)$, which is consequently determined by the Boltzmann equation:

$$\frac{\partial F}{\partial t} + \nabla_{\mathbf{r}}(\mathbf{v}F) - \nabla_{\mathbf{v}}\left(\frac{e\mathbf{E}}{m_e}F\right) = \left(\frac{\partial F}{\partial t}\right)_c. \quad (2.53)$$

The temporal evolution of the EEDF is due to fluxes in coordinate space and in velocity space (left hand side) as well as influences of collisions (right hand side). Fluxes in coordinate space may be caused by spatial inhomogeneities, i.e. density gradients. In the case of magnetized plasmas the Lorentz force also has to be considered in the third term. The collision term includes all kind of electron-heavy particle collisions, such as elastic, excitation and ionization collisions. Equation (2.53) is usually solved by expanding F in spherical harmonics in velocity space and a Fourier series in time. Under the assumption of a mainly

isotropic EEDF (which requires not too high electrical field strengths and frequent elastic collisions) and assuming that a small anisotropy can be expressed with sufficient accuracy by the first order correction, one derives the so-called two term approximation:

$$F(\mathbf{r}, \mathbf{v}, t) \approx F_0(\mathbf{r}, v, t) + \frac{\mathbf{v}}{v} \mathbf{F}_1(\mathbf{r}, v, t). \quad (2.54)$$

In the next step, the total electrical field is assumed to consist of a stationary field (the dc space-charge field E_s) and an applied RF field of frequency ω with complex amplitude E_p : $\mathbf{E} = \mathbf{E}_s + \mathbf{E}_p \exp(i\omega t)$. The limit $\omega = 0$ represents an applied DC field. Additionally, the temporal dependence of the distribution function is assumed to be the same as the electrical field. The problem is further simplified by assuming a time independent isotropic part of the EEDF, which is satisfied trivially for DC plasmas but not for RF plasmas. This requires a RF frequency higher than the energy relaxation frequency, the rate of energy change due to elastic and inelastic collisions. Equation (2.54) then becomes:

$$F(\mathbf{r}, \mathbf{v}, t) \approx F_{0,0}(\mathbf{r}, v) + \frac{\mathbf{v}}{v} (\mathbf{F}_{1,0}(\mathbf{r}, v) + \mathbf{F}_{1,1}(\mathbf{r}, v) \exp(i\omega t)). \quad (2.55)$$

Inserting (2.55) into (2.53) one obtains one scalar and two vector equations which then yield a kinetic equation for the isotropic part of the EEDF ($F_{0,0}$):

$$\begin{aligned} & -\nabla_{\mathbf{r}} \left(\frac{v^2}{3\nu_m} \nabla_{\mathbf{r}} F_{0,0} \right) + \frac{v e}{3 m_e} \nabla_{\mathbf{r}} \left(\frac{\mathbf{E}_s}{\nu_m} \frac{\partial F_{0,0}}{\partial v} \right) \\ & - \frac{e}{3 m_e v^2} \frac{\partial}{\partial v} \left[-\frac{v^3}{\nu_m} \mathbf{E}_s \cdot \nabla_{\mathbf{r}} F_{0,0} + \frac{e v^2}{m_e \nu_m} \left(E_s^2 + \frac{E_p^2}{2} \frac{\nu_m^2}{\nu_m^2 + \omega^2} \right) \frac{\partial F_{0,0}}{\partial v} \right] \\ & = C_0(F_{0,0}). \end{aligned} \quad (2.56)$$

The terms in $F_{0,0}$ describe the usual spatial diffusion of electrons, the mobility flux of electrons in the space-charge field, diffusion cooling, and the heating due to the stationary and the oscillatory electrical fields. The expressions for the collision terms can be found in standard literature. The heating by the RF field is represented by an effective field strength:

$$E_{eff}(\mathbf{r}, v) = \frac{E_p(\mathbf{r})}{\sqrt{2}} \frac{\nu_m(v)}{(\nu_m^2(v) + \omega^2)^{1/2}}. \quad (2.57)$$

This emphasizes the importance of collisions with frequency ν_m for momentum transfer. Without collisions the electrons oscillate in the electrical field with a phase delay of $\pi/2$ (due to their inertia) without gaining energy. Collisions disturb this phase correlation and can thus lead to an energy diffusion.

Solving the kinetic equation for the isotropic part (Eq. (2.56)) is still complicated and a number of approaches to this problem have been proposed. The most popular approaches are the local or the nonlocal approach. For the purpose of calculating EEDFs in low pressure discharges, which are spatially homogeneous (already assumed in the sections before) the local approach is described further

on. The local approach supposes that the EEDF at every position is determined by the local electrical field strength. In this case only a parallel electrical field component exists and, additionally, the diffusion term vanishes. Frequently the kinetic energy is used, expressed in volts: $u = mv^2/(2e)$, instead of particle velocity v . The simplified homogeneous Boltzmann equation is then given by:

$$-\frac{2e}{3m_e} \frac{\partial}{\partial u} \left[\frac{u^{3/2}}{\nu_m} \left(E_{s||}^2(\mathbf{r}) + \frac{E_p^2(\mathbf{r})}{2} \frac{\nu_m^2}{\nu_m^2 + \omega^2} \right) \frac{\partial F_0}{\partial u} \right] = u^{1/2} C_0(F_0). \quad (2.58)$$

Because of the possibility of spatially varying electrical field (local approach) the EEDF may have a spatial dependence. Neglecting any spatial inhomogeneity of the electron density allows the following separation:

$$F_0(u, \mathbf{r}) = n_e(\mathbf{r}) f_0(u, |\mathbf{E}(\mathbf{r})|), \quad (2.59)$$

with the one particle distribution function normalized by:

$$2\pi \left(\frac{2e}{m_e} \right)^{3/2} \int_0^\infty f_0(u, |\mathbf{E}(\mathbf{r})|) u^{1/2} du = 1. \quad (2.60)$$

For convenience the factor before the integral is frequently included in the definition for f_0 leading to the following normalization:

$$\int_0^\infty f_0(u) u^{1/2} du = 1. \quad (2.61)$$

It should be mentioned that the validity of the local model must be checked for each individual discharge, in particular, in RF discharges, where nonlocal effects like oscillating sheath boundaries may be dominant.

Cross sections are needed for input data: cross sections for momentum transfer, elastic collisions, and inelastic collisions such as excitation or ionization and in case of molecules vibrational (rotational) excitation. For each gas, the dominant excitation mechanisms have to be selected to represent the variety of excitations, i.e. ground state excitation into the first excited states and can be combined into one effective cross section. In case of rare gases metastable states may also be important. A further parameter in the calculation is the electrical field strength in the plasma, which has to be known either from measurements or calculations. In summary, the EEDF is characterized by the generator frequency, the electrical field strength, the neutral gas density (often combined to the parameter E/n_0 , the reduced electrical field strength), the electron density and the gas itself.

2.4 Experiments

Low temperature plasmas are frequently used for film deposition or etching in industrial applications. Such technical plasmas can be generated over a wide parameter range. On the other hand, the boundary layer of controlled fusion

experiments may have similar characteristics, so that diagnostics or modeling developed and checked in technical, laboratory plasmas can be transferred to these experiments. The great advantage of laboratory plasmas in contrast to fusion experiments is the possibility of detailed parameter studies together with simple plasma geometries.

2.4.1 Laboratory plasmas

Technical plasmas are generated at various generator frequencies which divide the discharges into DC, RF and MW discharges. Depending on the coupling mechanism, on additional magnetic fields, on pulsed or cw generation, on the geometry of the plasma etc., the possibilities of plasma sources are manifold. The most commonly used methods are compiled in the recent paper of Conrads and Schmidt [CS00], which also refers to further literature.

The discharges used in the underlaying work for diagnostics of hydrogen and deuterium containing plasmas will be described in the next paragraphs. The variety of plasma parameters in low pressure plasmas are covered by different kinds of discharge. This allows investigations over a range of electron densities from $10^{16} - 10^{18} \text{ m}^{-3}$, a pressure range of 1–1000 Pa and electron temperatures between 1 and 5 eV.

Glow discharge

Stationary DC glow discharge plasmas are generated in a water-cooled cylindrical glass tube with diameter 10 mm and 1 m length, formerly a CO₂ laser device (Fig. 2.6). The discharge current can be varied between about 5 and 50 mA, the pressure range is 100 to 1000 Pa. In order to reduce high voltage problems, the discharge is electrically split into two circuits with one anode in the middle of the tube and a hollow cathode at either end. For spectroscopic diagnostics (end-on measurements) of the plasma region close to the axis, the two hollow cathodes are displaced sideways several cm from the line of sight. They are mounted in insulated metal housings, which can be used as probes for electrical field measurements. By operating only one half of the discharge or the full length with the anode on one end, proper scaling of the observed light with column length can be checked proving that it is not significantly disturbed by end effects. Similarly, by subtracting results for full and half length, the electrical field in the discharge column is measured without the electrode fall regions. The cathode fall actually contributes only about 10% to the total voltage (1000–4000 V).

The discharge is used for spectroscopic diagnostics and is operated with various gas mixtures of mainly helium (90%), argon and nitrogen. Hydrogen, neon and krypton are added occasionally. The plasma parameters are typically: $n_e = 10^{16} - 10^{17} \text{ m}^{-3}$, $T_e = 1 - 3 \text{ eV}$ depending on pressure and gas mixture, whereas $T_g = 450 \text{ K}$ is constant in the investigated range. Due to the low degree of ionization ($\approx 10^{-6}$) the EEDF is Druyvesteyn-like and heavy particle collisions become important.

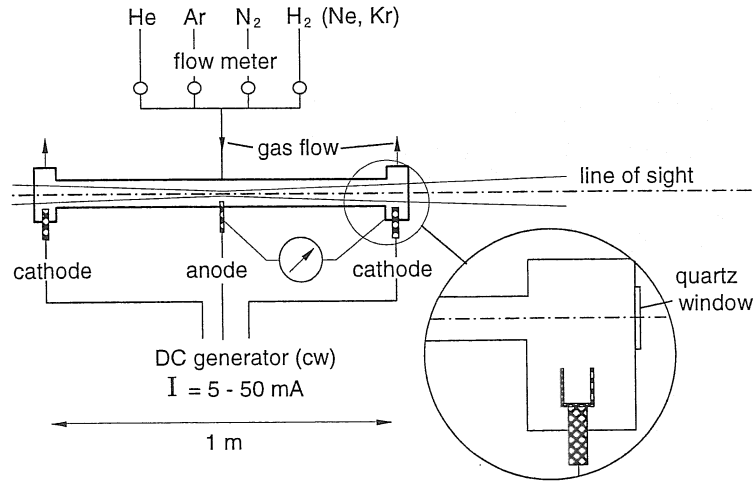


Figure 2.6: Experimental setup of the DC glow discharge used for spectroscopic diagnostics.

RF discharge

Radio-frequency discharges ($f = 13.56$ or 27.12 MHz) can be classified as capacitively or inductively coupled discharges in pulsed or cw mode. A promising source is the planar inductively coupled plasma (ICP), since electrode sheaths are small and electron densities are high in comparison to capacitive plasmas. Because of the low ion energies combined with high ion flux densities, the simple possibility to use bias, and the plasma homogeneity above a substrate, this type of plasma source has become more and more important in industrial applications.

The ICP described here is designed to study plasma wall interactions of H_2/He or D_2/He plasmas with carbon surfaces. The cylindrical symmetric chamber is equipped with five flanges for diagnostic purposes (Langmuir probe and optical emission spectroscopy). The discharge chamber is 150 mm in diameter (d) and 100 mm high (h) as shown in Fig. 2.7. The chamber wall is water cooled. Inductive coupling is achieved by using three coils above a quartz plate (thickness 10 mm) at a distance of 7 mm. A grounded Faraday shield is placed between the coils and the quartz plate in order to avoid capacitive components which might cause self biasing. An RF generator operating at a frequency of 27.1 MHz can deliver a maximum power of 300 W. A network consisting of two adjustable capacitors is used to match the generator output impedance of $50\ \Omega$ to the variable impedance of the plasma. A minimal background pressure of some 10^{-5} mbar is achieved with a turbo pump system. Typical operating conditions for helium plasmas are a gas inlet of 20 sccm, a RF generator power of 250 W and a pressure range of 2 – 400 Pa. The substrate (30×30 mm) is placed in the centre of the chamber, defining the origin of the r, z -cylindrical coordinate system as can be seen in Fig. 2.7.

Electron densities obtained in the ICP vary with input power, pressure and gas mixture and are typically: $n_e = 5 \times 10^{16} - 10^{18}\text{ m}^{-3}$. T_e is between 1.5

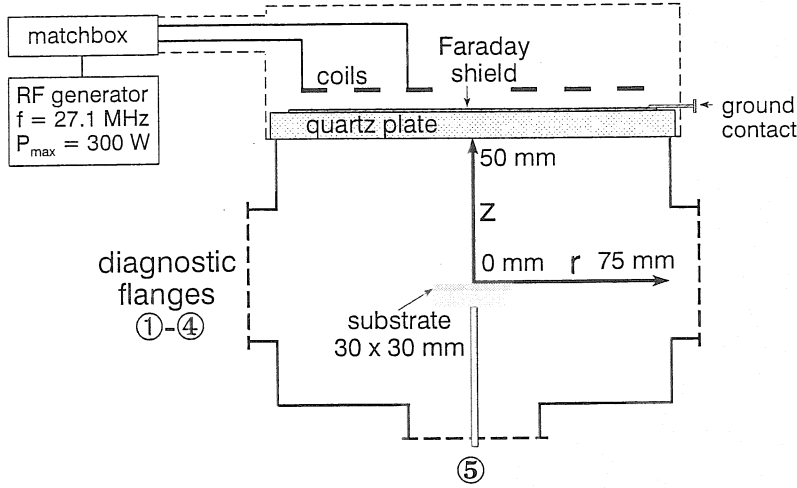


Figure 2.7: Experimental setup of the ICP reactor. The position of the substrate holder defines the coordinate system: r - and z -axis.

and 4.5 eV, whereas T_g ranges from 450 to 700 K. Depending on pressure the EEDF is between a Maxwellian and Druyvesteyn distribution. The substrate can be biased, resulting in (single ionized) ion energies of 5 – 40 eV. The substrate holder can be actively cooled or heated to cover a temperature range of $T_s = 300 - 1100$ K. Instead of the small substrate of 30×30 mm in the discharge centre a substrate of 150 mm in diameter can be placed at different z -coordinates, replacing the bottom of the chamber. This allows a variation in height of the chamber. Furthermore, spatially resolved measurements are possible above a substrate which is completely covered by the plasma along the line of sight.

MW discharge

Microwave discharges excited at a frequency of 2.45 GHz are suitable for producing large area plasmas with high densities of charged particles. As in RF discharges, the electromagnetic wave can be coupled to the plasma in different ways. Recent trends and developments are given, for instance, in [ML98].

For spectroscopic diagnostics, a linearly extended low pressure plasma device with high electron density ($\geq 10^{17} \text{ m}^{-3}$) and an EEDF which is almost Maxwellian in a wide pressure range (5 – 500 Pa) was built. The surface wave sustained MW discharge is based on the principle of a Duo-Plasmaline [Räu98]. Figure 2.8 shows the experimental setup with the main components of the Duo-Plasmaline. In contradiction to common surface wave plasmas where the plasma is produced within a tube at low pressure surrounded by atmospheric pressure, the inverse configuration is chosen. The plasma exists outside the dielectric quartz tube in the vacuum chamber whereas the tube inside is filled with air at atmospheric pressure. The electromagnetic waves are excited at the ends of the tube and propagate mainly within the tube along the inner conductor (copper rod) and within the plasma as radially decaying surface waves. This means the plasma forms the

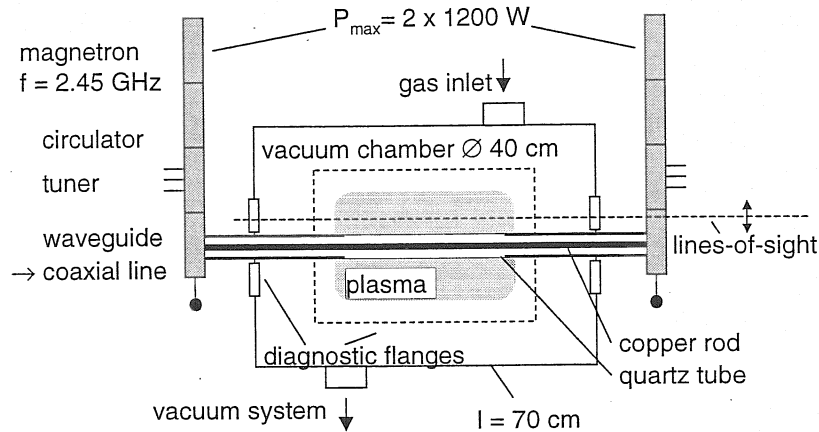


Figure 2.8: Experimental setup of the Duo-Plasmaline ([Räu98]) with the copper rod in a quartz tube under atmospheric pressure. In the vacuum chamber the plasma is the outer conductor of the coaxial transmission line.

outer conductor of a coaxial waveguide where the microwave power is consumed. The axial plasma extension can be controlled by the applied microwave power and can be increased up to the chamber length. The plasma extension in the radial direction depends on the pressure and the gas species.

Due to the high input power of max. 1.2 kW per magnetron (cw or pulsed), the inner tube ($d = 30$ mm) with the copper rod ($d = 8$ mm) is cooled by an air flow. The length of the chamber is 70 cm and the plasma length can be varied between 10 and 50 cm and is homogeneous in this direction. Of course, in the radial direction the plasma parameters show spatial profiles (cylindrical symmetry), decaying, from the tube towards the plasma edge. In order to make diagnostics on the plasma in each direction, diagnostic windows and flanges are located near the axial ends of the tube and a large window in front of the chamber allows radially resolved measurements at various lengths.

The plasma parameters in the investigated pressure range of 5 – 500 Pa are the following: $n_e = 0.8 - 6 \times 10^{17} \text{ m}^{-3}$, $T_e = 1.5 - 3.5 \text{ eV}$ and $T_g = 500 - 1000 \text{ K}$. The background pressure is around 10^{-6} mbar . The input power is typically some hundred Watts per magnetron (cw) and the plasma length around 40 cm.

ECR discharge

In microwave discharges ($f = 2.45 \text{ GHz}$) the electrons can be additionally heated by using electron cyclotron resonance (ECR) heating. In this case a magnetic field must be applied with a field strength producing a gyration frequency of the electrons equal to the microwave frequency (the relation $2\pi f = eB/m_e$ yields $B = 87.5 \text{ mT}$). Such ECR plasmas operate in a wide pressure range, in particular at low pressures (down to 0.001 Pa, depending on the input power) with high electron density which is typically the cutoff density for the microwaves

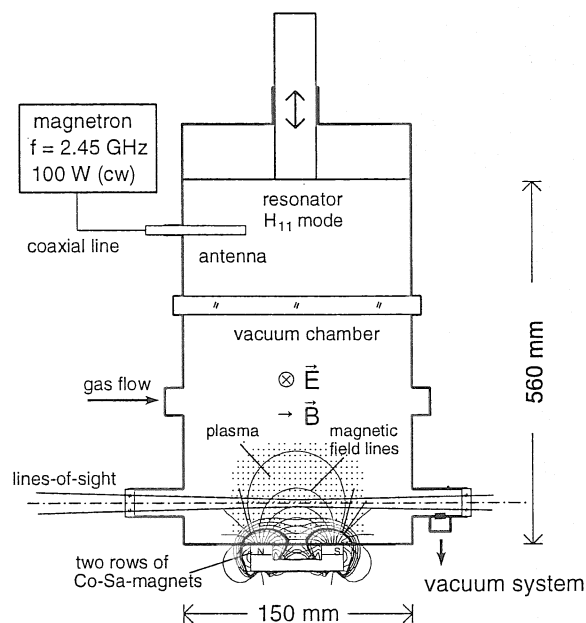


Figure 2.9: *Experimental setup of the ECR discharge. The magnetic rows (90° view) produce the resonance magnetic field strength of 87.5 mT at approx. 1 cm above the bottom plate.*

propagating in the plasma ($n_e^{cutoff} = (2\pi f)^2 m_e \epsilon_0 / e^2 = 7.6 \times 10^{16} \text{ m}^{-3}$).

The experiment used for diagnostics is shown in Fig. 2.9. The maximum generator microwave power is 100 W supplied by a magnetron source at the usual frequency of 2.45 GHz. The microwave power was fed into the reactor via a coaxial transmission line and a rod antenna. The reactor consisted of an upright cylinder divided by a glass plate to separate the vacuum chamber from microwave input coupling. The reactor was designed to act as a resonator for the H_{11} mode of the microwave. The top plate could be adjusted to tune the cavity. The resonator is divided in an atmospheric part with the coupling antenna, and the vacuum chamber, by a dielectric window. Below the base plate two rows of cobalt samarium magnets are installed to generate an inhomogeneous magnetic field with field lines perpendicular to the electrical field vector of the microwave. In the plasma reactor above the base plate at about 10 mm distance from each pole of the magnets the magnetic field strength is 87.5 mT corresponding to the electron cyclotron resonance frequency of 2.45 GHz. Therefore, plasmas are preferentially produced and heated in this region and expand by diffusion and drifts in the inhomogeneous magnetic field. The plasma can be observed through four diagnostic flanges which are located symmetrically around the plasma with lines of sight parallel or perpendicular to the magnetic rows. The centre of the diagnostic windows is 30 mm above the bottom plate, so that the magnetic field strength can be neglected here. The particle motion is dominated by diffusion which justifies the assumption of homogeneous plasma parameters in this region.

The plasma volume is $200 - 400 \text{ cm}^3$ depending on pressure $p = 2 - 20 \text{ Pa}$ and gas mixture. The plasma is not limited by the chamber walls (except the bottom plate) and can therefore change the size with input power whereas the electron density remains constant. Since the plasma dimensions are comparable to the vacuum wavelength of the microwave ($\lambda = 12 \text{ cm}$), the electron density can be higher than the cutoff density and is determined to be $n_e = 10^{17} \text{ m}^{-3}$. Electron temperature varies between 1.5 and 4.5 eV, whereas gas temperature is 450 K. Due to the ionization degree of $10^{-5} - 10^{-4}$, the EEDF is close to a Maxwellian distribution.

2.4.2 Edge plasmas in fusion experiments

Fusion experiments in the whole world are engaged to reproduce the energy production process occurring on the sun. A fusion power plant will derive energy from the fusion of atomic nuclei. To ignite the fusion fire, the plasma, composed of the hydrogen isotopes, deuterium and tritium has to be confined in magnetic fields and heated to temperatures of over 10 keV. Experiments are carried out with the isotopes hydrogen and deuterium in order to study the plasma physics principles: confinement of high-temperature hydrogen plasmas in magnetic fields, heating and refuelling, plasma diagnostics, magnetic field technology, electrical and electronic engineering, data acquisition and processing, systems studies, plasma theory and plasma-wall interaction. For magnetic confinement two torus configurations are favoured: the tokamak and the stellarator principle. At the moment the largest machine is the JET project in Culham (England) whereas in Germany (Garching near Munich) both types of fusion experiments are running: the ASDEX Upgrade tokamak and the WENDELSTEIN 7-AS stellarator. For details of magnetic confinement and experimental status the reader should refer to standard literature, e.g. [Che74, Sch93, Wes87] or Summer University Lectures on plasma physics summarized, e.g., in [ZB95].

One of the main topics in fusion experiments is the interaction between the hot fuel and the confining walls (in most cases carbon, i.e. graphite). The plasma sheath between the bulk plasma and the walls is called the scrape-off or boundary layer separated by the last closed magnetic flux surface. The plasma wall interaction can be concentrated on so-called limiters, which is one of the possibilities to control the particle fluxes to surfaces. By using a specially designed magnetic field configuration the charged particles are directed to a divertor, which is the more promising concept. In the divertor the incident particles (already cooled down) are deposited on the collector plates and are pumped off. Figure 2.10 shows a poloidal cross section of the ASDEX Upgrade tokamak (Axially Symmetric Divertor EXperiment). In divertor machines the last closed flux surface is called the separatrix. To reach the high plasma temperatures in the core the plasma heating consists of up to 20 MW neutral beam injection of atomic hydrogen or deuterium and 6 MW of RF heating. The neutral beams of the two injectors are injected through two large ports. The magnetic field is maximal 3.9 T, the plasma current is 2 MA and the pulse length is about 10 ms. The plasmas are

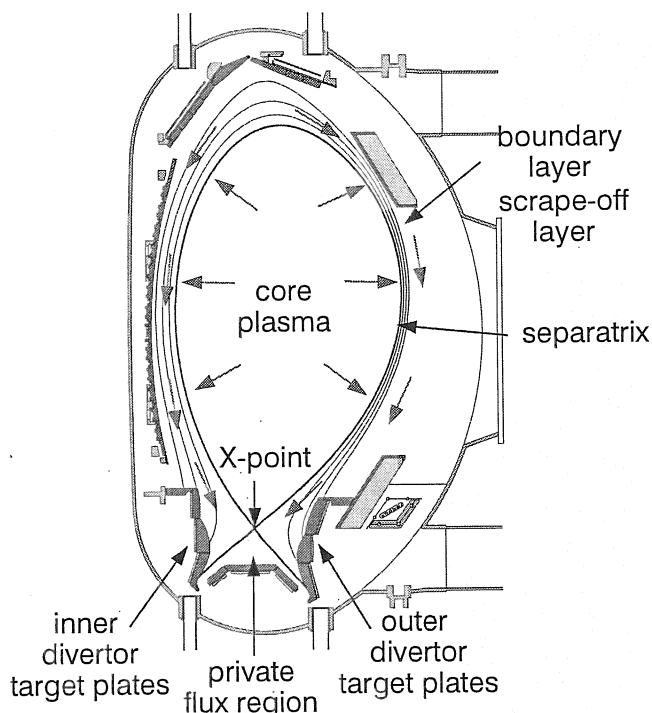


Figure 2.10: Poloidal cross section of the ASDEX Upgrade tokamak (torus radius $R = 1.6$ m, minor radius $r = 0.5 - 0.8$ m). Selected regions are indicated in common terms. Short arrows show the direction of particle transport.

investigated with about 40 diagnostics.

Since the results presented in this report are based on measurements at the ASDEX Upgrade divertor, only the divertor concept will be described further. Nevertheless, the principles and, in particular, the interpretation of emission spectroscopy data can be transferred to most of the boundary layer plasmas, such as limiter machines (for instance TEXTOR-94, a tokamak in Jülich designed for detailed study on plasma wall interaction). The recent textbook of Stangeby [Sta00a] gives a comprehensive overview of the physics of the plasma boundary regions in magnetically confined fusion plasmas.

Divertor concept

The design of a divertor is based on the formation of a cold, dense plasma in the divertor chamber, and the distribution of power over a large area. In the dynamic gas target divertor, radiation from hydrogen or impurities results in a transfer of energy from the plasma in the divertor to the walls of the chamber. Charge exchange collisions with neutrals that recycle in the divertor channels reduce ion momentum. This causes a reduction of the pressure in front of the target plates and a reduction of the ion flux to the plates. Thus leads to typical temperatures of about 5 eV and particle densities of 10^{19} to 10^{20} m^{-3} in the divertor.

The divertor can operate in different recycling regimes, which are not strictly separated. There is a low recycling regime, a high recycling regime (both attached regimes) and detachment. A transition from one regime to the other can be achieved, in principle, by increasing the plasma density in the midplane (upstream in the chamber) at constant heating power. In the attached regimes the plasma recombines at the target or in a small layer before the target. Momentum, energy and particles reach the target almost directly. In the low recycling regime the target temperature is approximately the upstream temperature and the target density is proportional to the upstream density in the scrape-off layer. Therefore, this is called a linear regime. Increasing the midplane density increases the upstream density whereas the upstream temperature decreases. This results in the same behaviour for the target parameters, but the relation is no longer one of proportionality. A further increase of the upstream density results in very low target temperatures (≤ 5 eV). In this temperature range the ionization rate of hydrogen strongly decreases and neutral processes, i.e. elastic and ion conversion collisions become important. In addition, the rate coefficient for hydrogen recombination (three-body and radiative recombination) increases and volume recombination occurs. As a consequence, the target load is reduced. This is the detached divertor regime, characterized by very low temperature and high density. For detailed physics of the regimes see [Sta00a]. Because of the low temperature in divertor plasmas, they are similar to those of low pressure laboratory plasmas and some properties can be transferred. The high electron densities, however, justify the assumption of a Maxwellian EEDF.

To analyse physical mechanism or extrapolate to future machines with changing divertor geometries and parameters, boundary layer codes have been developed and validated by present experiments. The B2-EIRENE code is a two dimensional many-particle fluid-code B2 [Bra87] for the boundary layer combined with a three dimensional neutral particle code EIRENE [Rei92] based on Monte-Carlo simulations. Iterative runs allow self-consistent modeling of neutral particles and plasma particles in the scrape-off layer and in the divertor region. The numerical grid is fitted to the chamber geometry. B2-EIRENE is the standard code used for ASDEX Upgrade (see for instance [SRZ⁺92, CSN⁺97]).

For divertor diagnostics a variety of methods are commonly used, e.g. Langmuir probes installed in the targets or divertor spectroscopy. The results to be presented here are based on spectroscopic measurements using divertor spectroscopy and code calculations. Therefore, the lines of sight (LOS) in the divertor and the divertor geometry, the so-called LYRA divertor of ASDEX Upgrade, are shown in a poloidal cross section in Fig. 2.11 together with the numerical grid of the B2-EIRENE code, the separatrix and the X-point. The LOS are numbered and divided into the inner (RIV, ZIV) and outer divertor (ROV, ZOV): R = radial view, Z = view in z-direction. They are installed in two sections of the torus distinguished by a V or N in the name. The s-coordinate denotes the length along the target plate. R and z are the major radius and the height of the torus.

In summary, the plasma parameters in divertors range from $T_e \approx 0.5 - 20$ eV

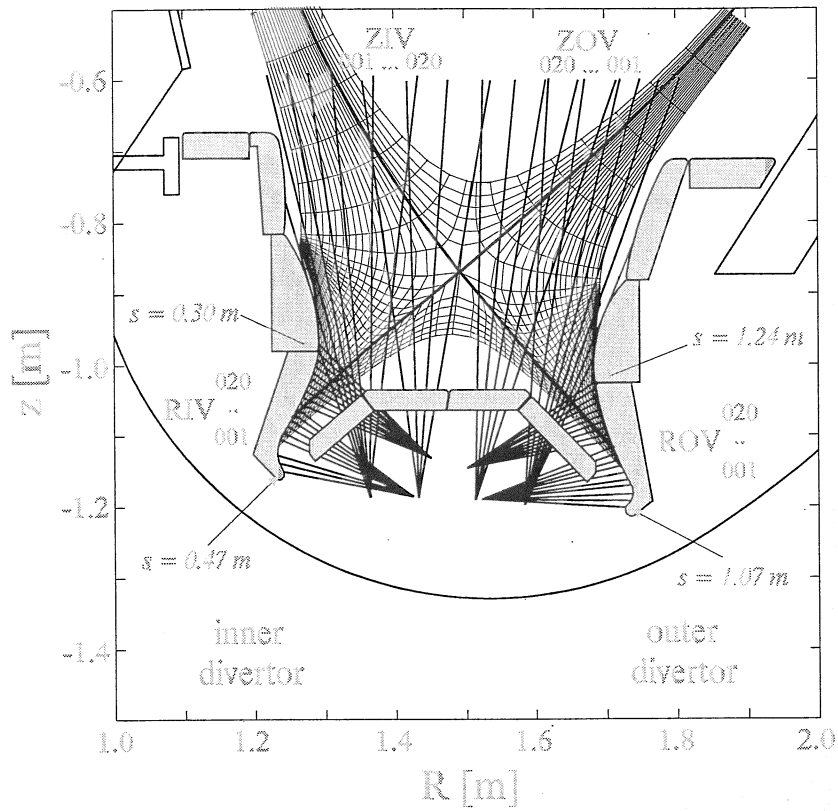


Figure 2.11: Poloidal view of the LYRA divertor of ASDEX Upgrade together with the lines of sight (LOS) from divertor spectroscopy and the numerical grid of the B2-EIRENE code.

at electron density of $n_e \approx 10^{21} - 10^{19} \text{ m}^{-3}$ for completely detached or attached plasmas, respectively. The dominant ion species is H^+ (D^+), the dominant neutral particle is H (D). Atomic hydrogen fluxes are in the range of some $10^{22} \text{ m}^{-2} \text{ s}^{-1}$, ion fluxes are around $10^{21} \text{ m}^{-2} \text{ s}^{-1}$.

Chapter 3

Diagnostic Methods

Diagnostic methods of plasmas can be divided in two groups: active and passive diagnostics. The first group interferes the plasma, by, e.g., probes or radiation, whereas passive diagnostics use signals from the plasma itself. Furthermore, it has to be distinguished between spatially resolved and line integrated measurements as well as time resolved and steady state measurements. For an overview of the variety of diagnostic methods see [Hut87, AF89, Jan92]. Active laser diagnostic methods are becoming more and more important in low temperature plasmas because of the advantage of a clear interpretation of the measured results. However, the experimental setup is very expensive and sensitive. A description of recent laser methods and their applications can be found in [KU00, DCG00]. For the understanding of plasma processes in detail a combination of these methods have to be used, often complemented by plasma modeling. An easy handled diagnostic method is the emission spectroscopy of plasmas, preferably in the visible spectral range. However, interpretation of spectra can be very complex due to the amount of information included. The radiation can be related easily to changes in plasma parameters, but the more plasma parameters are known the simpler quantitative diagnostics become. Therefore, after an introduction of the principle methods of emission spectroscopy, a description of the the supplementary diagnostic methods used in laboratory plasmas follows. Thus, the interpretation of spectra can be checked and confirmed by systematic studies in these plasmas and is applied to divertor plasmas, to complement the standard diagnostics.

3.1 Emission spectroscopy

Optical emission spectroscopy is a powerful tool for detecting a variety of plasma parameters. The method makes use of the light emitted by the plasma and is therefore non-invasive. Due to the easy handling of the diagnostic system it is applied almost everywhere. Low cost systems are used for detecting impurities in plasmas or as monitoring systems controlling the plasma stability by line intensities. The intensity of spectral lines contains information about electron

density, electron temperature, particle density whereas the line profile is correlated to neutral particle or ion temperature (if no other broadening mechanism is present). An overview of applications can be found in standard literature, e.g. [Gri64, LH68, AF89, TLJ99].

The methods of emission spectroscopy can be divided into two groups. The first one is based on relative measurements, i.e. changes in intensity of one or more lines simultaneously. Here, only a wavelength calibration is required which can be supported by a relative calibration of the sensitivity of the optical system over the investigated wavelength range. A common method for detecting radical densities in technical plasmas, e.g. atomic hydrogen density, is the so-called actinometry by a gas with known particle density. Assuming a corona equilibrium for the population of the electronic states, the ratio of both line intensities depends only on T_e and the densities (Eq. (2.22)). Using a gas with similar excitation energy, e.g. argon, and similar shape of the cross section, e.g. optical allowed, the ratio of the rate coefficients is almost constant. As a consequence, T_e must not be known precisely. In a similar manner T_e can be observed by using the ratio of two lines originating from two gases with different excitation energies and different shape of cross section. An example is the He-line at 667.81 nm and the Ar-line at 667.73 nm. Here, a relative calibration is not necessary because the lines are very close together. If the argon line increases in comparison to the helium line T_e decreases and the other way round. It is also possible to use line ratios of a single gas depending on T_e , which is, in the case of helium, a line of the singlet system and a line of the triplet system. Applying a CR-model, line ratios will also depend on n_e and the ratio of lines from the same multiplet system would yield n_e .

The second method is based on the evaluation of absolute line intensities, which implies the method of relative measurements. In the following sections the calibration of the optical systems is described together with the optical systems themselves and their possibilities for measuring plasma parameters. It should be mentioned, that in technical plasmas the most lines arise from neutral particles which is due to the low temperature and the low ionization degree. Therefore it is difficult to obtain information about ions.

3.1.1 Absolute intensity calibration of the optical systems

Since each of the experiments described in Sec. 2.4 is equipped with its own spectroscopic system the calibration procedure of systems with photomultiplier as well as CCD camera or ICCD camera (Intensified CCD) in the wavelength range from 120 nm to 900 nm will be described. The imaging by fibre optics or lens system belong also to the optical system. In principle, intensity calibration is carried out with a light source of known radiance, which is in the visible range either a tungsten ribbon lamp or an Ulbrecht sphere.

In the case of an imaging lens system the solid angle is limited by an aperture before the entrance slit of the spectrometer. Using fibre optics it has to be guaranteed that an additional aperture limits the solid angle. The tungsten ribbon

lamp is placed instead of the plasma. Since the plasma image is often reduced, the notch of the ribbon, which denotes the calibrated area, is too small to get a precise image at the entrance slit. Therefore it is more convenient to have a 1:1 image by moving the lens, however the same solid angle has to be guaranteed. For calibrating a spectrometer with photomultiplier the radiance of the source is measured depending on wavelength and then compared with the radiation of the grey radiator at the black body temperature. This yields the sensitivity of the optical system. Since the signals are weak below 400 nm stray light may be important and a subtraction method, recording signals with and without band-pass filters is used. For wavelengths above 510 nm a permanent bandpass filter (490 nm) suppresses the second order of the grating. For CCD cameras or ICCD cameras, a small pixel area in the centre of the chip is calibrated with this technique. The whole area of the chip is then relatively calibrated to the centre by homogeneous illumination which is achieved with an enlarged image of the tungsten band lamp. ICCD cameras may have an inhomogeneous photolayer which cause an additional wavelength dependency. A detailed description of calibrating such cameras is given in [Heg98, Mei00]. Comparing the CCD or ICCD camera with photomultiplier tubes, the cameras allow spatially and time resolved measurements. Spectrometers of divertor spectroscopy in ASDEX Upgrade equipped with CCD or ICCD cameras and fibre optics are calibrated in the same manner by an Ulbrecht sphere.

The ECR plasma experiment is equipped with an VUV/UV spectrometer which uses the same line of sight as the visible spectrometer. The spectrometer is evacuated to a background pressure of 10^{-7} mbar by differential pumping through an aperture, which limits also the solid angle. The detector is a solar-blind photomultiplier tube. Relative calibration was carried out by using the continuum radiation of a calibrated deuterium lamp (190 to 400 nm) whereas the absolute value was taken from helium lines in a helium plasmas around 300 nm detectable with either spectrometer [Mei00]. Since the VUV/UV spectrometer works without lens systems, the whole plasma is observed. For comparing results, space resolved signals from the ICCD camera have been averaged over the plasma volume. The wavelength range down to 120 nm was calibrated by applying the branching ratio method to molecular nitrogen bands in a nitrogen plasma [Mum72], i.e. the Lyman-Birge-Hopfield series.

All spectroscopic systems have an apparatus profile with a half width broader than the half width of a Doppler profile with gas temperature being slightly higher than room temperature (≈ 500 K). The profiles are always dominated by the apparatus profile and are not suitable for deriving plasma parameters in the investigated laboratory experiments.

3.1.2 Electron temperature, EEDF and particle densities

Measured radiation of atomic lines or molecular bands is related to the plasma parameters by the corona model or by CR-models (Sec. 2.2). The starting equation is Eq. (2.22) by using effective emission rate coefficients (Eq. (2.24)) to imply re-

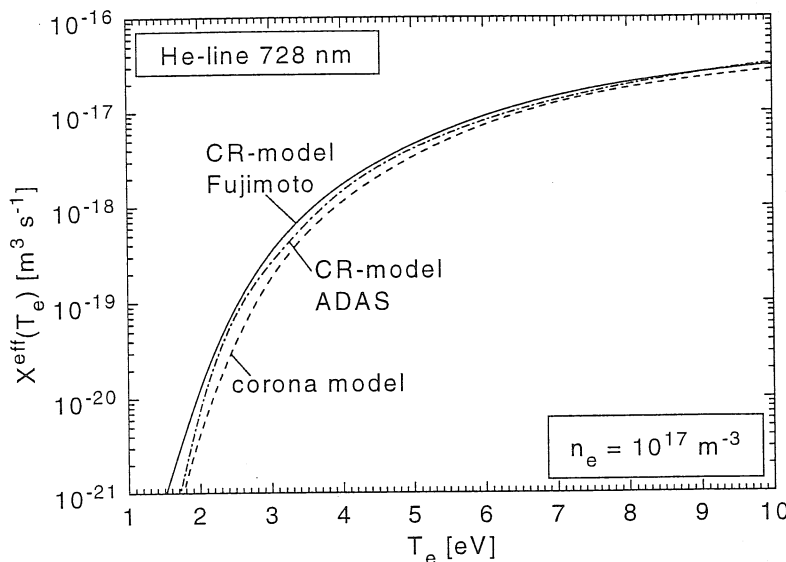


Figure 3.1: Effective rate coefficients for the He-line at 728 nm calculated with Fujimoto's CR-model and the ADAS code package as well as the rate coefficient for ground state excitation (corona model).

sults from CR-calculations. For convenience, the combined equation is repeated here:

$$\dot{N}_{p,j} = n_1 n_e X_{p,j}^{eff}(T_e, n_e, \dots). \quad (3.1)$$

Depending on the plasma parameters known from other diagnostics, the remaining parameters can be determined from emission spectroscopy. Since rate coefficients show in the majority of cases a steep dependence on T_e , the radiation is very sensitive on this parameter. Additionally, in the present case, T_e can be measured with Langmuir probes. However, they are not very accurate in determining T_e whereas n_e is measured more precise with probes (Sec. 3.4). Supplementary, line of sight integrated n_e can be determined by microwave interferometry. On the other hand, if T_e and n_e are well-known, particle densities can be measured which is relevant in the case of radical densities.

Precise electron temperature measurements from line intensities require the knowledge of the effective rate coefficients. The simpler the atomic or molecular structure, the easier is the construction and usage of a CR-model. Therefore, helium is chosen as diagnostic gas in laboratory plasmas, in particular the He-line at 728 nm. Additionally, this gas is used as buffer gas in order to vary actively the electron temperature in mixtures with hydrogen or deuterium. For helium two CR-models can be used, the one of Fujimoto [Fuj79a] which was improved by implementing a new data set [Fuj95] or, alternatively, the ADAS (Atomic Data and Analysis Structure) code package [Sum99]. This code package is developed originally for astrophysics and fusion plasmas providing data for atomic elements in each ionization stage. For helium a complete and revised data set exists, which

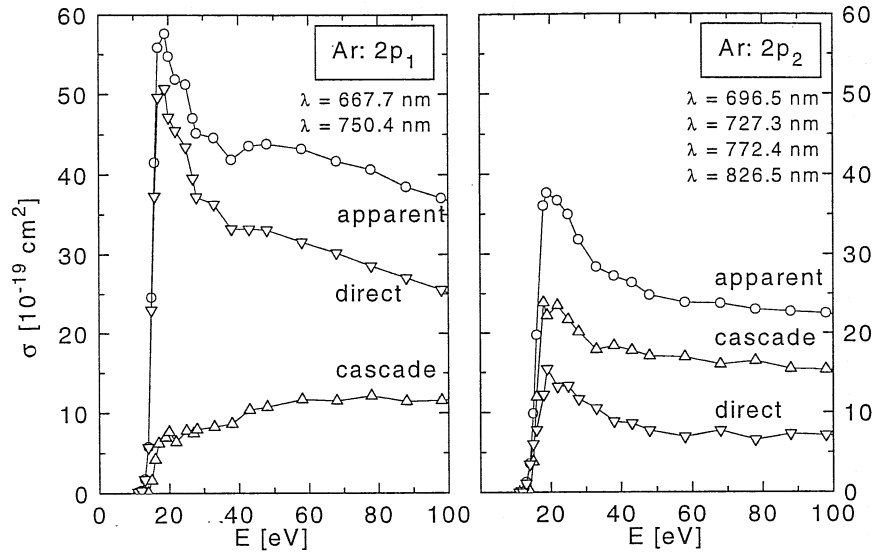


Figure 3.2: Argon cross sections for excitation from the ground state and cascading into the $2p_1$ and $2p_2$ states together with the apparent cross section for these states [CBSL98].

is also based on the new data implemented in Fujimoto's code. In particular, cross sections calculated with the R-matrix method are used, which provides accurate values close to the threshold energy [HHKS92]. Both CR-models implies the possibility to calculate populations of optical thick plasmas. However, Fujimoto uses the approximation for high opacity and would therefore overvalue the optical thickness of resonance lines. In the case of the ADAS code, the escape factors are calculated by an additional computer program which allows the adaptation to the individual experiment [Beh98, BF00]. Figure 3.1 shows the effective rate coefficients for the 728 nm line ($3^1S - 2^1P$ transition) for $n_e = 10^{17} \text{ m}^{-3}$ in the optically thin case calculated with both CR-models. For this individual emission line, the effective rate coefficients are almost identical. For comparison the rate coefficient derived from the corona model in its simplest form, i.e. ground state excitation only, is given. The application of the CR-model yields an enhancement which results in lower T_e at the same line radiance. In the temperature range relevant for low temperature plasmas, the steep dependence of the rate coefficient on T_e leads to a very sensitive T_e diagnostics.

Argon lines are also used for T_e -diagnostics, since this rare gas serves also as a buffer and diagnostic gas. Because of the remarkable lower threshold energies of argon lines, of $\approx 11.5 \text{ eV}$ instead of $\approx 21 \text{ eV}$ for helium, the T_e -dependence is not as steep as in the case of helium. The problem for argon is the complex atomic structure and the absence of a complete data set (cross sections) in order to build a CR-model. Based on a semi-empirical formulae for calculating cross sections Vlček introduces a CR-model [Vlč89, VP89].

Here, for argon the corona model is used to evaluate measured line radiations, which can be improved by considering excitations out of metastable levels

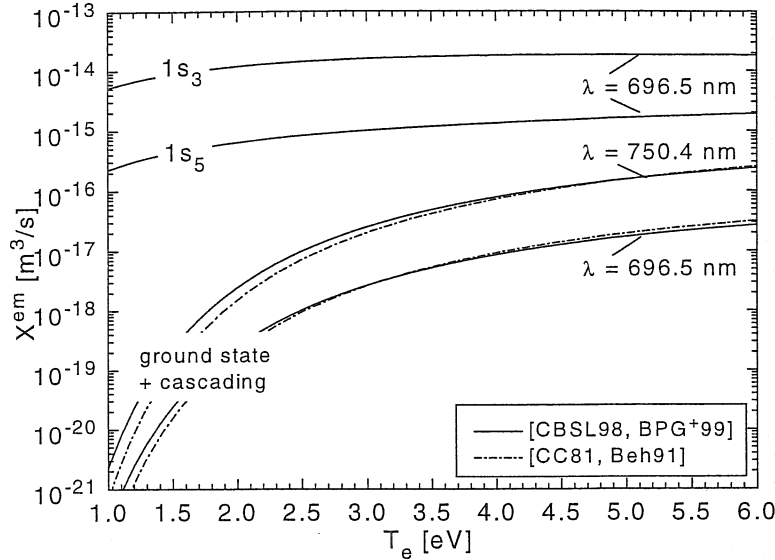


Figure 3.3: Emission rate coefficients for two argon lines using the apparent cross section [CBSL98] or data from [CC81, Beh91]. Additionally, rate coefficients for excitation out of the metastable argon levels ($1s_3$ and $1s_5$) [BPG⁺99] are shown for the $\lambda = 696.5$ nm line.

provided that their population density is known, for instance from absorption measurements. In addition, cross sections taken from literature imply corrections by cascading processes. Figure 3.2 shows examples of electron impact cross sections from the argon ground state into the $2p_1$ and $2p_2$ states (Paschen's notation) which are the direct cross sections. The cross sections for cascading are in the first case smaller than the direct one, whereas in the second case cascading is the dominant contribution for populating the $2p_2$ state. Direct and cascading cross sections are compiled to the apparent cross section. The data are taken from [CBSL98]. As a consequence emission spectroscopy of lines from the $2p_2$ state, (wavelengths are included in Fig. 3.2) is strongly affected by cascading.

In Fig. 3.3 the emission rate coefficients of lines originating from either states are given. The apparent cross section of [CBSL98] was used and compared with data of [CC81] corrected by cascading (described in [Beh91]). A Maxwellian EEDF was applied. Deviations can be seen for $T_e \lesssim 2.5$ eV, which are probably due to the better energy resolution of the experiments of [CBSL98]. Cross sections for excitation out of the two metastable levels, $1s_5$ and $1s_3$, are compiled in [BPG⁺99]. The corresponding emission rate coefficients are also shown in Fig. 3.3. Assuming a relative population of these metastable levels of $10^{-3} - 10^{-5}$, which is typical for low pressure discharges, the contribution may be relevant or even dominating. In case of the line at $\lambda = 750.4$ nm, i.e. a line originating from the $2p_1$ state, the rate coefficients out of metastable states are remarkable smaller [BPG⁺99]. All in all the preferred diagnostic lines are lines originating from the $2p_1$ state since, on one hand cascading is lower than direct excitation and, on the other hand excitation out of metastable states is not relevant, i.e. the knowledge

of these population densities is not required.

Combining diagnostics of emission lines from helium and argon reveals a possibility to determine the EEDF in the energy range where electron impact excitation occurs. Up to now, a Maxwellian distribution was presupposed. As discussed in Sec. 2.1.3 EEDFs in low pressure discharges are mostly between Maxwellian and Druyvesteyn-like distributions. Since the shape of both distributions is given by the exponential factor with E/kT_e in linear or quadratic form, an approach was made in [BF94] to use any non-integer value as exponent. The electron temperature is then defined by equating the average energy $m_e \langle v^2 \rangle = 3kT_e$. The EEDF with the parameter ν is given by:

$$f_\nu(E) = C_\nu \sqrt{E} \exp \left[-a_\nu \left(E / kT_e \right)^\nu \right], \quad (3.2)$$

with the constant C_ν for normalizing the integral to unity and a_ν determined by the condition for the average energy:

$$C_\nu = \frac{\nu a_\nu^{1.5/\nu}}{(kT_e)^{1.5}} \frac{1}{\Gamma(1.5/\nu)} \quad ; \quad a_\nu = \left(\frac{2}{3} \frac{\Gamma(2.5/\nu)}{\Gamma(1.5/\nu)} \right)^\nu. \quad (3.3)$$

The average velocity is then given by:

$$\langle v \rangle = \sqrt{\frac{3kT_e}{m_e}} \frac{\Gamma(2/\nu)}{\sqrt{\Gamma(1.5/\nu) \Gamma(2.5/\nu)}}. \quad (3.4)$$

The procedure of measuring the EEDF is the following: the evaluation of lines covering, if possible, a wide energy range yields a T_e for each line under the assumption of a Maxwellian distribution. If this assumption is not fulfilled the resulting T_e will differ in the order of their threshold energy. For instance, analysing a helium and an argon line (covering the energy range of $\approx 11 - 30$ eV) the argon line yields higher T_e than the helium line, because of the decay in the EEDF. In the next step the cross section is convoluted with a EEDF with higher ν until one receives the same temperature for either line. This requires reliable cross sections, in particular in the energy region close to the threshold energy. Details of the method are described in [BF94]. Since excitation energies of most atoms are in the energy range above 10 eV, no information can be obtained for the low energy range. However, this is particularly important if molecules are present in the plasma, which deplete the low energy range due to excitation of vibrational levels. In this case molecular radiation is used as diagnostic itself, but information about vibrational population is required which has to be obtained from calculations. In [Vin99] vibrational bands of nitrogen have been analysed for diagnostics, covering the energy range between 1.5 and 4.5 eV.

Particle densities of radicals can be measured by emission spectroscopy, in-situ and spatially resolved, if T_e , n_e and the emission rate coefficient are known (Eq. (3.1)). For instance, in methane plasmas, the radiation of CH, C₂ and H₂ as well as H is detectable in the visible spectral range. However, additional

excitation channels may occur. In case of Balmer radiation of H, besides the direct excitation within the atom, dissociative excitation from CH₄, H₂ and C₂H_y, formed in the plasma by heavy particle collisions can contribute to the radiation. Rate coefficients for direct excitation are mostly higher than those for dissociative excitation, however, the particle density of the dissociating molecules is considerable higher than the radical density. In order to determine the radical density, the part of the radiation originating from the dissociative excitation has to be subtracted:

$$n_r = \frac{\dot{N} - \sum_m n_m n_e X_{m,r}^{diss}(T_e)}{n_e X^{eff}(T_e)}. \quad (3.5)$$

Here, m is the index denoting the molecule from which the dissociative channel occurs, r denotes the radical species which will be determined. In pure hydrogen plasmas, where the molecular hydrogen density usually dominates, the part of the radiation which is due to dissociative excitation can dominate, in particular at low T_e , and determination of the atomic density is almost insensitive whereas the molecular density can be determined precisely. Therefore it has to be checked where the major part of the radiation comes from.

3.1.3 Population of electronic excited states

For detailed understanding of atomic and molecular physics, i.e. populating and depopulating mechanism, emission spectroscopy combined with absorption spectroscopy reveals the possibility to determine population densities in a variety of electronic states. These measured populations can be compared with CR-model calculations. This is usually done in a so-called Boltzmann-plot, i.e. the plot of the population density weighted with the statistical weights versus the energy, both relative to the ground state. In the case of a Boltzmann equilibrium of the states, the plot shows a straight line where the slope is related to T_e according to Eq. (2.12). Information about relevant physical processes populating selected levels can then be studied by varying the input parameters of the CR-model, i.e. metastable population density, diffusion times, opacity of resonance lines and even opacity of lines related to the metastable levels, etc.. Such an adjusted population can improve remarkably the T_e diagnostics. Furthermore, the collisional limit of the Boltzmann population (PLTE) can be obtained. The quantum number of the collisional limit should decrease with increasing electron density.

3.1.4 Rotational and vibrational populations of molecules

Analysing the radiation of molecular bands yields rotational and vibrational populations in the excited electronic state. The following discussion is restricted to diatomic molecules. Since emission spectroscopy is applied in the visible and ultraviolet spectral range, vibrational-rotational bands coupled with an electronic transition are observed. Additionally, homonuclear molecules do not have a dipole

moment and pure vibrational or rotational transitions are forbidden. Details of molecular spectra, electronic, vibrational and rotational transitions are given in the book of Herzberg [Her50].

Due to the significant smaller energy difference between rotational and vibrational states in comparison to electronic states, a Boltzmann distribution among these levels can be assumed. However, this may be fulfilled for populations in the ground state of the molecule but in excited states the situation can be altered by the electron impact excitation mechanism.

A vibrational temperature in the ground state will be transferred via the Franck–Condon principle into the excited state. If the equilibrium internuclear distance which refer to the minima of the potential curves of both states are shifted, diagonal transitions are not preferred and the vibrational distribution in the excited state can not be assigned with a temperature T_{vib} . Additionally, cascading might also influence the distribution among these levels. Deviations from a vibrational temperature can simply be obtained by a Boltzmann plot. Since vibrational levels are not degenerated, a plot of the relative population, i.e. $n(v')/n(v' = 0)$ against the energy difference is sufficient. It is common to mark the vibrational quantum number v with one tic to identify the upper state and with two tics for the lower state of a transition. The vibrational population of the upper electronic state is correlated to the radiation of the molecular band by the branching ratio $c_{v',v''}$:

$$\dot{N}_{v',v''} = n(v') \frac{A_{v',v''}}{\sum_{v''} A_{v',v''}} = n(v') c_{v',v''} \simeq n(v') \frac{q_{v',v''} \nu_{v',v''}^3}{\sum_{v''} q_{v',v''} \nu_{v',v''}^3}, \quad (3.6)$$

$q_{v',v''}$ is the Franck–Condon factor (FCF). If the excitation transfer from the ground state is the dominant mechanism populating an excited state, ground state and upper level of the transition are related via the Franck–Condon matrix and the ground state population can be obtained. For this purpose both Franck–Condon matrices have to be known.

Figure 3.4 shows the correlation between T_{vib} in the ground state and vibrational populations in an excited state for N_2 and H_2 . In the case of N_2 a T_{vib} can be assigned to the excited state population whereas in the case of H_2 the relative population in the upper state is not characterized by a temperature [FHB96]. In low temperature plasmas, vibrational temperatures are higher than the gas temperature but below electron temperature. Nevertheless, the vibrational population in the ground state may not be related with a temperature, which depends on the populating and depopulating mechanisms, and which, for instance, may empty a vibrational level selectively.

Concerning rotational population, each vibrational band in the excited state or in the ground state may have its own rotational temperature T_{rot} . As for vibrational populations, rotational populations in the ground state can be projected into the excited state in question. It is assumed that the rotational quantum number J remains unchanged under electron impact excitation, i.e. $\Delta J = 0$. Here, the change in the distance of rotational energy levels have to be considered, represented in a first approximation by the rotational constant B_v in each

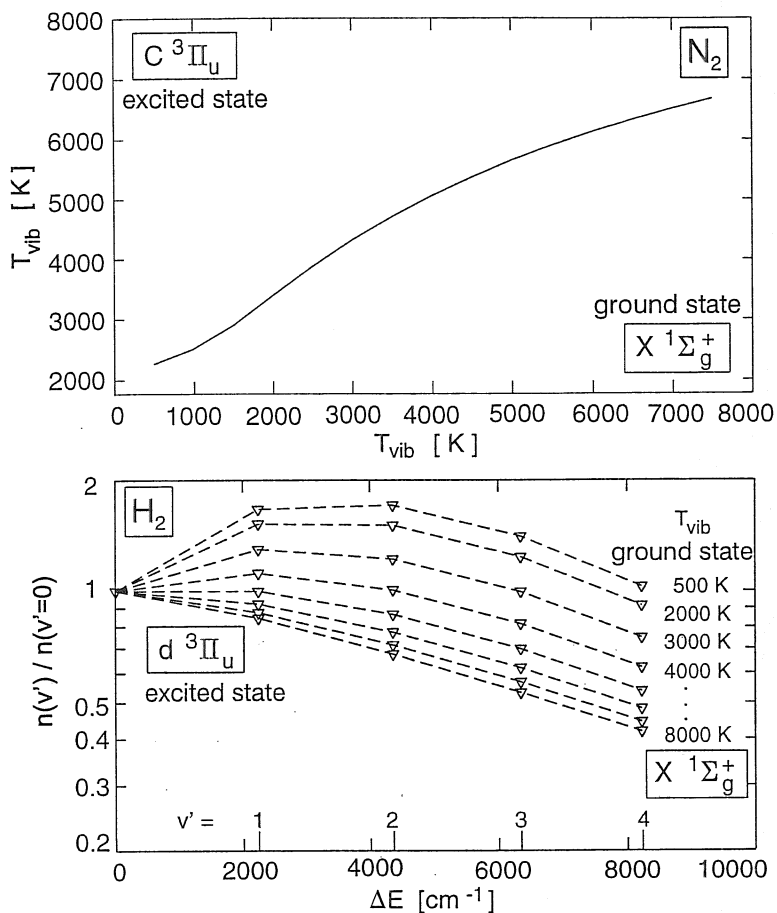


Figure 3.4: Vibrational populations in the excited state of N_2 and H_2 depending on the vibrational temperature in the ground state [FHB96].

vibrational state [Sob89]:

$$\underbrace{B_v T_{rot}}_{\text{ground}} = \underbrace{B_{v'} T_{rot}}_{\text{excited state}}. \quad (3.7)$$

The rotational temperature in an excited state can be obtained by a Boltzmann plot of rotational lines of the P , Q or R branch of the rotational band. For this purpose line strengths, statistical weights and alternation of intensities by the influence of the nuclear spin (homonuclear molecules) have to be considered. A compilation of line strengths (Hönl–London factors) for each type of electronic transitions can be found in the book of Kovács [Kov69]. If the rotational structure is not resolved and lines are not clearly identified because they are overlapped by each other, a computer simulation of the spectra can be carried out with T_{rot} as parameter. Comparing measured with calculated spectra, T_{rot} can be determined. This requires the knowledge of the molecular constants of all vibrational states involved. Additionally, the coupling case of the angular momentum, spin-splitting or even lambda splitting have to be considered which may differ for

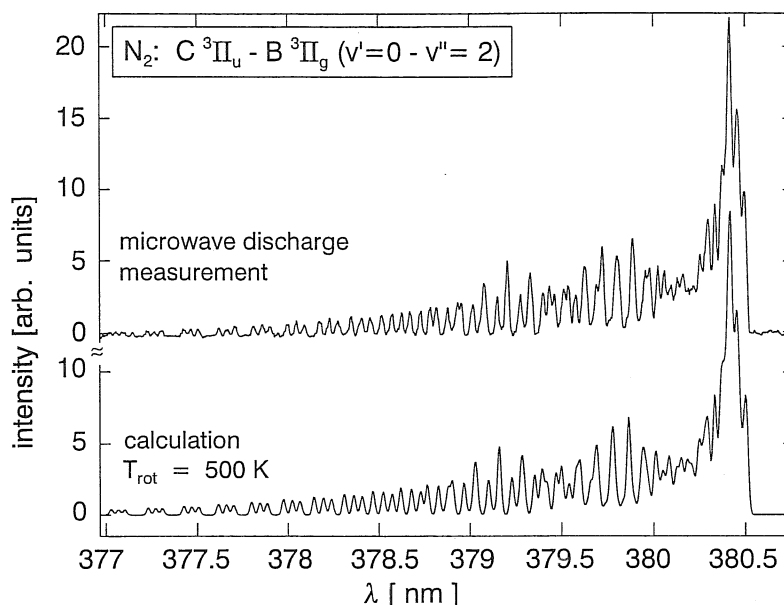


Figure 3.5: Comparison of calculated and measured spectrum of the vibrational band ($v' = 0 - v'' = 2$) in the second positive system of N_2 .

each electronic transition. The line strengths are then convoluted with the apparatus profile. Figure 3.5 gives an example of the N_2 transition ($C^3\Pi_u - B^3\Pi_g$, $v' = 0 - v'' = 2$) around 380 nm. The rotational temperature which fits best to the measured spectra is 500 K which is also T_{rot} in the ground state since the rotational constants of both states involved are very similar. If the population originates only from heavy particle collisions T_{rot} represents the gas temperature T_g . This method is suited as gas temperature diagnostics in low temperature plasmas and works very well particularly for the heavy molecule N_2 [Beh91]. For the light molecules as hydrogen and deuterium the rotational temperature in the ground state is not equal to the gas temperature [Sob89]. Concerning molecules as CH which are formed via dissociation processes of CH_4 and which may be populated by dissociative excitation, the rotational temperatures are remarkable higher than the gas temperature [Beh91]. In this case, the dominant population channel can be determined.

3.2 Absorption spectroscopy

Absorption spectroscopy in the optical wavelength range is a powerful tool for measuring densities of molecules, atoms and radicals in plasmas. In recent years it became more and more important since on one hand high stabilized continuum radiation sources with high power are available now and on the other hand the detection devices were improved. Photodiode arrays and CCD (or ICCD) cameras enable fast recording of multiple atomic spectral lines and complete molecular

bands. An review about high-sensitivity white-light absorption spectroscopy in processing plasmas is given in [AGL00]. There, the techniques and their limitations are discussed in detail as well as applications are presented.

The principle of the method consists of the experimental determination of the frequency integrated absorption coefficient, already discussed in Sec. 2.2.4, in particular in Eq. (2.29). The intensity of an external source absorbed in a homogenous plasma of length l is given by:

$$I_\nu(l) = I_\nu(0) \exp(-\kappa(\nu) l), \quad (3.8)$$

and can be expanded and approximated for weak absorption $\kappa(\nu) l \ll 1$ to:

$$\begin{aligned} I_\nu(l) &= I_\nu(0) (1 - \kappa(\nu) l + (\kappa(\nu) l)^2/2 - \dots) \\ &\simeq I_\nu(0) (1 - \kappa(\nu) l). \end{aligned} \quad (3.9)$$

The combination of Eqs. (2.29) and (3.9) yields the relation between absorption signal and population of the lower electronic state of the observed transition:

$$\int_{line} \frac{I_0 - I_\nu}{I_0} d\nu = \frac{c}{\lambda^2} \int_{line} \frac{I_0 - I_\lambda}{I_0} d\lambda = n_k A_{p,k} \frac{g_p}{g_k} \frac{\lambda^2}{8\pi} l. \quad (3.10)$$

For absorption measurements it is more convenient to change from frequencies to wavelengths.

It should be kept in mind, that the line profiles of emission and absorption are assumed to be equal. Depending on the spectroscopic system, i.e. spectrometer and detector, in most cases the line profiles are covered by the apparatus profile. For instance, the half width of a Doppler profile of a He-line around 600 nm at 500 K gas temperature is 4.5 pm, whereas the half width of a typical 1m spectrometer system is around 40 pm. As a consequence the line profile in Eq. (3.10) can be replaced by the apparatus profile:

$$\int_{line} \frac{I_0 - I_\lambda}{I_0} d\lambda = I_{max} \Delta\lambda_{1/2} P_f, \quad (3.11)$$

with P_f the profile factor, which is 1.064 for a Doppler profile. The population density is then given by:

$$n_k = \frac{8\pi c}{\lambda^4 l} \frac{g_k}{g_p A_{p,k}} I_{max} \Delta\lambda_{1/2} P_f. \quad (3.12)$$

The linear correlation of the absorbed intensity in the line centre I_{max} to the density n_k is valid only if peak absorption is small, which was the assumption for the approximation in Eq. (3.9). This must be checked for each spectral line and also depends on the line profile. The better the spectral resolution of the spectrometer the higher is I_{max} , which increases the signal-to-noise ratio. Additionally, if the apparatus profile is almost as small as the Doppler profile of the line, the linearity of the resulting peak absorption is also valid for higher signals. For remarkable broader line profiles, e.g. ten times broader than Doppler, the

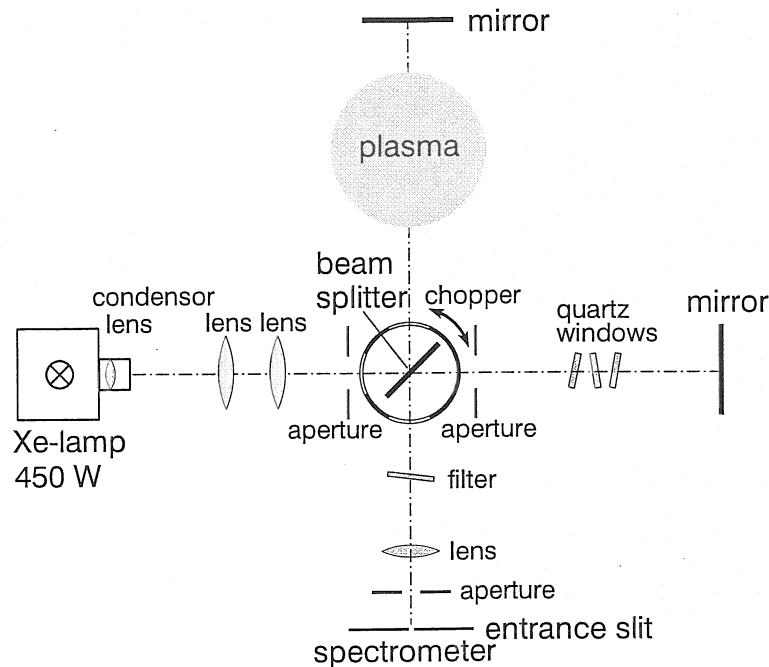


Figure 3.6: Michelson setup for absorption measurements. Filters and windows adjust the radiation of the two legs to the same intensity. The lenses are used for light focusing.

linearity holds only up to a few percent of the peak absorption. This means that the method becomes soon very insensitive and depends on the precise knowledge of the spectral line profiles.

The system used for diagnostics of low pressure plasmas is carried out in Michelson configuration (Fig. 3.6) as suggested in [BOSS95]. As continuum source a stabilized high pressure xenon arc lamp (450 W max. power) was chosen. The light passes parallel through the plasma which is achieved by the lens system. Light focusing is also a possibility but does not guarantee identical path ways through the plasma in forward and backward direction. Rotation of the chopper arranged around the beam splitter allows the measurement of four signals on a short time scale: (1) plasma light together with the light of the lamp, (2) plasma light (plasma emission), (3) light of the lamp, (4) background signal. Accumulating each signal and averaging of five passes, changes in time will be averaged. An absorption spectrum is then observed by subtracting the signals in the following procedure: $I_{abs}(\lambda) = ((1) - (2)) / ((3) - (4))$. An absolute calibration of the optical system is not required which is a great advantage of this method. Additional filters and windows in the light path adjust the signals of each leg and lowers the light to the detector. The light passes two times the plasma, thus increasing the absorption signal. The light is then focused to the entrance slit of a spectrometer system. For the results presented here two spectrometer systems were available. System 1 consists of a 1 m spectrometer with gratings of 600 or 2400 lines per mm and a CCD camera. System 2 is a combination of a 1 m spectrometer with grating of 1200 lines per mm and a ICCD camera. The spectral

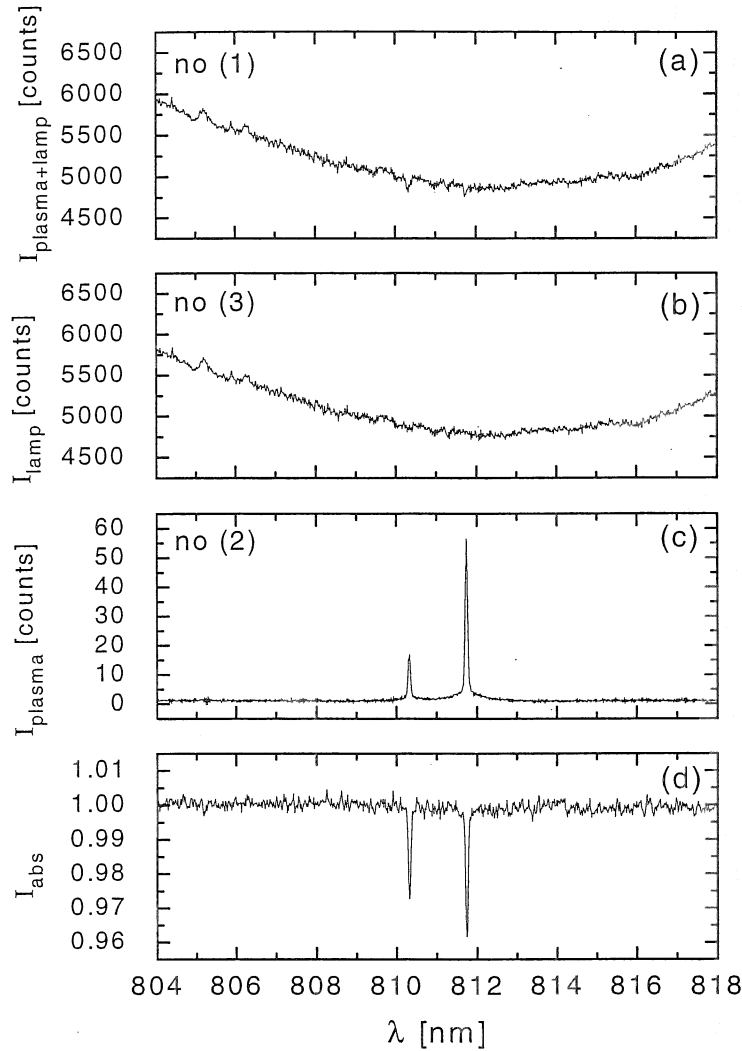


Figure 3.7: Argon absorption spectra around 810 nm (d) together with three of four signals (a)–(c) necessary for the evaluation.

resolution achieved with system 1 is typically 55 pm and 12 pm, respectively, and the with apparatus profiles are Doppler profiles, whereas system 2 has a spectral resolution of 55 pm, limited by the pixel size of the ICCD. Additionally, the profiles are broader in the wings, due to the characteristics of ICCDs. Here, the profile factor is determined to be 1.86, which reduces the peak absorption. Therefore, system 1 with the 12 pm resolution is preferred, but this system is limited by the wavelength limit of the grating and detects wavelengths lower than 750 nm only. Typical signals of system 2 of the spectra numbers (1) – (3) and I_{abs} are shown in Fig. 3.7 for the absorption of argon lines around 810 nm. The detection limit achieved with both spectroscopic systems is around 10^{-3} .

Since the absorption signal depends on the population of the lower electronic state of a transition, only ground state densities, metastable state densities and

the first excited state densities (upper state of resonance lines) can be observed. The latter is remarkably populated if self-absorption of the resonance lines takes place. Resonance lines of atoms itself are usually in the vacuum ultraviolet system whereas the spectroscopic systems used here are limited to detect light in the visible wavelength range (300 – 900 nm). Another criterion for selecting a transition is the Einstein transition probability for spontaneous emission which must be high enough, which usually fulfilled for optically allowed transitions in atoms. In contrast, the transition probability of an electronic state in molecules is spread over into the vibrational bands and rotational lines which, therefore, requires higher detection limits: $\approx 10^{-5}$. Additionally, these molecules are formed by dissociation processes in the plasma and their densities are considerably lower than the density of atomic gases (rare gases) which are used as diagnostic or buffer gases. All in all the method of absorption spectroscopy discussed in this section is used as a completion to the emission spectroscopy, yielding population densities of metastable states and resonant levels in helium and argon.

3.3 Microwave interferometry

Plasma interferometry is used for the determination of the electron density along a line of sight. An electromagnetic wave can propagate in a plasma if the frequency is higher than the plasma frequency ω_p . The dispersion relation without magnetic field is given by:

$$\omega^2 = \omega_p^2 + c^2 k^2 \quad \text{with} \quad \omega_p^2 = n_e e^2 / \varepsilon_0 m_e \quad (3.13)$$

For most laboratory plasmas ω_p is in the microwave range. Typical frequencies used are 28, 70 or 140 GHz for which the vacuum wavelength ranges from 10.7 to 2.14 mm. This makes spatially resolved measurements possible. Depending on the experimental geometry, two interferometer configurations are preferred: Mach-Zehnder or Michelson interferometer, both shown in Fig. 3.8. The interferometer can be carried out in waveguide configuration or in optical configuration due to the small wavelengths. By using parabolic antenna instead of Horn antenna, the radiation is focused in the plasma volume.

Comparing the signal of the leg including the dispersive medium, i.e. the plasma, with signal of the reference leg, a phase shift occurs and the plasma density (i.e. the index of refraction) can be determined. The phase shift is given by:

$$\Delta\phi = \frac{2\pi l_p}{\lambda} - \frac{2\pi l_p}{\lambda_p} = \frac{2\pi l_p}{\lambda} \left(1 - \sqrt{1 - \frac{\omega_p^2}{\omega^2}} \right), \quad (3.14)$$

with the plasma length l_p , the vacuum wavelength λ and the wavelength of the electromagnetic wave in the plasma λ_p . It is assumed that the plasma is homogeneous along l_p . For a small phase shift Eq. (3.14) can be expanded and

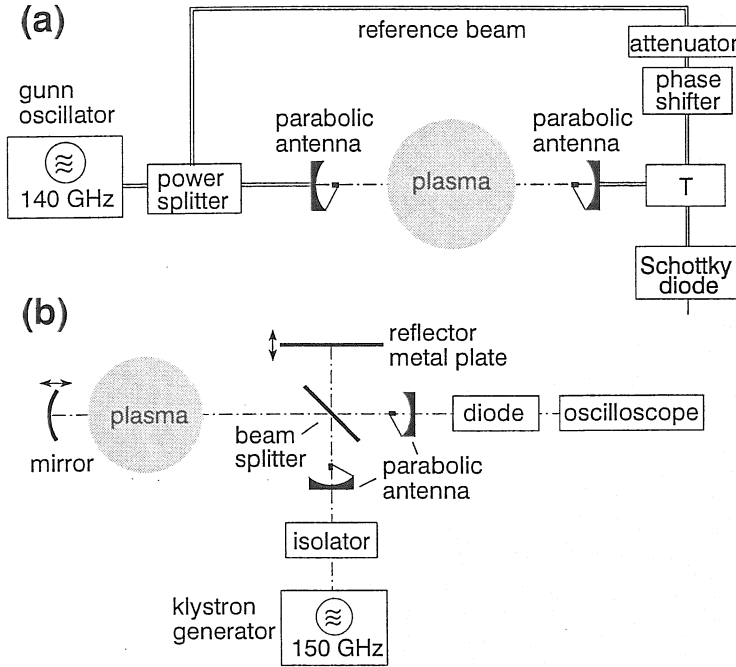


Figure 3.8: Microwave interferometer in Mach-Zehnder configuration (a) as well as in Michelson configuration (b), both carried out in quasi-optical transmission.

approximated by:

$$\Delta\phi = \frac{2\pi l_p}{2\lambda} \frac{\omega_p^2}{\omega^2} = \frac{2\pi l_p}{2\lambda} \frac{n_e}{n_e^{cutoff}}. \quad (3.15)$$

n_e^{cutoff} is the cutoff density of the microwave which is $2.4 \times 10^{20} \text{ m}^{-3}$ at $f = \omega/(2\pi) = 140 \text{ GHz}$. Since electron densities are typically three orders of magnitude below the cutoff density phase shifts are expected to be $1/10 - 1/100$ of one angular degree. To increase the signal-to-noise ratio and to avoid electrical drifts of the experimental setup the plasma was pulsed continuously.

It should be emphasized that the measured electron densities are line integrated densities, which is an advantage for spectroscopic measurements if the same line of sight in both setups is used. In this case it is not necessary to know the length of the plasma.

3.4 Langmuir probes

Langmuir probes are commonly used for spatially resolved measurements of n_e , T_e and EEDF in low pressure plasmas. They are based on the work of Langmuir [Lan24, MSL26]. The principle of the method is the following: a cylindrical symmetric filament is brought into the plasma. By applying a voltage ramp the

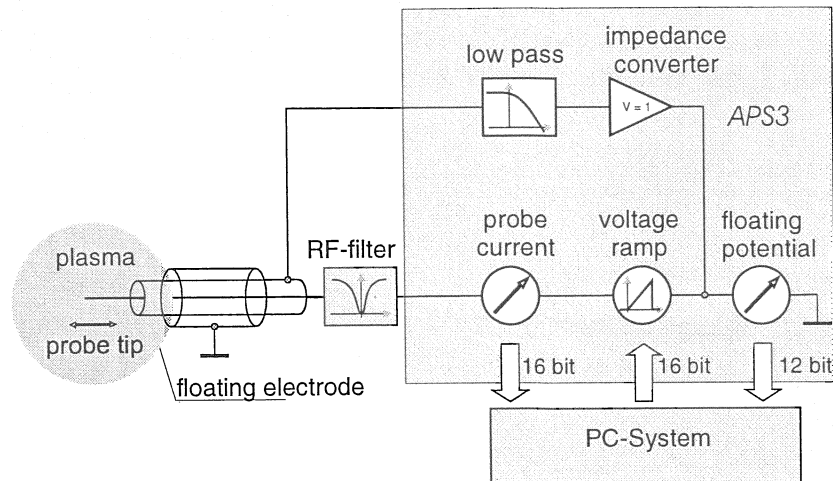


Figure 3.9: Schematic electrical drawing of the Langmuir probe system APS3.

resulting current is measured. The so-called I/V-characteristics contains information about the plasma parameters. Due to the application of probes in various plasma types, i.e. excitation frequency, pressure range, magnetic fields, reactive gases etc., the experimental and theoretical work has been further developed, however, a universal formula does not exist. Depending on the individual problem, solutions can be found in literature.

For measurements introduced here, the APS3-system [ACK95, Kas95] was used, especially designed for measurements in RF plasmas and in reactive plasmas. It allows spatially resolved measurements automatically by means of a high-speed stepping motor and membrane bellows. Because of a fast shift, coating or etching of the probe tip itself does not cause a problem in reactive plasmas. In order to minimize the disturbance of the plasma at the position where the measurement takes place, the probe tip (tungsten, $d = 50 \mu\text{m}$, $l = 5 \text{ mm}$) is guided in a small quartz or ceramics capillary tube mounted at one end of an aluminum oxide tube which enables radial or axial resolved measurements over this length. To prevent the probe tip from coating while remaining in the zero-position, it is automatically drawn back into the capillary tube. Figure 3.9 shows schematically the setup of the system. In order to suppress strong second and third harmonics in typical RF plasmas a passive compensation method is used [SFAP01]. For applications in MW discharges the probe tip is isolated. A voltage ramp ($\pm 80 \text{ V max.}$) is applied between probe tip and the reactor's grounded electrode or wall while the current to the probe is measured. The voltage-ramp is automatically centred around the floating potential which is achieved by an impedance converter. The corresponding DC-shift is limited to $\pm 320 \text{ V}$ which is sufficient for RF, MW and DC plasmas. The digital signals to the PC-interface are electrically decoupled by optocouplers. Due to these features, a symmetric current-voltage characteristic is always obtained in all plasmas where the electron density exceeds 10^{13} m^{-3} and is not higher than 10^{19} m^{-3} .

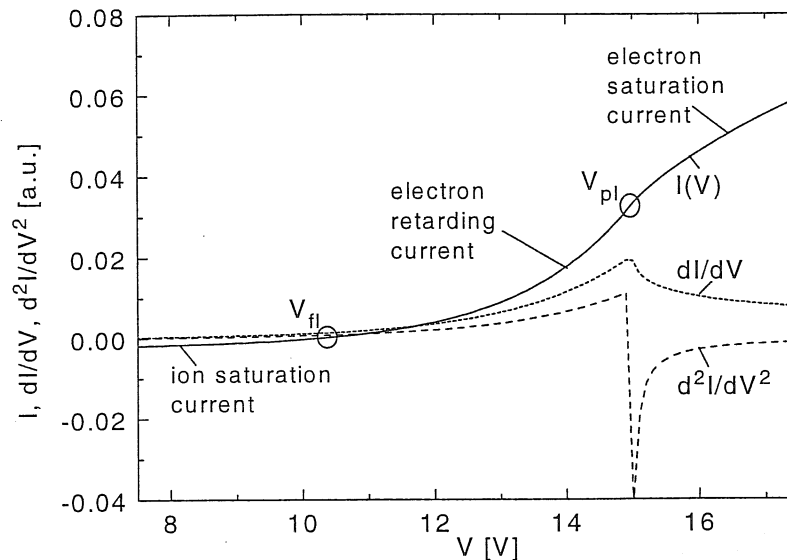


Figure 3.10: Typical current-voltage characteristic of the Langmuir probe APS3 together with the first and the second derivative. Marked are the floating potential (V_{fl}) and the plasma potential (V_{pl}).

A probe characteristic may be divided into three parts (Fig. 3.10): the small ion saturation current I_i obtained for a probe potential which is strongly negative against the plasma potential, the electron retarding current $I_{e,r}$ for probe potentials between the floating and the plasma potential (V_{fl} , V_{pl}) and the electron saturation current $I_{e,s}$ at which the electrons are accelerated against the probe surface. The floating potential V_{fl} is located where the electron and the ion currents are balanced and the overall current is zero. The plasma potential V_{pl} denominates the potential of the plasma bulk which allows all charged particles to reach the probe surface without being accelerated or retarded. For general relations between measured currents and plasma parameters see, for instance, [SS70]. Before evaluating the first and second derivative, the I/V -characteristic has been transformed with a Fast-Fourier-Transformation followed by a digital filter procedure in the frequency range. The second derivative is taken to derive the plasma potential where this plot is zero. The methods applied to determine plasma parameters n_e , T_e and EEDF from the probe characteristics are summarized in the next two sections.

3.4.1 Electron density

The standard evaluation method is based on the measurement of the electron current at plasma potential $I_{e,r}(V_{pl})$. The electron density is given by:

$$n_e = \frac{1}{A_p e} \sqrt{\frac{2\pi m_e}{kT_e}} I_{e,r}(V_p = V_{pl}), \quad (3.16)$$

with the surface of the cylinder electrode A_p and the probe potential V_p (the voltage drop between sheath edge and probe surface), which is equal to the plasma potential. The second method is based on the integral over the EEDF:

$$n_e = - \int_0^\infty f(V_p) dV_p. \quad (3.17)$$

This method does not depend on a special EEDF like the Maxwellian, which is assumed in Eq. (3.16) by using T_e . It should be mentioned that the ion saturation current is not used for evaluations, since the probe theory can be very complicated in this voltage range.

3.4.2 Electron temperature and EEDF

The electron temperature is derived from a fit of a Maxwellian EEDF by the logarithm of the measured probe characteristic in the low energy part. The slope of the electron retarding current $I_{e,r}$ yields the electron temperature:

$$T_e = \frac{e}{k} \frac{dV_p}{d \ln(I_{e,r})}. \quad (3.18)$$

Here, no other plasma parameters are needed to evaluate T_e . A second method is based calculating on the integral over the EEDF and is therefore independent from the aforementioned assumption of a Maxwellian EEDF. The mean electron energy becomes

$$\langle E \rangle = \frac{\int_0^\infty (eV_p) f(E) dV_p}{\int_0^\infty f(E) dV_p}, \quad (3.19)$$

with $\langle E \rangle = 3/2 k T_e$. In order to calculate the EEDF, the second derivative of $I_{e,r}$ yields:

$$\frac{d^2}{dV_p^2}(I_{e,r}) = \frac{2A_p \pi e^3}{m_e^2} f(E = -eV_p), \quad V_p < 0. \quad (3.20)$$

If the second derivative is disturbed by the RF modulation the undisturbed part of the logarithm of the second derivative is extrapolated linearly against the plasma potential.

3.4.3 Operation conditions

The electron density range, which can be measured with this probe system, is limited to $10^{13} \leq n_e \leq 10^{19} \text{ m}^{-3}$. Due to the chosen evaluation method the results are reliable and are obtained with an error of $\approx 10\%$. More critical is the evaluation of T_e which depends on a precise measurement of the electron retarding current in a wide voltage range. Additionally, an undisturbed Maxwellian distribution is required, if possible up to high energies which is often limited by

the detection limit for the measured current. For the same reasons, deviations from a Maxwellian distribution due to heavy particle excitations (around E_{thr}) are difficult to detect. In the case of molecular plasmas, the EEDF shows a sharp bend in the energy region of vibrational excitation (around a few eV) and fit by a slope in this region would lead to distorted results.

Apart from the detection problems, the influence of inserting a probe into the plasma on the plasma itself has to be checked carefully. Since the probe represents an additional surface in the plasma the plasma will react (local, around the probe) by a decrease of n_e and an increase of T_e which are then the measured values. In the case of large plasmas this influence is no problem at all, but in small plasmas the modifications may not be negligible. In summary, probe measurements are reliable for n_e diagnostics whereas for T_e and EEDF they can be used for comparison with other diagnostics. The great advantage of probe measurements is the possibility of getting spatially resolved results.

3.5 Mass spectrometry

Quadrupole mass spectrometers are used to determine partial pressures in a plasma. Depending on the system, either neutral densities or neutral, radical and ion densities as well as ion energies are measurable. By calibrating the system with known partial pressures absolute densities are observed. Since particle collisions in the detection system should be avoided, the background pressure is about 10^{-10} mbar which is achieved by differential pumping through a small aperture ($d \approx \mu\text{m}$). The low background pressure guarantees also small signals of impurities as water or oxygen in the detection system. The principle of mass spectrometry systems will be described briefly, for details the reader is referred to standard literature.

3.5.1 Residual gas analyser

For measuring neutral particle densities the mass spectrometer is placed in the residual gas of the chamber, far away from the plasma. Commonly such residual gas analysers are used for vacuum diagnostics or leak detection in a vacuum system. Due to the distance between plasma and detector no information of radicals produced in the plasma by dissociation can be derived. Therefore only gases filled into the chamber can be measured, e.g. H_2 , He, Ar as well as CH_4 and higher hydrocarbons, which will be formed as stable products in the plasma. Such a system gives information about demixing processes of gas mixtures in the vacuum chamber due to different pumping power for various particles and demixing at valves. Additionally, a dilution of gases such as CH_4 or SiH_4 can be quantified and the formation of higher hydrocarbons can be detected. Applying the fragmentation pattern of a gas at the detector, listed in tables (e.g. [CM71]), the composition of higher hydrocarbons can be determined. Such systems are

available in a wide mass range, the system used here was a QMG064 Balzers device working in the range between 1 and 64 amu.

3.5.2 Energy resolved mass spectrometry

Such types of analysers are used for the analysis of ions and neutrals in plasma processes. The aperture is located in the plasma sheath or in the surface in order to observe the ion energy distribution and the radicals hitting the surface. The analyser is sensitive on mass number and energy and detects neutrals and radicals as well as positive and negative ions, which is achieved by a suitable bias voltage. The working range and calibration procedure for plasma diagnostics is compiled in detailed for methane plasmas in [Pec98] and is therefore not described further here.

Chapter 4

Helium and Argon Plasmas

Helium and argon are used as diagnostic gases and to vary plasma parameters, essentially T_e in hydrogen plasmas. Therefore, diagnostics and results for pure rare gas plasmas are described first. Additionally, characteristics of the various experiments and underlying basic interpretations are discussed in principle.

4.1 Particle densities and gas temperature

Particle densities of those neutral species which do not dissociate can be calculated from the general gas equation (Dalton's law, Eq. 2.38) using the particle partial pressure. The partial pressures are either determined by the adjusted percentages through flow meters or measured by the residual gas analyser. If it is possible, the second method is to be preferred, since the pumping system, turbo pump and roughing pump, has different pumping speeds for different particle species. Furthermore, modulating valves and apertures have mass dependent flow rates. All of this can cause a change in the composition as determined by the flow meters. If the composition cannot be calculated directly, the demixing has to be determined for each operating condition. The procedure of measuring the actual composition through the additional aperture of the gas analyser is described in detail in [Sta00b]. Figure 4.1 gives an example of demixing measured in the ECR experiment depending on mixture (a) and pressure (b) for particle mixtures set by flow meters. In both mixtures, the correction factor is smaller than unity for the light species which means their actual percentages are lower than the values set by flow meters. In contrast, the heavier species accumulate. Since the total pressure is adjusted by an elbow valve which reduces the pumping speed of a turbo pump connected with a membrane pump, the demixing varies with pressure. In the case of argon or krypton, both being the heaviest species in either mixtures the changes in density are remarkable and have to be considered in further analysis. In the following the gas compositions are referred to values set with the flow meters but the actual percentages were used for the analysis.

The gas temperature was determined by the analysis of the vibrational band

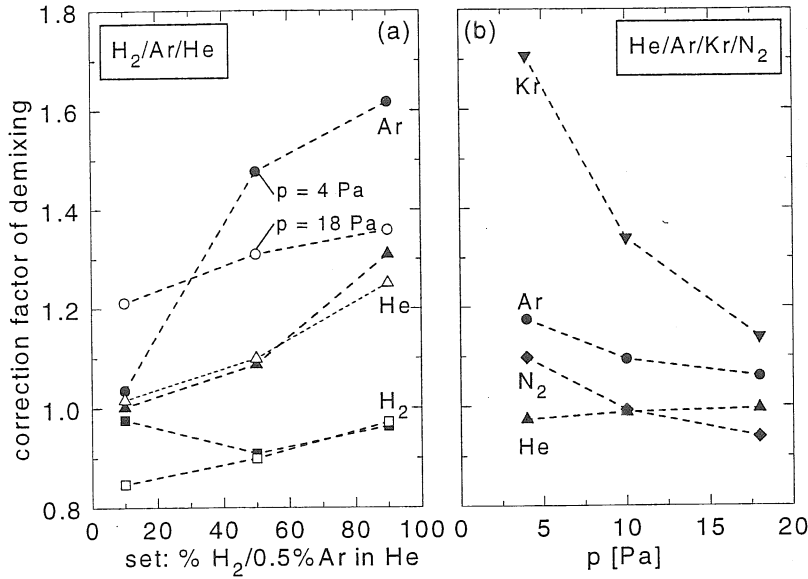


Figure 4.1: Demixing of individual species in a mixture of $x\%H_2/0.5\%Ar/He$ at 4 and 18 Pa (a) and of $91.4\%He/4.6\%Ar/2\%Kr/2\%N_2$ (b) in the ECR discharge.

0 – 2 of the electronic transition $C - B$ of N_2 . In order to avoid disturbing the plasma, small admixtures of N_2 ($\approx 1\%$) to the plasma were used for this purpose only. Figure 4.2a shows results of the ICP discharge in helium. As expected, the gas temperature increases with input power. The increase with pressure is caused by the decrease of the diffusion rate which reduces the thermal conductivity. If argon is present in the plasma the method fails, as illustrated in the Fig. 4.2b. Due to excitation transfer of excited argon states into the electronic state C of N_2 the rotational distribution of the vibrational states is disturbed and does no longer represent the gas temperature [FHB96]. With increasing argon admixture to the hydrogen plasma the rotational temperature strongly increases in the glow discharge at $p = 300$ Pa and the ECR discharge at $p = 5$ Pa, and is almost independent of pressure. In this case the vibrational band 0 – 0 of the electronic transition $B - X$ of the N_2^+ molecule around 391 nm is used for diagnostics. The energy level of the upper state is at 18 eV and higher than the ionization energy of argon. Thus, T_g of the glow discharge is almost constant at 400 K in the investigated parameter range (mixture, p , I) (Fig. 4.2b). For the ECR discharge $T_g = 450$ K was obtained which is independent of pressure, input power and mixture due to the possibility of adjusting the plasma size in the chamber.

4.2 Electron density

Electron densities in the ECR, MW and ICP discharges were measured with Langmuir probes and microwave interferometry [Sta00b]. However, in the case of

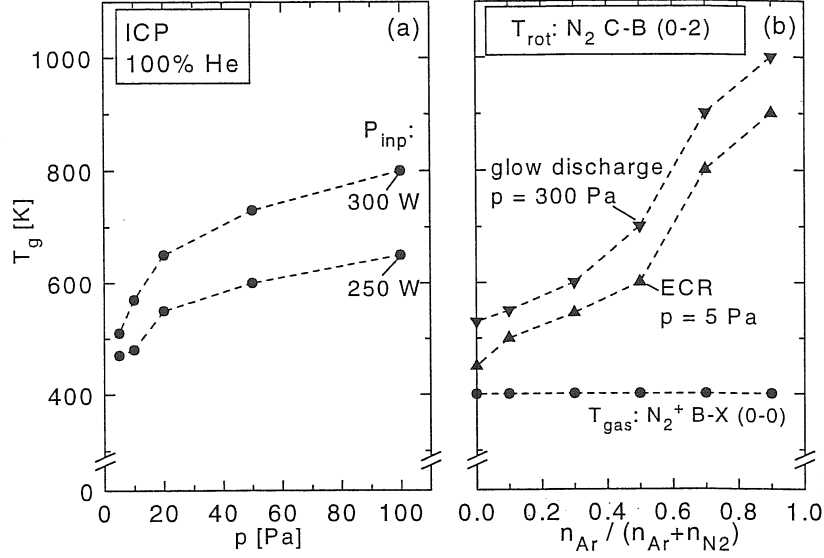


Figure 4.2: Variation of gas temperature determined from the radiation of the N_2 band around 380 nm (a). Part (b) shows the influence of excitation transfer from argon to nitrogen.

ECR discharges the plasma has a size of approximately 200 cm^3 and is strongly disturbed by the probe. The probe itself is surrounded by an additional sheath and measurements are not reliable since T_e increases whereas n_e decreases. Nevertheless, relative dependencies on parameters and spatial profiles can be obtained. Together with results from microwave interferometry the electron density was determined to be $n_e = 10^{17} \text{ m}^{-3}$ (almost spatially constant) independent of discharge parameters. However, since the plasma size varies and interferometric measurements make an average along the line of sight, the product $n_e l$ varies and the plasma length has to be estimated. Since emission spectroscopy uses the same line of sight, using the same length in the analysis gives results independent of the plasma size. Electron densities measured in the MW discharge show first an increase in radial direction with a plateau, which then drops with distance from the quartz tube. Dependencies on pressure, input power and gas mixtures have been observed [Heg02].

4.2.1 Spatial profiles in ICP sources

The ICP source is well suited for Langmuir probe measurements. The electron density varies with pressure, gas mixture and input power and has to be determined for each parameter set. The variation of n_e is between 5×10^{16} and $5 \times 10^{17} \text{ m}^{-3}$, increasing with increasing input power. As expected, argon plasmas have higher densities than helium plasmas. Results are given in [Pau00] and [SFAP01]. The measurements are reproducible within 10%. In the following only spatial profiles in helium discharges are discussed.

Figure 4.3 shows spatial profiles in the radial direction at axial position $z = 10$

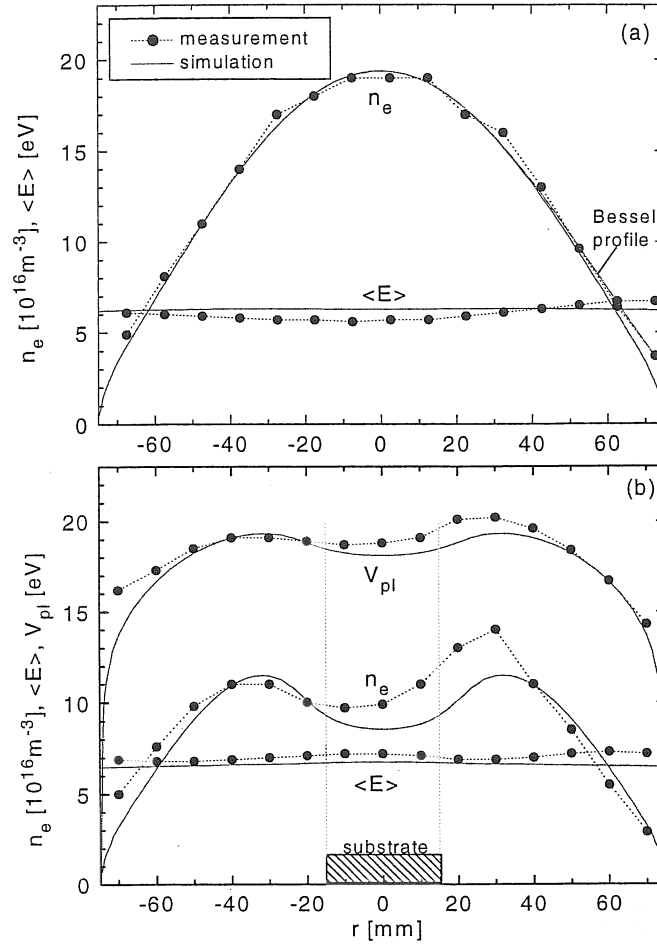


Figure 4.3: Radial profiles of n_e and $\langle E \rangle$ without (a) and with (b) substrate in the centre of the ICP discharge in helium at $p = 20$ Pa ($z = 10$ mm).

mm (Fig. 2.7) in a helium discharge at $p = 20$ Pa and $P_{inp} = 250$ W. Part (a) matches a Bessel profile indicated with a full line for $r > 0$ mm. The points refer to measured Langmuir probe data, whereas the full curve give results from simulations based on a hydrodynamic model [SFAP01] carried out for this special ICP source. The deviations near the chamber walls $|r| > 60$ mm are due to the diagnostic flanges which are not included in the simulations. The agreement between measurement and simulation is excellent. To match the peak electron density of the measurement the input power for the simulation has to be set to $P_{sim} = 95$ W with a coil current of $I_{coil} = 11.8$ A. This allows the determination of the losses and the overall efficiency of the system. Introducing a substrate holder (30×30 mm) into the centre of the discharge yields profiles (10 mm above the substrate) as presented in part (b) of Fig. 2.7. The electron density as well as the plasma potential drop locally and show a saddle like structure, whereas the mean energy $\langle E \rangle$ slightly increases. The measured profiles are unsymmetrical because

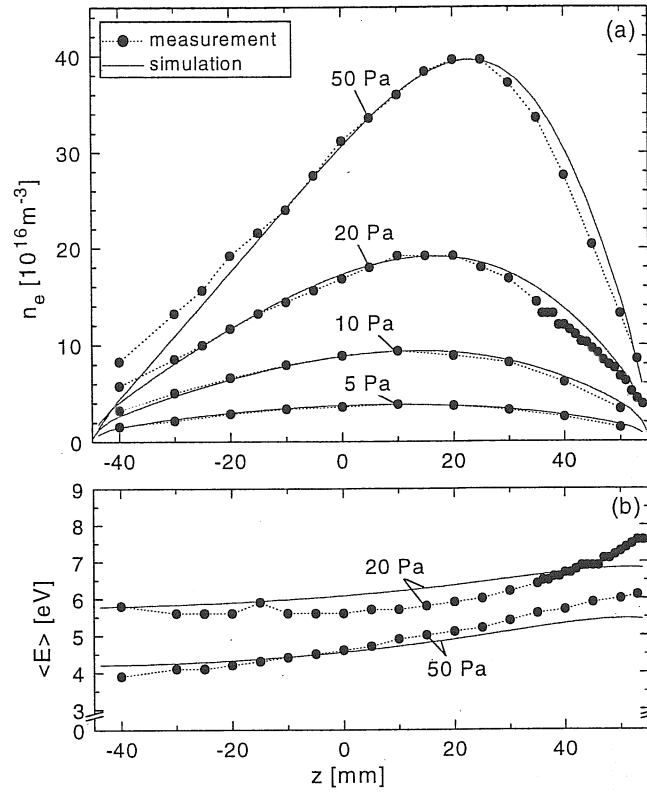


Figure 4.4: Profiles of n_e in axial direction ($r = 0$ mm) at various pressures in the ICP helium discharge (a). Part (b) shows the corresponding mean energy.

the Langmuir probe is introduced into the plasma from negative r directions. For positions $r \gtrsim 0$ the plasma is affected by the Langmuir probe and the substrate. Again, a good agreement between measurements and simulations is observed. For the analysis of data from emission spectroscopy the line averaged electron density has to be taken. This is derived from the peak electron density determined by Langmuir probes divided by the factor of the Bessel profile (without a substrate): $\bar{n}_e = n_{e,max}/1.6$.

In the axial direction the profiles depend on the discharge pressure as shown in Fig. 4.4. Again measurements and simulations are in excellent agreement. The deviations for small z -values are due to the diagnostic flange in the bottom of the chamber which is not included in the simulations. The maximum of the density is located closer to the quartz window than to the bottom plane of the chamber. This is a consequence of the discharge heating which only took place in the proximity of the coils, i.e. directly below the quartz window. Another aspect of the local heating is the behaviour of the electron temperature which shows a maximum at the quartz window in simulation and experiment. The peak electron density rises with increasing pressure (Fig. 4.4) and at the same time the position of the maximum moves towards the quartz window. The pressure dependence

can be explained as follows: from the electrodynamic model it is known that the heating of the discharge only occurs in a small region close to the quartz window. For lower pressure the high thermal conductivity of electrons causes a redistribution of the locally acquired energy over the whole plasma volume. With increasing pressure electron-neutral collisions become more frequent which results in a lower thermal conductivity. In order to transfer energy from the heating zone to the passive parts of the discharge, larger temperature gradients are necessary to drive the heat flux. Therefore a localized hot zone exists in which most of the particle generation takes place causing a contraction of the discharge in the region directly below the quartz window. This effect is also confirmed by the spatial dependence of the mean electron energy: the maximum is located directly below the quartz window.

The generator power input was kept constant at all four pressures ($P_{inp} = 250$ W). The coil current is derived from simulations (I_{coil} and the integrated power transferred to the plasma). With increasing pressure the coil current and the losses decrease by a factor of two. Electron density and conductivity rise and therefore the energy transfer from the coils to the plasma becomes more efficient. An increase from 20% to 45% efficiency corresponds to $P_{sim} = 50, 70, 95$ and 122 W at $p = 5, 10, 20$ and 50 Pa, respectively.

4.2.2 Measuring n_e in glow discharges

In the glow discharge neither Langmuir probes nor microwave interferometry was used since the diagnostic flanges are too small $d = 1$ cm. Since the plasma is cylindrically symmetric, a Bessel profile can be assumed in the radial direction. The averaged value was derived from the electrical conductivity (Eq.(2.52)) of the plasma by measuring the electrical current and voltage [BF94]. For gas mixtures the corresponding mobilities were used. In pure nitrogen discharges these results could be compared with spectroscopic determinations of electron densities, a diagnostic method which will be described briefly below. It has to be kept in mind, that spectroscopic results obtain the peak value of n_e , which is achieved by imaging the axis of the tube.

The diagnostic method is based on the measurement of the radiation of the vibrational band 0 – 2 of the electronic transition $B - X$ (first negative system) of the N_2^+ molecule (around 391 nm). The electronic state B can be excited by electron impact out of the ground state of the N_2 molecule and out of the ground state of the N_2^+ molecule. The first excitation mechanism has a threshold energy of $E_{thr} \approx 18$ eV whereas the second one needs only $E_{thr} \approx 3$ eV. In the case of a Druyvensteyn-like EEDF the second excitation mechanism would be dominant and the radiation of the molecular band is given by: $\dot{N}_{391} = n_{N_2^+} n_e X_{391}^{em}(T_e)$. Since the energy threshold is comparable with T_e , the dependence of the rate coefficient on T_e is weak. The rate coefficient itself was calculated from the optical f -value (optically allowed transition) using the impact parameter method [BS76] which holds only for energies well above threshold and is not really fulfilled in the present case. The rate coefficient was then adjusted experimentally and had to be

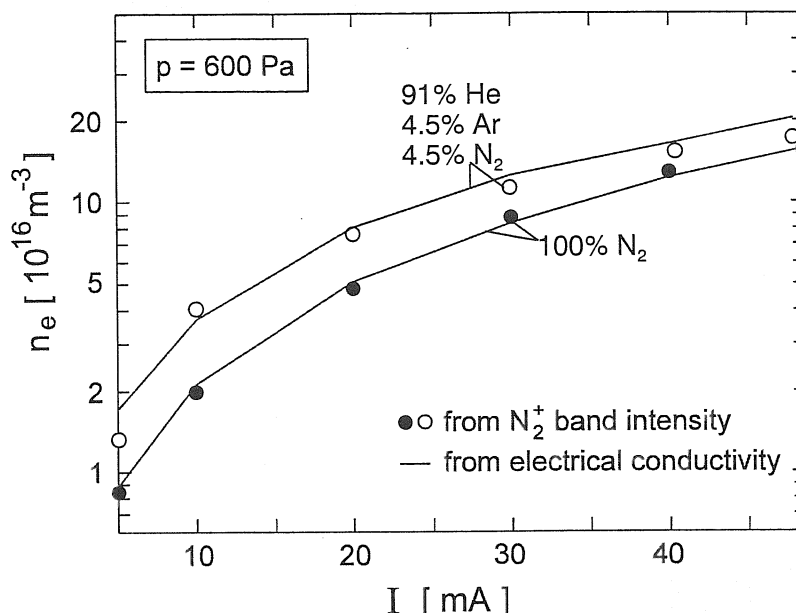


Figure 4.5: Electron density in the glow discharge measured by the radiation of the N_2^+ band in comparison with results from the analysis of the electrical conductivity.

increased by a factor of three [BF94]. Because of the low degree of dissociation in nitrogen plasmas (approx. $< 1\%$) the ions are N_2^+ rather than N^+ . Thus, the radiations becomes proportional to n_e^2 . This could be verified in the glow discharge by increasing the current, as shown in Fig. 4.5. The method can also be applied in gas mixtures taking into account both excitation mechanism (due to higher T_e) and the ion composition. The fraction of N_2^+ ions must be calculated from the relevant ionization rate coefficients and charge exchange processes. Results for a helium dominated discharge are also given in Fig. 4.5 and show good agreement with results from the analysis of the electrical conductivity.

4.3 Electron temperature and EEDF

Strictly speaking, the concept of T_e holds only in case of a Maxwellian EEDF, but is also used here to characterize non-Maxwellian distributions. The relation of T_e with the mean electron energy is given by: $\langle E \rangle = 3/2 kT_e$. In this section, results of spectroscopic determination of T_e or EEDFs from the radiation of (mainly) He and Ar lines in glow discharges, ICP sources, ECR and MW discharges will be described.

4.3.1 Glow discharge

To obtain information on the shape of the EEDF in glow discharges from spectroscopic measurements the intensities of spectral lines and molecular bands with

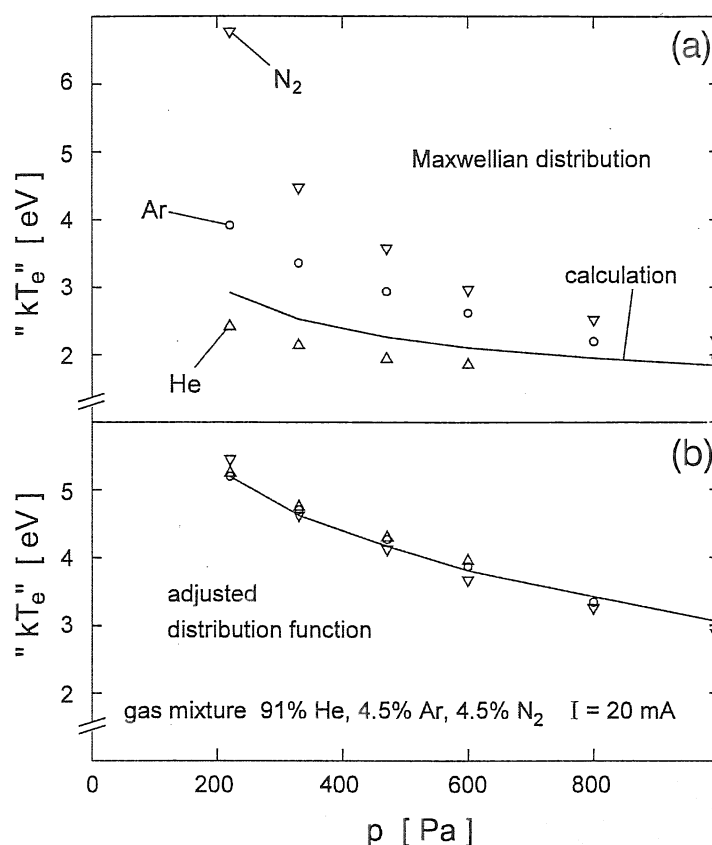


Figure 4.6: Spectroscopic determination of T_e in the glow discharge. Part (a) shows results obtained by assuming a Maxwellian EEDF whereas in part (b) the adjusted distribution function is applied [BF94].

different excitation thresholds were analysed (Sec. 3.1.2, [BF94]). The relevant electron excitation rate coefficients reflect weighted integrals over the distribution functions, which are one to several eV wide and centred somewhat above the excitation thresholds. Bands and lines of N₂, Ar and He provide information in the energy range from about 12 to 24 eV. For the analysis, the corona model was used with EEDFs of a Druyvesteyn-like shape (Eqs. (3.2–3.4)) with parameter ν , which was adjusted to fit the experimental results. Figure 4.6 presents results of a gas mixture depending on pressure. Under the assumption of a Maxwellian distribution each diagnostic line reveals a T_e in the reversed order of their excitation energies, i.e. the higher E_{thr} the lower is T_e , which indicates a decrease of the EEDF in the higher energy part. Using the adjusted distribution function with the parameter $1.8 \leq \nu \leq 2.9$ good agreement between the results is observed (part (b) of Fig. 4.6). The results were confirmed by calculations on the basis of the ionization rate coefficients and an ambipolar diffusion model (Sec. 2.3.2). The experiments show that the high-energy part of the distribution functions is approximately described by the Druyvesteyn-shape for a wide parameter range.

4.3.2 ICP reactor

The ICP source provides the possibility of comparing results of mean electron energies and EEDF from Langmuir probe measurements with results from emission spectroscopy and simulations for the ICP discharge (Sec. 4.2.1). Figure 4.7 presents results measured in pure helium discharges at $r = 0$ mm and $z = 0$ mm at various pressures. The corresponding n_e values were given in Fig. 4.4. As can be seen in the upper part of the figure, the Langmuir probe system is able to resolve the electron retarding currents with a resolution of three order of magnitudes. Therefore, depending on mean electron energy, EEDFs are reproducible up to energies of $E \approx 20$ eV for $p = 50$ Pa and $E \approx 30$ eV for $p = 5$ Pa. In the case of $p = 20$ Pa and $p = 50$ Pa the beginning of depletion in the high energy region, which is due to the influence of inelastic electron collision processes occurring at the threshold of the first metastable state of helium around 19.8 eV, is detectable. The shape of the EEDF is discussed in detail in [SFAP01]. The slope of the straight lines (Maxwell lines) in Fig. 4.7a represents the temperature determined by the probe analysis software (i.e. measured electron temperature).

Also shown in Fig. 4.7a is the cross section (arbitrary units in linear scale) for ground state excitation of helium into the 3^1S level, resulting in the emission of the He-line at 728 nm used for spectroscopic T_e diagnostics. Therefore, the spectroscopic results represent the slope of the high energy region (assuming a Maxwell distribution). The overlap of the energy region covered by the Langmuir probe and those necessary for spectroscopic analysis is small. This fact has to be kept in mind in the discussion of mean energies obtained from either diagnostic (Fig. 4.7b). The deviations at low pressures are correlated with an overpopulation of low energy electrons trapped in the potential well near the discharge center. The large number of low energy electrons causes a reduced mean energy, which is detected by the probe. In contrast, the measured overpopulation in the high energy region has no influence on the mean energy due to the small number of electrons. At higher pressures the EEDF can be considered as a composition of two Maxwellian distributions with different slopes, i.e. lower temperature at higher energies. As a consequence the spectroscopic mean energies are below the results of the probe at higher pressures. Also included in Fig. 4.7b are results from the simulation, showing good agreement with results from spectroscopy.

In mixtures of helium and argon the EEDF can be obtained by analysis of line radiations of both gases. In contrast to the method used in glow discharges, Langmuir probe measurements give additional information, in particular in the low energy region. In order to connect the energy regions where both diagnostics are sensitive, calculations of the EEDF were carried out based on the solution of the homogenous Boltzmann equation (Sec. 2.3.4). Since the electrical field strength of the discharge is unknown, E_{el} serves as a parameter in the calculations to match the EEDF of the Langmuir probe or/and measured line radiations.

EEDF calculations were carried out with the computer code HoBo [Kor93]. This code is based on the numerical solution of the isotropic part of the spatially homogeneous Boltzmann equation taking into account the total excitation cross

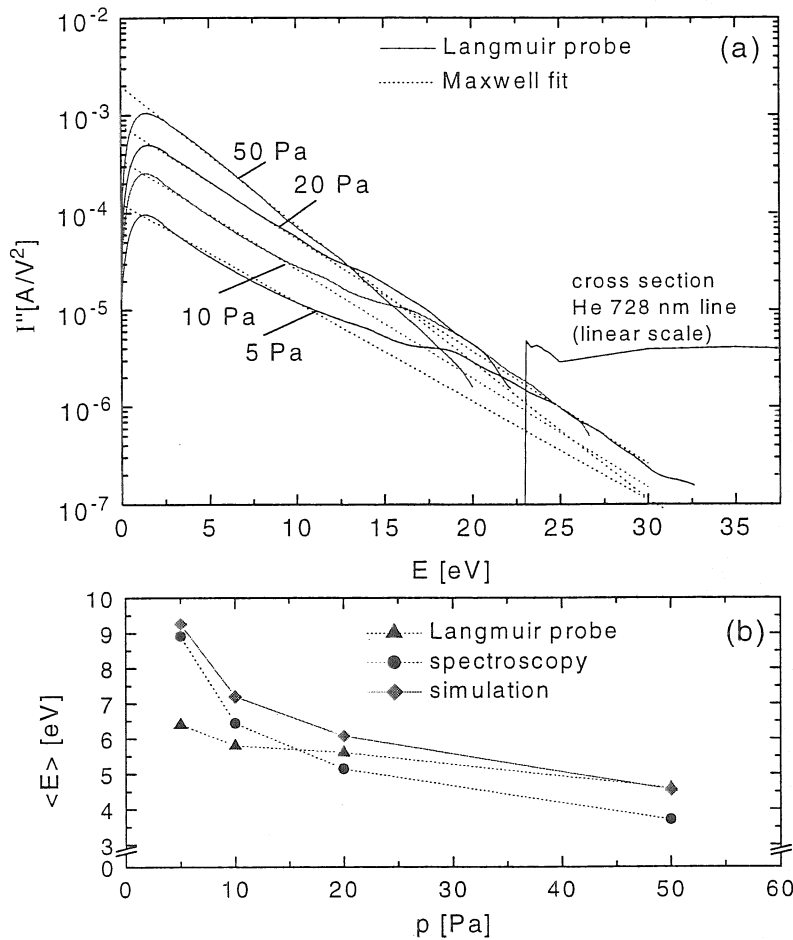


Figure 4.7: EEDF in pure helium ICP discharges at $P_{inp} = 250$ W measured with the Langmuir probe. Dashed straight lines refer to a Maxwell fit in the low energy range. Part (b) compares results of the mean energy $\langle E \rangle$ derived by various methods.

section in the local approach. Calculations can be carried out for a mixture of a maximum of four gases: He, Ne, Ar, N₂. The code was extended to the species H₂, CH₄ using the data base of [Sig00] for all species. The excitation cross sections of one species were compiled to an effective excitation cross section. Since almost all input data of the code are known (f , n_e , p , gas mixture) the remaining free parameter is E_{el} . Details of the code, the data implemented and applications to various discharges are given in [Ond00].

Investigations were carried out in He/Ar mixtures (Fig. 4.8). The EEDF obtained by the Langmuir probe is matched by calculations of HoBo using a electrical field strength of $E_{el} = 35$ V/m (curve 5 and 4 in (a) and (b), respectively). To match the spectroscopic data (radiation of Ar-lines at 696 and 667 nm and He at 728 nm) E_{el} was varied until the radiation calculated on the basis of the EEDF in HoBo is equal to what is measured: curve 1 for Ar₆₉₆, curve 2 for Ar₆₆₇, both in part (a), and curve 1 in part (b) for He₇₂₈. Only excitation from the ground

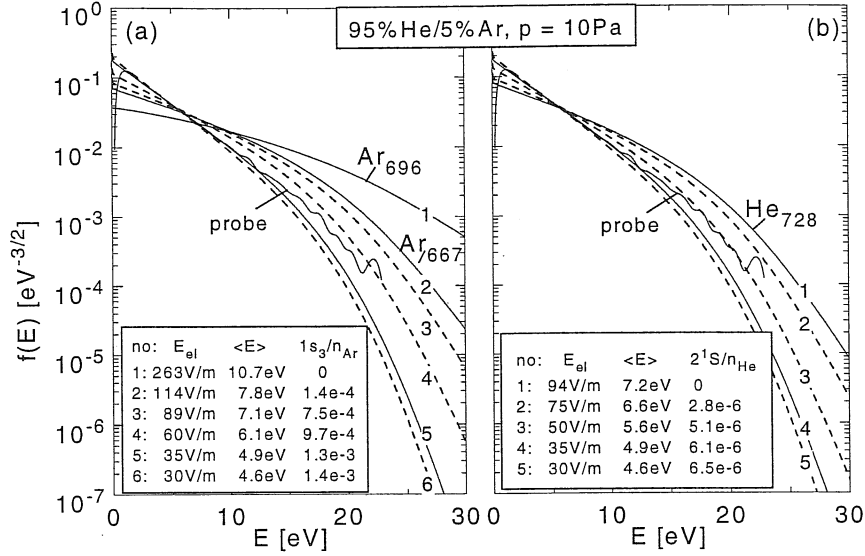


Figure 4.8: Calculated (HoBo) EEDFs in a He/Ar mixture (ICP discharges at $P_{inp} = 250$ W) fitted to probe measurements and argon radiation (a) as well as helium radiation (b) considering metastable populations.

state was assumed. Excitation out of metastable states of these atoms can be taken into account by extending the simple corona equation (Eq. (2.8)) with the appropriate terms. However, the population density of these levels have to be known together with the cross sections. Since the excitation out of these states requires an excitation energy of only 1–2 eV the low energy range of the EEDF is important. For a non-Maxwellian EEDF the ratio of this excitation mechanism to the ground state excitation is higher than in the Maxwellian case, assuming same population densities. Cross sections were taken from [HHKS92, LSAL92] for He and from [CBSL98, BPG⁺99] for Ar.

Variations of EEDFs are calculated under the assumption of additional excitation out of both metastable states ($1s_5$ and $1s_3$ in Paschen's notation, assuming a ratio of $1s_5/1s_3 = 10$) for the Ar_{696} line ($2p_2 - 1s_5$) (Fig. 4.8a) and the 2^1S metastable state for the He_{728} line ($3^1S - 2^1P$) (Fig. 4.8b). Population excited out of the triplet state 2^3S can be neglected since this requires spin change. Thus, one obtains the relative populations of the metastable states as 1.3×10^{-3} ($1s_3$) in Ar (curve 5) and 6×10^{-6} (2^1S) in He (curve 4). Since the population of the Ar_{2p_1} state is not as much influenced by metastable states [BPG⁺99], the radiation of the Ar_{667} line ($2p_1 - 1s_2$) is not corrected. However, the $2p_1$ state is directly related with resonance states ($1s_4$ and $1s_2$) and opacity of resonance lines may enhance the population of the $2p_1$ state too. This may explain the difference of the EEDF for the Ar_{667} line which is not identical with that of the Langmuir probe. Under the assumption of the same influence on the Ar_{696} line, the metastable density $1s_3$ would decrease to 1.4×10^{-4} (curve 2) and is in the range of populations one would expect in such discharges. In summary, this illustrates

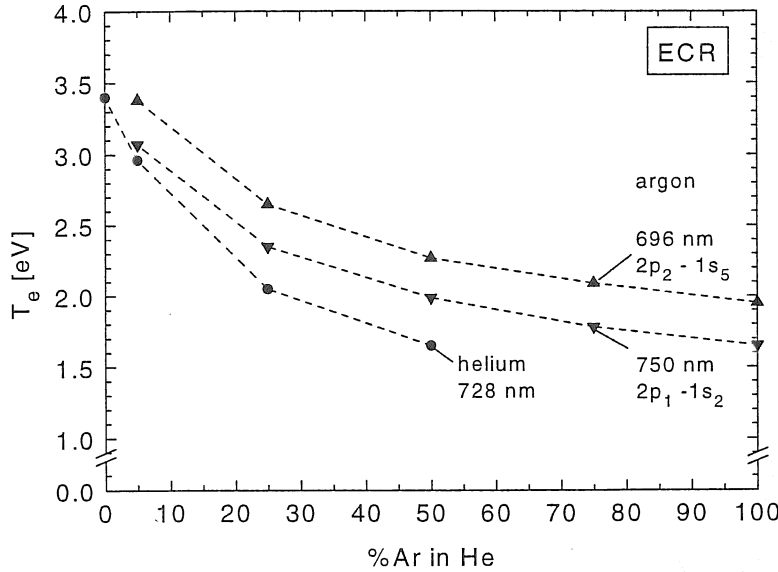


Figure 4.9: Spectroscopic diagnostics of T_e in the ECR discharge at $p = 10$ Pa using the radiation of argon and helium lines.

that for an analysis of spectroscopic data, excitation out of metastable states is relevant, in particular in the case of non-Maxwellian EEDFs. In addition, the influence of opacity of resonance lines has to be taken into account.

4.3.3 ECR and MW discharge

The starting point for spectroscopic investigations in ECR and MW discharges is a Maxwellian EEDF. Preliminary examinations with Langmuir probes and calculations with HoBo together with spectroscopic determinations of the adjusted EEDF (parameter ν) indicate that the EEDF is very close to Maxwellian. On this basis detailed analysis of T_e diagnostics from helium and argon lines were carried out. Since CR-models mostly consider rate coefficients implemented as polynomial fits based on a Maxwellian distribution their use is reasonable in these plasmas. Again two lines of argon (Ar_{696} and Ar_{750}) and one of helium (He_{728}) have been used for T_e determination. Figure 4.9 give results obtained from these three line radiations using the CR-model ADAS for helium (Sec. 3.1.2). For argon, the corona model (excitation out of the ground state only) was applied. As expected from the ionization balance, T_e decreases with increasing admixture of argon to helium. However, the absolute values differ significantly. Argon yields higher values than helium which might indicate a Druyvensteyn-like EEDF, as discussed in glow discharges. However, using also the corona model for helium, the analysis of He_{728} would yield higher T_e than Ar_{750} .

The application of the CR-model for helium makes T_e from He_{728} in Fig. 4.9 the more reliable ones. Using Fujimoto's CR-model instead of ADAS, T_e would be 0.24, 0.16, 0.6 and 0.01 eV lower at 0%, 5%, 25% and 50% Ar admix-

ture, respectively. This can be explained by the overestimation of the opacity in Fujimoto's code (Sec. 3.1.2).

The difference in the results of argon lines is due to the sensitivity of Ar₆₉₆ to cascading (Fig. 3.2) and to population excited out of metastable states (Fig. 3.3), as discussed in the previous paragraph for ICP discharges. Consideration of metastable populations will lead to a decrease of T_e and the remaining deviations of both argon lines may then be due to opacity of the resonance lines of argon. The increasing difference between Ar₇₅₀ and He₇₂₈ with increasing argon density may be used as an indication. To get a better agreement between the results of these lines, metastable populations and opacity have to be investigated in detail, as will be shown in the next section.

4.4 Metastable states and opacity

The influence of metastable state population and opacity of resonance lines on population of higher excited states and on line radiation originating from these states was investigated in the ECR discharge. In case of helium, comparison of population densities from absorption measurements and emission spectroscopy with results from CR-models allows systematic studies which can then be transferred to argon.

4.4.1 Energy level diagram

Figure 4.10 shows schematically the energy level diagram of helium with the spectroscopic notation and optically allowed transitions for the lowest excited states $n \leq 3$. The arrows are labelled with the wavelength of the lines emitted by spontaneous emission. Helium is split into singlet and triplet states (fine structure of the triplet levels is neglected). Transition between these systems are optically forbidden (intercombination lines). Each system has a metastable state, the 2^1S and the 2^3S level at 20.61 and 19.82 eV, respectively. The 2^1P state at 21.22 eV is resonant with the ground state whereas 2^3P (20.96 eV) is resonant with 2^3S .

In Fig. 4.11 an energy level diagram of argon is sketched. The coupling of the momenta is intermediate between LS- and jj-coupling. The system is characterized by the angular momentum of the core: $j_r = 1/2$ and $j_r = 3/2$, the second one marked with a prime in the spectroscopic notation. Transitions between these systems are allowed. The arrows indicate transitions used for determination of upper and lower level populations by emission and absorption spectroscopy, respectively. Paschen's notation for the electronic states of interest is given and will be used in the following for convenience. Argon has two metastable and two resonant states which are energetically very close: $1s_5 - 1s_2$ at 11.55, 11.62, 11.72, 11.83 eV. Thus, mixing of level populations due to heavy particle collisions can occur and similar populations for those four levels are expected.

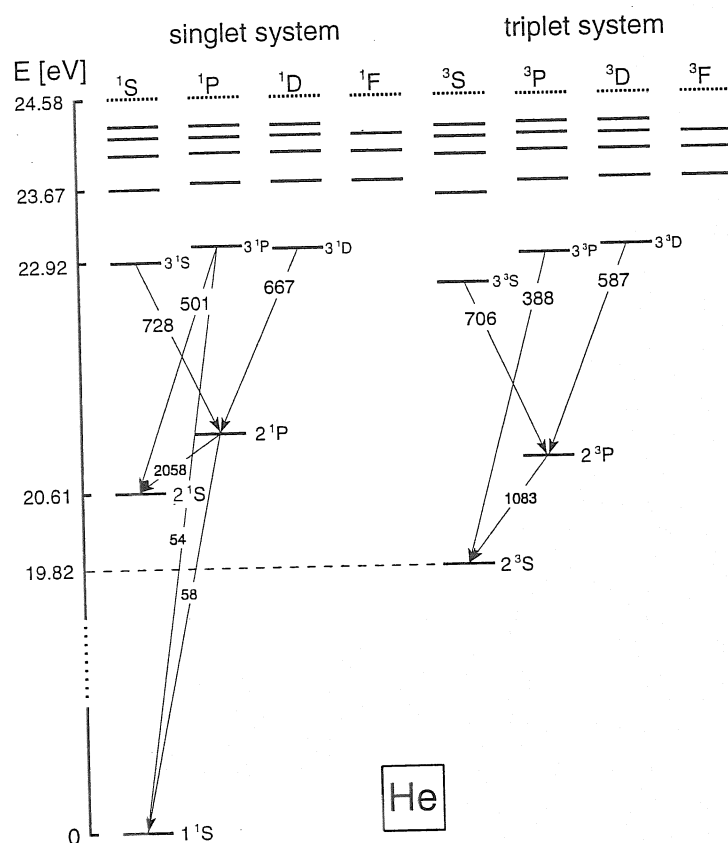


Figure 4.10: Energy level diagram of helium with optically allowed transitions and wavelengths [nm] for $n \leq 3$.

4.4.2 Population density of excited states

The population density of metastable and resonant states of helium and argon were measured in the ECR discharge by absorption spectroscopy [Lot00]. Since the optical system is equipped with a ICCD camera, a spectral resolution of 55 pm is achieved and the line profiles are Doppler profiles which are broadened in the line wings. Therefore special emphasis has to be given to the linearity of the peak absorption. Typical peak absorption signals of around a few percent were observed. Assuming a line profile with Doppler width corresponding to the gas temperature the full width at half maximum would be 4.5 pm for He and 1.4 pm for Ar at 600 nm, i.e. lower than one tenth of the spectral resolution. Thus, the linearity for helium peak absorption should be fulfilled whereas for argon lines the situation is different as shown by calculations [Beh00].

Attempts were made to measure as many lines as possible with the same lower level. This was unsuccessful for helium since lines other than those of the $n = 2$ to $n = 3$ are either below 400 nm, where the intensity of the light source drops, or the transition probabilities are so low that reliable signals cannot be got. For

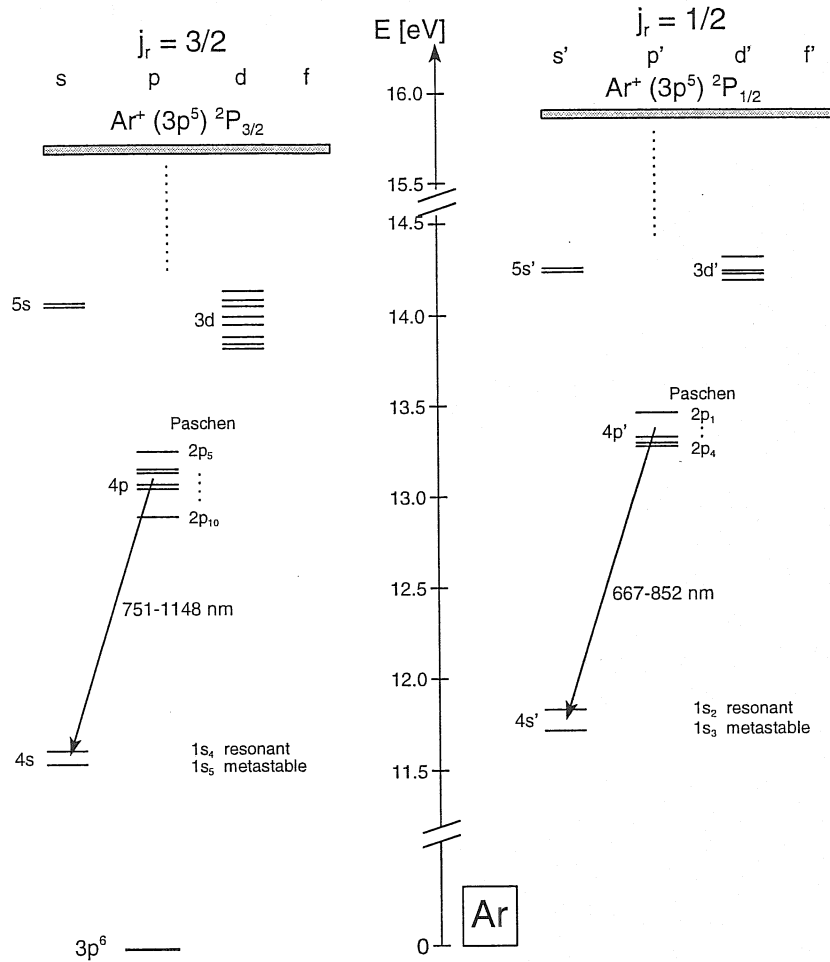


Figure 4.11: Energy level diagram of argon.

argon the situation is different. Here, more than one line could be measured to obtain the population density of the $1s_2 - 1s_5$ states. All of them are in the spectral range between 667 and 930 nm.

Comparing results from various lines referring to one level, the population density differs up to an order of magnitude. Lines with low peak absorption yield a higher density than lines with high signal. This indicates that the linearity of peak absorption no longer applies for some argon lines. Therefore, results of lines which yield the highest population densities were used for further analysis. However, even they might also be affected by nonlinearity and this would result in a higher density. Additionally, the signal-to-noise ratio enhances the error bar of these lines due to the low peak absorption. Replacing the standard optical system with one which is equipped with a CCD camera and a grating of 2400 lines per mm a spectral resolution of 12 pm can be achieved, but only in the wavelength range up to 750 nm, limited by the angle of rotation of the grating. Thus, only three argon lines could be checked which are correlated with two states

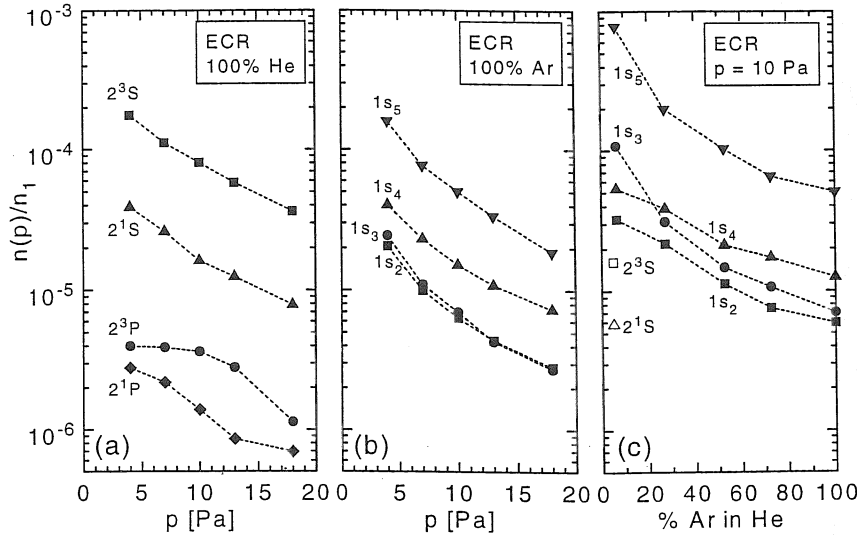


Figure 4.12: Relative population densities, depending on pressure, of He for $n = 2$ (a) and of Ar for $1s_x$ (b). Part (c) shows $1s_x$ Ar populations in Ar/He mixtures.

($1s_5$ and $1s_4$). The agreement with densities derived from the standard system was satisfying, yielding enhanced population densities. The error bars for the argon densities measured with the standard system are therefore estimated to be a factor of two. For helium lines the densities were reproducible to 30% with both system, which confirms the assumption of linearly increasing signals. The error represents more or less the reproducibility of the measurement and the operating conditions of the plasma itself.

Figure 4.12 shows relative populations of the metastable and resonant levels of helium in a helium discharge (a) and argon in an argon discharge (b), in each case as a function of pressure. The third part of the figure gives argon results at 10 Pa as a function of the admixture of argon to helium. Here, only two helium densities could be determined (open symbols) due to the decrease of T_e which is caused by increasing argon admixture. Thus, helium populations decrease and fall below the detection limit of the optical system.

In helium, population densities decrease with increasing pressure due to the decrease of T_e from 4.0 to 2.7 eV. The relative population densities of the metastable states are in the range of $10^{-4} - 10^{-5}$ in which the 2^3S state is a factor of five higher than the metastable state in the singlet system. This correlates with the lower threshold energy for electron impact excitation from the ground state. The relative populations of the resonant levels are more than one order of magnitude lower than those of the metastable states and show a somewhat different dependence on pressure. Here, two effects compete: the decrease due to T_e and an increase due to increasing neutral helium density which enhances the optical thickness of resonant transitions into the ground state and into metastable states. The latter becomes important at these high measured

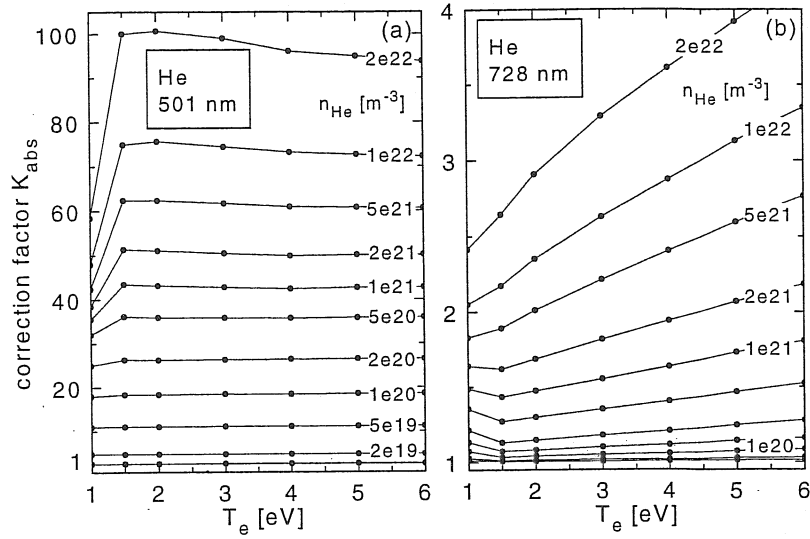


Figure 4.13: Opacity correction factors for the emission rate coefficient of the He-line at 501 nm (a) and at 728 nm (b) depending on T_e and the helium density.

populations. The 2^1P decays by spontaneous emission into the ground 1^1S and the metastable state 2^1S whereas 2^3P has only one possibility, namely decay into the 2^3S . Therefore, these two states show a different behaviour with increasing pressure.

In argon, the population densities of metastable and resonant states are close together. This indicates the expected repopulation processes among these levels, which is due to an energy difference of only 0.3 eV between them. This is further confirmed by the uniform decrease of all four populations with increasing argon density. Although the energy threshold of around 11.5 eV is noticeably lower than that of the helium states, the population densities relative to the ground state are similar. The reason is the lower electron temperature of argon plasmas compared to helium plasmas. In argon T_e falls from 2.4 to 1.7 eV with increasing pressure. Increasing T_e in argon plasmas by using helium as a background gas (Fig. 4.12c) increases all four argon population densities. A decoupling of the four states is indicated, i.e. a difference of behaviour between metastable and resonant states is observed. The latter show a lower decrease with increasing argon admixture due to increasing opacity, which works against the decrease of T_e . Because of the high population densities of metastable and resonant states of argon and helium, opacity and excitation out of metastable states is important for the population of higher excited states as already discussed in Sec. 4.3.2, Fig. 4.8.

In order to investigate the influence of the opacity of resonance lines on populations of higher excited levels which are used for diagnostics, systematic calculations with the CR-model ADAS were carried out for helium. The correction factors K_{abs} , which scale the optical thin effective rate coefficients (Sec. 2.2.4), were calculated as a function of n_{He} for the ECR discharge with the following

characteristics: $n_e = 10^{17} \text{ m}^{-3}$, homogeneous, cylindrical plasma with $r = 5 \text{ cm}$, Doppler profile with $T_g = 450 \text{ K}$. The results are given in Figure 4.13 for two helium lines in the singlet system: 501 nm and 728 nm. It is obvious that the He_{501} line is very sensitive on opacity in contrast to the He_{728} line. This is caused by a direct coupling of the upper level of the He_{501} line (3^1P) with the ground state. For example, at 10 Pa the helium density is $n_{\text{He}} = 1.6 \times 10^{21} \text{ m}^{-3}$ and the radiation of the He_{501} line is enhanced by a factor of ≈ 50 whereas the He_{728} line increases only a factor of ≈ 1.5 . Therefore, the latter is better suited for diagnostic purposes, e.g. the measurement of T_e . In case of the He_{501} line the optical thickness of the plasma has to be known precisely. However, this line allows a sensitive diagnostic of the opacity itself.

4.4.3 Boltzmann-plot of helium

In addition to the population densities obtained from absorption measurements higher excited state populations were obtained from the radiation of emission lines. In the case of helium, the population densities of $n = 2$, $n = 3$ and some of $n = 4$ can be measured in the visible spectral range and are compared with results from CR-model (ADAS) calculations. The comparison is carried out for a helium plasma (ECR discharge) at 10 Pa. Figure 4.14 shows the results in a Boltzmann-plot, which is basically discussed in Sec. 3.1.3. As expected, the populations are not in Boltzmann equilibrium, i.e. the values are not on a straight line. Furthermore, a Boltzmann-line in the plot according to the electron temperature of the plasma would be at remarkably higher populations (two orders of magnitude higher for the S -states of $n = 2$). The deviations from a Boltzmann-line and the lower absolute values are typical for non-equilibrium plasmas.

In Fig. 4.14 the ADAS calculations agree well with the measurements. The absorption signals were corrected slightly by adjusting the length of the plasma and by the beginning of the nonlinear relation of peak absorption and density of lines from the metastable states. Concerning the metastable states the agreement was achieved by reducing the lifetime of the neutral particles to the diffusion time (10^{-4} s) in the calculation. Another important result is the optical thickness of the transitions from the $n = 2$ P -state to the $n = 2$ S -state, thus enhancing the population of the P -states and changing the order of the reduced populations. This means that the value for the 2^1P state is slightly higher in the Boltzmann-plot than for the 2^3P state, a circumstance which is not found if only the opacity associated with resonance transitions to the ground states is taken into account. Regarding $n = 3$ states, the calculated S -populations seems to be too low whereas D -populations are too high. These deviations are outside the error bar for the measurements and are systematically observed for other pressures. It turned out that a better agreement can be observed if the electron density is reduced in the calculations by a factor of two followed by a re-adjustment of T_e . As a consequence, either n_e of the discharge is smaller, which is almost excluded since the error bars of results from microwave interferometry are around 20%, or the

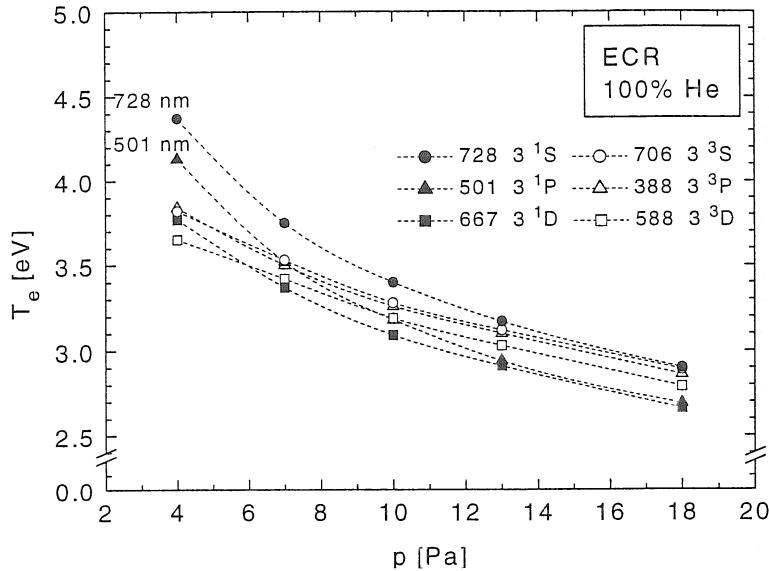


Figure 4.15: Electron temperatures derived from six helium lines ($n = 3 - n = 2$ transitions) by using the ADAS CR-model which was adjusted to $p = 10$ Pa.

data required for modeling populations are kept to a minimum. For comparison, the equivalent line in the triplet system can be used. However, the higher T_e derived from He₇₂₈ suggest to scale the corresponding rate coefficient by a factor of 1.5. This factor would reduce T_e of the He₇₂₈ line to the mean value of T_e derived from all triplet lines which are adjusted precisely to the measurements. To avoid the scaling, a review of data implemented in the CR-model and new calculations are in progress. However, in summary, the agreement between the results of the various lines are within the expected limits. The deviations are in the range of 0.3 eV, which is a very satisfying error range for the diagnostics of T_e in low pressure plasmas.

In the case of argon, lines originating from the $2p_1$ state, i.e. Ar₆₆₇ and Ar_{750m}, are preferred for T_e -diagnostics. The populations of the upper state are only little influenced by cascading, and excitation out of metastable states can be neglected. Since a complete CR-model was not available for the analysis, it has to be kept in mind, that the results must be corrected for opacity which will reduce the T_e obtained values.

Chapter 5

Hydrogen and Deuterium Plasmas

The application of atomic and molecular emission spectroscopy to laboratory plasmas and divertor plasmas and the results of this application will be presented in the following sections. The diagnostics methods and the investigations of plasma wall interaction in laboratory plasmas, i.e. mainly hydrogen and deuterium with carbon surfaces, will be described.

Concerning the isotopes, the consequences of the different masses of the nuclei have to be considered in the interpretation of atomic and molecular spectra. For atomic hydrogen and deuterium isotope effects on the energy level diagram and rate coefficients is negligible and the same atomic CR-model can be applied to both.

In contrast, although the electronic states and the potential curves are identical, molecules differ in their vibrational and rotational energies. The zero point energy and the energy separation between vibrational states is lower for deuterium than for hydrogen. Therefore, deuterium has more vibrational levels in each electronic state as hydrogen, e.g. the ground state of hydrogen has 15 vibrational levels in contrast to 21 for deuterium. Furthermore, rate coefficients may show an isotope dependence for pure electronic transitions and are certainly different for vibrationally resolved transitions. This is due to the difference in energy thresholds and Franck-Condon factors. Thus, different CR-models have to be used for the isotopes of the molecule. However, dependencies on rotational levels are mostly neglected in CR-models.

Figure 5.1 shows schematically an energy level diagram of molecular and atomic hydrogen. The ionization energy of H_2 is 15.42 eV and that of H is 13.6 eV. The repulsive state in the triplet system of the molecule is the main channel for dissociation into H atoms. The principal quantum numbers for the first two states are labelled for the atom as well as for the molecule in the united atom approximation. The energy level diagram of the molecule splits up into singlet and triplet states, $n = 2$ has three states in each multiplet system which are resolved in the diagram, whereas $n = 3$ has six levels in each multiplet system, etc. In

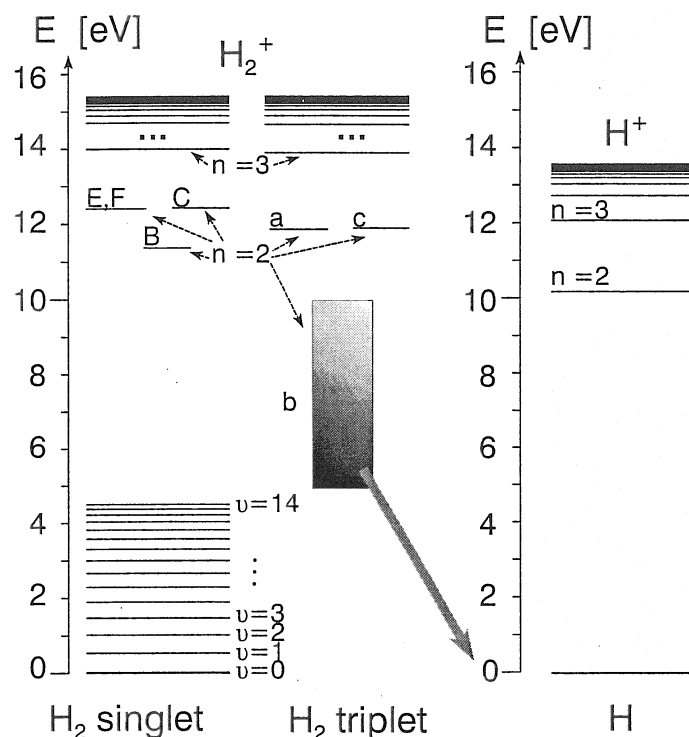


Figure 5.1: Schematic energy level diagram of molecular and atomic hydrogen. The 15 vibrational levels of the molecular ground state are shown, whereas the vibrational levels of excited states and the rotational levels are suppressed for clarity.

the ground state the vibrational levels are shown. They move closer with higher vibrational quantum number. The notation for electronic states labels them in alphabetical order, except X is used for the ground state. Capital letters are used for the singlet system and lower case letters for the triplet system. Figure 5.2 shows potential curves of H_2 , H_2^+ and the negative ion H_2^- which decays in H^- and H . This figure, which is taken from [Sha71], gives also the complete spectroscopic notation of the electronic states. The small dashes on the curves indicate the vibrational levels.

Emission spectroscopy in the wavelength range between 120 and 900 nm (covered by the calibrated spectroscopic systems) enables the measurement of the Balmer lines and the first Lyman line (L_α) emitted from atomic hydrogen in the plasma. Since the resonance line L_α is directly influenced by opacity, quantitative analysis is quite difficult, especially at poor spectral resolution. Therefore, this line is not used for an analysis. The Balmer lines of deuterium are slightly below the wavelength of the hydrogen lines and can be separated in the case of H_α . The fine structure is not resolved.

For molecules, pure rotational and vibrational spectra would be in the infrared or microwave wavelength region, but since the molecules are homonuclear, with a non-permanent dipole moment, these transitions are optically forbidden. Se-

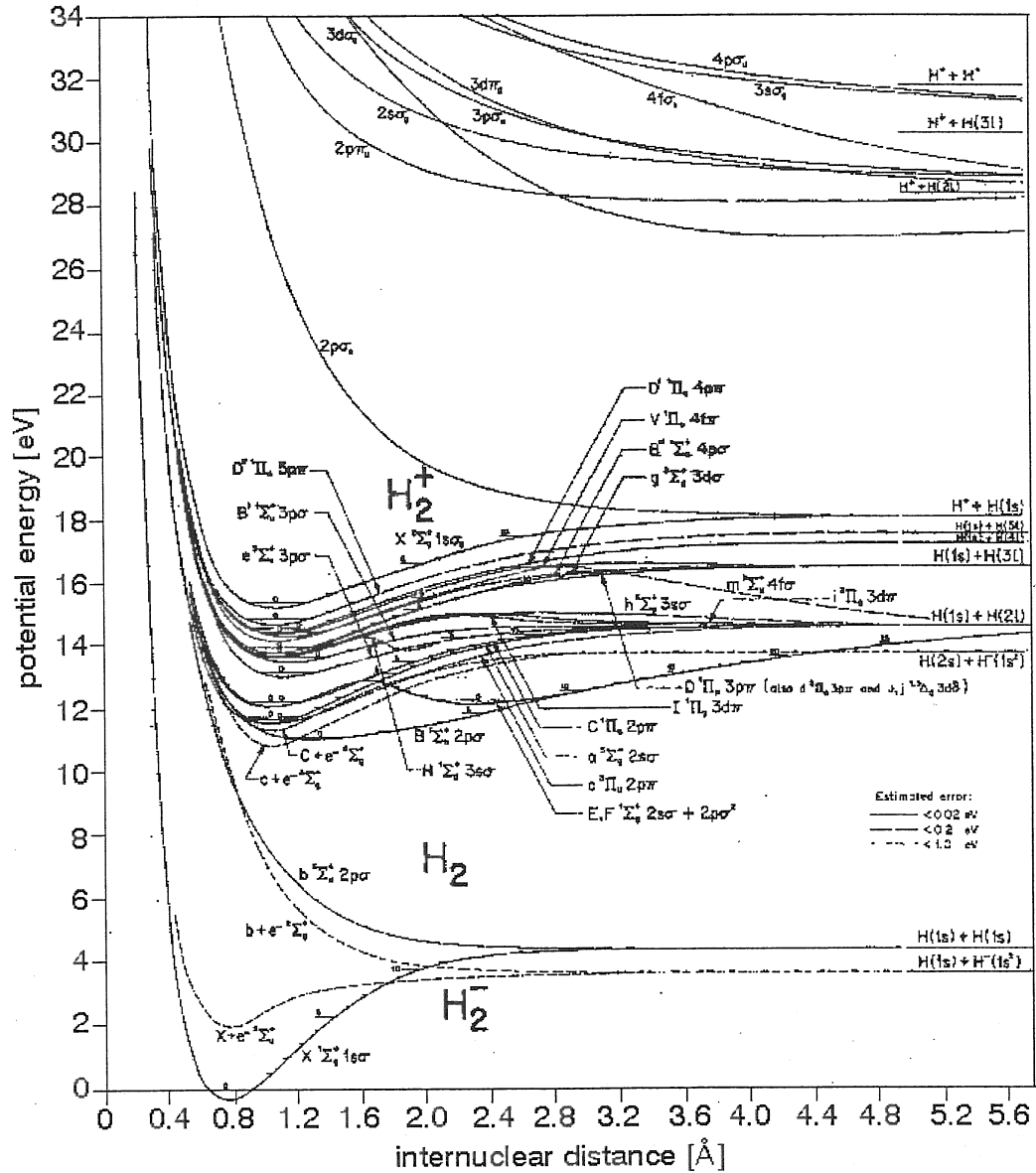


Figure 5.2: Potential energy curves of H_2 , H_2^+ and H_2^- [Sha71].

lection rules are fulfilled only if an electronic transition takes place, which means that electronic systems with vibrational bands and rotational structure are observed. Details of diatomic molecular spectra are given in the book of Herzberg [Her50]. In the visible spectral range transitions from the $n = 3$ into the $n = 2$ states can be observed.

The most prominent transition is the Fulcher transition ($d^3\Pi_u - a^3\Sigma_g^+$). Since the corresponding potential curves are almost not shifted in nuclear distance, Franck-Condon factors are high for diagonal vibrational bands. In the wavelength region of 600 – 650 nm the diagonal bands $v' = v'' = 0, 1, 2, 3$, can be observed. For higher vibrational bands pre-dissociation occurs. The vibra-

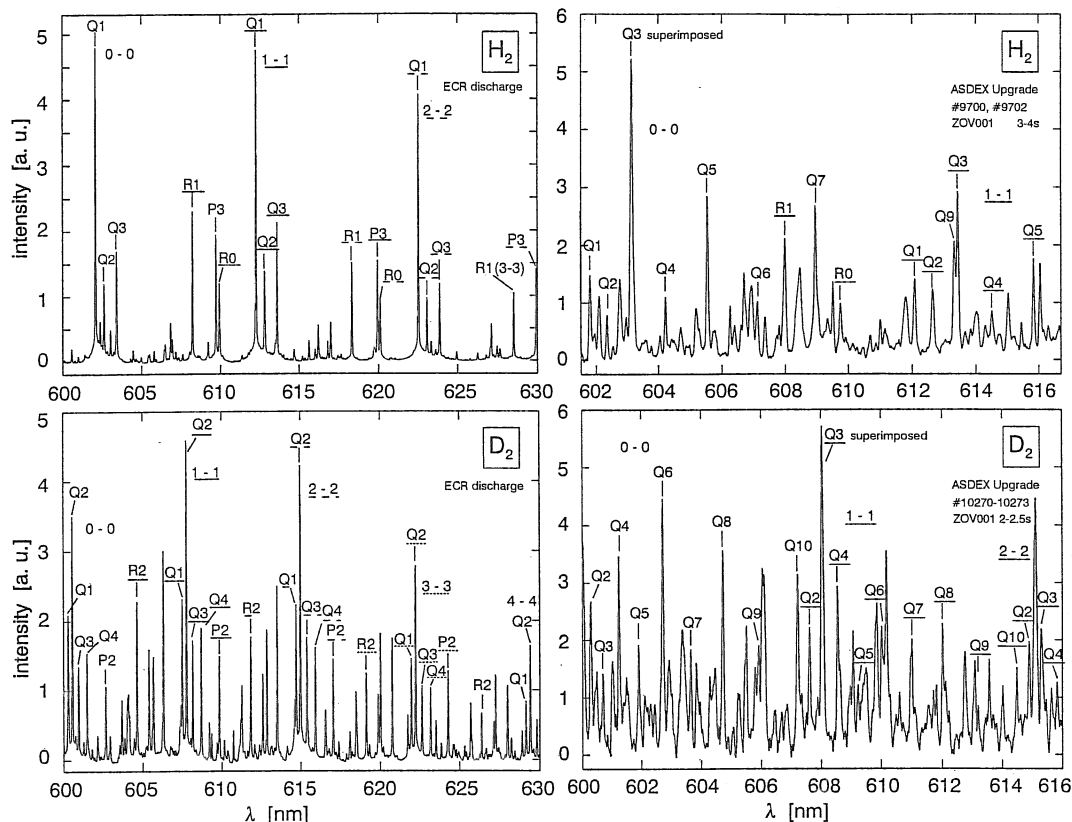


Figure 5.3: Emission spectra of the Fulcher band ($d^3\Pi_u - a^3\Sigma_g^+$) of H_2 and D_2 in an ECR discharge (left column) and in a divertor plasma (right column). Some rotational lines of various vibrational bands are identified.

tional bands are separated and the rotational lines can be clearly identified. The most intense rotational branch is the Q-branch, whereas radiation of the P- and R-branch is weaker. Examples of spectra for hydrogen and deuterium obtained in the ECR discharge and in the divertor of ASDEX Upgrade are given in Fig. 5.3. The comparison demonstrates the different appearance of this band system, which varies with rotational and vibrational population, spectral resolution and disturbing lines in the background signals. In particular, in the case of the ASDEX Upgrade spectra, rotational lines with higher rotational quantum numbers are more intense than in the ECR discharge which indicates a higher rotational population of the excited state of the molecule. The alternation of rotational lines, which is obvious in the first four Q-lines, is due to the effect of the nuclear spin which implies a ratio of 1 : 3 and 2 : 1 for H_2 and D_2 , respectively. Since molecular hydrogen and deuterium spectra are multiple-line spectra, in contrast to the heavier molecule N_2 , transition lines are spread over a wide wavelength range. The Fulcher transition with its various vibrational bands is the most intense transition and therefore particularly suited for diagnostics at low temperature plasmas, in both technical and divertor plasmas.

For comparison some other transitions have also been measured. In the VUV/UV spectral range, the Lyman bands ($B^1\Sigma_u^+ - X^1\Sigma_g^+$) and the Werner bands ($C^1\Pi_u - X^1\Sigma_g^+$) can be observed. Here, intense vibrational transitions are overlapping in the wavelength range of 140 – 165 nm and 95 – 140 nm, respectively. Since the transition probability of an electronic state is spread over into the vibrational and rotational lines, opacity of resonance transitions in molecules is weak and can be mostly neglected.

A prominent feature of spectra from hydrogen molecules is the hydrogen continuum originating from a transition of the $a^3\Sigma_g^+$ state into the repulsive $b^3\Sigma_u^+$ state. The continuum radiation is well-known from deuterium lamps used as a continuum source for absolute calibration of radiation in the wavelength range between 165 and 400 nm. The radiation of the complete system is spread over the range 120 – 600 nm.

To get all the radiation of a whole electronic transition, the individual rotational lines have to be summed up to give the radiation from the vibrational bands which in turn have to be summed to give the total radiation. The total radiation can be used for the determination of T_e or n_{H_2} , n_{D_2} . From the radiation of the individual vibrational bands vibrational populations in the excited state can be derived, whereas the analysis of rotational lines yields the rotational population.

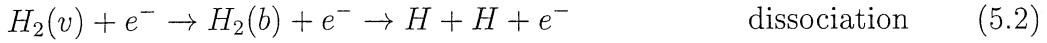
5.1 Collisional–radiative model

The interpretation of hydrogen radiation is supported by a CR-model for H_2 and H. Comparing molecules with atoms, the number of excited states which are to be considered in CR-models increases substantially due to vibrational and rotational levels. Since vibrational states and rotational states of homonuclear molecules must not decay by spontaneous emission in the same electronic state, the vibrational states in the electronic ground state have to be treated as metastable states. In principle, molecules are faster in population equilibrium than atoms, since more levels are available and the energy separation between the levels is smaller. Furthermore, the transition probabilities of electronic transitions are split into vibrational bands and rotational lines, which means that the decay of an electronic state becomes less important whereas the significance of depopulation processes by electron impact increases. As a consequence, Boltzmann equilibrium among the excited states is obtained at lower electron densities for molecules as for atoms.

In the CR-model of Sawada and Fujimoto [SF95] the electronically excited states of the molecule are split into singlet and triplet states. Furthermore, some levels of the molecule (in particular the repulsive state $b^3\Sigma_u^+$) are connected to the model for atomic hydrogen. Thus allows the modeling of loss processes for molecular population as well as the gain for the atomic population. Each multiplet consists of 40 electronically excited states and the $n = 2$ states are resolved into their electronic states. The basic energy level diagram is shown in Fig. 5.1.

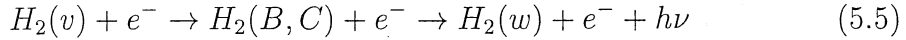
The ground state in the singlet system is vibrationally resolved (15 levels). In all other electronic states the vibrational and all rotational levels are neglected. As a consequence, a calculation of vibrational population in the ground state is independent of the population of excited states. The rate coefficients, which are input data for the model, are based on the data compiled in the book of Janev [JLEP87].

For the calculation of vibrational populations in the ground state of the molecule and effective rate coefficients which depend on the vibrational population, four reactions are included, namely:



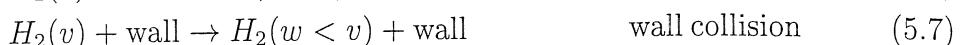
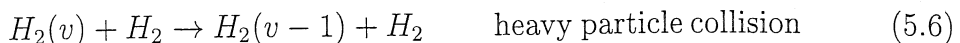
The first reaction is in principle a populating process, whereas reactions (5.2) – (5.4) depopulate the vibrational levels. Some rate coefficients implemented in the CR-model and extrapolated rate coefficients for higher vibrational levels have been revised by Greenland and Reiter [GR96]. This state of the model is called the original version of the CR-model throughout the report.

In a next step the model was extended by a new reaction channel, i.e. the electron impact excitation into the singlet states $B^1\Sigma_u^+$ and $C^1\Pi_u$, which is followed immediately by radiative decay:



The data for reaction (5.5) were taken from Celiberto *et al.* [CJ95]. Because of difference in positions of the minima of the of the lower and both upper potential curves the repopulation is influenced by the Franck–Condon factors, which prefer the population of higher levels, i.e. $v > 5$. In addition, new vibrationally resolved data exists for some reactions and have been implemented in the code. In order to predict vibrational populations for D_2 as well, the model was further extended by implementing data for the five reactions in D_2 , mainly based on the data taken from [CLC⁺99] and using extrapolation formula as suggested in [GR96].

In the case of boundary layer and divertor plasmas in fusion experiments, electron collisions are the dominant population and depopulation mechanism for the vibrational levels. Therefore, the aforementioned set of reactions ((5.1)–(5.5)) is sufficient for calculating vibrational populations. However, heavy particle collisions and depopulating wall collisions are important for applications in low pressure, technical plasmas. To get an insight into the influence of these kind of reactions on the populations, two typical reactions for each process have been optionally included in the model, namely:



These reactions are independent of T_e and lead to a strong depopulation of vibrational levels.

This state of the model is called the modified version and is described in detail in [WF01] and [FHW01]. During the revision of the original model it was found out that the lifetimes of the first two electronic states ($c^3\Pi_u$ and $a^3\Sigma_g^+$) had to be corrected. This is specially important since the vibrational level $v = 0$ of the $c^3\Pi_u$ state is metastable.

The CR-model is used to calculate population coefficients of excited states which are coupled to the species H_2 , H_2^+ , H^- for molecular populations and H_2 , H_2^+ , H , H^+ for atomic populations. According to [Gre01] these particle densities belong to the P -space, i.e. slow particles, whereas the excited states belong to the Q -space, i.e. fast particle species. As a consequence, the matrix which solves the coupled system of equations in a CR-model is divided in these two spaces [Gre01]. Since the vibrational levels in the ground state can be treated as metastable, they belong to the P -space.

For calculations of population densities and effective rate coefficients of molecular states and transitions, the modified version of the CR-model is used. Furthermore, it is applied for the prediction of vibrational populations in the ground state of H_2 and D_2 in divertor plasmas. As mentioned before, in technical plasmas numerous heavy particle and wall collisions depopulate the vibrational levels which are not considered explicitly in the code so that predictions are not reliable in this case.

For atoms, the H-model has been used in a variety of applications (e.g. [FMS88, FST89, SEF93]) for diagnostics of fusion experiments, but because of the increasing importance of opacity in both detached divertor plasmas and technical plasmas, the ADAS package is to be preferred. Additionally, the input data, i.e. rate coefficients, of the ADAS code was recently updated.

5.1.1 Population of excited states

For diagnostics of molecules the Fulcher transition ($d^3\Pi_u - a^3\Sigma_g^+$) is commonly used. In principle, the band intensity depends on the population density of the $n = 3$ state, which is unfortunately not resolved in the CR-model. Since the six levels are energetically close together, the population distribution amongst them is dominated by the statistical weights of the respective electronic states. The gain and loss processes into and from the $n = 3$ state are shown in Figs. 5.4 and 5.5 as a function of electron density at $T_e = 3$ eV. On one hand, this temperature is typical for technical plasmas, but at higher T_e ($\gtrsim 10$ eV, e.g. in the plasma edge of fusion experiments) the molecules ionize and dissociate rather than radiate.

In Fig. 5.4 the contributions to the $n = 3$ population from the Q -space and the ground state are given. Even at very low n_e excitation out of the ground state is not the only process for populating $n = 3$. Approximately 20% of the population is due to cascading from higher excited states. With increasing electron density the $c^3\Pi_u$ state becomes more and more important because of its long lifetime of 40 μs followed in importance by the $a^3\Sigma_g^+$ state, with a lifetime of 7 μs . Typical

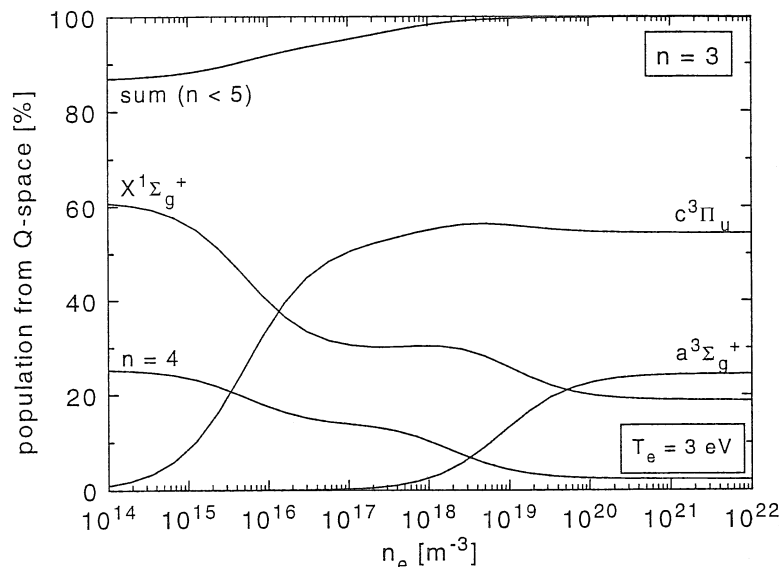


Figure 5.4: Percentage population from the Q -space into the $n = 3$ triplet state of H_2 in comparison to ground state excitation.

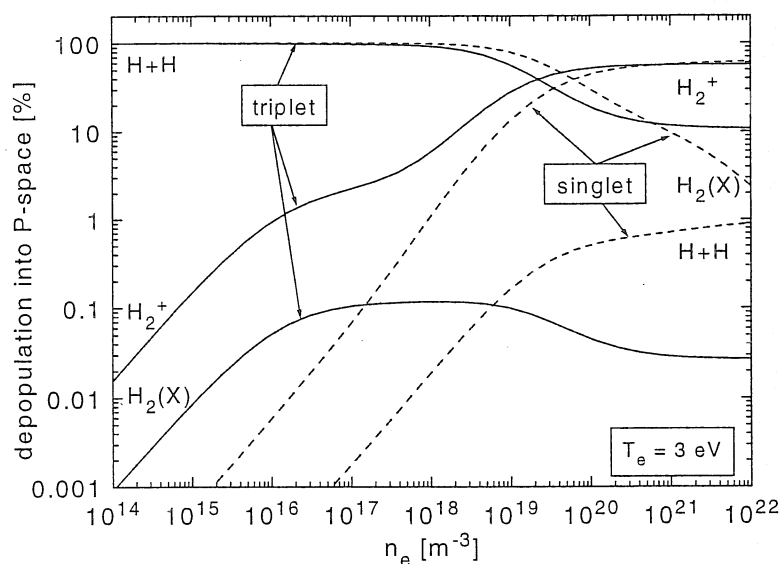


Figure 5.5: Depopulation processes of singlet and triplet states of H_2 into the P -space.

lifetimes of other excited states are some ten of ns. This means that in technical plasmas the upper Fulcher state, $d^3\Pi_u$, is populated in comparable portions by ground state excitation and excitation out of the $c^3\Pi_u$ state. In contrast, at divertor conditions ($n_e \approx 10^{20} \text{ m}^{-3}$) excitation out of the metastable state is dominant. Concerning the loss processes, the triplet states decay almost totally

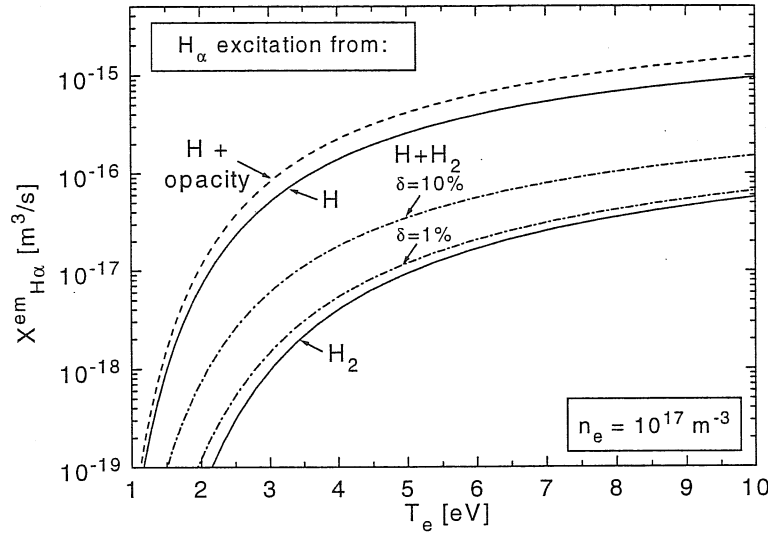


Figure 5.6: Emission rate coefficients of the H_{α} -line for direct (H) and dissociative (H_2) excitation as well as for a combination of both, which is defined by the dissociation degree δ .

into the repulsive $b^3\Sigma_u^+$ state and dissociate, which is shown in Fig. 5.5. Ionization out of excited triplet states becomes important at densities above 10^{19} m^{-3} . The decay of excited triplet states into the ground state is a process of minor importance in contrast to the decay of excited states in the singlet system. This emphasizes the significance of the contribution of excited triplet states to H atoms with an energy gain per particle of $\approx 3 \text{ eV}$ from the dissociation of the $b^3\Sigma_u^+$ state, which is the so-called Franck-Condon energy. Higher excited states contribute to the population of excited H atoms, whereas singlet states are not of importance for dissociation.

The population mechanisms from the P -space into the $n = 3$ state of the atom are presented in Fig. 5.6 for parameters of technical plasmas. The effective emission rate coefficient for the H_{α} line originating only from the H atom is the largest one. The enhancement by opacity of Lyman lines is given by the dashed curve and will be discussed in detail in Sec. 5.2.1. The rate coefficient for dissociative excitation of the molecule into the excited state of the atom is a factor of 50 – 100 below the rate coefficient for direct excitation. However, if molecules are the dominant species in the plasma, the contribution of this excitation mechanism to the population of $n = 3$ can be substantial. The combination of both excitation processes is characterized by the degree of dissociation in the plasmas, which is typically around a few percent. As shown in Fig. 5.6 the contribution of direct excitation to the H_{α} radiations becomes important if $\delta > 1\%$. This limits the sensitivity of the atomic hydrogen density diagnostic of the H_{α} line (Sec. 5.2.1).

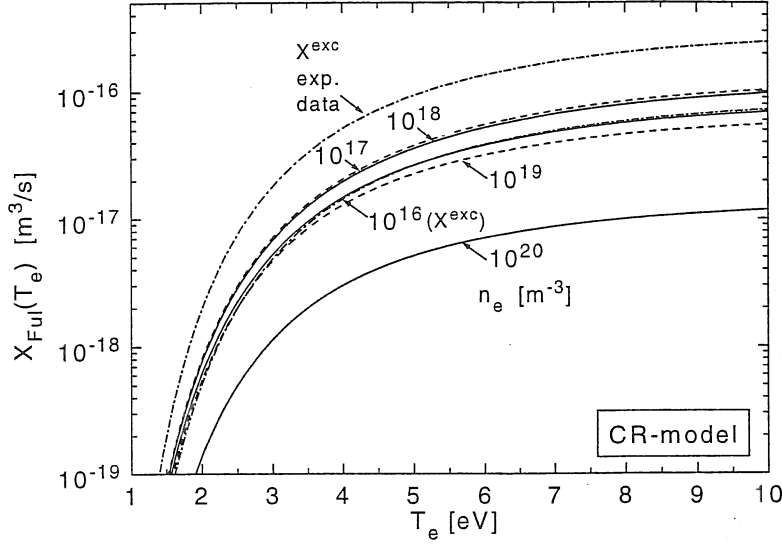


Figure 5.7: Electron density dependence of the rate coefficient for Fulcher radiation calculated by the CR-model. For comparison experimental data of X_{Ful}^{exc} [MH76] is given.

5.1.2 Electron density dependence

As a result of CR-model calculations, emission rate coefficients depend not only on T_e but also on n_e . Figure 5.7 shows examples for the emission rate coefficient of the Fulcher transition $X_{Ful}(T_e)$ at various electron densities. The rate coefficient is calculated from the molecular $n = 3$ population density: $X_{Ful}(T_e, n_e) = n(3) \times 2/9 \times A_{ful}/n_e/n_{H_2}$, with $n_{H_2} = 1$. The ratio $2/9$ is the ratio of the statistical weights of the $d^3\Pi_u$ state to the sum of all six $n = 3$ states. The lifetime of the upper Fulcher state is 40 ns, corresponding to the transition probability of $2.5 \times 10^7 \text{ s}^{-1}$. If only a few vibrational bands are observed in the plasma, the branching ratio of the measured to all possible vibrational transitions has to be taken into account as discussed in Sec. 3.6. In the case of vibrational transitions $v' = v'' = 0 - 3$ this ratio is $19.1/50$ for H_2 and $11.3/50$ for D_2 . Rate coefficients shown in Fig. 5.7 refer to the whole band system. At low n_e (up to 10^{16} m^{-3}) the effective emission rate coefficient is almost identical with the rate coefficient used in the corona case (excitation out of the ground state only), i.e. X^{exc} . For higher n_e the effective emission rate coefficient first increases, which is due to a growth of cascading processes from higher levels and excitation out of the $c^3\Pi_u$ and $a^3\Sigma_g^+$ states. Above $n_e \geq 10^{18} \text{ m}^{-3}$ the effective rate coefficient is falling off again, e.g. a factor of two between 10^{18} and 10^{19} m^{-3} . For higher densities the decrease becomes even stronger. This behaviour indicates that the population of the electronic states approaches a Boltzmann equilibrium where the population is proportional to $1/n_e$. As a consequence, in the analysis of measured molecular radiation for diagnostics in divertor plasmas with typical electron densities of $10^{18} \leq n_e \leq 10^{21} \text{ m}^{-3}$, the electron density has to be known precisely.

Figure 5.7 highlights a common problem in the evaluation of spectroscopic data: which excitation rate coefficient or cross section from literature should be used for the analysis? Often rate coefficients differ by a factor of two to ten for the same transition which is due to different methods used for the determination of the cross section, i.e. experimental measurements depend on the experimental method (apparatus) and theoretical calculations depend on the underlying theoretical model. In the case of the CR-model, theoretical data were used as input data. Here, the rate coefficients are based on the calculations of Miles [MTG72] (labelled by X^{exc}). Experimental cross sections for the first four diagonal Fulcher bands are given in [MH76] resulting in the rate coefficient: X^{exc} exp. data. A comparison yields a difference of a factor of four. This fact should always be kept in mind in the evaluation of data. On the other hand, if the plasma parameters and the molecular density are known precisely, the proper rate coefficient can be determined from the measurements. Preliminary results confirm the rate coefficient of Miles which is implemented in the CR-model. Nevertheless, further detailed investigations must be carried out in various experiments which should cover a wide electron density range.

5.1.3 Influence of vibrational population on rate coefficients

Vibrationally excited molecules can, on the one hand, increase rate coefficients for processes such as ionization and dissociation, or, on the other hand, take part in reactions which are resonant with selective vibrational states. The increase of the rate coefficients is due to the reduction of the threshold energy (≈ 0.5 eV per vibrational level in H_2). Furthermore, a shift of the maximum cross section to lower energies coupled with an enhancement of the cross section itself can occur. This was calculated recently for the electron impact excitation of the repulsive state $b^3\Sigma_u^+$ [ST98]. Since the calculations are based on the R-matrix method, the results are very precise for low electron energies, in particular around the threshold energy. Maxwell convoluted dissociation rate coefficients for the vibrational levels $v = 0$ and $v = 4$ of the ground state into the repulsive state are shown in Fig. 5.8 (Tennyson data). The enhancement of the rate coefficient is a factor five at low T_e (≈ 3 eV) and a factor two at higher T_e . Data of Celiberto [CLC⁺99] result in nearly the same rate coefficient for $v = 0$ but the enhancement with increasing v is weaker. These calculations are based on the Gryziński method in which the accuracy at low electron energies is lower than the accuracy of the R-Matrix method. In addition, for $v = 0$ data taken from the book of Janev [JLEP87] are plotted. These data give highest values, however, they are based on Born–Ochkur–Rudge extrapolations (valid for the high energy range) and consider cascading from $a^3\Sigma_g^+$ and $c^3\Pi_u$ states and apply an averaged energy threshold for these states. Furthermore, Janev’s data must be extrapolated to the vibrational levels $v > 0$ which was done in the original version of the CR-model. In the modified version, data of Celiberto were implemented since the corresponding rate

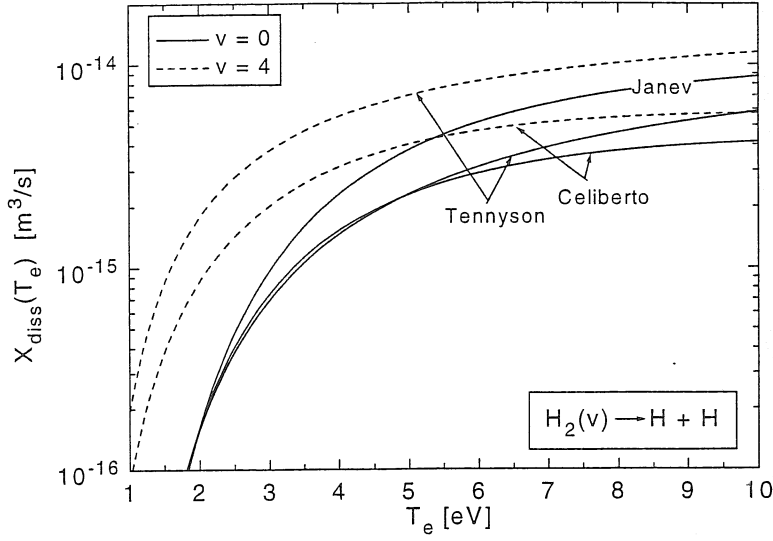


Figure 5.8: Rate coefficients for dissociation of $H_2(X, v = 0, 4)$ into $H + H$ via the repulsive state $b^3\Sigma_u^+$ taken from Tennyson [ST98], Celiberto [CLC⁺ 99] and Janev [JLEP87].

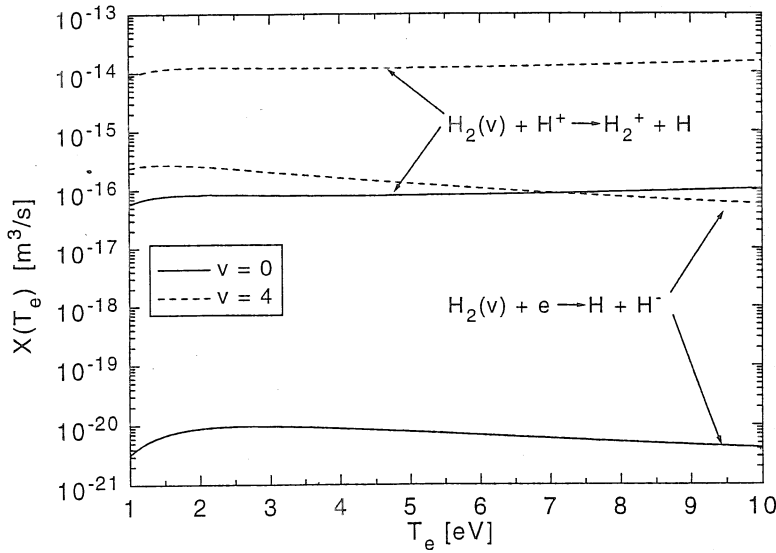


Figure 5.9: Rate coefficients for dissociative attachment and ion conversion as implemented in the modified version of the CR-model for different vibrational levels of H_2 .

coefficients are compiled for H_2 and D_2 . By applying the data of Tennyson, the model calculations will yield higher degrees of dissociation and lower vibrational populations.

Ion conversion (5.3) and dissociative attachment (5.4) are reactions which are very sensitive to the vibrational state of the molecule and become important in

plasmas for the vibrational level $v = 4$ and $v = 6$ for H_2 and D_2 , respectively, because of resonant enhancement. Ion conversion is negligible in technical plasmas due to a low H^+ density, whereas in detached divertor plasmas this is the main channel for producing molecular ions which then take part in further reactions and contribute, for example, to the molecular assisted recombination (Sec. 5.3.5). In Fig. 5.9 rate coefficients, as implemented in the modified version of the CR-model, are compiled for $v = 0$ and $v = 4$ of H_2 . The rate coefficients of ion conversion out of the level $v = 0$ is enhanced by a factor of ≈ 100 if the level changes to $v = 4$. For higher v 's the rate coefficient decreases again. In contrast, the rate coefficient for dissociative attachment increases continuously with increasing vibrational quantum number but slows down for larger v . The enhancement of the rate coefficient for $v = 4$ over that for $v = 0$ is remarkable (nearly four orders of magnitude). In summary, Figs. 5.8 and 5.9 demonstrate the strong influence of vibrational population on rate coefficients and emphasize the necessity of knowledge of the vibrational populations in the ground state of H_2 and D_2 .

5.2 Laboratory plasmas

The dominant neutral particle species in low pressure, low temperature hydrogen plasmas is molecular hydrogen. Typical degrees of dissociation are around one percent. The particle densities can be determined by using a residual gas analyser (H_2 , D_2) or emission spectroscopy (H_2 , D_2 , H , D).

The measurement of the ion composition is more complicated. Ion densities can be measured directly with conventional energy resolved mass spectrometers, except for H^+ , which requires improved systems. Therefore, calculations of particles densities, as described in Sec. 2.3.1, can be utilized for the determination of the ion composition. For each of the three possible ion particle species, i.e. H_3^+ , H_2^+ and H^+ , the loss and gain processes were balanced by taking into account ten reactions and diffusion losses. The rate coefficients were taken from [Rei00] which is a revised and supplemented compilation of data from the book of Janev [JLEP87]. The selection procedure was according to the magnitude of the rate coefficient. Two of the eight electron impact reactions are ionization of H and H_2 , followed by dissociative ionization of H_2 , dissociation of H_2^+ and recombination of H^+ , as well as ion conversion which is a heavy particle collision. The dominant reaction which leads to the formation of the H_3^+ ion is a heavy particle collision: $\text{H}_2^+ + \text{H}_2 \rightarrow \text{H}_3^+ + \text{H}$ ($X \approx 10^{-15} \text{ m}^3/\text{s}$). The two loss processes for this density are electron impact dissociation into H atoms and hydrogen molecules. The reactions are listed explicitly in [WF01] which also describes the developed computer program KALLIOPE. Results for the ECR discharge in hydrogen are shown in Fig. 5.10 depending on the pressure of the discharge. T_e and δ which are input parameter of KALLIOPE were taken from measurements in a mixture with a small amount of He as diagnostic gas. As expected, the dominant ion species is H_3^+ , whereas the density of H_2^+ is one order of magnitude lower. The

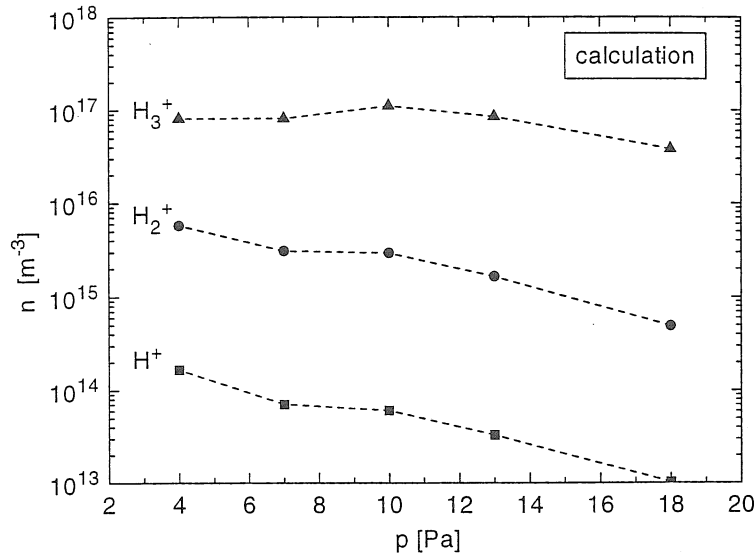


Figure 5.10: Calculated ion densities of hydrogen in the ECR hydrogen plasma as a function of pressure at $n_e = 10^{17} \text{ m}^{-3}$, $\delta = 0.33\%$ and $T_e = 2 - 3 \text{ eV}$.

H^+ ion density is negligible in comparison to the other ion densities and therefore not relevant in technical plasmas.

In the following sections, results of measurements in laboratory plasmas will be presented. In general, helium was used as diagnostic gas (T_e) and to vary T_e actively by changing the admixture of He.

5.2.1 Interpretation of Balmer lines

The atomic hydrogen density in technical plasmas was determined from the radiation of the Balmer lines. First of all, the dominant excitation mechanism was identified which was followed by a detailed analysis of the influence of opacity of the Lyman lines on the population of the upper states of the Balmer series.

Dissociative excitation

Dissociative excitation from molecular hydrogen into the excited states of atomic hydrogen can be the dominant population channel, particularly, at very low degrees of dissociation. Since the ion densities are approximately three orders of magnitude below the atomic hydrogen density, due to an ionization degree of 10^{-5} and dissociation degree of 1%, contributions from dissociative excitation of the ions, in particular H_2^+ is negligible. The contribution of dissociative excitation to atomic population was already mentioned in Sec. 5.1.1 but will be discussed in more detail here. Figure 5.11 shows the rate coefficients of direct excitation [Sum99] and dissociative excitation [MHL77] for the first three Balmer lines. While the rate coefficients of direct excitation are identical for hydrogen and deuterium, the rate coefficients of dissociative excitation are lower for deuterium

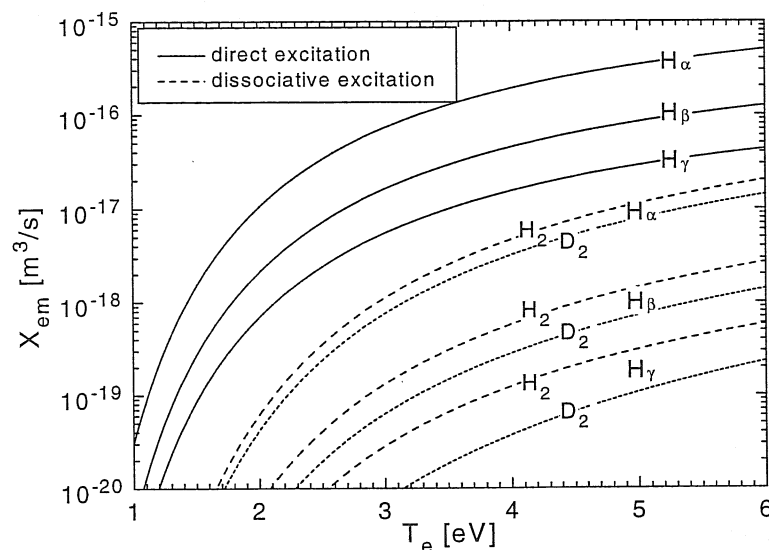


Figure 5.11: Emission rate coefficients of the first three Balmer lines for hydrogen and deuterium originating from direct and dissociative excitation.

than for hydrogen. In addition, dissociative excitation becomes less important for the higher quantum numbers. In principle, rate coefficients for dissociative excitation are two or three orders of magnitude lower than those for direct excitation. Assuming a degree of dissociation of 1% the contribution from the molecules to the radiation of Balmer lines is 50% – 10%. Therefore, dissociative excitation has to be taken into account in the analysis of the Balmer lines.

Opacity

The influence of opacity of Lyman lines on hydrogen excited state population in technical plasmas is discussed in detail in [BF00]. The escape factors, introduced and defined in Sec. 2.2.4, have been calculated for the requirements of the ECR plasma: Doppler profile and cylindrical geometry in a homogeneous plasma. For the calculation of effective rate coefficients the CR-model ADAS was used. The standard input file, necessary to run ADAS, contains the direct rate coefficients and was extended by the rate coefficients for dissociative excitation. This allows the calculation of the molecular contribution to the Balmer radiation. The correction factors for opacity are shown in Fig. 5.12 for each Balmer line at $n_e = 10^{17} \text{ m}^{-3}$ and $T_e = 2 \text{ eV}$. They are valid for a 1 eV Doppler profile and have to be scaled to the actual T_g . Because of the mass dependence of the absorption coefficient, an additional scaling is necessary for deuterium. K_{abs} depends on electron density and on electron temperature, the last one is of minor importance. Since dissociative excitation is included in ADAS, correction factors were also obtained for the molecular part, which are quite similar to the factors for the atoms. It is obvious that H_γ is much less affected by opacity than H_β or H_α . This, together with the significant lower influence from dissociative excitation on population,

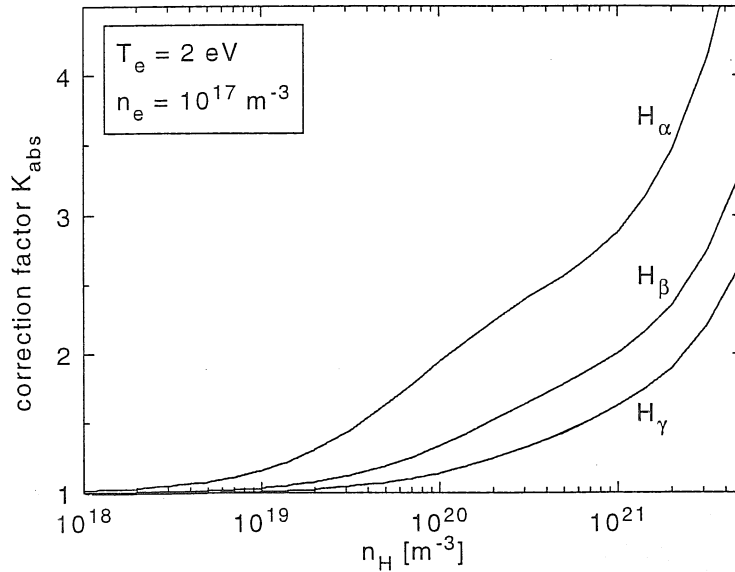


Figure 5.12: Correction factors for three Balmer lines due to opacity of Lyman lines adjusted to the parameters of the ECR discharge.

prefer H_γ as the diagnostic line for the determination of atomic hydrogen densities. Nevertheless, the following results were taken from the analysis of each of these Balmer lines to demonstrate the influence of opacity and dissociative excitation for each line separately. In addition, line ratios were used to determine the degree of dissociation.

Results for atomic densities

Detailed investigations were carried out in the ECR discharge [BF00]. The atomic density was determined in various hydrogen and deuterium plasmas with helium. The atomic density is related to the measured intensity, e.g. for H_α , by:

$$n_H = \frac{\dot{N}_{H_\alpha} - n_{H_2} n_e X_{H_2 \rightarrow H_\alpha}^{eff}(T_e)}{n_e X_{H \rightarrow H_\alpha}^{eff}(T_e)} \quad (5.8)$$

$X_{H_2 \rightarrow H_\alpha}^{eff}(T_e)$ is the effective rate coefficient for dissociative excitation of H_α from H_2 . For the analysis, T_e was taken from the He_{728} line for which opacity of the helium resonance lines was taken into account. Since helium reveals information about the high energy range (≈ 20 eV) of the electron distribution function, whereas hydrogen represents the energy region around 10 eV, deviations from a Maxwellian EEDF would result in atomic densities which are too high. On the other hand using argon as diagnostic gas, a method commonly known as actinometry, will solve this problem but raise another problem: excitation transfer from argon to Balmer lines, i.e. the Balmer lines are enhanced selectively. In addition, helium is the better actinometer for the dissociative part of excitation,

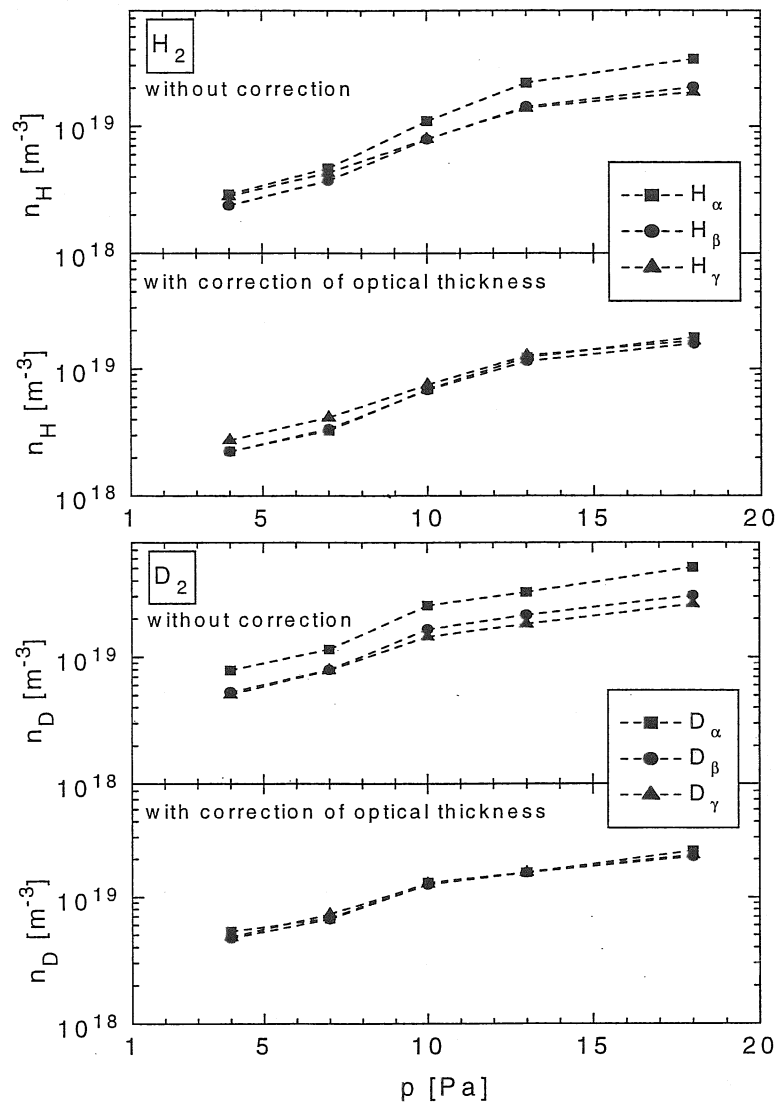


Figure 5.13: Measured atomic hydrogen densities in a 10% $\text{H}_2(\text{D}_2)/\text{He}$ mixture (ECR discharge) with and without taking into account opacity of Lyman lines.

which has a threshold energy of about 18 eV. Applying the spectroscopic method for the determination of EEDFs by using a small admixture (1%) of argon for this purpose only, the results justify a Maxwell distribution up to mixtures of 50% hydrogen. For higher admixtures of hydrogen to helium, deviations occur, the resulting fit coefficient ν for the EEDF is then around 1.5. Figure 5.13 give results of a 10% H_2/He and 10% D_2/He mixture with and without taking into account the optical thickness of the Lyman lines. Under the assumption of optically thin plasmas, the Balmer lines give different atomic densities, particularly the results from H_α deviate. The discrepancy is somewhat larger for deuterium than for hydrogen (smaller Doppler profiles, higher reabsorption).

Taking into account the influence of optical thickness the evaluation leads to consistent results. The parameters for the correction of optical thickness were as follows: cylinder geometry with $b = 5$ cm, Doppler profile with " T_g " = 700 K (line width due to thermal motion and fine-structure), parabolic spatial profile for emission and atomic mass $m = 1$ for H, $m = 2$ for D. In a first step the H_γ line was used for calculating the n_H density. This line is least influenced by opacity. Using this density, the correction factor for the excitation rates K_{abs} was determined from Fig. 5.12 and scaled to the lower gas temperature. Subsequently, the correction was applied to the radiation of all lines. In plasmas with 10% H_2 or D_2 dissociative excitation contributes less than 20% or 8% to the measured radiation, respectively. Therefore, the correction to the molecular part is relatively uncritical. Evaluating the measured data consequently by the described procedure, densities derived from all three Balmer lines agree well for both hydrogen and deuterium. In the cases shown, H_γ or D_γ could be used directly because these lines contain the smallest molecular contribution and are least affected by opacity. However, they are the weakest lines and, depending on the ionization balance, they are most susceptible to recombination and are very sensitive on electron density. For higher admixtures of hydrogen, the molecular contribution to the radiation is much higher and the error bar of the atomic density increases significantly due to the subtraction of two large values in Eq. 5.8.

5.2.2 Degree of dissociation

The dissociation degree in the 10% H_2 (D_2)/He mixtures was 4% – 6% for hydrogen in the pressure range of 4 – 18 Pa and slightly higher (5.5% – 7.5%) for deuterium due to a higher dissociation cross sections for deuterium than for hydrogen [CLC⁺99]. Since the molecular contribution to the line intensity increases with higher hydrogen contents in the plasma, the determination of the dissociation degree from absolute line intensities becomes insensitive and can be replaced by the evaluation of line ratios. The H_α to H_β line ratio is given by:

$$\frac{\dot{N}_{H_\alpha}}{\dot{N}_{H_\beta}} = \frac{n_H X_{H \rightarrow H_\alpha}^{eff}(T_e) + n_{H_2} X_{H_2 \rightarrow H_\alpha}^{eff}(T_e)}{n_H X_{H \rightarrow H_\beta}^{eff}(T_e) + n_{H_2} X_{H_2 \rightarrow H_\beta}^{eff}(T_e)} \quad (5.9)$$

with upper and lower limits for pure molecular and pure atomic excitation. The measurements are expected to be between these two limits, which are plotted in Fig. 5.14 for the line ratios H_α/H_β and H_α/H_γ . Theoretical line ratios are included also for different degrees of dissociation ($\delta = 0.1\%$, 1% and 5%). The ratios depend on T_e , but to a much lesser extent than the results in Eq. (5.8).

Line ratios were measured in a various mixtures of hydrogen(deuterium) with helium and are shown in Fig. 5.14. Here, again the influence of optical thickness is quite important and was taken into account in the analysis. The results are precisely in the expected range and can be interpreted in terms of dissociation degree δ . Both measured line ratios (H_α/H_β and H_α/H_γ) yield quite consistent results for the dissociation degree in hydrogen and deuterium plasmas. The line

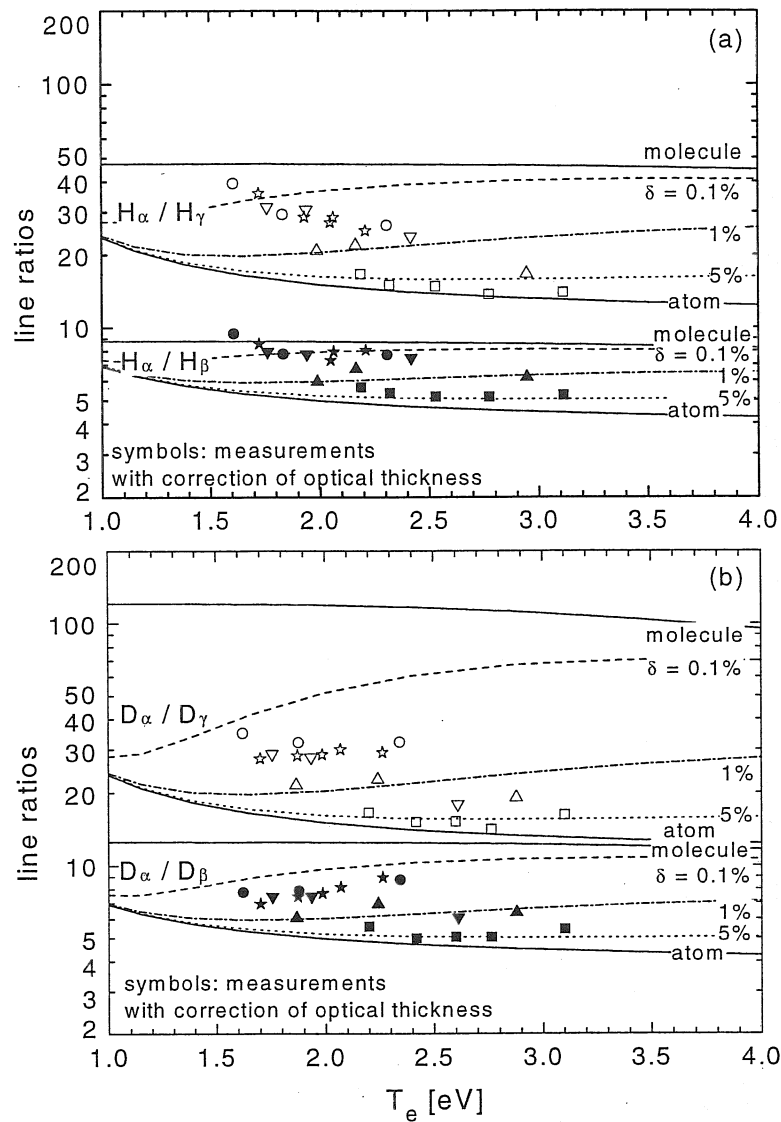


Figure 5.14: Balmer line ratios of $H_2(D_2)/He$ mixtures at various pressures of the ECR discharge (■: 10%, ▲: 20%, ▼: 50%, ●: 80%, ★: 90% molecules in helium) together with calculations for various degrees of dissociation.

ratio method is apparently sensitive in the range between about 0.1% and 5% dissociation degree, but requires very accurate measurements of line radiations. An estimated uncertainty in relative calibration of $\approx 10\%$ already leads to an error bar of a factor of two or more in δ . The H_α/H_γ ratio is superior, however, it becomes very dependent on electron density at higher n_e . In deuterium, the ratio of atomic and molecular excitation differs from that of hydrogen, which means that the results from the line ratio method have a higher accuracy in the case of deuterium.

A summary and comparison of the two methods for measuring the dissociation

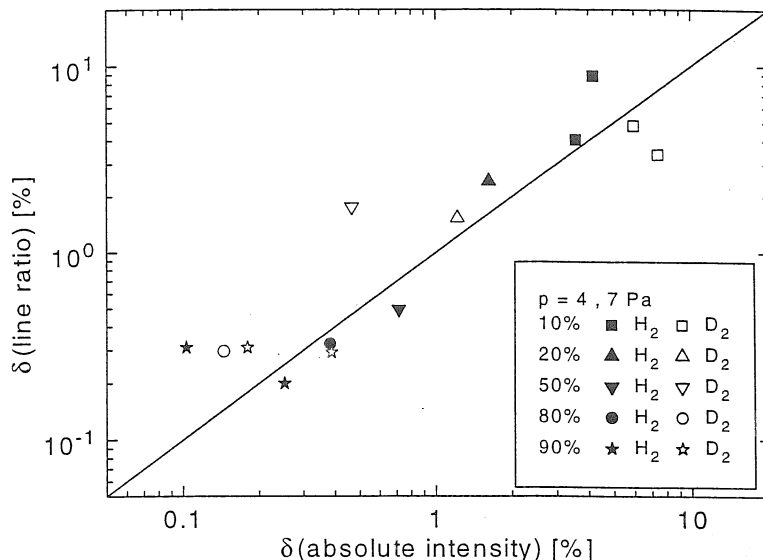


Figure 5.15: Comparison of results for the dissociation degree from absolute line intensities (average of H_α , H_β and H_γ) and from line ratios (average of H_α/H_β and H_α/H_γ).

degree is shown in Fig. 5.15 for the discharge pressures of 4 and 7 Pa. The degree of dissociation varies in a wide range depending on the molecular mixture: $0.1\% < \delta < 10\%$. Considering the limited sensitivity and the experimental uncertainties, the results agree very well. When comparing the data, it must be kept in mind that the line ratio method is no longer suitable for diagnostics above a few percent for δ and the absolute measurements are superior. On the other hand, at dissociation degrees of the order of 1% or less, two comparable number must be subtracted in the latter case, substantially increasing the error bars. Assuming 10% accuracy for the rate coefficients, plus 10% for the system calibration and the spectral line integration of H and He lines, the error bars are a factor of two or three for the results.

5.2.3 Atomic hydrogen fluxes

In the ICP discharge atomic hydrogen fluxes were obtained by measurements of atomic hydrogen densities above a surface. For this purpose, additional material, with the chamber size as diameter, was installed in the centre of the discharge $z = 0$ (Fig. 2.7). This allows space resolved measurements of the Balmer lines in the z -direction, because the substrate influences the plasma homogeneously in radial direction, which is the line of sight. Electron densities profile were measured by the Langmuir probe system in z -axis using a small hole in the substrate. Measurements were carried out in 10% H_2 (D_2)/He mixtures at a pressure of 20 Pa and an input power of 250 W. Since the gas temperature is 650 K, the results refer to a substrate temperature of 650 K. The sheath potential is around 10 eV which represents the energy of the ions (mass one) bombarding the surface. The

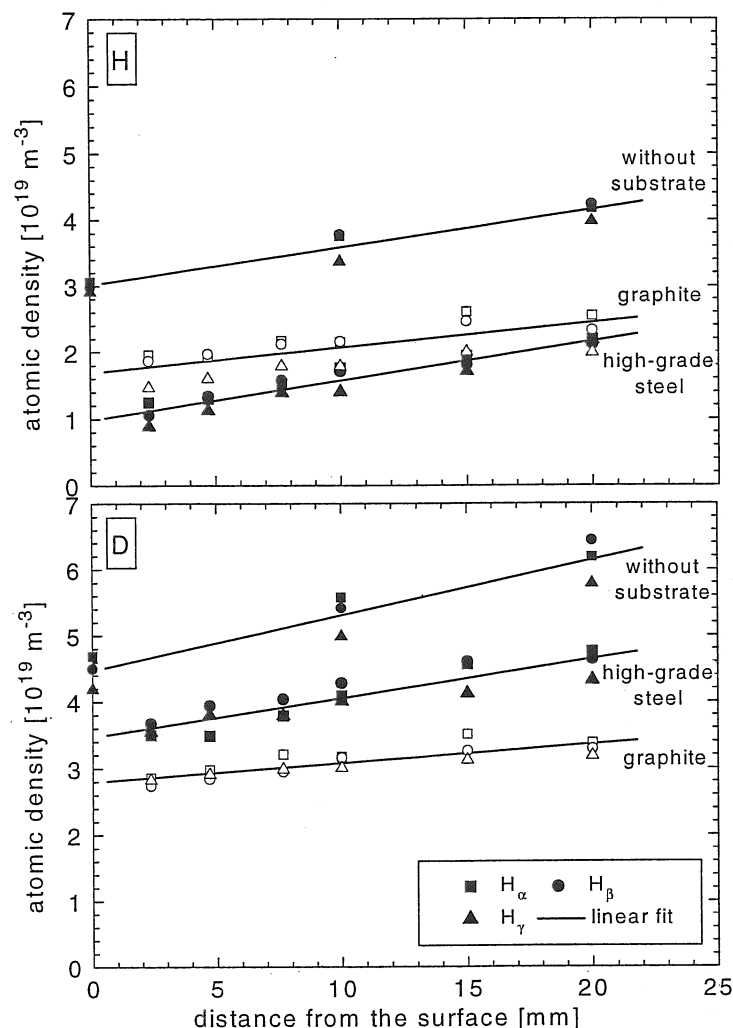


Figure 5.16: Atomic hydrogen densities above a surface introduced in a hydrogen and deuterium plasma ($10\%H_2(D_2)/He$) in the ICP discharge at 20 Pa. Symbols refer to the three Balmer lines which were fitted by a regression line.

degree of dissociation in these mixtures is around 10% which yields together with an ionization degree of 10^{-5} a ratio of atomic to ion density of approximately 100. The atomic densities of H and D in the plasma were determined by emission spectroscopy of the Balmer lines H_α , H_β and H_γ . In the analysis of line intensities, opacity of Lyman lines and dissociative excitation were taken into account as described in Sec. 5.2.1. Space resolved measurements above a surface were carried out by moving the lens of the imaging system vertically. A spatial resolution of 2 mm was achieved.

Results were obtained for high-grade steel and fine-grain pressed graphite as shown in Fig. 5.16 for hydrogen and deuterium plasmas. For comparison, atomic densities without an additional surface in the centre of the plasma chamber were

also measured. The densities derived from the three Balmer lines are in very good agreement for either isotopes. As already shown in ECR discharges deuterium plasmas have a higher degree of dissociation. The absolute values as well as the slope of a regression line through the measured points change with the material.

To get fluxes from the measured densities, a simplified theoretical description of the motion of the neutral particles in the plasma chamber is used. In stationary plasmas the motion of the particles is forced by a density gradient and the particle motion can be described by diffusion. A one-dimensional model gives a linear decay of the density towards the vessel walls. Sources lead to a curvature of the straight line and result in a reverse parabola with the maximum at the centre of the chamber, if the atoms are produced homogeneously in the whole chamber and recombine completely at the chamber walls. However, in the ICP discharge the plasma parameters vary in z -direction so that production of particles via dissociation of molecules is different in each radial disc of the plasma. Furthermore, reflection coefficients of surfaces influence the density profile. On the other hand a diffusive flow is justified at a pressure of 20 Pa which was used for the investigations. The density profile which is shown in Fig. 5.16 covers only 2 cm in z -direction (from the centre to the quartz plate), whereas the chamber is 10 cm in height. The strongest inhomogeneities in particle production are directly below the quartz plate which is located at 5 cm. Therefore it is assumed that the particles in the observed plasma volume are produced homogeneously so that a linear density gradient is expected as confirmed by the measurements. An additional surface in the centre of the plasma at $z = 0$ will influence only the density close to the surface. Measured densities are obtained at a distance above 2 mm from the surface (limited by the lines of sight) and the pronounced influence is not visible in Fig. 5.16.

For the evaluation of atomic fluxes from the space resolved densities, the diffusive flux is applied which is proportional to the density gradient:

$$\Gamma = \frac{dn}{dz} D_n \quad \text{diffusive flux} \quad (5.10)$$

with the diffusion coefficient for neutral particles D_n ($D_H = 4.3 \text{ m}^2/\text{s}$, $D_D = 3.3 \text{ m}^2/\text{s}$ at $p = 20 \text{ Pa}$ and $T_g = 650 \text{ K}$).

The atomic flux in the 10% $\text{H}_2(\text{D}_2)/\text{He}$ plasma at 20 Pa was determined to be $\Gamma_H = \Gamma_D = 2.6 \times 10^{21} \text{ m}^{-2} \text{ s}^{-1}$ without an additional substrate in the chamber. The gradient is getting smaller by introducing high-grade steel, or even more drastically by introducing graphite, and the effective fluxes decrease (Tab. 5.1). It must be kept in mind, that the diagnostic method makes no difference between particles flowing onto the surface and particles coming from the surface.

If the mean free path is shorter than the distance of the line of sight to the surface, the particle motion must be described by molecular flow. Therefore, the absolute value of the atomic density close to the surface yields the molecular flux:

$$\Gamma = n_H \frac{v_{th}}{4} \quad \text{molecular flux} \quad (5.11)$$

material	isotope	$\Gamma_{diff.} [m^{-2} s^{-1}]$	$n_{atom} [m^{-3}]$	$\Gamma_{mol.} [m^{-2} s^{-1}]$
-	H	2.6×10^{21}	-	-
-	D	2.6×10^{21}	-	-
high-grade steel	H	2.5×10^{21}	1.0×10^{19}	9.2×10^{21}
high-grade steel	D	1.6×10^{21}	3.6×10^{19}	2.3×10^{22}
graphite	H	1.6×10^{21}	1.8×10^{19}	1.7×10^{22}
graphite	D	0.9×10^{21}	2.8×10^{19}	1.8×10^{22}

Table 5.1: Atomic hydrogen fluxes determined from diffusive and molecular particle flow.

with the mean particle velocity v_{th} ($v_{th}(H) = 3700$ m/s, $v_{th}(D) = 2600$ m/s at $T_g = 650$ K).

The mean free path at 20 Pa is ≈ 1 mm, whereas the first line of sight refers to 1 – 2 mm above the surface. The densities at 2 mm and the molecular fluxes obtained with these densities are compiled in Tab. 5.1.

The molecular fluxes are always considerably higher (an order of magnitude) than the diffusive fluxes. Since the mean free path of the particles is lower than the spatial resolution of the measured densities, the transition regime from diffusive to molecular flux in front of a surface is not observed well enough. Here, the spatial resolution has to be enhanced or the pressure has to be lowered which results in longer mean free paths. As a consequence, the measured molecular fluxes do not represent the particle flux which flows to the surfaces. However, the diffusive flux represents the atomic hydrogen flux in the plasma.

5.2.4 Reflection coefficients

In principle, measurements of diffusive fluxes in the plasma and molecular fluxes onto surfaces enable the determination of the reflection coefficient for particles on surfaces. The reflection coefficient R is then given by: $R = (\Gamma_{mol.} - \Gamma_{diff.})/\Gamma_{mol.}$. The fluxes compiled in Tab. 5.1 result in $R = 73\%$ for H and $R = 93\%$ for D in case of high-grade steel and $R = 91\%$ for H and $R = 95\%$ for D in case of graphite. As discussed in Sec. 5.2.3, the molecular fluxes onto additional surfaces in the ICP discharge were not obtained precisely enough and the reflection coefficients represent an upper estimation. However, the diffusive fluxes and the atomic densities are clearly influenced by the surface and show in particular differences for the isotopes: atomic hydrogen and atomic deuterium. The atomic densities close to the surface increase whereas the diffusive flux decreases. This indicates that the surface reflects the atomic particles to a considerable amount. Furthermore, the diffusive fluxes in the plasma without an additional surface are the highest atomic fluxes and are equal for the isotopes. A comparison of diffusive fluxes with and without an additional surface in the plasma, gives an lower approximation value for the reflection coefficients of atoms for surfaces: $R = (\Gamma - \Gamma_{material})/\Gamma$. Thus, the following reflection coefficients are obtained: $R = 5\%$ for H and $R = 40\%$ for

D in case of high-grade steel and $R = 40\%$ for H and $R = 65\%$ for D in case of graphite.

In general, reflection coefficients of graphite are higher than reflection coefficients of high-grade steel. Furthermore, a clear isotope effect is observed. In addition to the dependence of R on material and isotope a dependence on substrate temperature, hydrogen flux and hydrogen energy may be added. Few data is available concerning reflection or adsorption of hydrogen atoms on surfaces at low energies. In [VWH99], reflection coefficients are given for both isotopes for various graphite surfaces which are measured to be between 65% and 90% (time-of-flight measurements). There, no variation with substrate temperature was observed. The neutral particle beam temperature was 2400 K which is higher than the gas temperature of the experiment here. On the other hand, calculated reflection coefficients decrease to zero at energies below 1 eV. A comparison of measured data and a discussion of the effects can be found in [VWH99].

Reflection coefficients of atoms are important to know for a variety of plasma and surface parameters, since on one hand they are used in plasma edge codes for fusion experiments (modeling of hydrogen recycling) and, on the other hand, they influence the modeling of the atomic hydrogen density in technical plasmas, i.e. they increase the degree of dissociation. In the first case, as an example, hydrogen atoms can be reflected as atoms or as molecules, a fact which was measured to be dependent on the surface temperature [PMS⁺99]. The higher the temperature the more atoms leave the surface. In technical plasmas, the temperature and material dependence of R can be used to increase actively the degree of dissociation in order to improve, e.g., the formation of thin films [OSS95]. The lower the temperature of the surfaces, the higher is the degree of dissociation.

5.2.5 Particle densities and molecular radiation

For the determination of molecular hydrogen densities the radiation of a variety of molecular bands is available. Here, selection criteria are as follows: strong intensity of the emission band, clear identification and separation of rotational lines and/or vibrational bands and the knowledge of emission rate coefficients. As mentioned before, the Fulcher transition ($d^3\Pi_u - a^3\Sigma_g^+$) is in particular suited for diagnostics but difficulties arise concerning the selection of the proper rate coefficient (Sec. 5.1.2). Further candidates for diagnostics are the Werner band ($C^1\Pi_u - X^1\Sigma_g^+$, 90–140 nm), the Lyman band ($B^1\Sigma_u^+ - X^1\Sigma_g^+$, 140 to 165 nm), the hydrogen continuum ($a^3\Sigma_g^+ - b^3\Sigma_u^+$) which is most intense and undisturbed between 165 and 300 nm, and the singlet transition around 460 nm ($G^1\Sigma_g^+ - B^1\Sigma_u^+$, only one rotational branch of the vibrational band 0–0). For all of these bands cross sections or rate coefficients are given in literature. However, in the following discussion the data, which were already implemented in the modified version of the CR-model, were used to take into account other population mechanism than only the ground state excitation. For deuterium, the same data were applied corrected by the corresponding Franck-Condon factors. Measurements were carried out in the ECR discharge at various pressures and mixtures with

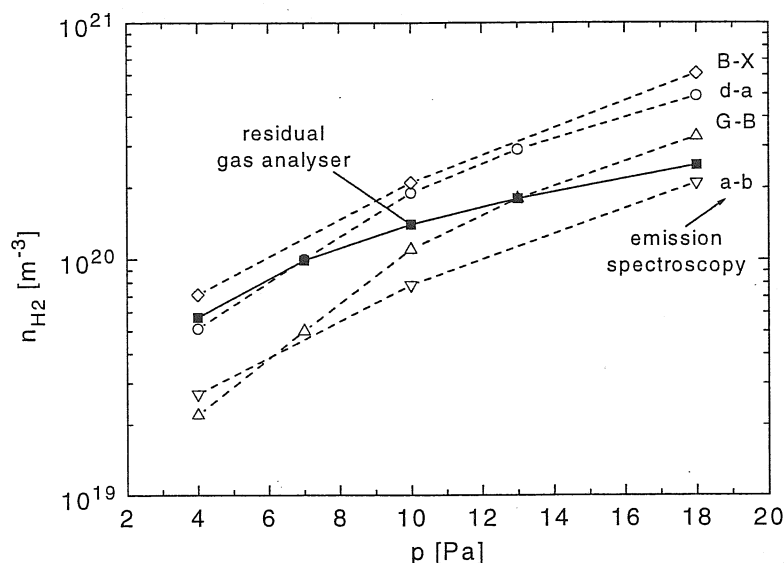


Figure 5.17: Densities of molecular hydrogen in a 10% H_2 /He ECR plasma measured with the residual gas analyser and by emission spectroscopy of various molecular bands.

helium. Using the effective rate coefficients taken from the CR-model [WF01] and using T_e from the analysis of the He_{728} line, the molecular density was determined from each measured band individually. In addition, the molecular density was measured with the residual gas analyser.

Figure 5.17 shows the results of a 10% H_2 /He plasma, which is representative for all investigated mixtures as well as for deuterium. The results from each band differ by a factor of three and show slightly different dependencies on pressure in comparison with results from the residual gas analyser. Since the residual gas analyser provides the most reliable molecular density, either the rate coefficients of the bands in question are not precise enough or additional population and depopulation processes occur which are not included in the CR-model. Such processes may be heavy particle collisions like quenching or excitation transfer with resonant energy levels, i.e. repopulating processes.

Repopulating processes

In order to investigate quenching or excitation transfer of individual states, the Fulcher transition and its competing transitions with almost identical energy levels of the upper and lower state were recorded in the MW discharge in a broad pressure range [HFB00, Heg02]. Figure 5.18 represents a magnification of the energy level diagram for the $n = 3$ and $n = 2$ states of the triplet system of molecular hydrogen. The transitions of four measured bands are indicated with an arrow and were abbreviated, namely: $d-a$, which is the Fulcher transition and $g-c$, $i-c$, $j-c$ with the same final level. They emit all in the wavelength region of the Fulcher transition. In the CR-model the $n = 3$ state is not electronically resolved. However, its population or the effective rate coefficient can be derived

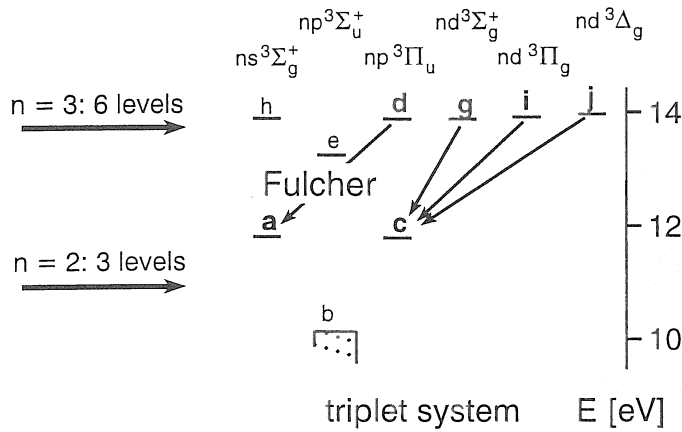


Figure 5.18: Zoom of the energy level diagram for the $n = 2$ and $n = 3$ triplet states of molecular hydrogen. The arrows indicate the measured transitions.

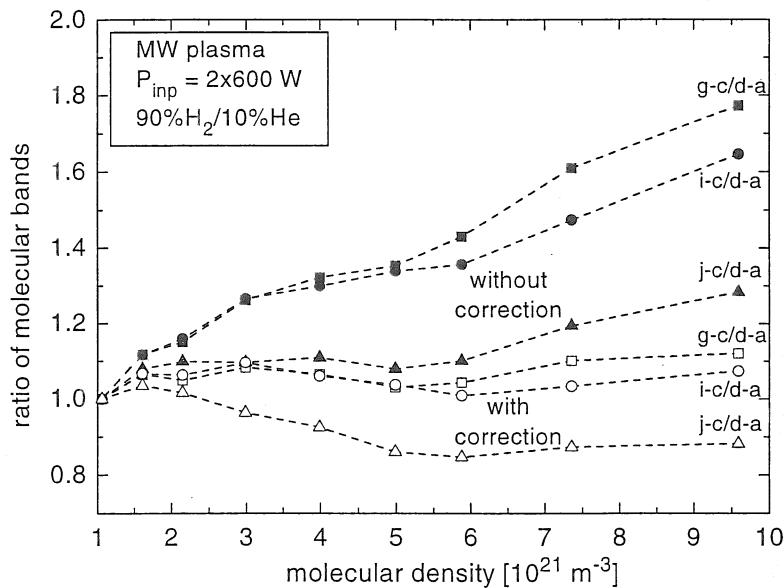


Figure 5.19: Intensity ratio of molecular bands. Open symbols refer to results obtained by taking into account quenching processes.

from the $n = 3$ population by applying the statistical weights and the lifetimes as already done for the Fulcher transition (Sec. 5.1.2). As a consequence, the calculated intensity ratios of these bands are independent of T_e and n_e .

The intensity ratios were measured in a 90% H_2 /He mixture depending on pressure, i.e. molecular density. All measured bands originate from $v' = 0$ level. The results are given in Fig. 5.19 and show an increase with increasing density.

This indicates that quenching is more important for the upper Fulcher state than for the other states. Quenching can be described as radiationless depopulation of a state by heavy particle collisions and can be considered in the measured radiation by the quenching coefficient $Q > 1$:

$$\dot{N}_{corr} = \dot{N}_{measured} Q \quad \text{with} \quad Q = \tau X_q n_{H_2} + 1. \quad (5.12)$$

τ is the lifetime of the electronic state and X_q is the rate coefficient of quenching depending slightly on gas temperature. Unfortunately, X_q is only well-known for the d state and is determined to be $4 \times 10^{-15} \text{ m}^3 \text{ s}^{-1}$ for the first vibrational level ($v' = 0$). Assuming the same quenching rate coefficient for the three other levels and taking into account different lifetimes ($\approx 15 \text{ ns}$ for g, i, j and 40 ns for d), the measured intensity ratios can be corrected by quenching. The results are presented also in Fig. 5.19 (open symbols). The dependence of the intensity ratios on molecular density vanishes as expected if quenching is the responsible process. In contrast, the $e - a/d - a$ intensity ratio increases with molecular density despite quenching corrections [Heg02] which indicates a special role of the e state being energetically lower than the other five levels of the $n = 3$ state. The presented results demonstrate that the Fulcher transition with a lifetime of 40 ns is influenced by heavy particle collisions in technical plasmas. This fact has to be kept in mind, particularly for the interpretation of the Fulcher emission in plasmas at pressures higher than $\approx 50 \text{ Pa}$.

5.2.6 Vibrational population in the ground state

The radiation of the diagonal Fulcher bands yields information about the vibrational population of the upper Fulcher state $d^3\Pi_u$ which can be correlated to the vibrational population of the ground state (Sec. 3.1.4). This implies two main assumptions: first, the assignment of a vibrational temperature in the ground state which is transferred into the upper state via the Franck–Condon principle. Calculations of the modified version of the CR-model justify the assignment of T_{vib} for the first five levels and the results are independent of either the heavy particle collisions are enabled or not in the code. Furthermore, the diagnostic method is only sensitive for level populations which are approximately 1% or higher than that of $v = 0$. The second assumption concerns the Franck–Condon principle which may not be justified for the light molecule H_2 , which means the Born–Oppenheimer assumption is not fulfilled strictly. Since no evidence was found in literature, this assumption has to be presumed. Additionally, if the dominant population mechanism is not only the excitation from the ground state but also excitation out of the $c^3\Pi_u$ state (Fig. 5.4) or cascading, then a mixture of all Franck–Condon matrices involved will determine the vibrational population. However, since the potential curves of almost all triplet states have a very similar shape and the minima are at almost the same equilibrium distances, the mixing is not of importance for the upper Fulcher state.

Figure 5.20 shows the correlation between the vibrational temperature in the ground state ($T_{vi}(X^1\Sigma_g^+)$) and the relative population in the upper Fulcher state

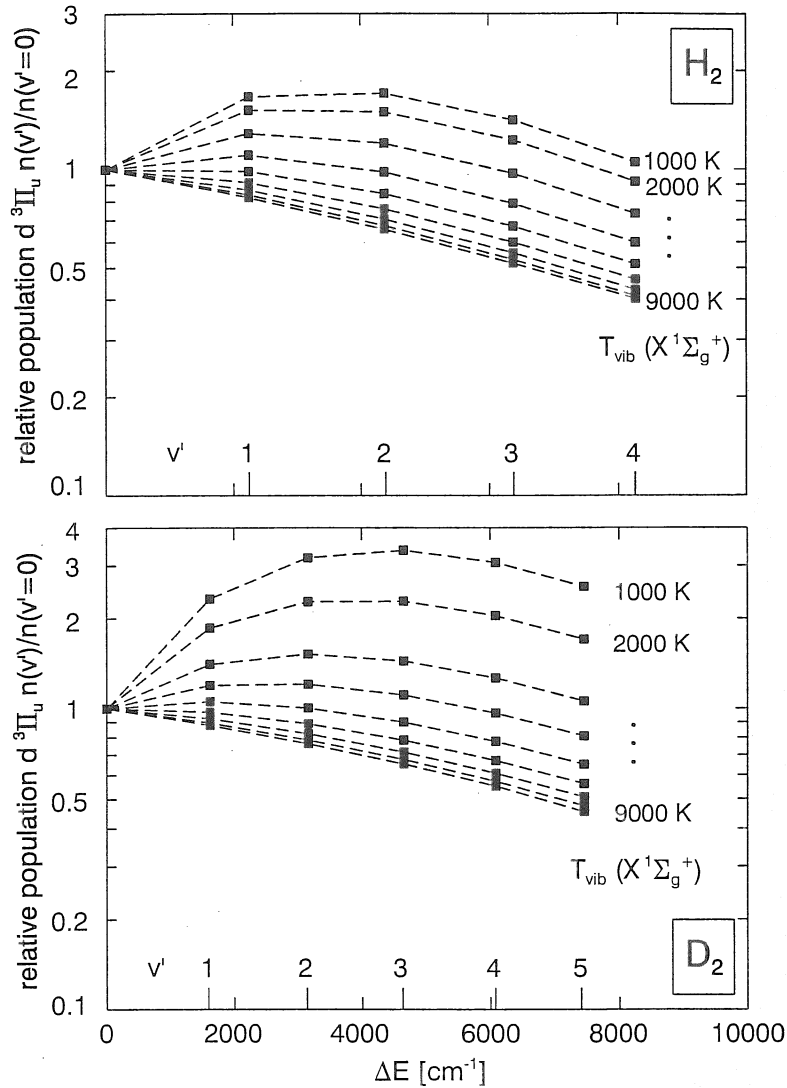


Figure 5.20: Relative vibrational populations in the upper state of the Fulcher transition ($d^3\Pi_u$) of hydrogen and deuterium depending on the vibrational temperature of the ground state $T_{vib}(X^1\Sigma_g^+)$ which is assigned to the first five v -levels.

($d^3\Pi_u n(v')/n(v' = 0)$) for hydrogen and deuterium. The Franck–Condon factors corresponding to the two transitions involved for the diagnostics ($X - d$ and $d - a$) were calculated by using the FCFRKR computer program of Telle [TT82]. The evaluation of measured intensities of Fulcher lines and the branching ratios together with a detailed analysis of the sensitivity of the diagnostic method is described in [FH98]. Furthermore, the different lifetimes and selective quenching of the vibrational levels of the $d^3\Pi_u$ state were taken into account as well as corrections which were obtained by using vibrationally resolved rate coefficients for the excitation. The latter is important at low temperatures ($T_e \approx 3$ eV or lower) since each vibrational level in the ground state reduces the threshold

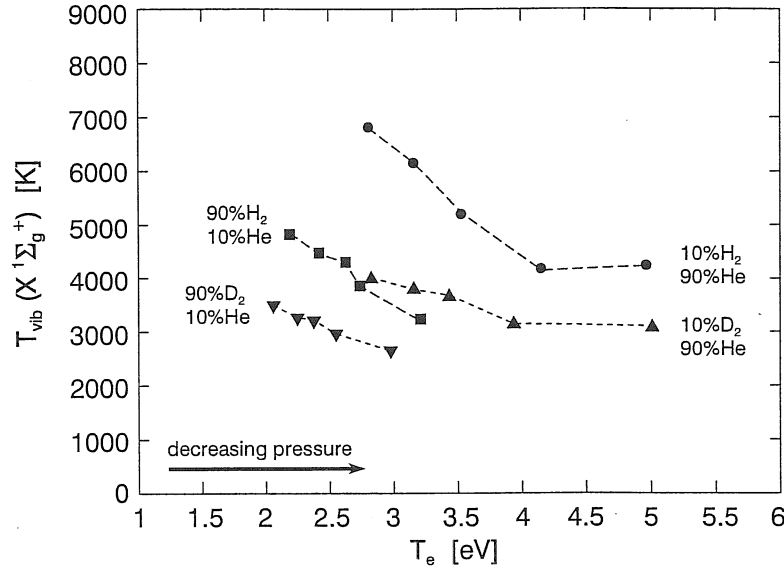


Figure 5.21: Measured vibrational temperatures assigned to the first five v -levels in the ground state depending on gas mixture and pressure of the ECR discharge.

energy (≈ 14 eV) of about 0.5 eV. These corrections are applied to the measured ratios which are then compared with the calculated ratios of Fig. 5.20.

The described diagnostic method has been applied to various hydrogen (deuterium)/helium plasmas [FH98]. The comparison of measured and calculated relative vibrational population of the upper Fulcher state shows that experimental results are well mirrored by the theoretically derived populations up to $v' = 3$ for H₂ and $v' = 4$ for D₂. Because of the lack of data for D₂ and a remaining discrepancy at $v' = 4$ and $v' = 5$ for H₂ and D₂, respectively, these levels are not recommended for the method. The very good agreement of the levels $v' = 0 - 3$ (4) confirms the validity of the Franck-Condon principle for the electron impact excitation of the $d^3\Pi_u$ state. Furthermore, it indicates that there is no collisional redistribution among the excited vibrational levels. The results also show no major difference in the quality of the fits for hydrogen and deuterium.

Results for the vibrational temperatures are given in Fig. 5.21 for two mixtures with helium. A variation of T_e was achieved by a pressure variation. $T_{vib}(X^1\Sigma_g^+)$ ranges from 3200 K to 6800 K and from 2600 K to 4000 K for H₂ and D₂, respectively. The fit quality results in error bars of 50 K at about 1000 K and of 500 K at about 7000 K and are in the range of the experimental error. The ground state population in H₂ and D₂ is very similar. This is mirrored by apparent lower T_{vib} for D₂, which is due to the lower energy separation of the vibrational levels caused by the greater mass. In Fig. 5.21 T_{vib} decreases with increasing T_e , however, in this figure several effects are mixed. Since the pressure decreases with increasing T_e the number of wall collisions increases leading to a depopulation. The comparison of different gas mixtures (1/9, 9/1) reveals also a depopulation because the number of heavy particle collisions rises. The pure effect of increasing

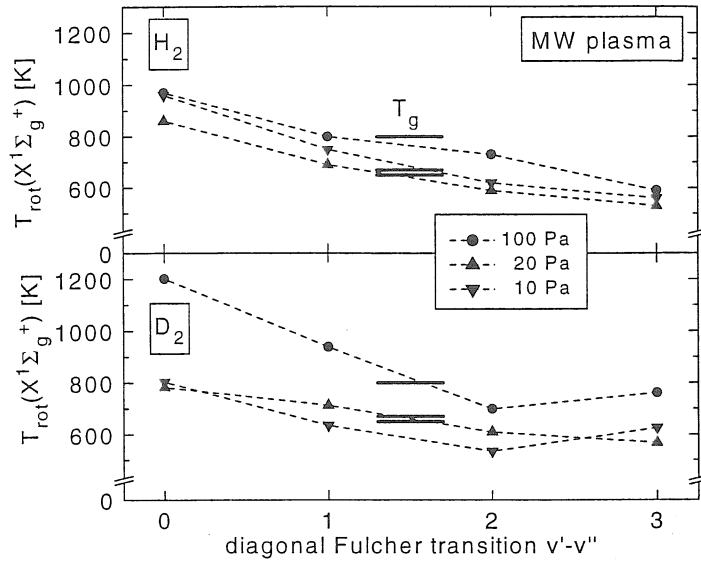


Figure 5.22: Measured $T_{rot}(X^1\Sigma_g^+)$ derived from the upper Fulcher state depending on the degree of the diagonal transition in comparison with T_g .

T_e is a decrease of T_{vib} due to increasing dissociation which leads to an effective loss of vibrationally excited molecules. The interpretation of these measurements is confirmed by calculations by the modified CR-model.

An supplementary result of the analysis is the rotational population of the various vibrational levels of the excited state ($T_{rot}(d^3\Pi_u)$). The intensities of the first five measured rotational lines of the Q -branch are on a straight line in the Boltzmann-plot and a rotational temperature can be assigned to the population. Because of the very weak intensity of lines with higher rotational quantum number no information could be obtained for higher rotational levels. Using Eq. (3.7) the rotational temperature in the excited state is related to the rotational temperature in the ground state. Thus, for all vibrational levels of the excited state a single rotational temperature in the ground state should be obtained which may represent the gas temperature (Sec. 3.1.4).

Figure 5.22 gives a comparison of rotational temperatures in the ground state $T_{rot}(X^1\Sigma_g^+)$, which were obtained from each diagonal vibrational transition, with the gas temperature. The latter was derived from diagnostics of molecular nitrogen by adding 1%N₂ to the plasma. Both, T_{rot} as well as T_g increase with increasing pressure of the MW discharge. The results derived from the various diagonal bands show a decrease with increasing vibrational quantum number. Remarkable are the high values of the 0–0 transition. Similar results were measured in diver-tor plasmas and in the plasma edge of fusion experiments [HFBA01, BMP⁺00]. This is a feature which is not explained yet, and it demands a measurement of the rotational lines of each vibrational band individually in order to derive the overall radiation of the Fulcher band. To derive the gas temperature of the plasma the Fulcher radiation is not as well suited as the radiation of nitrogen molecules.

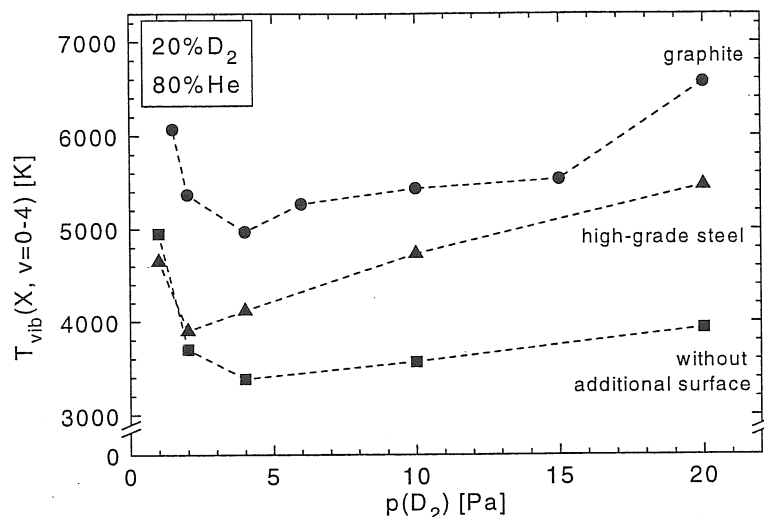


Figure 5.23: Vibrational temperatures in the ground state of deuterium in a MW discharge with and without introducing an additional surface into the plasma.

In order to determine the influence of surfaces on the vibrational population in the ground state measurements in MW plasmas were carried out. High-grade steel and pressed graphite (EK98, a material typically used in divertors) were introduced into the plasma. The plasma was observed by lines of sight parallel to the surface. Figure 5.23 shows measured vibrational temperatures in D_2/He plasmas as a function of the discharge pressure for various surface materials. Similar results have been obtained in H_2/He plasmas. The diagnostic method can not distinguish between the vibrational population which originates from the surface and the vibrational population which is produced in the plasma. Surfaces may release vibrationally excited molecules by atoms which recombine at the surface. Furthermore, surface reactions as the Langmuir–Hinshelwood mechanism and the Eley–Rideal mechanism may take place. The measurements show that high-grade steel increases T_{vib} and graphite even exceeds results of high-grade steel. The high T_{vib} for graphite is remarkable and may be due to the formation of hydrocarbons by chemical erosion of graphite under the bombardment of hydrogen atoms and ions. In addition, interaction of hydrocarbons with hydrogen molecules may occur.

Whether the strong increase of $T_{\text{vib}}(X^1\Sigma_g^+)$ of hydrogen by introducing graphite into the hydrogen plasma is attributed to a pure surface effect or to the presence of methane in the plasma can be checked by measurements carried out in methane plasmas. During the breakup of the CH_4 or C_xH_y molecules in the plasma, H_2 will be formed already vibrationally excited. Figure 5.24 gives a comparison of $T_{\text{vib}}(X^1\Sigma_g^+)$, obtained in the ECR discharge at $p = 10$ Pa, for different mixtures of H_2/He with the corresponding CH_4/He mixtures. In general, $T_{\text{vib}}(X^1\Sigma_g^+)$ decreases with increasing molecular fraction where depopulating heavy particle collisions become more and more important. Furthermore,

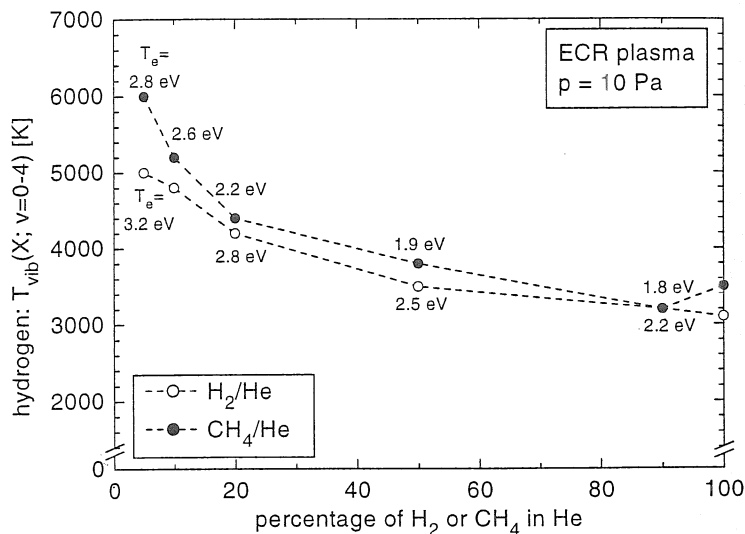


Figure 5.24: Vibrational temperatures in the ground state of hydrogen in H_2/He and CH_4/He plasmas at 10 Pa.

a trend with T_e can be observed. At small molecular concentrations methane plasmas result in considerable higher $T_{vib}(X^1\Sigma_g^+)$ as hydrogen plasmas, an effect which seems to vanish at high molecular concentrations. If vibrationally excited molecules are formed during the breakup of hydrocarbons by electron impact dissociation a T_e dependence is expected which is indicated in 5.24. For high molecular concentrations the dominating heavy particle collisions may be more effective for collisions with hydrocarbons than for collisions with the hydrogen molecules. In summary, the investigations have shown that $T_{vib}(X^1\Sigma_g^+)$ of hydrogen or deuterium molecules is sensitive on the material of a surface and on the reaction channel which produces the molecule.

5.2.7 Continuum radiation

The radiation of the hydrogen continuum which originates from the $a^3\Sigma_g^+ - b^3\Sigma_u^+$ transition is intense and can be observed readily in the near ultraviolet spectral range. The most intense part of the spectrum is between 170 and 400 nm whereas the whole continuum spectrum extends from 120 to 600 nm. For diagnostic purposes of T_e and $T_{vib}(X)$ the measured spectra have to be compared with calculations of the spectra with T_e and $T_{vib}(X)$ as fitting parameter. On the basis of potential curves of the three states involved ($X^1\Sigma_g^+$, $a^3\Sigma_g^+$, $b^3\Sigma_u^+$) and the electronic transition dipole moment (Fig. 5.25), the wave functions and transition probabilities as well as the lifetimes were calculated for all hydrogen isotopes [FSB00]. Using the corona model for excitation from the ground state and the corresponding excitation rate coefficient, absolute intensities were obtained, which were then compared with measurements.

The absolute intensity of the continuum radiation depends on T_e whereas

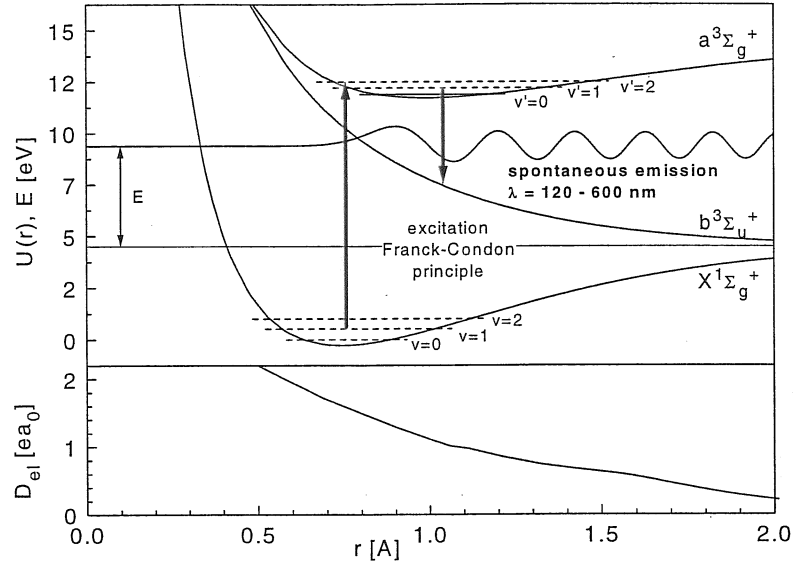


Figure 5.25: Potential energy curves of the three electronic states which contribute to the continuum radiation of molecular hydrogen. The lower part shows the electronic dipole transition moment for the $a^3\Sigma_g^+ - b^3\Sigma_u^+$ transition.

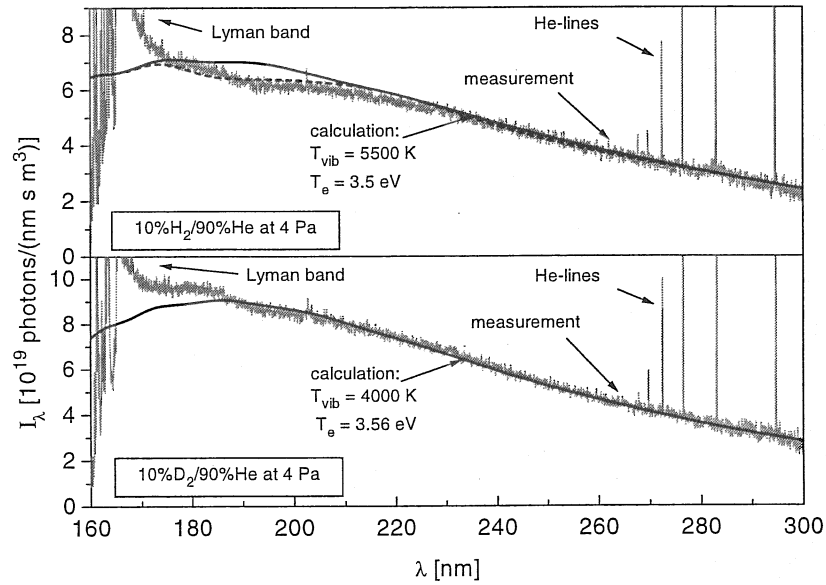


Figure 5.26: Continuum spectra of H₂ and D₂ at 4 Pa in the ECR discharge. Measurements are compared with results from calculations by using the fit parameters $T_{vib}(X)$ and T_e .

the shape of the continuum radiation reflects the vibrational population of the upper state ($a^3\Sigma_g^+$), which can be related to T_{vib} in the ground state. Figure 5.26 shows examples for measured and calculated spectra in ECR plasmas. The agreement is very good in the wavelength range between 210 and 300 nm by

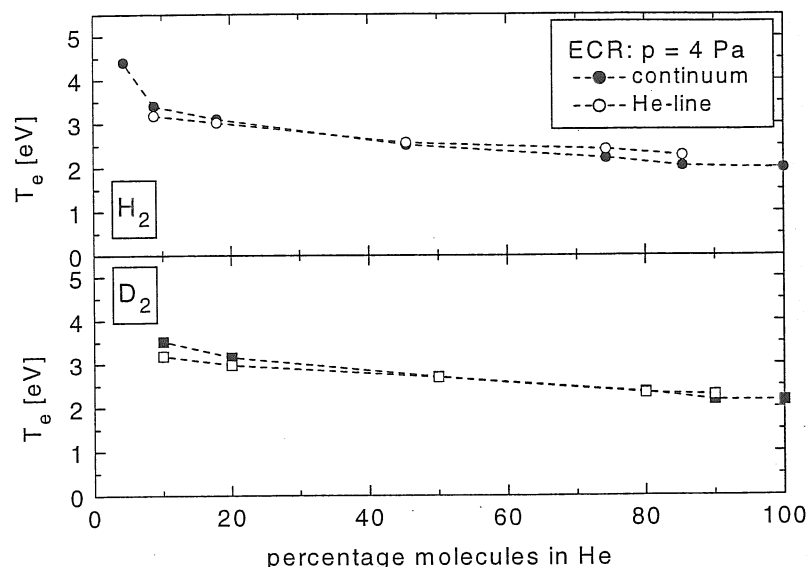


Figure 5.27: Electron temperatures derived from the continuum spectra in various H_2/He and D_2/He ECR plasmas at 4 Pa compared with results from the radiation of the He_{728} line.

using $T_{vib} = 5500\text{ K}$, $T_e = 3.5\text{ eV}$ for H_2 and $T_{vib} = 4000\text{ K}$, $T_e = 3.56\text{ eV}$ for D_2 . The sensitivity is estimated to be 500 K for lower T_{vib} and increases to 1000 K for higher T_{vib} . The deviation in the shape at lower wavelengths is about 15% of the radiation and has various reasons: the radiation of the Lyman band, which has a maximum at 162 nm, is ten times higher than the continuum radiation. In addition, the Lyman band continuum, caused by the transition of the $v' = 9$ level of the $B^1\Sigma_u^+$ state into the dissociation limit, contributes to the radiation near 170 nm. Therefore, the measurements show an increase rather than a decrease. In the case of hydrogen, the radiation of the measured spectrum around 200 nm is lower than the spectrum predicted by the calculation. A detailed analysis of the individual vibrational levels of the upper state has shown that this enhancement is correlated with radiation from $v'(a^3\Sigma_g^+) = 2$. The population of this level was reduced by the small amount of 15%. The resulting spectrum is given by the dashed line in the measured hydrogen spectrum. This demonstrates the sensitivity of the method.

For the determination of T_e from the continuum radiation, the measured absolute radiation was correlated with calculations using T_e as a parameter and applying the adjusted T_{vib} . The integral of the fitted spectrum over the whole wavelength range gives the total radiation of the transition. It turns out that nearly 50% of the radiation is either below 190 nm (30%) or above 300 nm (20%) for the whole parameter range. These values are valid within 5% for both hydrogen and deuterium and they can be used generally for the determination of the total radiation, if only the part between 190–300 nm is measured. The results for hydrogen and deuterium mixtures in helium are shown in Fig. 5.27. The electron

temperature decreases with increasing amount of molecules and is very similar in H_2 and D_2 plasmas. For comparison, T_e derived from the standard diagnostic method (He 728 nm line) is also plotted in Fig. 5.27. The good agreement between both methods validates the applicability of the continuum radiation as a diagnostic tool for T_{vib} and T_e in hydrogen and deuterium plasmas. Since calculations were carried out for all isotopes, i.e. T_2 , HD and DT, the method can be applied for these molecules as well, which is of particular interest in divertors of fusion experiments.

5.2.8 Formation of HD molecules

In future fusion experiments the plasma composition will always be a mixture of deuterium and tritium. In present-day experiments hydrogen or deuterium discharges are commonly used for investigations. During a changeover from hydrogen to deuterium discharges (or the other way around), mixtures of these molecules are present. Therefore, in cold plasma regions HD or DT molecules will be formed. The formation of HD can be investigated in laboratory plasmas. Furthermore, the spectroscopic diagnostic methods of molecules will be extended to HD in order to check the transferability to these heteronuclear molecules.

Figure 5.28 shows a fraction of the Fulcher spectrum in a ECR discharge containing 50% H_2 /50% D_2 . The first four rotational lines of the Q -branch in the $v' = v'' = 0$ band are indicated for H_2 and D_2 as well as for HD, which is between those of H_2 and D_2 . The lines of HD are clearly identifiable and it is obvious that the intensity alternation vanishes for the heteronuclear molecule. In Fig. 5.28b, mass spectra obtained with the residual gas analyser are given at three discharge pressures, normalized to the H_2 signal. With increasing pressure the HD signal increases, which means that in spite of a decrease in T_e more HD is produced. This emphasizes the role of heavy particle collisions in the HD formation. Remarkable is the lower D_2 than H_2 signal although same concentrations are used as inlet gas. This is either due to the demixing of gases in the plasma chamber or indicates a depletion of D_2 by dissociation.

Systematic measurements were carried out in mixtures with helium. However, mass spectrometer results are overlapped by the helium signal and are therefore not suited for the analysis. Molecular densities were obtained from the Fulcher spectra by using the same rate coefficient for all three isotopes. The atomic densities, i.e. the degree of dissociation, were taken from the analysis of the H_α and D_α lines. It turned out that at equal molecular concentrations of the inlet gases, the atomic densities in the plasmas of H and D differ. Therefore, concentrations were chosen in which equal atomic densities were obtained in the plasma. The percentage of HD molecules to the sum of molecules in the plasma is plotted in Fig. 5.29 as a function of the degree of dissociation. The gas mixtures at 10 Pa are labelled, the background gas was helium. The HD density increases with the degree of dissociation and a maximum concentration of 50%HD molecules in the plasma is achieved. The more helium is in the plasma, the higher is T_e and the higher is the degree of dissociation and the density of H and D atoms which can

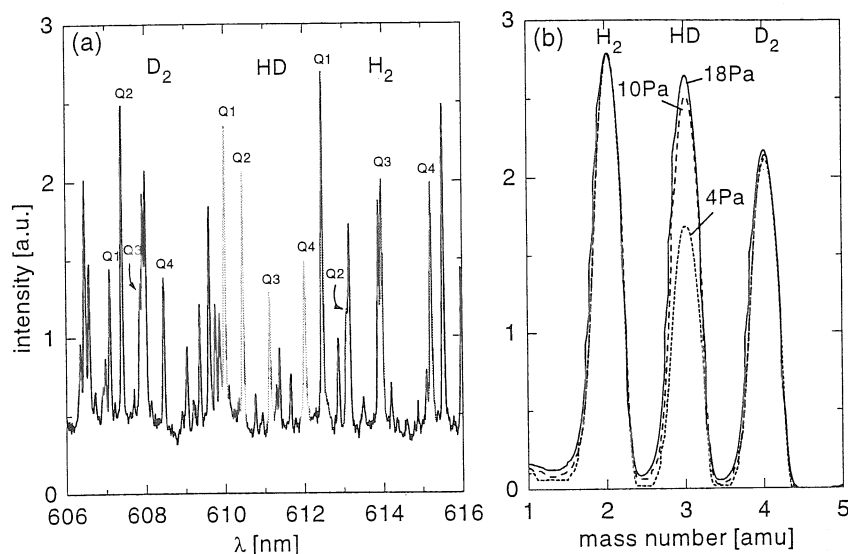


Figure 5.28: Fulcher spectrum (a) in a 50% H_2 /50% D_2 ECR discharge ($p = 20$ Pa) in which the most prominent lines of the H_2 , D_2 and HD molecules are indicated. Mass spectra (b) of the same discharge at various pressures.

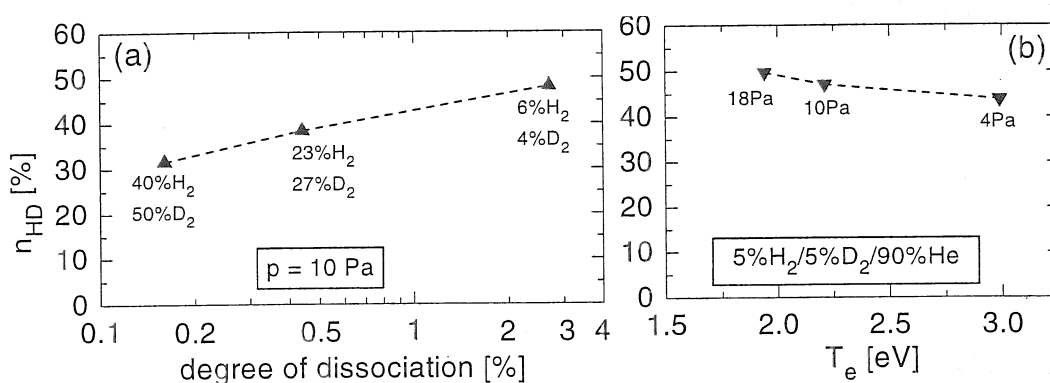


Figure 5.29: Percentages of HD produced in H_2/D_2 plasmas depending on mixture and, therefore, degree of dissociation (a) and T_e (b) which is achieved by a variation of pressure.

then in the next step recombine to HD molecules. Thus gives the dependence on pressure as already shown in Fig. 5.28b but is also given in Fig. 5.29b. In addition, recombination of atoms at surfaces, i.e. the chamber walls, may play an important role in the formation of HD molecules.

In heteronuclear molecules transitions between vibrational and rotational states are optically allowed since they have a permanent dipole moment, but in the case of isotopes these transitions are weak. Therefore, the vibrational population in the ground state of the HD molecule in comparison to the H_2 and the D_2 molecule is an interesting point of discussion. $T_{vib}(X)$ of all three molecules was derived from the Fulcher band in a mixture with high HD formation, i.e.

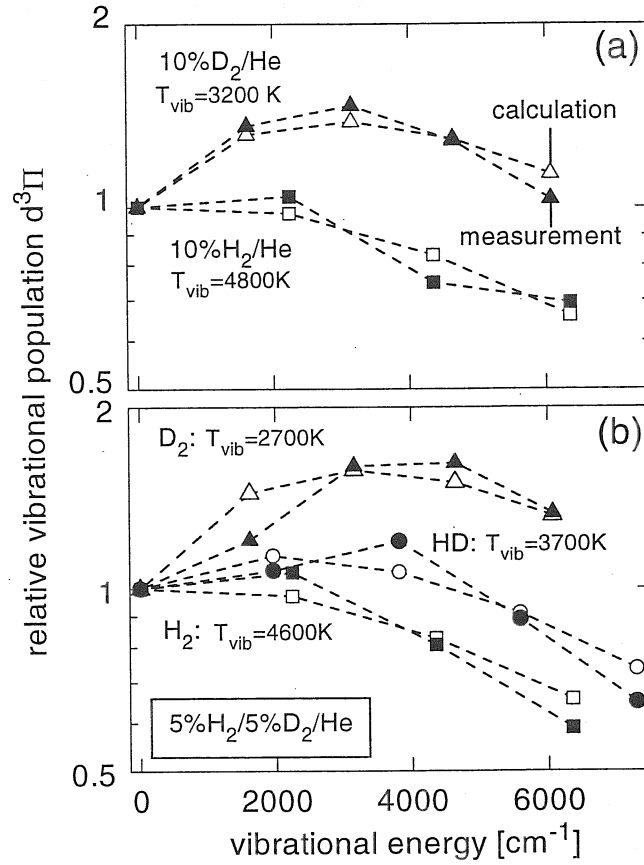


Figure 5.30: Vibrational populations of H_2 and D_2 in a H_2/He and D_2/He discharge (a). Part (b) shows results obtained in a mixture. Open symbols refer to calculations with the best fit to measurements (filled symbols).

5% $\text{H}_2/5\%\text{D}_2/90\%\text{He}$ at 4 Pa. The measured relative vibrational populations in the upper Fulcher state are compared with calculations where $T_{\text{vib}}(X)$ is the fit parameter. First of all, Fig. 5.30a shows calculated and measured populations in mixtures with helium separately. The molecular concentration was kept constant to ensure similar T_e . The agreement between calculations and measurements is good for all five upper vibrational levels. The D_2 plasma yields a lower $T_{\text{vib}}(X)$ (3200 K) than the H_2 plasma (4800 K). In the mixture (Fig. 5.30b) the $v' = 1$ value of D_2 is not mirrored by the calculation, whereas for H_2 only small deviations are obtained. HD populations are disturbed in $v' = 2$ and $v' = 4$. This indicates repopulation among the molecules themselves. $T_{\text{vib}}(X)$ of D_2 and H_2 are slightly smaller in the molecular mixture than in pure plasmas of H_2 and D_2 . As expected from the isotope effect (i.e. the influence of the distance of the vibrational energy levels), $T_{\text{vib}}(X)$ of HD is between those of D_2 and H_2 . In summary, the applicability of the spectroscopic methods for heteronuclear isotopes of hydrogen was demonstrated, at the example of HD , providing a diagnostics tool for DT molecules.

5.3 Divertor plasmas

Diagnostics in divertor plasmas need a higher effort than diagnostics in laboratory plasmas since on one hand the plasma is inhomogeneous along a line of sight and on the other hand the plasma can change the recycling regime from an attached to a completely detached plasma. In the latter case the plasma parameter like the electron density varies two or three orders of magnitude whereas the electron temperature ranges from some ten eV to below 1 eV. This requires either a diagnostic method with a high dynamic range or different diagnostic methods which complete each other. Using emission spectroscopy, interpretation of line radiation and population mechanism of an electronic state, depends on the plasma regime, i.e. an ionizing plasma in the attached case or a recombining plasma in the completely detached regime. Furthermore, the inhomogeneity of the plasma along the line of sight results in a selective weighting of plasma regions.

Besides the radiation from hydrogen, the radiation of impurities originating from the plasma wall interaction, can be detected and used for diagnostics. Depending on the wall material, which is in most cases carbon (graphite), line radiation (CI-CVI) and molecular bands (CH, CD) are observed.

In general, the concept of determining particle densities from the line radiation has to be replaced by the determination of particle fluxes. Concerning hydrogen, atomic hydrogen fluxes or proton fluxes will exceed the molecular hydrogen fluxes, a situation which is completely different from parameters of technical plasmas. This has to be kept in mind when comparing these two types of low temperature plasmas.

5.3.1 Atomic hydrogen fluxes from S/XB

The radiation of the Balmer lines is used to determine atomic hydrogen fluxes. Provided that the neutral particles, which start at the surfaces, are excited and ionized by electron impact collisions during their way through the plasma, the ionization processes per emitted photon relate the measured photon flux with the atomic hydrogen flux, e.g. for H_α :

$$\Gamma_H = \frac{S}{XB} \Gamma_{H_\alpha} . \quad (5.13)$$

S is the effective rate coefficient for ionization, XB is the effective emission rate coefficient for the H_α line. The principal method and its applications are described in [BSD⁺89]. The ratio S/XB can be taken from calculations which are usually carried out with CR-models. Like the effective rate coefficient itself, the ratio depends on n_e , T_e and, if relevant, on recombination, opacity or dissociative excitation from molecules.

Figure 5.31 shows the dependence of S/XB for H_α on T_e and n_e for direct excitation, i.e. excitation of the atom, and dissociative excitation, i.e. H_α radiation originates only from dissociation of the molecule. In the latter case, the ionization of the molecule was considered because of the assumption that molecules start

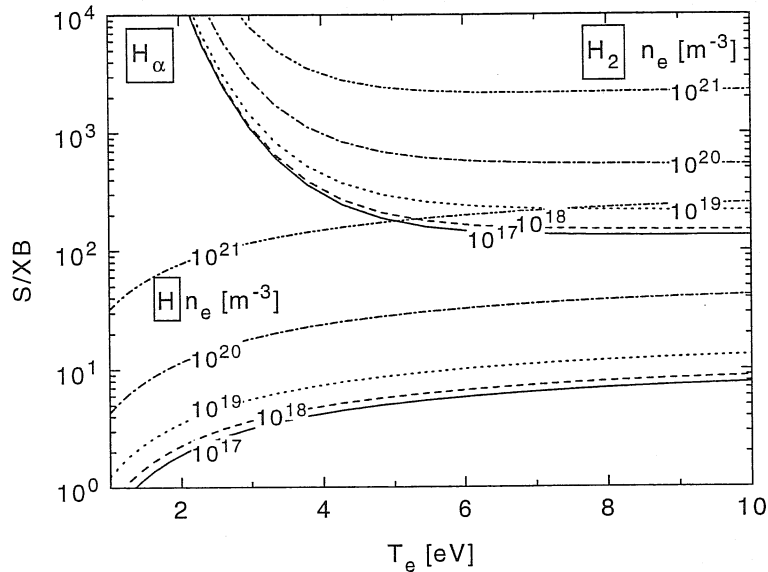


Figure 5.31: Ionization processes per emitted H_α photon for atomic and molecular hydrogen.

at the surface and are excited and ionized in the plasma whereby the excited states dissociate directly in the $n = 3$ state of the H atom. For the calculations the modified CR-model for H_2 and H was used (Sec. 5.1). At $T_e \gtrsim 5$ eV the temperature dependence vanishes whereas the n_e dependence is distinctive for $n_e \gtrsim 10^{19} \text{ m}^{-3}$. This means that the electron density is a crucial parameter in the diagnostics as well as the knowledge of T_e in cold, detached plasmas ($T_e < 5$ eV). In addition, the neutral particle density increases in this plasma regime and opacity becomes important as well as recombination. As discussed for technical plasmas, it is helpful to measure more than one Balmer line since the influence of opacity and recombination is different for each Balmer line.

5.3.2 Balmer line ratios

Balmer line ratios can be used as diagnostics for electron density and for the ratio of atoms to molecules, i.e. the degree of dissociation, as suggested by Fujimoto [FMS88, FST89, SEF93]. Dependencies of the ratios on T_e , n_e and δ are shown in Fig. 5.32 which were calculated with the modified version of Fujimoto's CR-model. The best sensitivity on n_e provides the H_δ/H_α ratio in the range of $10^{17} - 10^{20} \text{ m}^{-3}$. The variation with T_e is shown for excitation out of the atom (Fig. 5.32a) and the variation with the degree of dissociation is given in Fig. 5.32b for $T_e = 5$ eV. This diagnostics is suggested to be applied for ionizing plasmas since opacity and strong recombination is not taken into account in the presented ratios. This restriction does not affect the method, because the ratios are only sensitive for densities of $n_e \lesssim 10^{20} \text{ m}^{-3}$, which are typical for ionizing plasmas.

The Balmer line ratio is utilized as an indicator for detachment since the

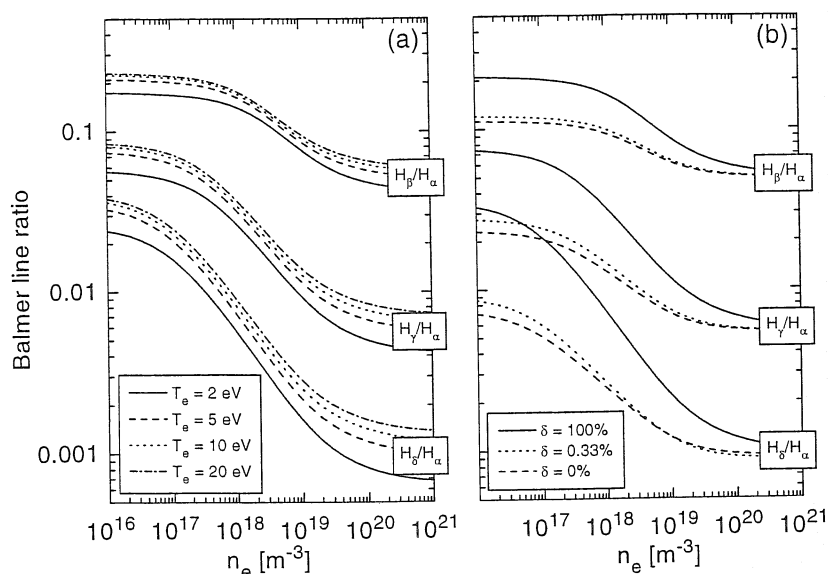


Figure 5.32: Balmer line ratios for various T_e in case of direct excitation (a) and variation of δ in case of direct and molecular excitation (b) at $T_e = 5$ eV.

ratio depends on the degree of recombination. Part (a) of Fig. 5.33 gives the line ratios taken from the ADAS code package for three different recombination factors. A recombination factor of zero refers to no recombination (three-body and radiative recombination) at all. Taking into account recombination processes the ratios decreases for low T_e . Again the best sensitivity can be found for H_α/H_γ . In Fig. 5.33b measurements of Balmer line ratios during a hydrogen discharge are presented. The time interval of detachment is 3.2 – 3.6 s, as indicated by arrows. Before and after this interval the plasma is in an attached regime. The fluctuation of the measured signals is due to the usage of two spectrometers to observe all four Balmer lines in two identical discharges simultaneously. This is caused by the demand of having exactly the same discharge and to take the same time interval for the evaluation. Furthermore, the error bars of two intensity calibrations contribute to the noise of the ratios. Additionally, neighbouring lines of sight were used, i.e. ROV007, ROV006 and ROV008 (Fig. 2.11). Nevertheless, the rapid decrease of intensity ratios in the detached time interval is evident.

Comparing absolute intensity ratios with predictions from ADAS, the measurements seem to be too high in the ionizing, i.e. the attached, regime. Therefore, ratios calculated with Fujimoto's code (Fuji) in the modified version and the code of Johnson and Hinnov (J&H) [JH73] are included in Fig. 5.33a. It is obvious, that results from Johnson and Hinnov are almost identical with ratios from Fujimoto's code. This is due to the implementation of almost the same input data in the CR-models. In comparison with ADAS they yield higher intensity ratios. Unfortunately, it is not obvious on the basis of these measurements which are the proper calculations. However, it has to be kept in mind that measurements carried out in technical plasmas have validated results for Balmer lines

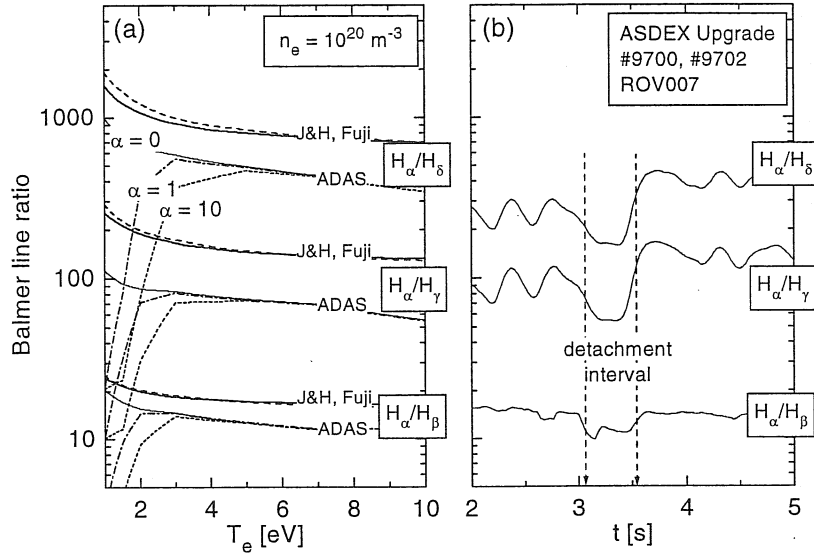


Figure 5.33: Balmer line ratios calculated with different CR-models. In case of ADAS calculations the variation due to the recombination factor α is shown in (a). Part (b) shows measurements depending on the time of the discharge, i.e. recycling regime.

from ADAS. Details of Balmer line measurements, their applications and results for the divertor of ASDEX Upgrade are given in [Sch00b].

5.3.3 Molecular fluxes from $(S + D)/XB$

In a similar manner as the determination of atomic hydrogen fluxes works, molecular fluxes are obtained from the radiation of molecular bands. In addition to ionization processes, the dissociation processes have to be considered for molecules. Furthermore, vibrational population in the ground state enhances ionization and dissociation rates and has to be considered as well. The molecular flux is then given by:

$$\Gamma_{H_2} = \frac{S_{eff} + D_{eff}}{XB} \Gamma_{Fulcher}, \quad (5.14)$$

using the radiation of the Fulcher system. XB is the effective emission rate coefficient of the complete Fulcher system, S_{eff} and D_{eff} are effective ionization and dissociation rate coefficients of the hydrogen molecule, respectively. The $(S + D)/XB$ ratio was calculated with the modified CR-model and is shown in Fig. 5.34 as a function of T_e and n_e as parameter. Just as for atomic hydrogen, the ratio is almost constant for $T_e \gtrsim 5$ eV, whereas a strong n_e dependence is obtained. As discussed in Secs. 5.1.2 and 5.1 this is correlated with the beginning of a Boltzmann population between the excited states. In this case the $(S + D)/XB$ ratio is proportional to n_e . For $n_e = 10^{20} \text{ m}^{-3}$, the ratio is also calculated by neglecting vibrational population. This leads to a strong decrease at low

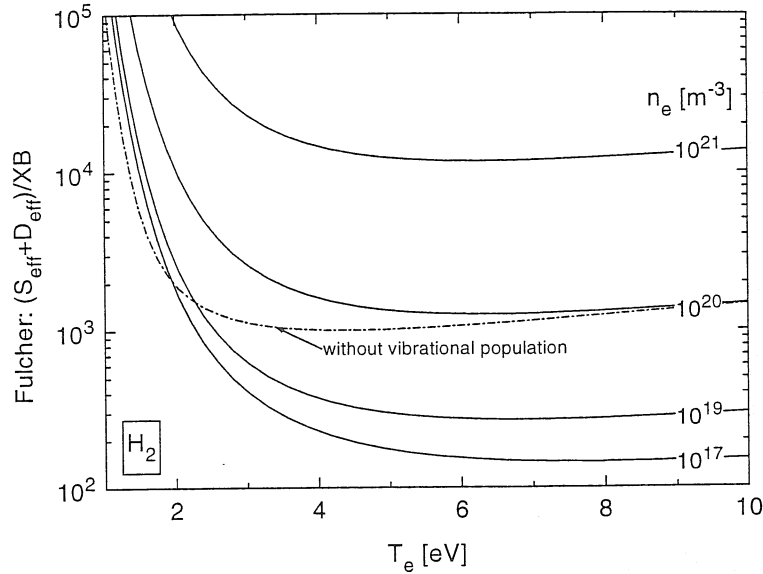


Figure 5.34: Effective ionization and dissociation processes per emitted Fulcher photon calculated with the modified CR-model.

temperature and is mainly caused by the influence of vibrational population on the effective ionization rate coefficient. At low temperatures the ion conversion process (Eq. (5.3)) becomes efficient, if vibrational levels are populated. Due to different vibrational energies and vibrational populations, $(S + D)/XB$ ratios for D_2 are different from ratios for H_2 , whereas for H and D the S/XB ratios are equal.

In the majority of the cases, molecules fluxes can be determined in the temperature range of $1\text{ eV} \lesssim T_e \lesssim 20\text{ eV}$. On one hand the molecules rather dissociate or ionize than radiate at temperatures considerable higher than the threshold of dissociation ($\approx 8\text{ eV}$) and ionization ($\approx 15\text{ eV}$). On the other hand, at very low temperatures $T_e < 1\text{ eV}$, the excitation process is ineffective which results in a weak radiation of the molecule. The strong dependence on the parameters in this T_e -range requires the knowledge of T_e and n_e as accurate as possible to analyse measured photon fluxes.

Measurements of Fulcher photon fluxes were carried out in two identical hydrogen discharges of ASDEX Upgrade [FBG⁺99]. The discharges were characterized by a variation of neutral injection power and midplane electron density during the time of the discharge. The precise parameters are given in [GBC⁺99]. Of special interest for the present discussion is the transition of the plasma recycling in the outer divertor from an attached to a detached recycling regime followed by a re-attachment. Therefore, the electron density first increases and then decreases, whereas the electron temperature shows the opposite behaviour. These plasma parameters were measured by Langmuir probes and by emission spectroscopy of the Paschen/Balmer continuum. As a sensitive indicator of detachment or attachment the CIII and the H_α line intensities were recorded [GBC⁺99]. The former

decreases with decreasing T_e , whereas the latter increases due to strong volume recombination in detached plasmas. The emission lines of the Fulcher bands of the hydrogen molecule were detected by using a 1 m spectrometer with a CCD camera as detector. Within each discharge a wavelength range of about 7.5 nm was covered, which provides sufficient spectral resolution for separating the rotational lines. Two identical discharges were necessary to measure the $v' = 0 - v'' = 0$ and the $1 - 1$ vibrational transition. Four lines of sight in the outer divertor have been used (ZOV001, ROV018, ROV014, ROV011, Fig. 2.11). The method for evaluating the radiation of the whole band from the two measured vibrational transitions is described in detail in [FBG⁺99].

As an intermediate result from the evaluation of measured vibrational bands the rotational temperatures in the excited state ($d^3\Pi_u$) were obtained using a Boltzmann-plot for the first five rotational quantum numbers of the Q -branch. $T_{rot}(d)$ derived from each vibrational band was then transferred to the ground state yielding $T_{rot}(X)$. The time dependence of $T_{rot}(X)$ is plotted in Fig. 5.35a. The $0 - 0$ vibrational transition gives a higher T_{rot} than the $1 - 1$ transition. This fact was already observed in technical plasmas (Fig. 5.22). The various lines of sight show almost identical results, an increase with time at the beginning which is followed by a decrease. It has to be mentioned that measured intensities (with an integration time of the CCD camera of 100 ms) are time averaged values which represent a time interval of 500 ms. Thus, the signal-to-noise ratio was improved.

In a next step, the ratio of vibrational population ($v' = 1/v' = 0$) in the excited state was obtained which was assigned to a vibrational temperature in the ground state (Fig. 5.20). $T_{vib}(X)$, shown in Fig. 5.35b, is high (around 8000 K) in the time range 2.5–3.5 s and decreases to values of 3000 K. The error bar is ± 500 K. To give numbers of populations a $T_{vib}(X)$ of 5000 K represents a population of 71%, 20%, 6% and 2% for the levels $v = 0, 1, 2$, and 3, respectively.

Since the plasma changes the recycling regime during the time of the discharge and since Langmuir probes yield an electron temperature and density dependence, the changes of $T_{vib}(X)$ can be correlated to T_e . A correlation with n_e can be neglected in a first approximation due to a stronger dependence of the population and depopulation processes of vibrational levels on T_e than on n_e . Thus, the molecular bands themselves offer a convenient possibility to measure electron temperatures (Sec. 5.3.4), which must be known for the analysis of molecular fluxes.

Figure 5.35c gives molecular fluxes using T_e from the molecular radiation itself and n_e from the Langmuir probes (in the attached time interval) and from the analysis of the Paschen/Balmer continuum (in the detached regime). The fluxes show a pronounced increase during the time of detachment (3.2–3.6 s). In the raw signals, this increase is partly masked by the fact that $(S_{eff} + D_{eff})/XB$ also increases due to lower electron temperatures. The atomic hydrogen fluxes, as derived from H_β intensities or Langmuir probe saturation currents, show a very similar behaviour with time. A typical ratio of molecular-to-atomic particle fluxes of 0.5 was obtained by the B2-EIRENE calculations [SBC⁺99, CBSA99]. A density scan was simulated and the molecular flux is expected to be between

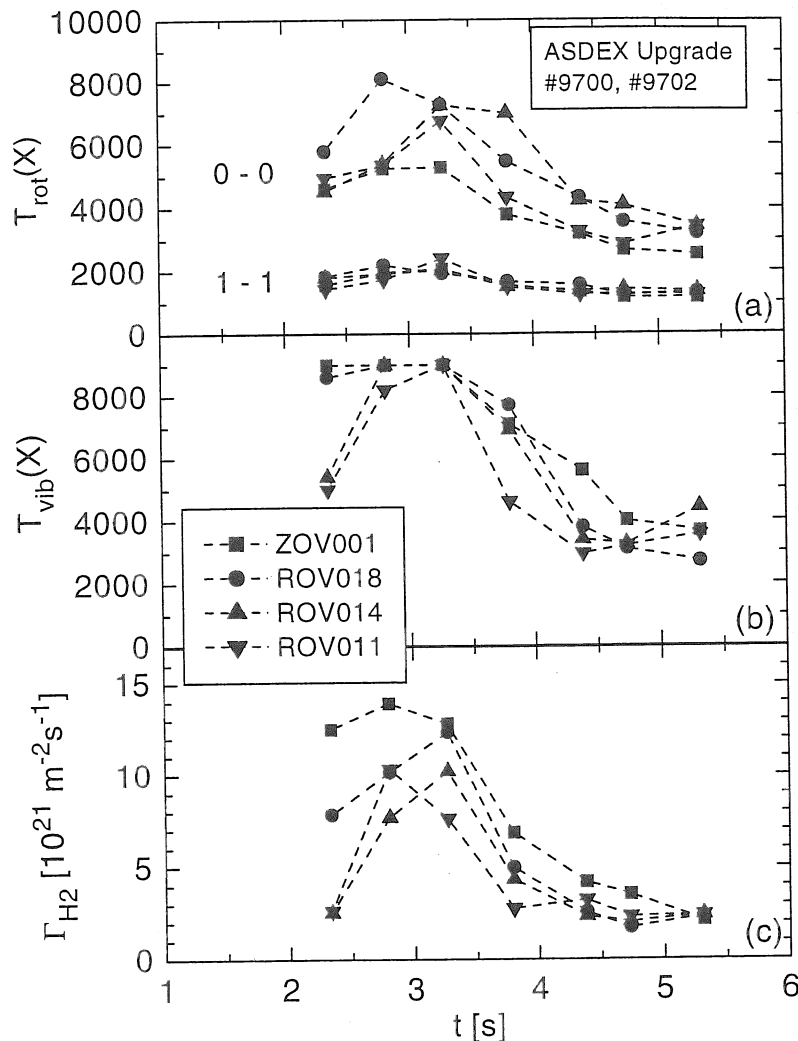


Figure 5.35: Measured rotational and vibrational population temperatures in the ground state of H_2 ((a) and (b)) as well as molecular fluxes (c) depending on the time of the discharge.

$1 - 4 \times 10^{22} \text{ m}^{-2} \text{ s}^{-1}$ depending on discharge time. As can be seen in Fig. 5.35c, measured absolute values are about a factor 5 lower than expected. This discrepancy may still be within the error bars of the method, the measurements and the calculations, where the latter are carried out for typical discharges and not for the individual discharges in question. In addition, vibrationally excited hydrogen molecules were not included in the B2-EIRENE code at the time of running the code. Nevertheless, it can be concluded that molecular fluxes are comparable to atomic fluxes in detached plasmas. Furthermore, the hydrogen molecules have a high vibrational population in the ground state, which may affect plasma kinetics in the divertor.

5.3.4 Electron temperature diagnostics using molecular radiation

The radiation of hydrogen molecules can be used for electron temperature diagnostics of divertor plasmas [FHW01]. The modified CR-model (Sec. 5.1) provides a correlation between the vibrational population in the ground state of H_2 or D_2 and the electron temperature. The ground state population is transferred into a vibrational population of the electronically excited state ($d^3\Pi_u$) which is easily accessible by emission spectroscopy of the Fulcher transition. In contrast to the diagnostic method introduced in Sec. 5.2.6 the assignment of a vibrational temperature for the first five vibrational levels is no longer necessary due to the predictions of the CR-model considering all 15 vibrational levels. As discussed in Sec. 5.1 this requires the assumption that population and depopulation processes are dominated by electron collisions and radiative decay, i.e. heavy particle and wall collisions are negligible.

Figure 5.36a shows the predicted relative vibrational population for a characteristic electron temperature ($T_e = 4$ eV) depending on the population processes (Sec. 5.1). Considering reactions (5.1) to (5.4) (indicated as (1)-(4) in the figure) the population decreases rapidly with increasing vibrational quantum number, e.g. $v = 4$ is approx. 1 % of $v = 0$. Since the data points are almost on a straight line in the logarithmic scale, the slope describes a vibrational temperature which is around 6200 K. Switching on the repopulating reaction (5.5) (labelled with (1)-(5)), higher vibrational levels show a population of nearly 4 % from $v = 4$ onwards. The lower levels are shifted to somewhat higher populations too. By changing the input data for reaction (5.2), i.e. dissociation, from Celiberto data [CLC+99] (labelled (2a)) to Tennyson data [ST98] (labelled (2b)) the calculations yield lower populations in the higher vibrational states (factor 2), as expected. However, R-matrix calculations were not available for the deuterium molecule. Therefore, in the modified version of the CR-model, data of Celiberto [CLC+99] were implemented as standard for both isotopes.

In order to demonstrate an influence of heavy particle collisions and wall collisions, which are important for technical plasmas but negligible for divertor plasmas, the populations considering reactions (5.1) to (5.7) are also presented in Fig. 5.36a ((1)-(7)). Here, the vibrational population is considerably lower and depends no longer only on T_e but also on n_{H_2} , pressure and gas temperature. The influence of T_e on the population is getting smaller. The data implemented in the modified version of the CR-model for H_2 and D_2 and the applied extrapolations are described in detail in [WF01, FHW01].

Part (b) of Fig. 5.36 shows the dependence of the relative vibrational population in the ground state for H_2 and D_2 on electron temperature for reactions (5.1) – (5.5), i.e. divertor plasma conditions. With increasing T_e the populations for the lower v 's do no longer decrease exponentially with increasing vibrational energy and the populations for $v > 4$ increase drastically. This is caused by the strong influence of reaction (5.5) since the excitation of the $B^1\Sigma_u^+$ and $C^1\Pi_u$ states in the singlet system increases with rising T_e . Obviously, both isotopes

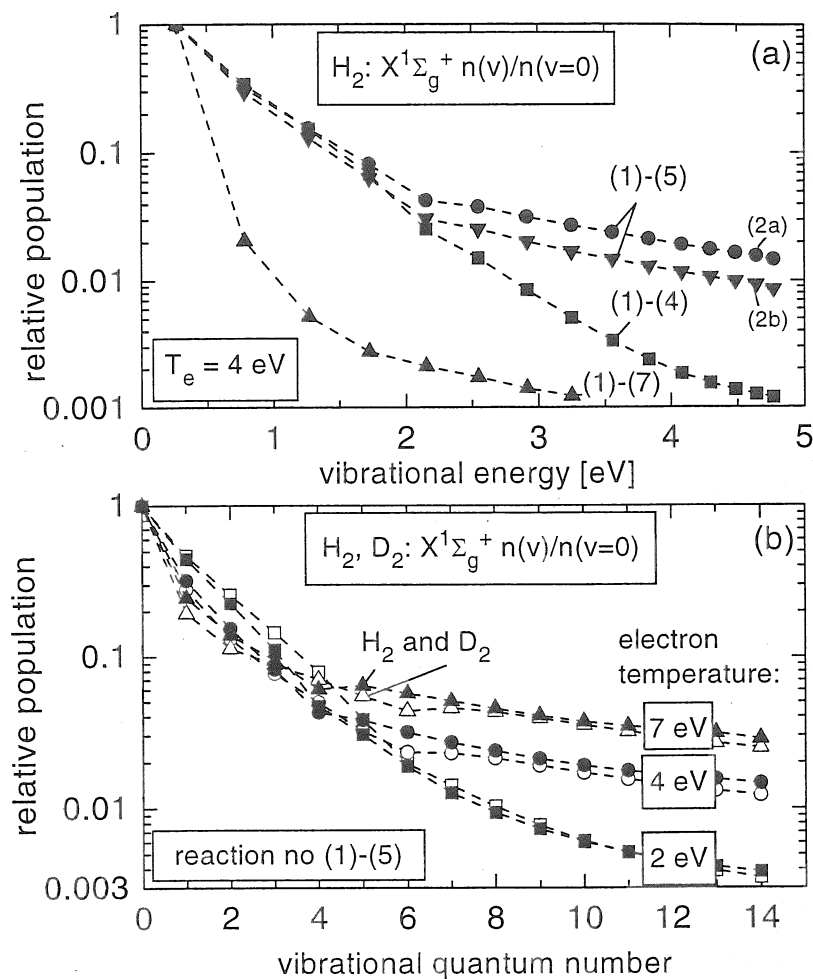


Figure 5.36: Calculated relative vibrational populations in the ground state taking into account different reactions (a). Part (b) gives a comparison of H_2 and D_2 at different T_e 's.

show almost equal vibrational populations which was already confirmed by measurements carried out in laboratory experiments [FH98]. The discussed isotope effect concerning the resonant character of reactions (5.3) and (5.4) appears in the slightly different populations around the levels $v = 4$ and $v = 6$ for H_2 and D_2 , respectively.

The predicted vibrational population in the ground state was projected into the electronically excited state in the same manner as already discussed in Sec. 5.2.6. Figure 5.37 gives the relative populations in the upper Fulcher state for both isotopes as a function of electron temperature and is represented by the ratios $v' = 1(2, 3)/v' = 0$. These ratios vary in the plotted temperature range within a factor of two. Particularly suited for T_e -diagnostics are the ratios $v' = 2/v' = 0$ and $v' = 3/v' = 0$. The influence of vibrationally resolved rate coefficients on the ratios can be estimated by comparing results with and without $X_v(T_e)$ shown in

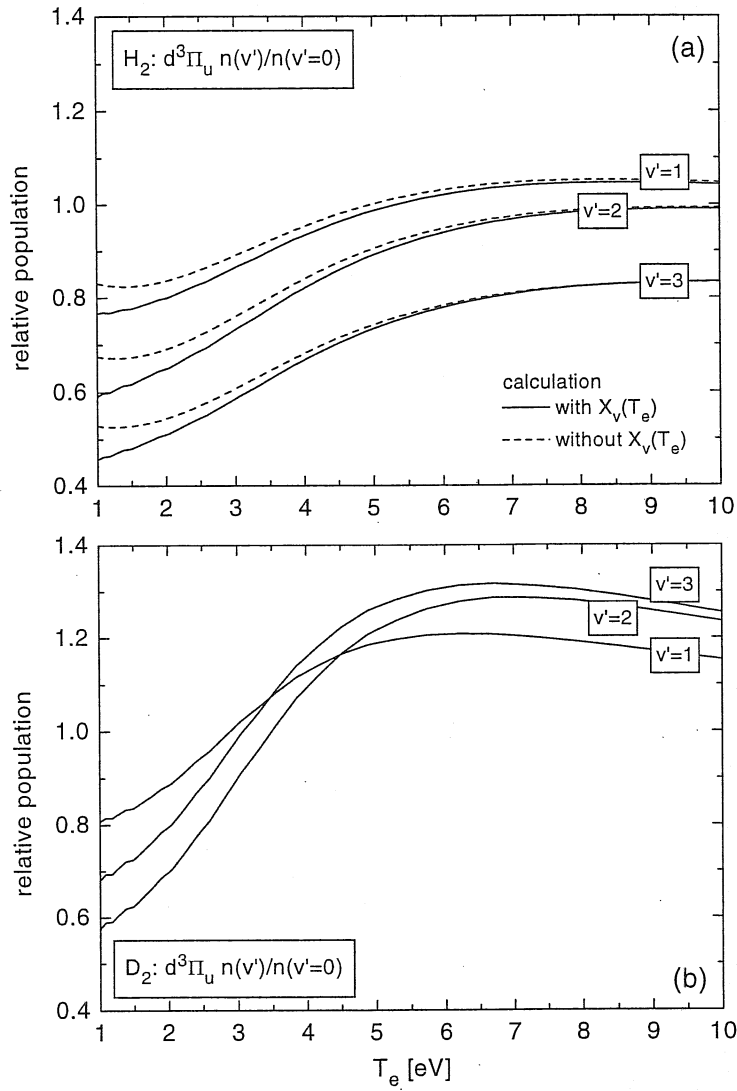


Figure 5.37: Calculated ratios of vibrational populations in the upper Fulcher state ($d^3\Pi_u$) and T_e for H_2 and D_2 .

Fig. 5.37a. The flat shape of the ratios above 7 eV is mainly caused by the strong influence of reaction (5.5). Deuterium ratios (5.37b) show a stronger dependence on T_e than hydrogen ratios, which is due to the different Franck–Condon matrices for the isotopes. In summary, the ratios can be used for diagnostics in the temperature range between 1 eV and 7 eV.

For a discussion of the influence of the electron density on this diagnostic method, the effect of reaction (5.5) must be specified. This is the only reaction which correlates the vibrational distribution in the ground state to bound electronically excited states. However, the absolute population as well as the vibrational population in these states can be influenced by other electronically excited states (cascading, electron impact de-excitation into the B, C states).

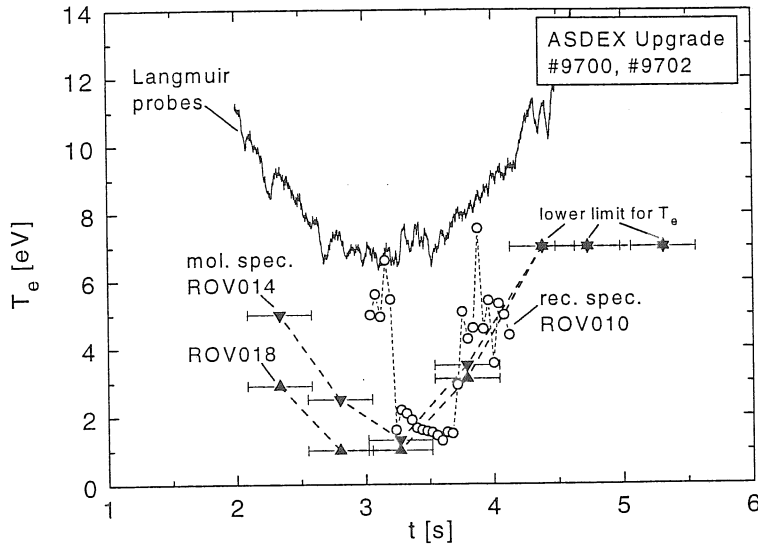


Figure 5.38: T_e measured in a hydrogen discharge by means of three diagnostic methods.

For a correct treatment of these processes all excited states involved have to be vibrationally resolved. Since this requires an enormous extension of the CR-model and, additionally, needs vibrationally resolved data, only the excitation from the ground state is considered. Together with the reasonable assumption of an H^+ density being equal to electron density (reaction (5.3)) the vibrational population in the ground state does not depend on electron density. However, it was estimated that the influence is considerable only at electron densities above $n_e \approx 10^{20} \text{ m}^{-3}$. In this case the higher vibrational levels of the ground state are depleted ($v > 5$) but only for electron temperatures higher than 4 eV. This results in a higher sensitivity of the projected upper Fulcher state population on electron temperature for $T_e > 4 \text{ eV}$ in comparison with Fig. 5.37. However, in typical divertor plasmas, high electron densities refer to low electron temperatures whereas low densities refer to higher temperatures. Therefore, the correlation presented in Fig. 5.37 is sufficient for the T_e -diagnostics in divertors.

The diagnostic method for T_e was applied in the pure hydrogen discharge already described in Sec. 5.3.3. Instead of assigning a vibrational temperature in the ground state (Fig. 5.35b) to measured relative populations in the excited state, T_e was determined. Figure 5.38 shows results for two lines of sight (ROV014 and ROV018). Measured temperatures decrease in the first three time intervals (averaged signals, 500 ms), which indicates the beginning detachment, and are around 1 eV in the completely detached outer divertor. Afterwards T_e increases due to a re-attachment of the plasma. The error bars are $\pm 0.2 \text{ eV}$ due to uncertainties in the measured ratios. However, after $t = 4 \text{ s}$ all measured ratios correspond to the upper sensitivity limit of the method which is 7 eV (Fig. 5.37). These points were therefore set to 7 eV in Fig. 5.38 which has the meaning of a lower limit for T_e . For comparison, results from Langmuir probes and recombination spec-

troscopy are shown also, referring to similar s-coordinates (Fig. 2.11) and lines of sight, respectively, as used for the molecular spectroscopy. All three diagnostics yield comparable dependencies of electron temperature on time. Probe measurements are more reliable at high temperatures and low electron densities and yield $T_e = 10 - 15 \text{ eV} \pm 2 \text{ eV}$ and $n_e \approx 4 \times 10^{19} \text{ m}^{-3}$ in the attached plasma. The recombination radiation, on the other hand, is only sensitive below $T_e \simeq 2 \text{ eV}$ and therefore reliable in the detached plasma only. In this case the temperatures derived are between 1 eV and 2 eV at electron densities around $n_e \approx 4 \times 10^{20} \text{ m}^{-3}$. As can be seen in Fig. 5.38, the molecular emission spectroscopy is sensitive in the range between these standard diagnostics. Absolute values are not expected to be identical since all three diagnostics refer to different weighting of plasma volumes along the same line of sight.

A second scenario of plasma discharges was started in order to confirm the method with results from the vibrational transition 2 – 2 of hydrogen and in order to test the transferability to deuterium. Therefore, some identical deuterium discharges were carried out, which included hydrogen injections in the outer divertor during two time intervals. This allows simultaneous measurements of H_2 and D_2 . The small amount of hydrogen (volume $\approx 1 \text{ cm}^3$) did not change the plasma performance in the divertor, just a local cooling of the plasma may arise. Due to increasing neutral particle injection and electron density the divertor plasma achieves a strong recycling regime. A detailed description of this scenario is given in [HFBA01]. For the present analysis, deuterium radiation was detected at three time intervals ($t_1 = 2.1 - 2.6 \text{ s}$; $t_2 = 3 - 4 \text{ s}$; $t_3 = 4.3 - 4.8 \text{ s}$) using the line of sight ZON003, which is equivalent to ZOV003 except being in another section of the torus. Hydrogen radiation was observed during the injection (t_1) at ZOV001–ZOV003. These lines of sight have a direct view onto the divertor valve, located in the outer divertor tiles. The four discharges allow recording of the first three vibrational transitions of hydrogen and four (up to 3 – 3) of deuterium. Particularly, the first six rotational lines of the Q-branch were investigated. Concerning deuterium, only three of the four measured vibrational transitions were suitable for diagnostics. The Q-lines of the 2 – 2 transition were obviously disturbed, showing strong fluctuations. Figure 5.39 displays the derived electron temperatures from molecular hydrogen and deuterium radiation.

As demonstrated in Fig. 5.37 each vibrational band ratio yields a different dependency on electron temperature. The temperatures derived from the separate ratios are in good agreement for hydrogen as well as for deuterium. In addition, Fig. 5.39 includes the T_e which fits best to the combination of the set of ratios. For hydrogen different temperatures were obtained for the various lines of sight, indicating the spatial variation of T_e . At t_1 hydrogen and deuterium give similar electron temperatures (between 4.3 eV and 3.6 eV). The assumed local plasma cooling due to the hydrogen injection is not visible. The time dependence of T_e is mirrored by the deuterium results. The recycling is getting stronger and the electron temperature decreases to 2.2 eV. This decrease is confirmed by Langmuir probes yielding mean electron temperatures of $12, 10$ and $7 \text{ eV} \pm 2 \text{ eV}$ for t_1, t_2 and t_3 , respectively. The difference in absolute values is based on the same

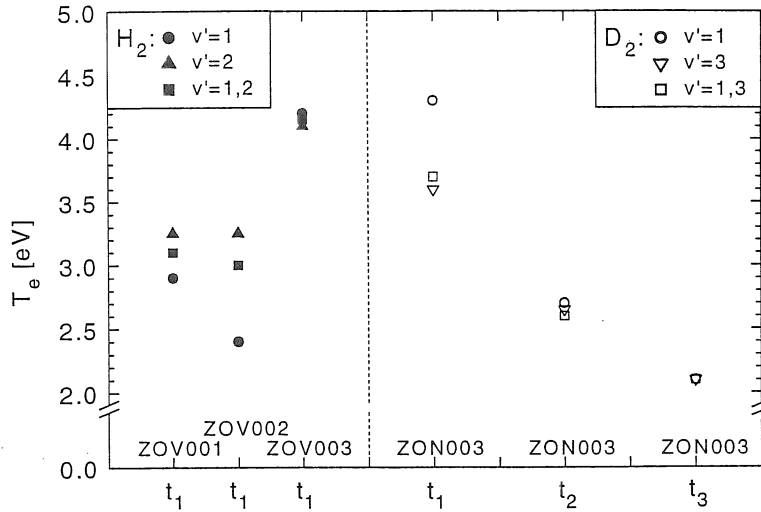


Figure 5.39: T_e derived from molecular radiation in deuterium discharges in ASDEX Upgrade (#12554-#12557). The discharges include hydrogen injections at time interval t_1 .

reasons as discussed above for the pure hydrogen discharge. In summary, the results prove the applicability of the diagnostic method for T_e using the radiation of molecular hydrogen and deuterium. The advantages are on one hand that the method is independent of the precise knowledge of n_e and on the other hand, this T_e must be used for the determination of molecular fluxes, since it represents T_e in the plasma volume, where the molecules are present.

Concerning the isotopes, the CR-model yields very similar vibrational populations in the ground state for hydrogen and deuterium which may also indicate possible extrapolations to tritium plasmas. In addition, mixtures of isotopes will lead to the formation of heteronuclear molecules (HD or DT) for which the presented method can be applied also.

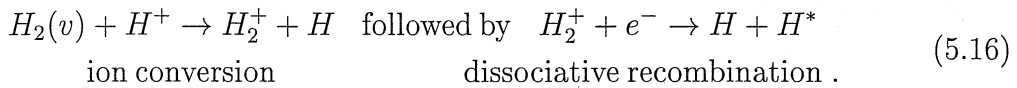
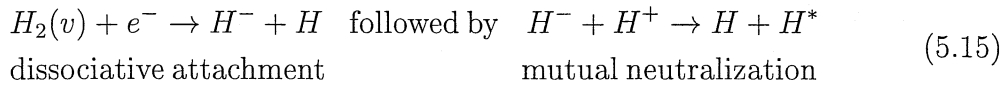
5.3.5 Molecular assisted recombination (MAR)

In order to reduce the power load onto the target plates detached divertor conditions are often preferred. Detached divertor plasmas are characterized by an increase in electron density and a decrease in electron temperature such that the plasma flux drops with increasing upstream density ("roll-over"). This is typically accompanied by a strong increase of volume recombination, i.e. three-body and radiative recombination. Due to the low T_e (0.5 – 5 eV) hydrogen molecules, which are produced at the surfaces by recombining atoms and ions, can penetrate into the plasma and may play a role in divertor dynamics. In particular, it was suggested, that molecules assist the volume recombination process.

The role of molecules in divertors was examined by a combination of experimental results (emission spectroscopy of molecules) with plasma edge simulations

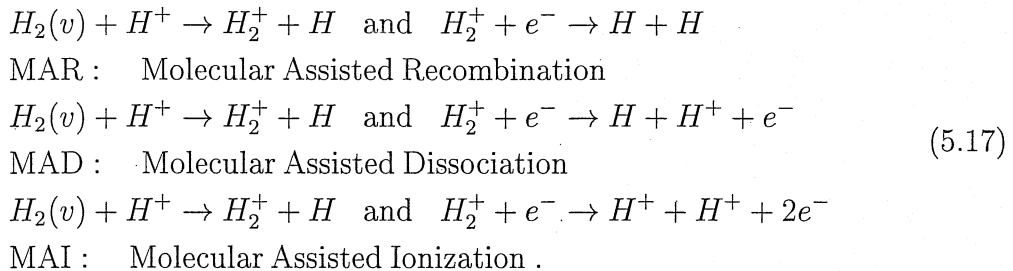
(B2-EIRENE) and the CR- model for H_2 [FBC⁺99, FRHC01].

Molecules can enhance the volume recombination in detached plasmas by the so-called molecular assisted recombination (MAR). Here, vibrationally excited molecules ($H_2(v)$, $D_2(v)$) contribute to plasma volume recombination due to the following chains of reactions:



In each channel an electron-ion pair recombines to H-atoms and the molecule is dissociated. Inspecting the rate coefficients for these reactions, the ion conversion channel (Eq. (5.16)) dominates over the negative ion channel (Eq. (5.15)) [RMBB97, KPSS97]. Under the assumption of radiative decay of all excited atoms the amplification of volume recombination was predicted to be in the range of a factor of 30 [KPSS97, ITE99]. However, considering both, re-ionization of the electronically excited state (H^*) and decay into the ground state, the recombination enhancement factor was found to be much smaller (factor 2 – 3) [RMBB97].

The possibilities of the excited atoms produced by Eq. (5.16) can be distinguished into three processes:



Only MAR contributes to the recombination, whereas in the other two cases ions are produced, which leads effectively to an increase of potential energy and is quite the opposite of the true volume recombination. In Fig. 5.40 a comparison of rate coefficients of MAR and MAD is presented with the electron density as parameter. Rate coefficients for MAI are considerably smaller and are therefore not included. MAD increases slightly with density and is always higher than MAR, which, in contrast, shows a steep decrease with higher electron densities. For detached plasma conditions, i.e. high electron density and low electron temperature, the two rate coefficients (and also the rates themselves) differ by 1 – 2 orders of magnitude. Besides the much smaller values of MAR with accounting for re-ionization of the excited fragments, it is more important that the very large MAD rate coefficient leads to a rapid destruction of H_2 , which is then no longer available for the MAR channel. In order to obtain rates for these processes the knowledge of hydrogen densities and vibrational populations are necessary. The

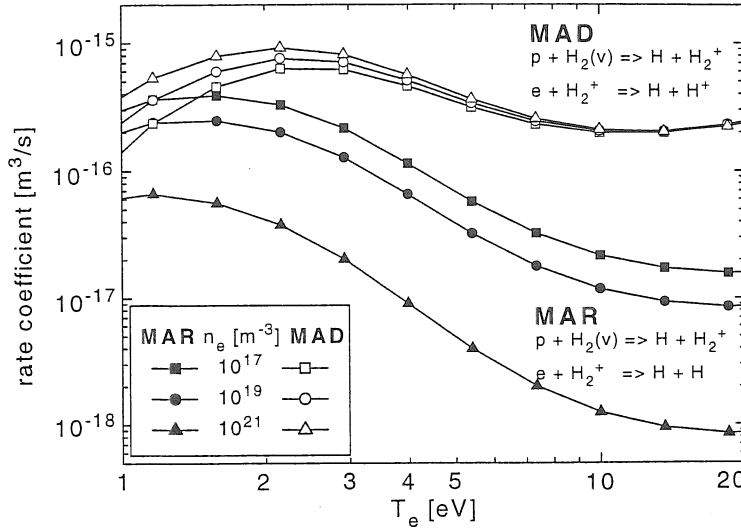


Figure 5.40: Rate coefficients for molecular assisted recombination (MAR) and dissociation (MAD) at various electron densities.

latter play an important role for ion conversion due to the resonance with the $v = 4$ level of hydrogen.

Investigations were carried out at the same hydrogen discharge where measured results were already available, i.e. results presented in Sec. 5.3.3 and Sec. 5.3.4. B2-EIRENE calculations were initially carried out for pure plasma conditions, where effects from impurities were taken into account only implicitly via the boundary conditions. However, the vibrational levels of H_2 are treated as distinct particles in the EIRENE code, a modification which was necessary as compared to earlier versions by an assessment of vibrational relaxation times vs. transport times under the relevant plasma conditions. In addition, effective rate coefficients from the CR-model for the electronically excited levels were used. With these modifications of the code line of sight integrated and spatially resolved results were obtained.

The total intensity of the Fulcher system, i.e. the measured Fulcher radiation, was compared directly with predictions. The relevant section of the computational domain of the code and the lines of sight used are shown in Fig. 2.11. On the basis of the consistent numerical solution of B2-EIRENE, e.g. n_{H_2} , n_e , T_e , line of sight integrated Fulcher photon fluxes were calculated and directly applicable to the experimental data. Using the experimental emission rate coefficient of [MH76] the calculated values of the Fulcher radiation were more than one order of magnitude (a factor 50) above the measured values [FBG⁺99]. This discrepancy vanishes by considering the steep n_e dependence of the Fulcher emission rate coefficient calculated with the CR-model (Fig. 5.7).

Figure 5.41 shows the satisfactory agreement between measured and calculated Fulcher photon fluxes for the detached time interval. In a next step, cal-

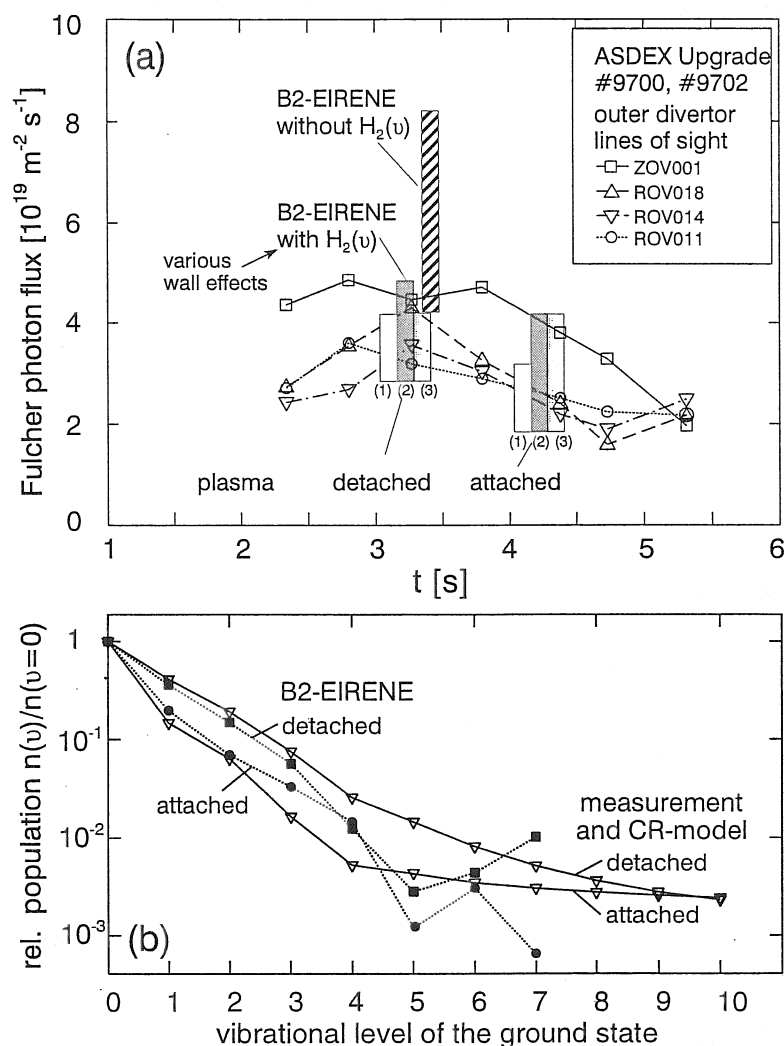


Figure 5.41: Comparison of measured and calculated Fulcher photon fluxes (a) as well as vibrational populations (b).

culations were performed accounting for vibrational states in H_2 by treating the vibrational levels as distinct particles. This leads to a reduction of the calculated flux of a factor of 2 – 3. Then a good agreement of measurements with calculations is observed in the detached and attached case. The three bars represent the influence of three different wall effects, i.e. atoms and ions recombine at the surface and form the molecule in its vibrational ground state (1), in $v = 2$ (2) and in a vibrational population characterized by $T_{vib}(X) = 3000 \text{ K}$ (3). This is described in detail in [FBC⁺99].

The lower part of Fig. 5.41 gives vibrational populations in the ground state of the molecule for the detached and the attached case. Here, again, good agreement between measurements and calculations is achieved. Both methods show higher populations in the detached plasma phase than in the attached plasma

phase. This indicates that vibrational population has to be taken into account in spectroscopic rate coefficients and in plasma edge simulations. The agreement between measurements and B2-EIRENE calculations may be taken as a first indication for a correct treatment of molecules in the code and especially for the validity of the collisional-radiative approximation for electronically excited states.

On the basis of the overall confirmation of calculations with measurements the contribution of molecules to volume recombination in detached divertor was calculated by using B2-EIRENE results. For this purpose, spatially resolved plasma parameters and rates, i.e. processes per volume and time, along a line of sight (ROV014) were analysed. Of special interest is the direct comparison of MAR, MAD and MAI with the three-body and radiative volume recombination rate R^{3+r} . The results are given in Fig. 5.42, where in the upper part of the figure the calculated densities n_e , n_{H_2} and n_H are shown together with the electron temperature which are necessary to form rates. The dependence of the molecular and atomic density is clearly correlated with the temperature shape. In the regions of low T_e and near the surface the molecule density dominates over the atomic density until the molecules dissociate, leading to a strong decrease of n_{H_2} further inward. The atomic density is more stable due to the gain from the molecules until ionization occurs. The comparison of rates is shown in the lower part of Fig. 5.42. The three-body and radiative recombination rate is nearly constant along the plasma volume whereas MAD and MAR strongly decrease away from the divertor walls. This is due to the combination of high electron temperature and low molecular density. The process of MAD dominates the molecular reaction chains. This clearly confirms the picture that the molecules dissociate (MAD) and ionize (MAI) before they have a chance to contribute to recombination (MAR). Only in a very thin layer close to the walls molecules contribute to the plasma recombination. The effect in the plasma volume is more or less an effect of a few ten percent. Instead of the predicted contribution of molecules to recombination the molecules dissociate and "assist ionization".

The increase of dissociation and ionization due to MAD and MAI, reduces the ionization length of the particles. As a consequence, the potential energy stored in the divertor plasma increases, the plasma re-attaches. This conclusion was derived from a comparison of B2-EIRENE runs with and without full (vibrational) treatment of the molecules. Starting point was a detached divertor plasma, which results from B2-EIRENE with its conventional treatment of molecules, i.e., without accounting for vibrational excitation. Turning to the full treatment of molecules, with otherwise identical model parameters everywhere, lead to re-attachment of the divertor plasma into a moderately high recycling regime. In order to recover the initial detached state a ramp up of the midplane density was carried out. The outer target profile is plotted in Fig. 5.43 with the midplane density as input parameter in the calculations. First, the decrease of the divertor density is demonstrated by a comparison of the results at a midplane density of $5 \times 10^{19} \text{ m}^{-3}$ without and with molecules. Increasing the density at the scrape-off layer, the starting point is recovered again only after an enhancement

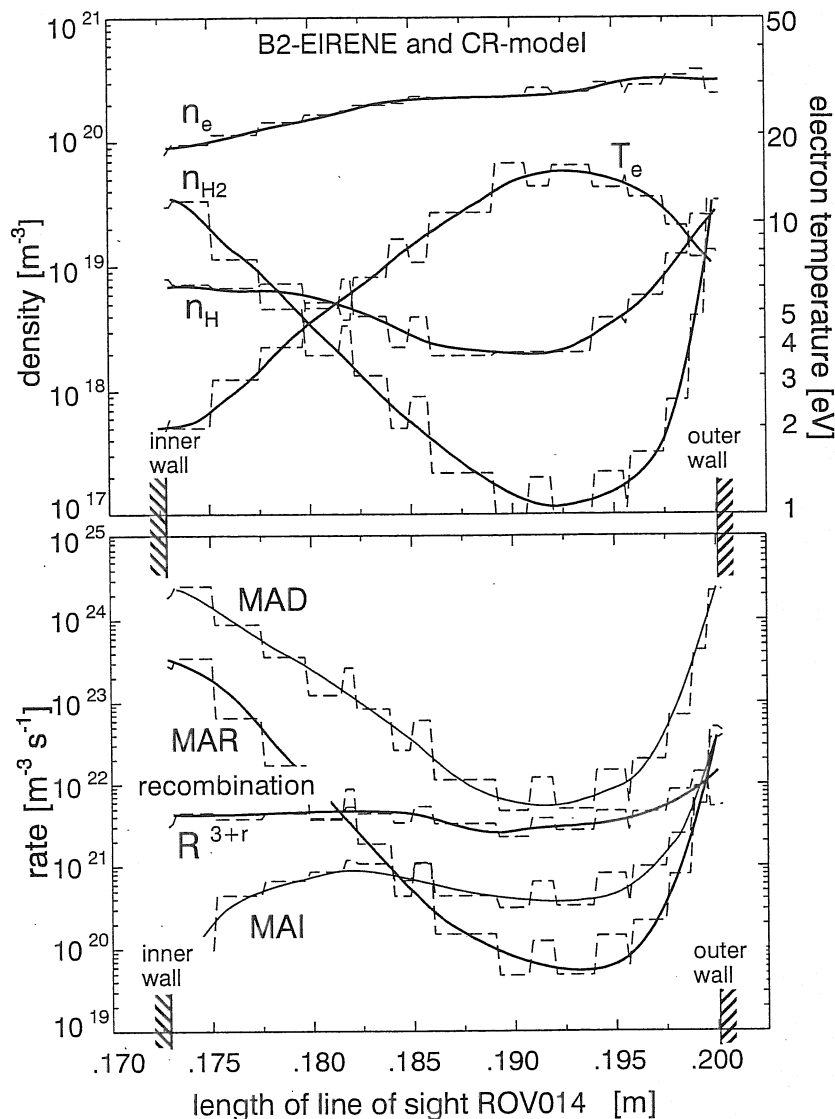


Figure 5.42: Densities (n_e , n_H , n_{H_2}) and T_e as well as rates for MAR, MAD, MAI and R^{3+r} obtained from a combination of B2-EIRENE and CR-model.

in the upstream density by a factor of at least 1.5. One may assume that the effect is somewhat weaker, if impurities are explicitly taken into account as well and if the whole burden of achieving detachment is not only on the hydrogenic species. However, the trend remains, as the first multi-fluid B2-EIRENE runs for the same conditions have confirmed.

Other series of calculations were carried out, explicitly including carbon atoms and ions as impurity species. Chemical erosion is accounted for as an effective carbon-atom source in addition to the physical sputtering term. Experimental carbon radiation profiles have carefully been matched by the code. The results of calculations with the original model for hydrogen molecules have already been

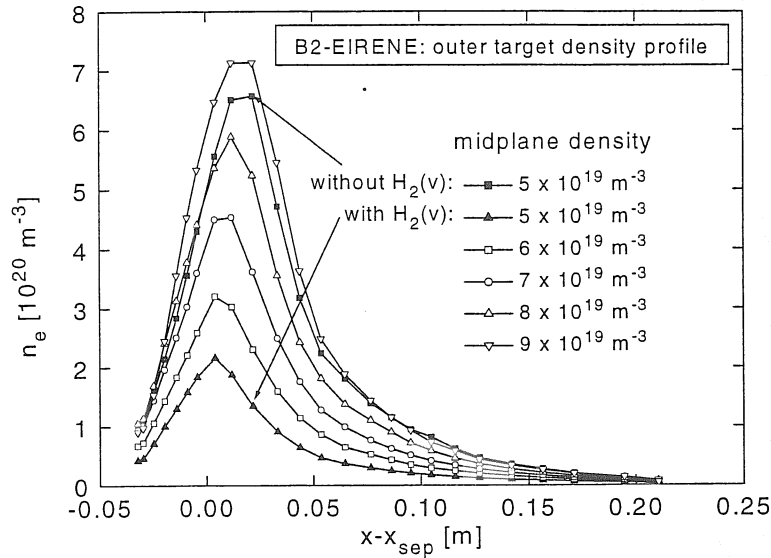


Figure 5.43: Outer target density profiles from B2-EIRENE calculations with and without vibrationally resolved molecules.

published [GBC⁺99]. They are discussed there with respect to the combination of detachment and occurrence of flow reversal. In addition, the diagnostic method for verifying the flow reversal is introduced there and measurements were carried out for the identical hydrogen discharges as discussed above. The first analysis of this identical model case, but with proper account for the effects of vibrationally excited molecules, gives similar results as calculations for pure plasma conditions described above [Sch00a]. The plasma re-attaches after activating the vibrational excitation of H_2 (and resulting resonances) in the code. In addition the predicted parallel velocity shows a somewhat weaker flow reversal for CIII as compared to the case with the conventional model for H_2 . In the pure plasma case mentioned above the flow reversal at the inner target has disappeared entirely after turning to the more complete treatment of molecules and re-attachment.

Concerning the isotopes, it has to be kept in mind, that quantitative predictions may be different for hydrogen and deuterium. Since measurements of vibrational populations in the ground state have shown that the isotopes have quite similar populations and since the relevant processes such as ion conversion and dissociative attachment are resonant to a higher vibrational quantum number in deuterium than in hydrogen, it can be expected that the effect of MAR is getting smaller. Nevertheless, precise analysis, i.e. measurements and calculations (including impurities, i.e. carbon) must be carried out. This has recently become possible due to the transfer of the original version of the CR-model for H_2 to D_2 (modified CR-model), which will be implemented in the B2-EIRENE code in future.

5.4 Chemical erosion of carbon

The plasma wall interaction of hydrogen plasmas with carbon surfaces is of high importance for fusion devices. Carbon (pressed graphite) is the most frequently used surface material which is in contact with the plasma. Carbon is chosen because of its favourable properties, which are for example the high thermal conductivity and the low nuclear charge Z (low Z material). The first is important for the removal of the heat load on the surface, whereas low Z materials have the advantage that as impurities they ionize completely in the plasma edge before they diffuse into the bulk plasma. Thus, the plasma cooling by line radiation plays a minor role for low Z materials than for high Z materials. A cooling of the core plasma has to be compensated by an enhancement of the heating power. In contrast, radiative cooling in the plasma edge is favoured since this effect reduces the heat load to the surfaces. A large disadvantage of carbon is the substantial wall erosion due to the bombardment of the surface with plasma particles. As a consequence, the degradation of the wall material is immense and the surfaces have to be replaced from time to time in future fusion plants. Other materials which are relevant for fusion devices are Be, Si, B, W, doped materials such as SiC, TiC and structured materials such as one, two or even three-dimensional carbon fibre compounds (CFC). A summary of possible materials and basic physical processes at the surface is presented in, e.g., [PB86].

Concerning the plasma wall interaction of hydrogen with carbon a variety of experiments have been carried out in laboratory and fusion experiments. The different questions which arose are divided into the following problems: interaction of high energy ions with the surfaces and interaction of cold hydrogen atoms with the surfaces. Furthermore, a dependence on the composition of carbon (pure graphite or soft and hard a-C:H films) exists. A review is given, for example, in [Jac98]. Since plasma parameters of present fusion experiment differ and since carbon tiles are mounted at different locations in the machine, the types of strain to the surface vary strongly and a comparison of data is difficult. In particular, predictions for large scale machines, like ITER, are uncertain. For this case, model calculations are used, which are based on the physical principles and fitted to the available data base. One of such a semi-empirical model was established by Roth [RGR96, RGR97] and gives an analytic description of the chemical erosion of graphite by hydrogen ions. This model describes the erosion as a composition of three components: the physical sputtering, the thermal erosion and the surface erosion. A very recent synopsis of erosion and redeposition is given in [Rot01], summarizing in particular the status of the latest measurements and calculations.

The manifold parameters affecting erosion and redeposition of carbon require detailed investigations which can be carried out in laboratory plasmas with well defined bombardment of particles to a well defined surface. Ion beam experiments cover the subject area of physical sputtering, in which the energy ranges from some ten eV to several hundred keV. Interactions of pure atomic hydrogen are studied by dissociating hydrogen on hot filaments, which is described by the process of H-induced chemical erosion. In this case, the model of Küppers

[HSB⁺94] provides a theoretical analysis of the chemical processes depending on the surface temperature. Since the plasma provides ions with various energies and cold atoms, a combined effect may occur, which depends on the ratio of the respective fluxes. This synergistic effect is of special interest in low temperature plasmas and is described in the review of [Jac98] as well. Concerning erosion processes in divertor plasmas, laboratory plasmas are particularly suited for providing erosion data with well defined parameters.

In the following measurements and results will be presented which were carried out in the ICP and ECR discharge and fill a gap of data for erosion yields: chemical erosion at low ion energies and low temperature. Special emphasis is given on the isotope effect, which is not expected from pure atomic hydrogen bombardment but from ion bombardment because of the higher momentum of deuterium than hydrogen.

5.4.1 Determination of erosion yields

The characteristic quantity for describing erosion processes is the erosion yield Y which is defined by the ratio of the carbon flux Γ_C leaving the surface and the incoming hydrogen flux Γ_H :

$$Y = \frac{\Gamma_C}{\Gamma_H}. \quad (5.18)$$

The erosion yield depends on the hydrogen flux, the composition of the flux (ions and/or atoms), the hydrogen isotope, the kind of material and the temperature of the surface.

As already discussed in Sec. 5.3.1 in fusion experiments the hydrogen flux from a surface into the plasma can be determined by measuring, e.g., H_α and applying the corresponding S/XB ratio. The hydrogen flux to the surface can be measured with Langmuir probes, i.e. from the electron saturation current. In the case of a complete particle recycling at the surface both fluxes are identical. In a similar manner as atomic and molecular hydrogen fluxes, the carbon fluxes can be derived from measurements of the CH or CD band spectra around 431 nm [Beh90]. Their intensity is related to the CH_4 or CD_4 flux by either empirical calibration for a number of plasma parameters or by the corresponding D/XB ratio. The latter can be taken from calculations considering the break-up of the methane molecule and the transport losses. The dissociation of the methane molecule leads to a CH radical which is electronically excited (via electron impact) to the $A^2\Delta$ state followed by the radiative decay into the ground state $X^2\Pi$. On the basis of known dissociation and excitation rate coefficients no isotope effect exists in the D/XB ratio. This fact was also measured in laboratory ECR plasmas where methane or deuteride methane plasmas were investigated in detail by emission spectroscopy and LiF measurements [Sch95]. Since the rotational temperature of the CH or CD molecule does not depend on the discharge conditions, only a part of the spectrum, which is not overlapped by other lines or molecular bands, can be used for integration. The relation to the whole band spectra can then

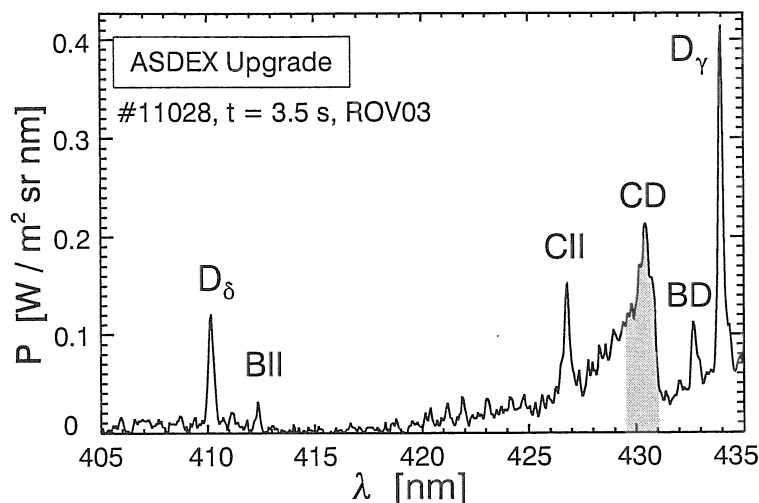


Figure 5.44: Emission spectrum of the CD band around 431 nm which is superimposed by a line of CII. The D_γ and D_δ lines are marked as well as the emission of the impurities: BII line and BD band.

by taken from undisturbed spectra or from simulations of spectra. Figure 5.44 shows a spectrum observed in ASDEX Upgrade after a boronization of the walls for oxygen gathering. Therefore, the BD band emission and the BII line are visible. Simultaneously, in the same spectral window the Balmer line D_γ can be observed which represents the hydrogen flux. The part of the spectrum which is taken for the analyses is grey shaded.

It should be kept in mind, that higher hydrocarbons (C_xH_y), which may be produced at the surface as well, are counting multiple to the carbon flux. These hydrocarbons can also dissociate into the CH radical and therefore contribute to the band emission. Such a path is not included in the calculations up to now, since either the fluxes of C_xH_y have to be measured separately or their formation has to be calculated. Additionally, the hydrocarbons can be produced at the surface or can be formed in the small, cold plasma layer in front of the surface. Here, further investigations have to be carried out if, e.g. the radiation of the C_2 band will provide C_2H_y fluxes, a subject which is tested in laboratory plasmas and will be described later on.

In low pressure plasmas, the fluxes can be determined for the diffusion dominated regime by the measurement of the density gradient and in case of molecular flow by the density and mean velocity of the particles (Sec. 5.2.3). However, for methane, the radiation of the CH radical has contributions from direct excitation of the CH radical and from dissociative excitation of methane. The latter can be the dominant excitation source in low pressure plasmas, since the dissociation degree of methane is low. Furthermore, higher hydrocarbons, i.e. C_2H_y , are produced very effectively by heavy particle collisions in the plasma and contribute also via dissociative excitation to the CH radiation. Details of methane plasmas

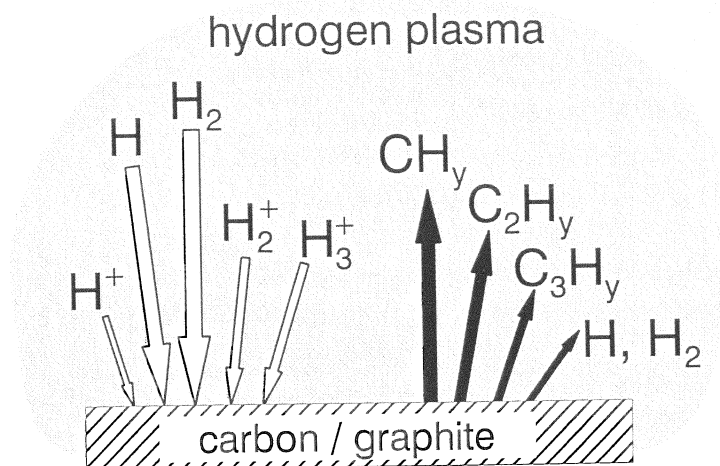


Figure 5.45: Particles of a hydrogen plasma bombarding a carbon surface and particles formed at the surface and penetrating into the plasma.

will be given in Sec. 6.1. In contrast to fusion experiments, the density of the C_2H_y particles can be measured directly by mass spectrometry. Thus, a possible correlation between the radiation of a C_2 band and C_2H_y particle densities can be figured out.

In general, laboratory plasmas enable weight loss measurements for the determination of carbon fluxes. However, direct weight loss measurements are restricted to pure materials, i.e. doped materials need additional surface analysis techniques. If redeposition occurs during the erosion process, weight loss measurements result in erosion yields which are too low. Nevertheless, results from weight loss measurements can be compared with results from emission spectroscopy. Furthermore, the correlation of carbon fluxes with radiation of the CH radical and the C_2 molecule can be calibrated.

5.4.2 Parameter range and diagnostics

Measurements of erosion yields of fine-grain pressed graphite (EK98) were carried out mainly in the ICP discharge but also in the ECR discharge. The homogeneous plasma parameters above a surface in the ICP plasma and the possibility to install a substrate holder which provides the possibility of active heating and cooling as well as biasing, favours the ICP discharge. Due to the excitation mechanism of the ECR plasma, each additional conductive material disturbs the resonator cavity and the plasma generation becomes difficult.

Figure 5.45 shows schematically the manifold of the bombardment of particles on the substrate and particles which may be formed, reflected or recombined at the surface. These particles penetrate into the plasma and can undergo further reactions such as dissociation, excitation and ionization. The plasma parameters

parameter	value
gas mixture	10% $\text{H}_2(\text{D}_2)/\text{He}$ at 20 Pa
electron temperature	$T_e = 3 \text{ eV}$
electron density	$n_e = 10^{17} \text{ m}^{-3}$
heavy particle temperature	$T_g = 650 \text{ K}$
dissociation degree	$\delta = n_{\text{atom}}/(n_{\text{atom}} + n_{\text{mol}}) = 10\%$
atomic flux	$\Gamma_H = \Gamma_D = 2.6 \times 10^{21} \text{ m}^{-2} \text{ s}^{-1}$
atomic/ion flux	$\Gamma_{\text{atom}}/\Gamma_{\text{ion}} \simeq 70$
ion species	$\text{H}_3^+ \approx \text{H}_2^+ \simeq 100 \times \text{H}^+$
bias	$U_{\text{bias}} = -40 - 40 \text{ V}$
ion energy	$E_{H_x^+} = 54 - 5.6 \text{ eV}$
substrate temperature	$T_s = 300 - 1000 \text{ K}$
material, size	fine-grain graphite: EK98, $30 \times 30 \text{ mm}$

Table 5.2: *Parameters of the ICP plasma used for measurements of erosion yields.*

and, particularly, the flow of particles to the substrate must be known precisely for the interpretation of erosion yields. For convenience, the parameters of the ICP discharge are compiled in Tab. 5.2. Parameters in the ECR plasma are quite similar. The range of additional substrate biasing which varies the ion energy, and the range of the substrate temperature are given also. The correlation of bias and voltage accelerating the ions was determined by measuring the modification of the plasma potential with bias in the grounded chamber using Langmuir probes. It is obvious, that in such low pressure plasmas, chemical erosion of carbon can be studied at low atomic temperatures and low ion energies. Due to a combination of atomic and ion fluxes a synergistic effect is expected. Systematic investigations concerning the isotope effect of hydrogen and deuterium can be worked out.

As diagnostic methods for erosion yields, emission spectroscopy and weight loss measurements were applied. Atomic hydrogen densities and fluxes were observed from the radiation of Balmer lines. The absolute values of carbon fluxes result from weight loss measurements, whereas relative dependencies were obtained from the CH/CD band emission around 431 nm. In addition, the Swan band around 516 nm of the C_2 molecule was measured, which provides information on the formation of higher hydrocarbons (C_2H_y). In the case of ECR plasmas, mass spectrometry measurements (residual gas analyser) were carried out as well. Details of the ICP parameters and diagnostics as well as the results presented in the following are given in [Pau00, FP01].

5.4.3 Formation of methane and higher hydrocarbons

The formation of methane and higher hydrocarbons by plasma wall interaction of hydrogen and deuterium plasmas with carbon surfaces can be proved with a

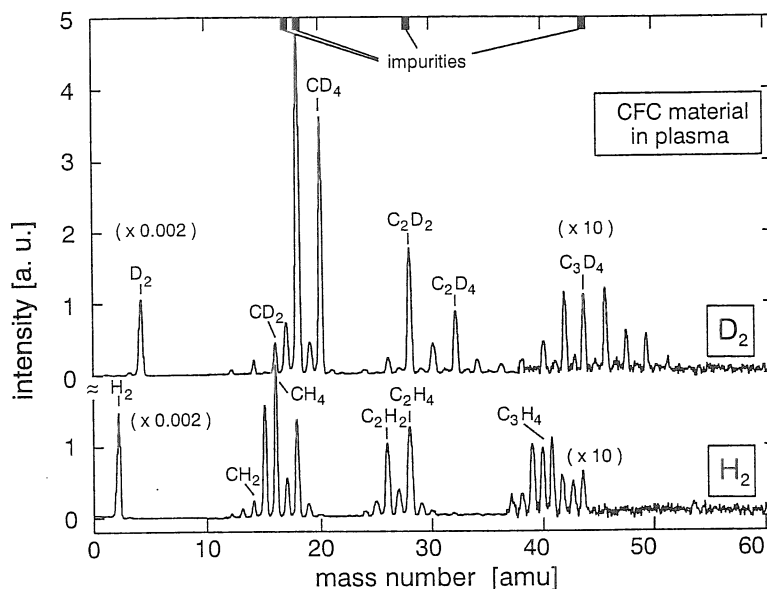


Figure 5.46: Mass spectra of hydrocarbons in the ECR discharge. Shown are measurements of hydrogen and deuterium plasmas interacting with carbon fibre material (CFC).

mass spectrometer. A comparison of measurements with a residual gas analyser in ECR hydrogen plasmas with those of deuterium plasmas is given in Fig. 5.46. A one dimensional carbon fibre composition (CFC) was used as substrate at 500 K substrate temperature. Some selected peaks are marked as well as the magnification of the hydrocarbon groups. Obviously, each group is represented by its fragmentation pattern, for example, the C_2H_y group represents a mixture of C_2H_2 , C_2H_4 and C_2H_6 fragmentation. Calibration of the gas analyser with these gases allows to specify the composition of the C_2H_y group and the densities of the three components. For hydrogen, the density ratio of methane to the C_2H_y density was measured to be four, which means that higher hydrocarbons must be taken into account for the determination of carbon fluxes and erosion yields. Due to the lack of calibration gases, the determination of absolute C_3H_y densities and deuterides were not possible, but a closer look at Fig. 5.46 suggests a similar ratio for deuterium as for hydrogen.

Results of emission spectroscopy (CH/CD band) are shown in Fig. 5.47 and are compared with intensity signals of CH_4/CD_4 obtained by the gas analyser. The dependencies on the substrate temperature agree very well, the isotope effect is obvious (factor of three). The measurements were carried out in the ECR discharge in a 10% $H_2(D_2)$ /He mixture at 15 Pa. Helium was added in order to increase T_e of the plasma so that the signal-to-noise ratio of emission bands was improved. Since the substrate holder was floating, the ion energy is around $3kT_e$, i.e. 10 eV. The edge observed at 800 K in all four signals together with the strong isotope effect indicate chemical enhanced erosion (synergistic effect). Measurements with pure atomic bombardment would result in a peak, located

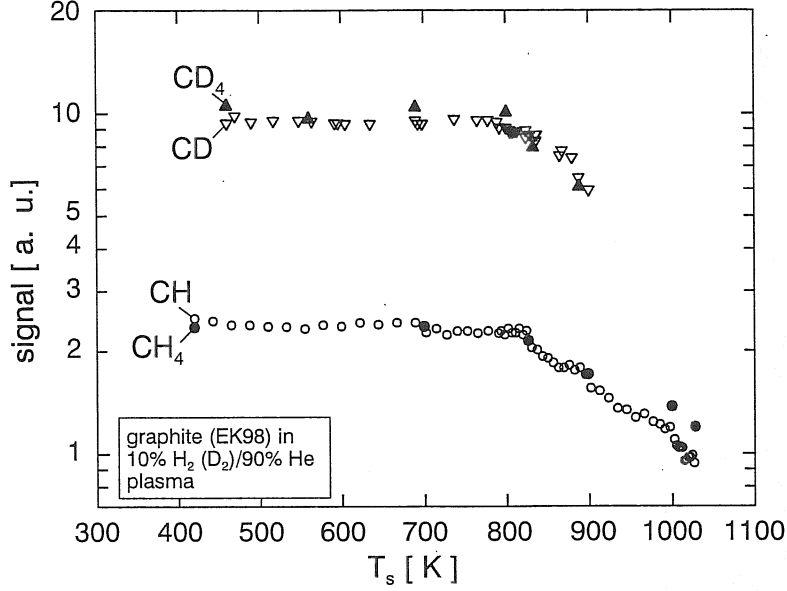


Figure 5.47: Intensities of the CH(CD) band measured by emission spectroscopy and the $CH_4(CD_4)$ signal measured by mass spectrometry in $H_2(D_2)$ -ECR discharges on graphite.

around 600 K ($\Gamma_H = 2 \times 10^{17} \text{ m}^{-2} \text{ s}^{-1}$, [HSB⁺94]). Additionally, no isotope effect is expected. Measurements in a tokamak plasma (TEXTOR-94, which is a limiter machine) showed a weak peak around 1000 K at hydrogen fluxes of approx. $10^{22} \text{ m}^{-2} \text{ s}^{-1}$ [PPE⁺97]. The synergistic effect hides the peak at low temperatures so that only the decrease at higher temperatures is obtained. This means that below 800 K the ion bombardment causes the erosion whereas at higher temperatures atomic fluxes dominate. As a consequence the isotope effect should vanish at high T_s , which could not be observed in the measurements (Fig. 5.47). Nevertheless, a stronger drop off is indicated for deuterium than for hydrogen. Furthermore, it should be kept in mind that the shape of the curves depend on the absolute fluxes and the ratio of ions to atoms.

Detailed investigations were carried out in the ICP discharge using graphite as substrate (EK98). First of all the radiation of the Swan band of $C_2(H)(C_2(D))$ around 516 nm was detected simultaneously with the radiation of the CH(CD) band in hydrogen (deuterium) plasmas. Since the densities of the radicals (n_{CH}, n_{C_2}) are very low in these plasmas the direct excitation channel can be neglected and the main excitation process is dissociative excitation. The radiation, \dot{N}_{CH} and \dot{N}_{C_2} , is then correlated to the densities of CH_4 and C_2H_y , respectively:

$$\dot{N}_{CH} = n_{CH_4} n_e X_{CH}^{em}(T_e) \quad \text{and} \quad \dot{N}_{C_2} = n_{C_2H_y} n_e X_{C_2}^{em}(T_e). \quad (5.19)$$

$X_{CH}^{em}(T_e)$ and $X_{C_2}^{em}(T_e)$ are the dissociative excitation emission rate coefficients. The energy threshold of the cross sections for both processes is very similar ($\approx 15 \text{ eV}$ for CH and $\approx 18 \text{ eV}$ for C_2). Therefore, variations in plasma parameters, particularly in electron temperature, will have the same effect on either radiation.

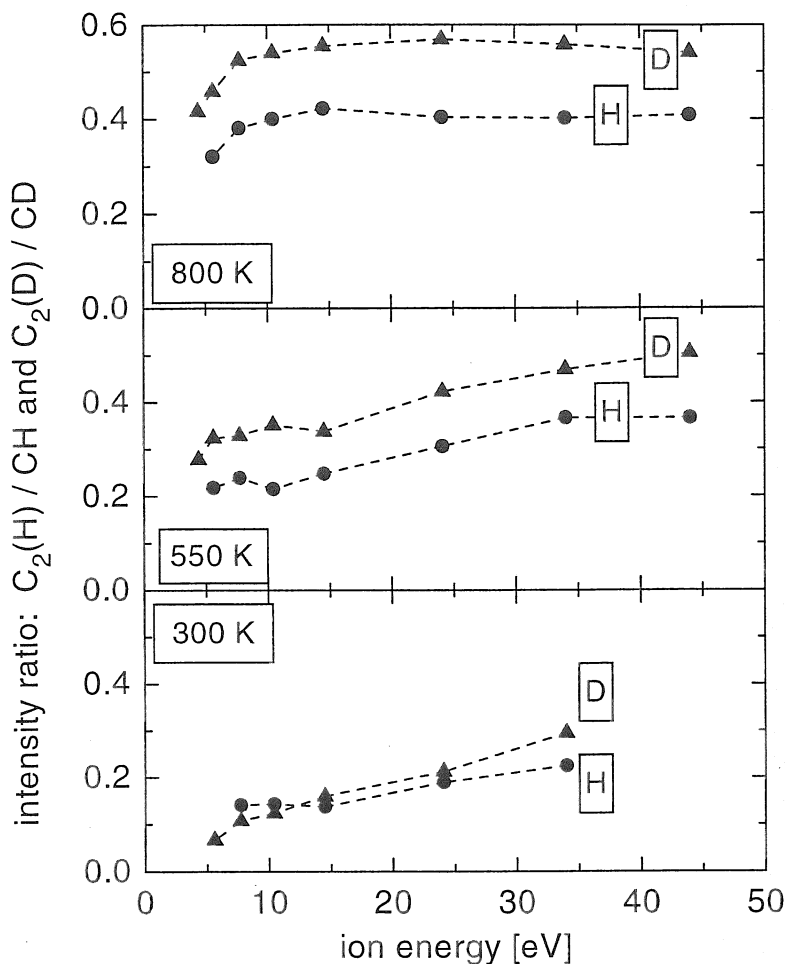


Figure 5.48: Intensity ratios of $C_2(H)/CH$ in hydrogen and $C_2(D)/CD$ in deuterium plasmas as a function of ion energy for three substrate temperatures (EK98).

The dissociative excitation of the C_2H_y molecules into CH may contribute to the radiation of CH also, but was neglected here for simplification, since the density of the higher hydrocarbons is not well known.

Measured intensity ratios of $C_2(H)/CH$ and $C_2(D)/CD$ are plotted in Fig. 5.48. The ion energy was varied between 5 eV and 45 eV at 300 K, 550 K and 800 K substrate temperature. At 300 K the formation of higher hydrocarbons increases with ion energy (factor two). For higher temperatures deuterium indicates more C_2 formation than hydrogen and is highest at 800 K (factor 1.4). The increase with ion energy becomes smaller and reaches a saturation at maximum substrate temperature.

In order to emphasize the differences for the isotopes, Fig. 5.49 shows the $C_2(D)/C_2(H)$ and CD/CH ratios depending on substrate temperature at 8 eV ion energy. At room temperature equal intensities were observed for the isotopes. With increasing substrate temperature erosion due to deuterium particles be-

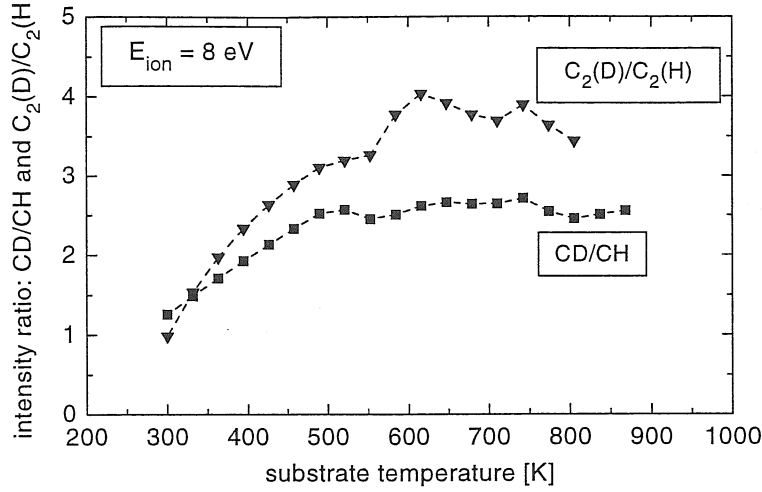


Figure 5.49: Intensity ratios of $C_2(D)/C_2(H)$ and CD/CH in hydrogen/deuterium plasmas depending on substrate temperature (EK98).

comes more efficient. Supplementary, higher hydrocarbon production is favoured in deuterium discharges.

As a consequence of the different dependencies of CH and $C_2(H)$ (CD and $C_2(D)$) intensities on substrate temperature and ion energy both radiations were considered for the determination of carbon fluxes:

$$\Gamma_C = \Gamma_{CH_4} + 2 \times \Gamma_{C_2H_y} = n_{CH_4} \bar{v}_{CH_4} + 2 \times n_{C_2H_y} \bar{v}_{C_2H_y} . \quad (5.20)$$

The fluxes are written in terms of densities and mean velocities. Using Eq. 5.19 the densities can be replaced by the measured radiations:

$$\Gamma_C = \dot{N}_{CH} \frac{\bar{v}_{CH_4}}{n_e X_{CH}^{em}(T_e)} \times \left(1 + \frac{\dot{N}_{C_2}}{\dot{N}_{CH}} 2 \frac{\sqrt{m_{CH_4}}}{\sqrt{m_{C_2H_y}}} \frac{X_{CH}^{em}(T_e)}{X_{C_2}^{em}(T_e)} \right) . \quad (5.21)$$

The velocity ratio was replaced by the mass ratio and Eq. 5.21 was simplified:

$$\Gamma_C = A \times \dot{N}_{CH} \left(1 + B \times \frac{\dot{N}_{C_2}}{\dot{N}_{CH}} \right) , \quad (5.22)$$

where B is a factor which can be calculated using the mass of C_2H_2 for the higher hydrocarbons. Rate coefficients for dissociative excitation were derived from the cross sections given in [ABH71] and [TIN+90] for CH_4 and C_2H_2 , respectively. As discussed before, the threshold energies of the excitation processes are similar. As a consequence the ratio for the rate coefficients is almost independent of T_e and is 4.0 for hydrogen which was also used for deuterium. The factor A can be taken from a calibration of carbon fluxes which were gained from weight loss measurements as described in the next section.

5.4.4 Erosion yields at low temperatures and low ion energies

Erosion yields were determined by using two experimental methods: the first method is based on weight loss measurement of the substrate before and after plasma exposure. Since the typical time scale of a substrate being in the plasma was approximately eight hours, re-deposition can occur. In this case the carbon fluxes is somewhat underestimated. Furthermore, the surface can also be modified during the deposition time. The second method, which was carried out in situ, is the spectroscopic measurement of the CH and C₂ band emission and gave in a first step only relative dependencies of carbon fluxes but were then absolutely calibrated with results from weight loss measurements. Here, the carbon flux at 300 K substrate temperature and 10 eV ion energy was chosen as calibration point. The calibration factors A and B (Eq. 5.22) were determined to be: $A = 0.57$, $B = 6.27$ for hydrogen and $A = 0.38$, $B = 6.76$ for deuterium. Thus, erosion yields gained from spectroscopy consider the formation of methane and higher hydrocarbons. The measurements are compared with calculations carried out with Roth's model [RGR96, RGR97]. The measured atomic and ion fluxes and the scaling for the ion energy were used as input data. It was assumed that H₂⁺ is the dominant ion species and the ion energy will be split up at the surface in equal energies for H and H⁺. Since only the ions have the energy mentioned and since the dominant particles are atoms a enhanced chemical erosion (synergistic effect) is expected, which is not included in the model explicitly. This must be taken into account when comparing the results.

Dependencies on ion energy at 300 K, 550 K and 800 K graphite temperature

Erosion yields obtained from weight loss measurements, emission spectroscopy and Roth's model are shown in Fig. 5.50 for three substrate temperatures. Spectroscopic results agree very well with weight loss measurements. The erosion yields increase with increasing ion energy, whereas at higher temperatures saturation occurs. At 800 K measurements in deuterium give a factor of two higher erosion yields ($Y \simeq 2\%$) than results in hydrogen ($Y \simeq 1\%$). The isotope effect becomes smaller at lower substrate temperatures and lower ion energies. At 300 K and 5.6 eV ion energy the isotope effect vanishes completely. At this point pure chemical erosion occurs. The measured erosion yield is 0.15%. With increasing ion energy the additional ion bombardment becomes important, the erosion yield increases as well as the difference in the isotopes. Here, the chemical enhanced erosion takes place, i.e. the synergistic effect. At 800 K the influence of atomic hydrogen is completely covered by the effect of ions in the whole energy range.

Model calculations agree in principle with measured results. Satisfying agreement is observed for ion energies above 15 eV. In contrast to the measurements, the isotope effect is predicted to decrease with substrate temperature. Generally, the difference in the isotopes vanishes at low ion energies because of the dominating term of thermal chemical erosion. Sputtering or desorption processes in the

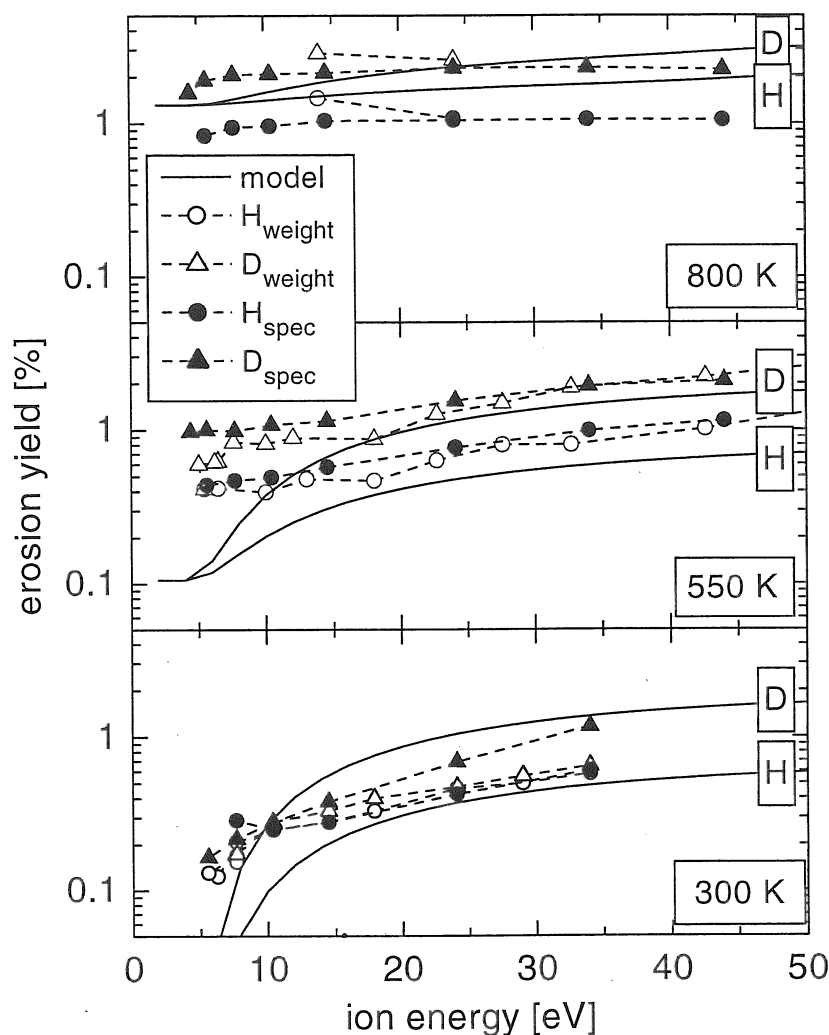


Figure 5.50: Erosion yields of graphite (EK98) in hydrogen and deuterium plasmas as a function of ion energy (dominant species: H_2^+) for three substrate temperatures.

calculation are assumed to have an energy threshold. Discrepancies between measurements and calculations are significant at lower ion energies, and are largest at 550 K and 5 eV: results from modeling give an erosion yield of 0.1% for either isotope, whereas measurements reach 0.4% for hydrogen and 0.6 – 1% for deuterium. It is concluded, that the deviations are probably due to the synergistic effect which is not included in the calculations. The chemical erosion is based on the model of Horn *et al.* [HSB⁺94]. Furthermore, higher hydrocarbons are not considered in the formula.

Dependencies on substrate temperature at 8 eV ion energy

Figure 5.51 shows erosion yields as a function of the substrate temperature at 8 eV ion energy, i.e. 4 eV per particle (H and H^+ or D and D^+). Both diag-

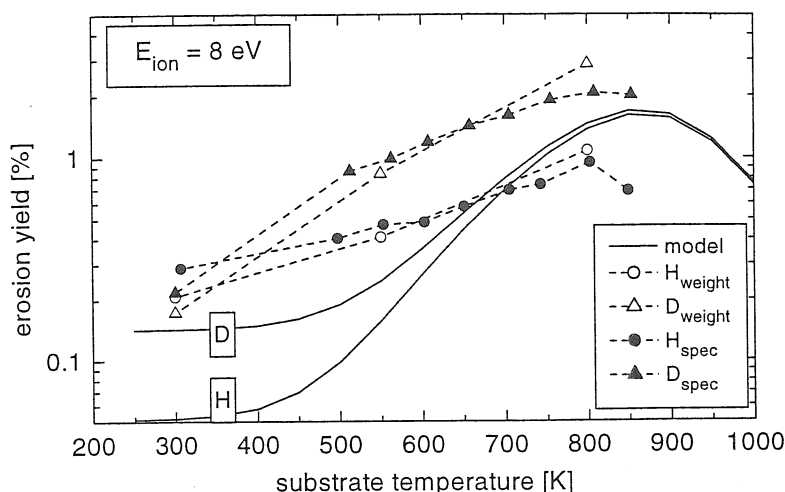


Figure 5.51: Graphite (EK98) temperature dependence of erosion yields at 8 eV ion energy (4 eV per H and H^+ particle).

nostic methods agree very well and show an increase of the isotope effect with substrate temperature, whereas modeling yields only a minor isotope effect at higher substrate temperature. Spectroscopic measurements indicate a maximum at a substrate temperature of around 800 K which is in agreement with the calculations. Maximum erosion yields are 2% for deuterium and 1% for hydrogen, calculations are between these values. Remarkable is the contrary behaviour of measurements and calculations for the isotope effect with substrate temperature. At room temperature an erosion yield of 0.2% remains whereas calculations predict 0.14% for deuterium and 0.05% for hydrogen. This may be due to the use of a fit parameter in the calculations, which describes the physically enhanced chemical erosion. This parameter Q is set to be different for D and H ($Q = 0.1$ for D and $Q = 0.035$ for H), and the ratio is the same as the ratio of the predicted erosion yields. Furthermore, deviations between measurements and modeling might again be explained by the contribution of higher hydrocarbons. Spectroscopic results derived from the radiation of CH alone, i.e. without considering C_2 , would result in a weaker dependence on substrate temperature.

Summary

Measurements of erosion yields of carbon (pressed graphite: EK98) at low atomic temperatures and low ion energies in hydrogen and deuterium ICP plasmas were carried out. Due to the properties of the low pressure plasma, the bombardment of the surface is a combination of cold atoms ($\Gamma_H = \Gamma_D = 2.6 \times 10^{21} \text{ m}^{-2} \text{ s}^{-1}$) and low energy ions (5 - 40 eV). The ion flux was two orders of magnitude below the atomic flux. Weight loss measurements and emission spectroscopy were applied for the determination of absolute carbon fluxes. Special regard was given to the formation of higher hydrocarbons by analysing the radiation of the C_2 Swan

band. Results from emission spectroscopy are only consistent with results from weight loss measurements if CH as well as C₂ emission is considered. This shows clearly the contribution of higher hydrocarbons to the erosion yield. At room temperature and low ion energy no isotope effect occurs, but an erosion yield of 0.1% still remains. With increasing ion energy an isotope effect becomes visible due to the synergistic effect of atoms and ions, i.e. the chemical enhanced erosion. An increase of substrate temperature results in a maximum yield of $Y = 2\%$ for deuterium and $Y = 1\%$ for hydrogen around 800 K. The isotope effect increases with temperature. Comparisons with the semi-empirical model of Roth are in good agreement for ion energies above 15 eV. However, at low ion energies and, particularly, room temperature discrepancies occur. Since the model is based on data which is taken from either pure ion beam experiments at high ion energies or from pure atomic particle bombardment on surfaces and from fusion experiments, the presented results from laboratory plasmas fill the gap in the data base for low ion energy and low substrate temperature.

Chapter 6

Other Molecular Plasmas: Methane, Silane, Nitrogen, Oxygen

The analogy between other molecular low pressure plasmas and hydrogen plasmas is one of the main topics in the following sections. In particular, spectroscopic diagnostics of the particle densities and the degree of dissociation will be emphasized. Here, atomic lines and molecular bands suitable for determination of particle densities will be identified. Methane and silane plasmas are of special interest, since on one hand their application in plasma technology is manifold (production of thin films) and on the other hand the dominant particle species is mostly molecular hydrogen (main dissociation product). Nitrogen and oxygen plasmas are also used for technological processes and the atomic densities, i.e. degree of dissociation, is one of the most important parameters for the applications. Additionally, the gases are the same simple diatomic gases as hydrogen and comparison of dissociation degrees under the same discharge conditions will improve the understanding of molecular processes. A summary of plasma chemical deposition and etching of thin films, in particular, a discussion of carbon and silicon films, is giving for example, [Gri94].

6.1 Methane and silane plasmas

Methane plasmas are commonly used for the deposition of thin films, i.e. diamond-like coatings or amorphous carbon films (a-C:H). In the case of silane plasmas, amorphous silicon films (a-Si:H), polycrystalline or monocrystalline silicon films are of special interest. The main interest is usually focused on optimizing film characteristics by varying plasma conditions, however a detailed analysis of plasma processes and parameters is often neglected. For a better understanding of the deposition and plasma processes, measurements of plasma parameters are

highly desirable. Additionally, these measurements can contribute to a better interpretation of chemical erosion measurements of carbon and silicon layers with hydrogen plasmas which is important in fusion experiments. In particular, the dissociation channels can be investigated in detail in such laboratory experiments. Since carbon and silicon are elements from the same periodic group, a comparison of these plasmas and their processes is of special interest.

A compilation of the efforts in understanding methane plasmas is given in the introduction of [MRDR01]. [PLB96] and references herein, give an overview about silane chemistry. Spectroscopic diagnostics and modeling of methane plasmas and silane plasmas are described in [Beh91] and [Fan98], respectively.

The following sections will describe, in extracts, the application of emission spectroscopy in methane and silane plasmas which was expanded by mass spectrometry and by modeling of radical densities. In order to identify excitation channels of radicals, densities of higher hydrocarbons and silanes, which are formed by heavy particle collisions in the discharge, were measured as well. Details of the measurements and results can be found in [Mei00] for methane and [Fan98] for silane plasma. All investigations were carried out in the ECR discharge.

6.1.1 Dissociation channels

Figure 6.1 gives the dissociation and ionization chain of methane and silane by electron impact collisions, which are the dominant reactions in low pressure discharges. In contrast to methane, the silane ion SiH_4^+ is an unstable ion. It predissociates immediately into SiH_2^+ . Of course, each dissociation reaction produces molecular or atomic hydrogen and a hydrogen chain has to be added to the pure methane and silane chains. Since higher hydrocarbons and silanes are formed in the plasma as well, their dissociation and ionization channels have to be added also. The threshold energy for dissociation is around 10 eV for methane whereas for silane 8 eV is necessary. Figure 2.4 gives the comparison of dissociation cross sections. Thus, one expects a higher dissociation of silane than of methane plasmas, leading on one hand to a dilution of the input gas and to the other hand to higher growth rates for films. The dominant parameter for dissociation is T_e due to the strong dependence of the rate coefficients on this value. It is further expected, that in methane the CH_4^+ ion is the most dominant ion whereas in silane plasmas SiH_3^+ should dominate. However, depending on the amount of higher hydrocarbons or silanes the dominant ion species may be C_2H_y^+ or Si_2H_y^+ ions. Since their ionization energies are 2 – 3 eV lower than those of methane or silane and since their masses are considerable higher, these plasmas will have low T_e (around 1 – 2 eV).

6.1.2 Formation of higher hydrocarbons and silanes

Higher hydrocarbons (C_2H_y , C_3H_y) and silanes (Si_2H_y , Si_3H_y) are produced in the plasma by heavy particle collisions. Here, molecule–molecule as well as molecule–

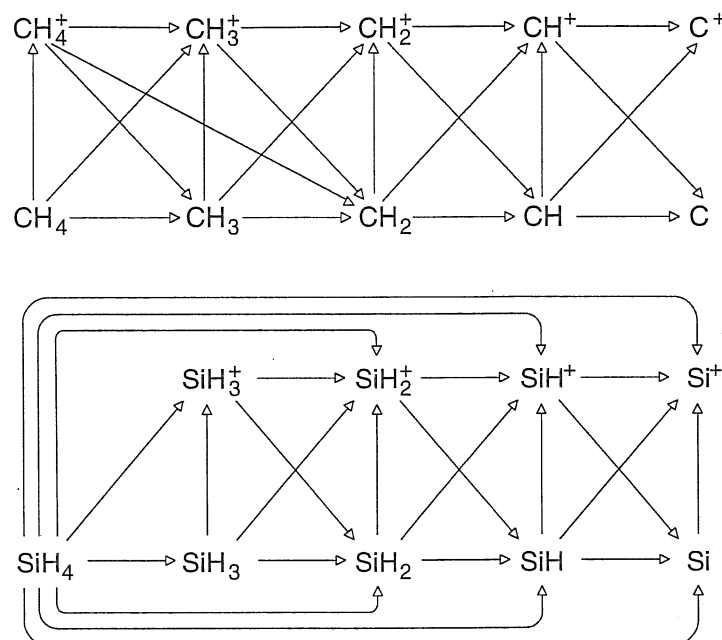


Figure 6.1: Dissociation and ionization channels of CH_4 and SiH_4 induced by electron impact collisions. SiH_4^+ is an unstable ion.

ion reactions occur. For example, $\text{CH}_3 + \text{CH}_3 \rightarrow \text{C}_2\text{H}_6$ is one of the main reactions. In the case of silane plasmas the dominant reaction is $\text{SiH}_4 + \text{SiH}_2 \rightarrow \text{Si}_2\text{H}_6$. Since these reactions depend strongly on neutral densities, discharge pressure and dissociation degree are important parameters. The rate coefficients depend only slightly on gas temperature.

However, at gas temperatures above approximately 1000 K, additional chemical reactions become important leading to, e.g., dissociation. A simulation of the pure methane chemistry (without electron impact dissociation) can be carried out with the CHEMKIN code package [KRMM96]. Since the gas temperatures of the plasmas investigated here are around 500 K plasma chemical reactions are negligible.

Since densities of SiH_4 and CH_3 are high in low densities plasmas, higher silanes and higher hydrocarbons are produced very effectively and may therefore dominate the plasma behaviour. In particular, ions of these particles become important.

6.1.3 Particle densities

Obviously, in methane and silane plasmas the species of particles are manifold and the more particle densities of different species can be measured the better will be the identification of dominant reactions channels which is important for improving and optimizing film growth. In order to get as many particle densities

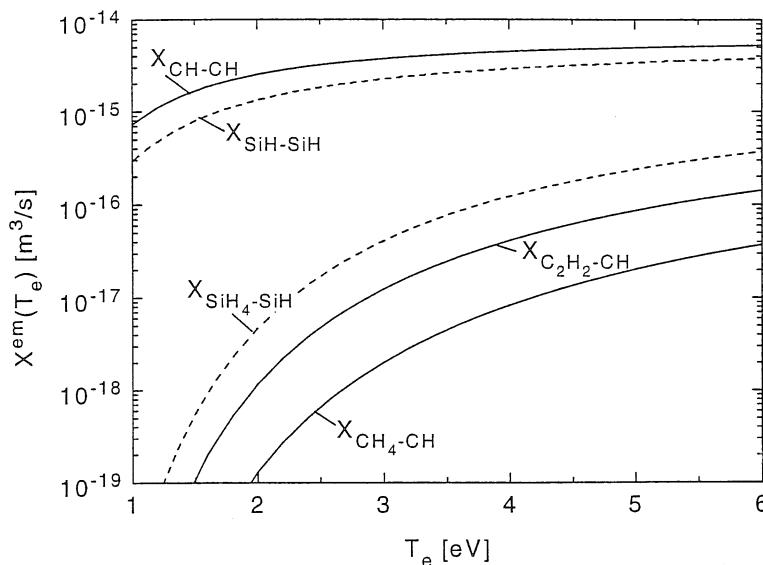


Figure 6.2: Emission rate coefficients for the CH and SiH band originating from direct excitation of CH and SiH as well as dissociative excitation from CH_4 (C_2H_2) and SiH_4 , respectively.

as possible three diagnostics were combined: spectroscopic diagnostics, residual gas analyser and modeling.

Emission spectroscopy

From the dissociation chains, the radicals which are accessible for emission spectroscopy can be identified: CH or SiH and C or Si radicals emit in the visible spectral range (around 430 nm) and in the near UV (around 250 nm, 190 nm and 160 nm), respectively. Polyatomic molecules radiate preferably in the infrared spectral range and absorption becomes more frequent than emission of light. Of course, H_2 and H radiation is accessible as well. In the case of methane plasmas, radiation of the C_2 molecule is easily detectable (Swan band around 516 nm). Radiation of the Si_2 molecule is generally too weak. Radiation from ions is also too weak for observation, since ion densities are very low.

In order to obtain radical densities, the excitation channels have to be identified and rate coefficients as well as the plasma parameters n_e and T_e have to be known. The latter was taken from the absolute radiation of the He_{728} line (helium was used as buffer and diagnostic gas) and n_e was taken from microwave interferometry. Figure 6.2 shows emission rate coefficients for the CH and SiH band excited by direct electron impact from the ground state of the radical, and excitation due to dissociation of the CH_4 , C_2H_2 molecule and the SiH_4 molecules, respectively. Although the direct rate coefficients exceed more than two orders of magnitude those for dissociative excitation, the latter can dominate the contribution to the measured radiation. This is due to the low density of the radicals in comparison to the methane and silane density. Remarkable is the higher rate coefficient for dissociative excitation from C_2H_2 than from CH_4 molecules. Assuming

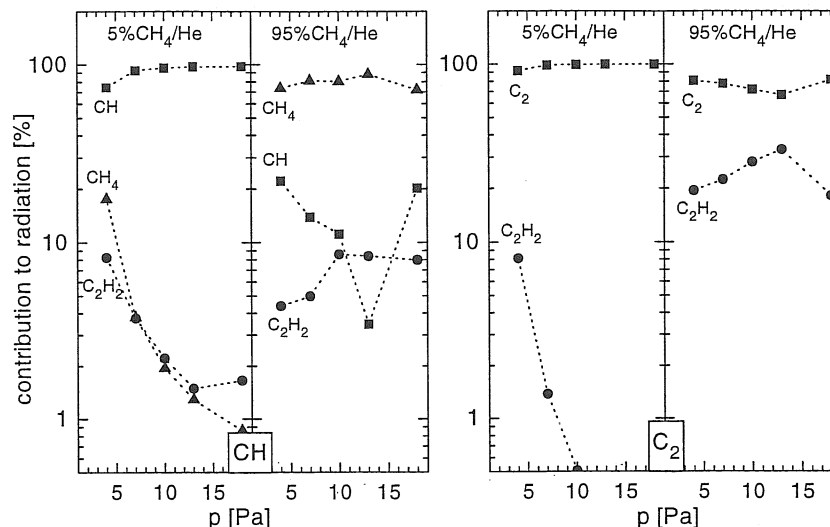


Figure 6.3: Contribution of CH, CH₄ and C₂H₂ excitation to the CH emission as well as C₂ and C₂H₂ excitation to the C₂ emission in two mixtures of methane in helium.

a density ratio of 1/10, the contribution of both dissociative excitation paths to the radiation is comparable. In the case of C (Si) radiation direct excitation out of the ground state and the metastable states of the atoms and dissociative excitation from C₂H₂ (Si₂H₂) have to be taken into account. The population of the metastable states can be obtained from measurements of the corresponding lines in the triplet system. For the evaluation of the Swan band (C₂) excitation out of the C₂ and C₂H₂ molecule is important. For Balmer line excitation, contributions from methane (silane) have to be considered. Molecular hydrogen is excited only by direct excitation. A compilation of rate coefficients for silane are given in [Fan98], the data for methane is summarized in [Mei00].

Figure 6.3 shows the contribution of CH, CH₄ and C₂H₂ excitation to the CH emission as well as C₂ and C₂H₂ excitation to the C₂ emission in two mixtures of methane in helium. In the helium dominated discharge direct excitation dominates over the dissociative excitation and the densities of CH and C₂ can be determined with good accuracy. In methane dominated plasmas, where electron temperature is low, the degree of dissociation is low, which means that the radiation originates mainly from the dissociative excitation of methane. Nevertheless, the determination of the molecular carbon density is possible whereas the determination of CH densities result in large error bars.

From the CH and SiH radiation, the rotational temperature in the excited state was obtained by comparing measured spectra with calculated spectra where T_{rot} is the parameter for the fit. However, a good fit could only be obtained by introducing two rotational temperatures: a smaller one for lower rotational quantum numbers (800 – 1200 K) and a higher one for higher quantum numbers (1200 – 2000 K). The limit is at $J = 8$ for CH and $J = 10$ for SiH. The rotational temperatures vary with gas mixture and pressures. It is assumed that dissociative

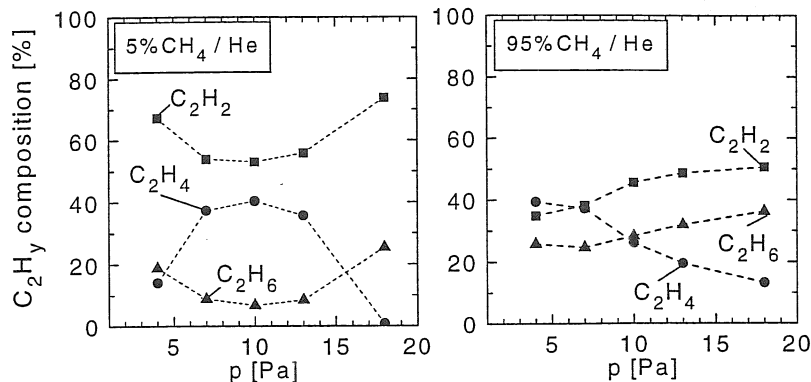


Figure 6.4: Composition of the C_2H_y group as measured in two mixtures of methane in helium.

excitation populates preferable higher quantum numbers. In the case of C_2 , T_{rot} was observed to be 450 K and is identical with the gas temperature.

Mass spectrometry

Since the mass spectrometer was used as a residual gas analyser, only stable neutrals could be observed. Stable particles are methane and silane itself and here, the dilution, i.e. the dissociation, could be measured directly. The demixing of gases in the vacuum vessel was determined as well as the formation of molecular hydrogen higher hydrocarbons and silanes in the plasma. Together with a calibration of the system the composition of the C_2H_y group was obtained. Results measured in two methane/helium mixtures are given in Fig. 6.4. For low methane contents, C_2H_2 gives the most contribution to the C_2H_y group and is dominant even at higher methane contents. These results agree well with those presented in [Pec98] which gives a detailed discussion concerning the composition of higher hydrocarbons in such ECR discharges.

Modeling

In order to get densities for all particles in the plasma, modeling is necessary. From the particle balance (Sec. 2.3.1) the densities of neutrals and ions are obtained. The ionization balance (Sec. 2.3.2) allows the determination of T_e . n_e can either be taken from a power balance or can be used as input parameter for the modeling, where the latter was done in the present case. Modeling requires a lot of input data which have to be compiled. Furthermore, the dominant reactions channels have to be identified and, due to lack of data, scaling may be necessary for rate coefficients. It is obvious that such a model needs confirmations from measurements with as many densities as possible. A model for methane is described in [Beh91], however, neglecting higher hydrocarbons. The self-consistent model for silane is described in [Fan98] and [Sch94]. In this particular model higher silanes, sticking coefficients of particles at surfaces as well as Penning reactions with the He and Ar were considered.

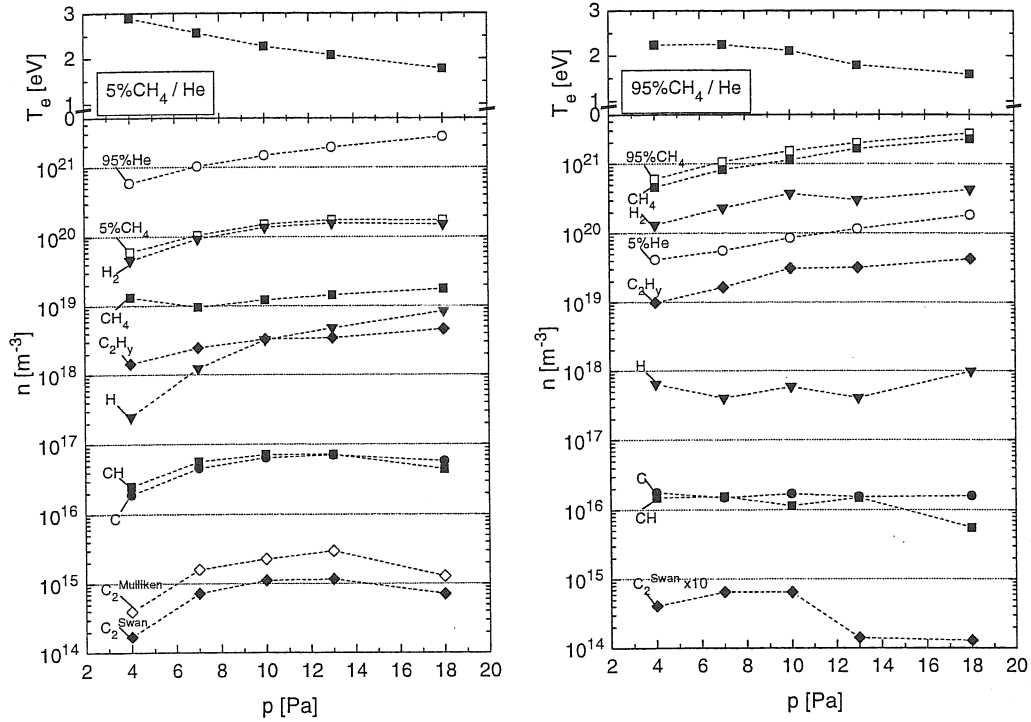


Figure 6.5: Electron temperatures and particle densities in two methane mixtures determined by emission spectroscopy and mass spectrometry.

Results

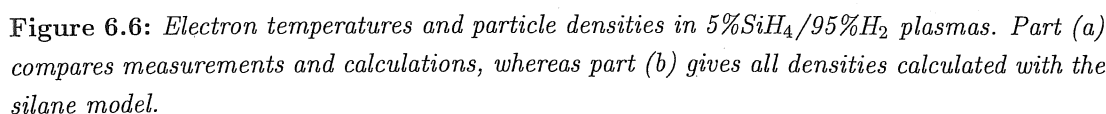
Electron temperatures and particle densities of two mixtures of methane in helium were measured in the ECR plasma depending on discharge pressure. The results are shown in Fig. 6.5. In the 5%CH₄/He plasma T_e ranges from 3 eV to 1.7 eV and the dissociation of methane is considerable. The methane density in the plasma is 1/10 of input gas density. The sum of the gas flows of both gases was 20 sccm. The gas density of methane was replaced by molecular hydrogen which exceeds then clearly the methane density in the plasmas. In plasmas with 95%CH₄/He and lower T_e the decrease of the methane density in the plasma is small and is always the dominant species. Here, molecular hydrogen is about 1/5 of the methane density. Concerning the sum of the C₂H_y densities, these particle densities are 1/10 – 1/3 and 1/50 of the methane density in the plasma with low and high methane contents, respectively. Due to the high degree of dissociation, in the first case, CH₃ and CH₂ densities are high also and heavy particle collisions become effective, in particular with increasing pressure, and produce the higher hydrocarbons. As mentioned before, the species H₂, CH₄ and C₂H_y were measured by the residual gas analyser and were then used for calculating the contribution to the radiation of the radicals which is necessary to determine radical densities from emission spectroscopy.

Atomic hydrogen densities are low in methane plasmas, indicating a separating of molecular hydrogen rather than atomic hydrogen in the dissociation of

hydrocarbons. The dissociation degree of molecular hydrogen δ is below 1% in methane plasmas and comparable with δ in H_2/He plasmas. The radical densities of CH and C were measured as nearly identical in both methane mixtures. This behaviour is not expected since it is assumed that dissociation of CH leads to C which then should be below the CH density. Additionally, recombining particles of C would result in C_2 . The C_2 densities were measured to be more than two orders of magnitudes below the C densities. In the case of low methane mixtures in helium, the C_2 densities were measured from the Mulliken band around 230 nm supplementary to the Swan band. This transition is a very weak transition but is coupled directly to the ground state whereas the Swan band is coupled to the metastable state. The agreement between both results is satisfactory and indicates a similar population for both states. The most probable channel for producing molecular carbon is the dissociation of the C_2H_y group into C_2H which then dissociates via mutual heavy particle collision to C_2 and C_2H_2 .

Results of silane plasmas are shown in Fig. 6.6. T_e was measured by adding 1% helium to the 5% SiH_4/H_2 mixture, for this purpose only. Part (a) compares measured results with results from the modeling of silane/hydrogen plasmas. Filled symbols refer to spectroscopic diagnostics whereas open symbols denote results from mass spectrometry. For molecular hydrogen both techniques were applied, using the radiation of the Fulcher bands for emission spectroscopy. As discussed in Sec. 5.2.5 spectroscopic results from the Fulcher bands show always some deviations to mass spectrometry results, which was attributed to uncertainties in the emission rate coefficient. However, the agreement between measurements and calculations is very good for all densities, thus confirming the model for silane. The model allows a detailed study of processes affecting individual particle densities. For example, the decrease in SiH and Si densities with pressure is due to more heavy particle collisions with silane and molecular hydrogen. The identified reactions are: $SiH + SiH_4 \rightarrow Si_2H_3 + H_2$ and $SiH + H_2 \rightarrow SiH_3$ in the case of SiH, $Si + SiH_4 \rightarrow 2SiH_2$ and $Si + H_2 \rightarrow SiH_2$ in the case of Si. Both collision partners are the dominant species in silane plasmas. As in methane plasmas, molecular hydrogen is identified to be the preferred dissociation product. With increasing pressure the disilane density comes up as the higher hydrocarbons densities do as well. It is noticeable that silane plasmas show the expected behaviour in lower Si densities than SiH densities which was not given in methane plasmas for C and CH densities.

The confirmation of the model by measurements in some densities allows reliable predictions for all densities which are included in the model and which are not accessible by the applied diagnostic methods. Figure 6.6b gives the neutral and ion densities of the 5% SiH_4/H_2 plasma, which is very similar to plasmas used for film deposition. At high pressure, the SiH_3 density is higher than the SiH_2 density, whereas at low pressure the number densities are almost equal as expected from electron impact dissociation of silane (36% SiH_3 , 43% SiH_2). Due to the heavy particle collisions at higher pressure the SiH_2 density is reduced by the following reactions: $SiH_2 + H \rightarrow SiH_3$ including production of higher silanes with silane and disilane $SiH_4 + SiH_2 \rightarrow Si_2H_6$ and $Si_2H_6 + SiH_2 \rightarrow Si_3H_8$. The disilane



The ion densities follow the ionization energies and the densities of the corresponding neutral radicals. Because of the high Si_2H_6 density and the lowest ionization energy, the ion density of Si_2H_4^+ is predominant in all plasmas. In addition, the confinement times of these ions are high due to their great mass.

In summary, model calculations provide an insight into the kinetics of reactions in silane/hydrogen plasmas and silane/noble gas mixtures. The good agreement of experimental and theoretical data allows a prediction of densities, which are not accessible by the present diagnostics. This applies especially to SiH_3 and SiH_2 which are identified to be the dominant species in film growth. Additionally, the role of disilanes and trisilanes, which contribute considerable to plasma reactions, could be studied. Such a model would be very useful for methane plasmas in particular for improving the evaluation of spectroscopic measurements of chemical erosion in laboratory plasmas as well as in fusion experiments.

6.2 Degree of dissociation

The degree of dissociation is one of the key issues in plasma processing. The plasmas are used to produce atomic and ion densities which modify the surface. In the case of nitrogen, silicon films are doped whereas oxygen or hydrogen plasmas

are applied for film cleaning and etching. In the following sections the degree of dissociation in nitrogen, hydrogen and oxygen plasmas, generated in the ECR discharge, are compared. Atomic densities were measured by emission spectroscopy and suitable diagnostic lines were identified. Molecular densities were measured by the residual gas analyser accounting for the demixing of gases in the plasma chamber. Details of the results presented here are given in [Mei00].

6.2.1 Nitrogen and nitrogen/hydrogen plasmas

In nitrogen plasmas, radiation of molecular nitrogen bands are the most prominent band systems which are partly superimposed by emission of the molecular ion. The radiation of the molecular band around 380 nm was already used for the determination of gas temperature and is therefore a good candidate for measuring the N_2 density by emission spectroscopy. Additionally, the N_2^+ band around 391 nm (first negative system, 0-0) can be used for the N_2^+ density. In this case two excitation channels have to be considered, i.e. direct excitation from the ion itself and excitation from N_2 . Applications have already been introduced in Sec. 4.2.2 and Sec. 4.3.1 and rate coefficients are presented in [Beh91].

Atomic nitrogen lines in the visible spectral range are not identifiable in most cases due to the strong molecular emission. Using the VUV/UV spectrometer nitrogen lines at 113 and 120 nm (resonance lines) as well as 124, 149 and 174 nm (out of the metastable system) were detectable. The first three lines are weak and vanish at low T_e of the plasma. Furthermore, resonance lines may be optically thick which makes data evaluation more complex. The multiplet lines are intense and suitable for diagnostics. Rate coefficients for direct excitation were taken from the ADAS code package. Additionally, dissociative excitation from the molecule has to be taken into account. All rate coefficients are compiled in [Mei00]. For nitrogen/hydrogen mixtures the atomic hydrogen density was derived from the emission of the H_β line.

Electron temperatures and particle densities were measured in N_2/He and $N_2/H_2/He$ plasmas at 10 Pa, the results are compiled in Fig. 6.7. In all plasmas, T_e is around 2 eV. Molecular nitrogen densities which are spectroscopically measured are clearly below the real densities and show a decrease with increasing nitrogen contents in the plasmas. This indicates that depopulation of the excited level due to heavy particle collisions, i.e. quenching, occurs. In nitrogen/helium plasmas it is expected that the dominant ion density is N_2^+ and is therefore comparable to n_e . However, the radiation from this ion is decreases with increasing nitrogen density indicating also quenching effects.

Atomic nitrogen densities determined from two atomic lines are in good agreement and decrease one order of magnitude with increasing nitrogen density. This result is attributed to the decreasing T_e (2.5 to 1.5 eV) and is supported by the almost constant atomic density in nitrogen/hydrogen mixtures (≈ 2 eV). The degree of dissociation is low in nitrogen plasmas, ranging from 10% to 0.1% in N_2/He mixtures and from 0.01% to 0.001% in $N_2/H_2/He$ mixtures. The degree of dissociation for hydrogen is between 0.5% and 0.01% and is higher than the

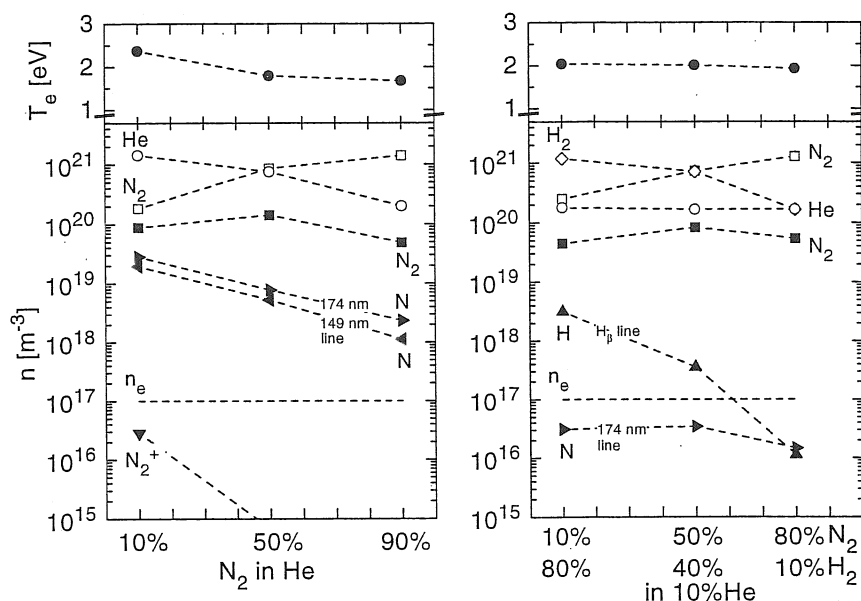


Figure 6.7: Electron temperatures and particle densities in N_2/He and $N_2/H_2/He$ plasmas determined by mass spectrometry (open symbols) and emission spectroscopy (full symbols).

one for nitrogen in N_2/H_2 mixtures. Evaluation of the nitrogen resonance lines in N_2/He plasmas results in atomic densities which are a factor of 20 below the densities derived from the line in the metastable system (174 nm line). This demonstrates that resonance lines are optically thick and their radiation is reabsorbed in the plasma. It has turned out that the 174 nm line is the most suitable line for diagnostics of atomic nitrogen densities.

6.2.2 Oxygen plasmas

In oxygen/helium plasmas various emission bands of O_2^+ have been observed from the first and second negative system of the molecular ion. In the case of molecular oxygen, the atmospheric absorption system was measured in emission. Due to the lack of data for emission rate coefficients for these molecular bands, only dependencies of the radiation with plasma parameters were observed. A variety of atomic oxygen lines were detected in the visible range as well as in the VUV/UV range. The following lines were chosen for diagnostics: 130 and 135 nm lines, both ending in the ground state. The first one is a resonance line whereas the second one is optically forbidden and is therefore weak. In the visible spectral range the multiplet lines at around 777 nm (in the metastable system) and 845 nm (in the ground state system) were measured. Cross sections for direct and dissociative excitation were taken from literature and are compiled in [Mei00].

Figure 6.8 shows results for three mixtures of oxygen with helium at a discharge pressure of 10 Pa. The electron temperature is between 3 eV and 2 eV decreasing with more admixture of oxygen. The contribution of dissociative ex-

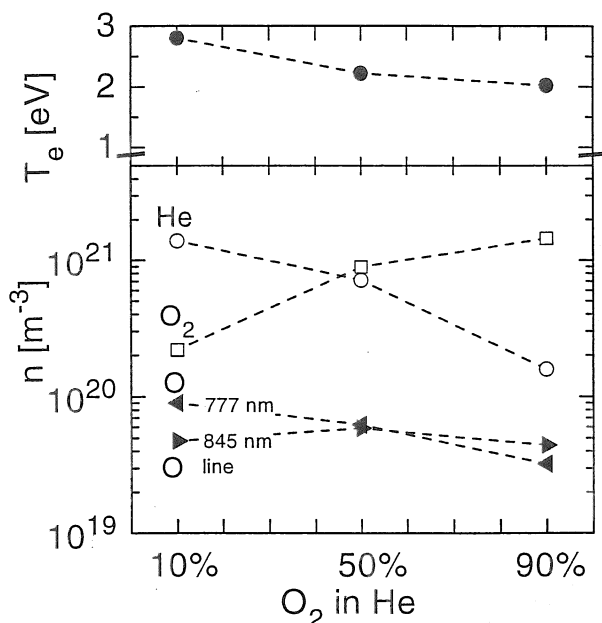


Figure 6.8: Electron temperatures and particle densities in O₂/He plasmas determined by mass spectrometry (open symbols) and emission spectroscopy (full symbols).

citation from O₂ to the 135 nm line was always dominant so that this line is not suitable for diagnostics. As in nitrogen or hydrogen plasmas, the resonance line of oxygen (130 nm) is optically thick. The intensities of the individual lines of the multiplet system vary with molecular density and are only for the lowest oxygen densities in agreement with the transition probabilities. Thus can be taken as a further indication of reabsorption. Atomic densities obtained from both lines in the visible spectral range agree well. The densities obtained are considerably high, resulting in dissociation degrees of about 30% – 3%. It should be mentioned that the lower electronic states of these lines are connected with resonance lines. As a consequence, the radiation of the lines in question may also be enhanced as it is the case for atomic hydrogen (reabsorption of Lyman lines have increased radiation of Balmer lines, Fig. 5.12). Therefore, oxygen densities shown in Fig. 6.8 represent an upper limit. Nevertheless, both lines in the visible range are suitable and very convenient for the determination of atomic densities.

6.2.3 Comparison of N₂, O₂, H₂ and D₂ plasmas

Figure 6.9 compares dissociation degrees of molecular plasmas in the ECR discharge for 10% and 90% contents of molecules in helium plasmas. The radiation of the following atomic lines were analysed: 845 nm line (O), 174 nm (N), H _{β} and D _{β} . Oxygen plasmas show the highest degree of dissociation in the plasmas investigated. In the case of 10% molecules in helium, nitrogen plasmas have a degree of dissociation of around 10%, which is between those of oxygen and hy-

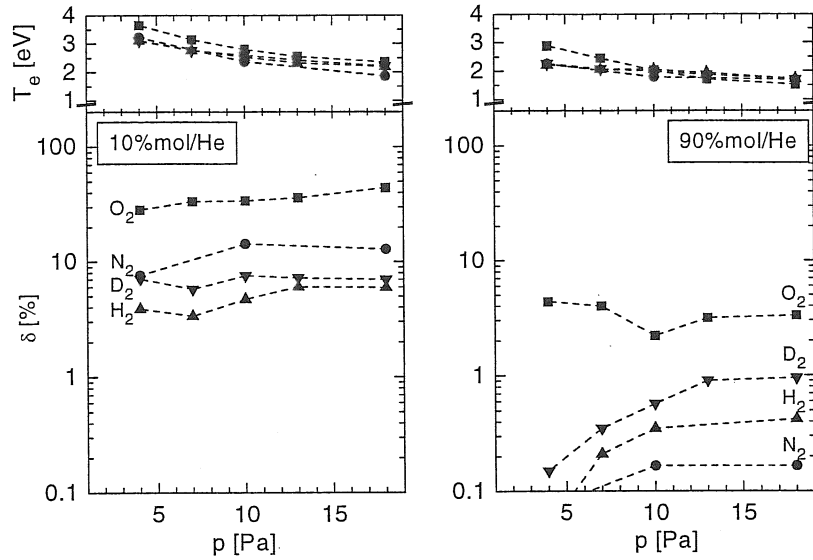


Figure 6.9: Comparison of dissociation degrees in 10% molecules/He plasmas as well as in 90% molecules/He plasmas using N_2 , O_2 , H_2 and D_2 as molecular gases.

drogen plasmas. Except for oxygen plasmas, T_e are comparable in all plasmas. The comparison of the two admixtures of molecules to helium show a strong decrease of δ with increasing molecular density. The degree of dissociation of oxygen plasmas remains almost constant with pressure at around 4%, whereas δ for the three other gases is between 1% and 0.1% or even lower. Here, nitrogen shows the lowest degree of dissociation. These results demonstrate the variation of atomic densities in diatomic molecular plasmas depending on the plasma conditions. Therefore it is necessary to measure atomic densities for each discharge in question separately. For this purpose, suitable lines for spectroscopic diagnostics, which has the advantage of in situ measurements, are now identified and checked for their application.

Chapter 7

Summary and Conclusions

Emission spectroscopy of low temperature plasmas was shown to be a powerful tool for the diagnostics of a variety of plasma parameters. Special emphasis was given to the diagnostics of hydrogen and deuterium plasmas, which are used in the wide field of plasma technology as well as in fusion experiments. The diagnostic methods for atoms and molecules in hydrogen and deuterium were established in laboratory experiments. The transferability to the cold divertor plasmas of fusion experiments was demonstrated with various examples.

Interpretation of atomic and molecular emission spectra depends strongly on plasma parameters and was supported by collisional-radiative models. The more plasma parameters are known the better is the possibility to study atomic and molecular processes in these plasmas in detail. Therefore, investigations were carried out in four types of laboratory plasmas, commonly used in plasma technology, i.e. glow discharges, RF, MW and ECR discharges. The plasma parameters were determined by a multitude of complementary diagnostics, and, in addition, could be varied over a wide range. Parameters which are not accessible by the diagnostic techniques were calculated using balance equations, for instance the particle balance to predict radical densities in the plasma. However, such calculations were checked for individual parameters by results from measurements.

Collisional-radiative models and modeling of plasma parameters require a lot of input data: cross sections or rate coefficients for excitation, ionization and dissociation for each excited state and particle species, to name a few of them. Interpretation of spectra and calculations of particle densities rely on the quality of these data. Therefore, data necessary for the presented investigations were compiled from literature, critically reviewed and selected if necessary. In particular, this work compiles data for the interpretation of molecular and atomic radiation, which enables measurements of particle densities and electron temperature by emission spectroscopy.

The electron energy distribution function was measured either with Langmuir probes or by spectroscopic methods, assisted by calculations based on the solution of the homogeneous Boltzmann equation. Electron densities were taken from Langmuir probe measurements, which provide spatially resolved results. Further-

more, microwave interferometry which gives results integrated along a line of sight through the plasma was used. In the case of glow discharges, electron densities were determined by measurements of the electrical conductivity. If the power coupled into the plasma is known rather than simply the generator power, a power balance also provides the electron density.

The demixing of gases in the plasma chamber, due to the vacuum system and valves or apertures, could be determined with a mass spectrometer. Thus, the neutral gas densities and the precise composition of the gas mixture were known. It was shown how compositions displayed by mass flow meters would lead to erroneous results for the densities. Additionally, the residual gas analyser was used to measure the dilution of dissociating gases in CH_4 or SiH_4 plasmas. A calibration of these systems, which contain higher hydrocarbons, led to a determination of the densities of such species in the plasma.

Emission spectroscopy of helium lines was applied as a standard diagnostic for electron temperature in laboratory plasmas. In most cases helium was used as buffer gas providing in addition, a method for the active variation of electron temperature in molecular plasmas. Since argon was also utilized as buffer or diagnostic gas, argon and helium plasmas were investigated in detail. Both gases have electronic states which are either metastable, or coupled directly with the ground state by spontaneous emission, so that the opacity of the resonance lines becomes important. In order to treat these levels correctly in the evaluation of emission lines originating from higher electronically excited states, their population have to be known. For this purpose absorption measurements were carried out in helium and argon plasmas as well as in gas mixtures. It turned out that metastable states and upper levels of resonance transitions are highly populated and have to be taken into account in the interpretation of emission lines. Therefore the simple coronal model is not sufficient for spectroscopic diagnostics and has either to be extended by including excitation mechanism out of the metastable states and opacity, or has to be replaced by a CR-model. The first method was chosen for argon since in this case a CR-model was not available. In the case of helium, two CR-models were used. Because the latest data are implemented in ADAS, and, because of its many fields of application, the ADAS code package was preferred. Opacity was also taken into account. It was shown that in these low pressure laboratory plasmas the opacity of resonance lines, and even the opacity of lines corresponding to transitions from metastable states to higher levels plays an important role and has to be considered in the determination of electron temperature. In particular, the enhancement of the population of those excited states higher in energy than both the resonance and metastable levels was demonstrated, and its effect included, by introducing so-called correction factors. The helium line at 728 nm was identified as the preferred diagnostic line, being the least sensitive of all the $n = 3$ to $n = 2$ transition lines to variations of opacity, metastable population etc.. In the case of argon, the 750 nm or 667 nm lines were recommended, since excitation out of metastable states and cascading from higher excited states play a minor role in their population mechanisms.

For hydrogen a CR-model was introduced which predicts populations of elec-

tronically excited states for atoms as well as for molecular hydrogen. Both systems are coupled with each other, so that dissociation of the molecule affects the population of atomic levels. In particular, the molecular ground state is vibrationally resolved, which allows predictions of vibrational populations. The original model was critically revised and some reactions were added. Furthermore, rate coefficients relevant to the population of vibrational levels in the ground state of the hydrogen molecule were transferred to deuterium molecules using similar data sources. This allows predictions for vibrational populations for deuterium as well as for hydrogen. Additionally, it was shown how effective rate coefficients for ionization or dissociation can be calculated by considering vibrational populations, leading to a considerable enhancement of these processes. Here, isotope effects are of special interest, in particular for predictions in cold regions of fusion experiments where also tritium is of importance.

The ADAS code package was preferred for the CR-model for atomic hydrogen since it contains the latest data. In addition, the opacity of resonance lines (Lyman series) was treated in the same manner as for helium. The modified version of the CR-model, discussed in the last paragraph, uses approximations valid for high opacity. In order to consider dissociative excitation from the molecule to the upper states of the Balmer lines, the corresponding rate coefficients were integrated into the ADAS input files. In contrast to the atomic case, dissociative excitation differs between the isotopes, and is smaller in the case of deuterium.

The radiation of the Balmer lines was analysed to determine atomic hydrogen densities in technical plasmas. A very good agreement between the results of each Balmer line was obtained only if the opacity of the Lyman lines and dissociative excitation of the molecule were taken into account. A method of analysing line ratios of Balmer lines for the determination of the degree of dissociation was introduced. The results of either method agreed well within their error bars. Typical degrees of dissociation which were observed in the laboratory plasmas investigated were 0.1% to 20%, varying with discharge pressure, helium admixture to hydrogen and, slightly, with the isotope.

Spatially resolved density measurements were presented in order to determine atomic hydrogen fluxes in the plasma. The measured density gradient, together with the diffusion coefficient yields the atomic flux directly. The atomic fluxes of hydrogen and deuterium are identical at comparable plasma parameters. By introducing additional surfaces into the plasma chamber atomic fluxes to the surface were obtained. Here, a dependence of atomic fluxes and densities on the material (high-grade steel and graphite) was measured as well as an isotope effect. The reflection coefficient derived from the measurements is low for hydrogen on high-grade steel whereas the reflection coefficient for deuterium on graphite is much higher.

Molecular radiation was investigated in order to determine molecular densities which were then compared with results from the gas analyser. The purpose of these investigations was to identify suitable molecular bands for diagnostics and, in particular, to check emission rate coefficients taken from various data bases. The preferred diagnostic band was identified to be the Fulcher band, in the visible

spectral range around 600 nm. It was also found to be suitable for diagnostics of vibrational and rotational populations. Nevertheless, discrepancies in molecular densities from emission spectroscopy were observed and are attributed to the uncertainty of the corresponding emission rate coefficients which will have to be examined in the future. Additionally, it was shown that the electron density dependence of rate coefficients has to be taken into account. This is important, in particular for the diagnostics of a divertor plasma undergoing a change in recycling regime, which leads to a change in electron density of more than one order of magnitude.

A new diagnostic method for the vibrational population in the ground state of the molecules was established. The radiation of various diagonal vibrational transitions of the Fulcher band yields the vibrational population in the excited state. For this purpose, selective quenching, lifetimes and predissociation as well as the Franck-Condon factors have to be taken into account. Under the assumption of a vibrational population distribution in the ground state, characterized for example by a vibrational temperature, the population transferred into excited states can be calculated via the Franck-Condon principle. The influence of vibrational excitation on the rate coefficients was taken into account by reducing threshold energies. The comparison of the measured and calculated vibrational population yields the vibrational temperature in the ground state of the molecule, which is the sole parameter for the fit. Since the method is only sensitive for the first five vibrational levels in the ground state, the assumption of a vibrational temperature is reasonable, a fact which was verified by calculations. Results of hydrogen and deuterium plasmas have shown a considerable vibrational temperature in the ground state, varying with hydrogen particle pressure from 2000 K up to 8000 K in the case of hydrogen. Deuterium was found to have lower vibrational temperatures. However, since deuterium has more closely spaced vibrational energy levels, the vibrational population of these levels was found to be almost identical to that of hydrogen. The method introduced has the great advantage of being easily applicable, in particular if the experiment is already furnished with spectroscopic systems.

Detailed investigations were carried out for the continuum radiation of hydrogen molecules which is intense in the spectral range of 160 – 400 nm. A computer program was developed to calculate Franck-Condon factors, transition probabilities and lifetimes of excited states in diatomic molecules. In the case of continuum radiation, the transition probabilities depend not only on the vibrational level in the excited state but also on the wavelength. If the corona model for the population of the electronically excited state is used, and a vibrational population is assumed, the whole continuum spectrum in the wavelength range between 120 and 600 nm can be predicted for all isotopes of hydrogen. On the other hand, calculated spectra can be fitted to measured radiation with electron temperature and vibrational population as parameters for the fit. The shape of the continuum is sensitive to the vibrational population, whereas the absolute radiation is sensitive to electron temperature, suggesting a diagnostic method for both parameters. The applicability was checked by a variety of measurements in

hydrogen and deuterium plasmas.

Proper diagnostic methods for the HD molecule in mixtures of hydrogen and deuterium have been presented. Again, as well as mass spectrometry, the Fulcher band is a possible candidate. Analysis of the Balmer lines gives atomic densities in the mixture and provides information about the formation of this molecule. Furthermore, vibrational temperatures were also measured and were found to be between those of hydrogen and deuterium molecules, as expected from the behaviour of the isotopes. It was found that the most effective way to produce HD molecules was to enhance heavy particle collisions ($H + D \rightarrow HD$) by increasing the pressure. Simultaneously, the degree of dissociation had to be high enough to provide as many atoms as possible for collision. This can be achieved by increasing the electron temperature, for instance by adding helium.

The diagnostic methods developed and established in laboratory plasmas at the Universität Augsburg were then applied to divertor plasmas of ASDEX Upgrade at the Max-Planck-Institut für Plasmaphysik. In contrast to low pressure laboratory plasmas, atoms and protons, rather than molecules and molecular ions dominate the divertor plasma. The Balmer line emission was related to the atomic hydrogen flux by using the S/XB ratio. In a similar manner, molecular radiation is related, by the $(S + D)/XB$ ratio, to the molecular flux. Both ratios rely on effective rate coefficients, which are adjusted by a CR-model to the pertinent plasma parameters. These parameters depend on the recycling regime of the divertor plasma, i.e. whether the plasma is attached or completely detached. Electron temperature and electron density dependencies were found to be as important as the degree of recombination or opacity and even as important as the molecular contribution to atomic radiation. Examples of calculated Balmer line ratios were given for determining some of these parameters.

In the analysis of molecular radiation, $(S + D)/XB$ was shown to be very sensitive to T_e in the low temperature region. Radiation of molecules can be observed only if T_e is high enough to excite the upper electronic state of the transition but, in this case, the molecules dissociate and ionize and their density decreases. Furthermore, molecules are produced only at the divertor tiles by recombining hydrogen atoms. As a consequence T_e (and, of course, also n_e) have to be known precisely for determining molecular fluxes. CR-model calculations of $(S + D)/XB$ have demonstrated that vibrational population in the ground state of the molecules is a further important parameter. The combination of CR-model and emission spectroscopy was shown to be a reasonably good tool for determining vibrational populations, T_e and molecular fluxes. In detached plasmas, molecules have a high vibrational population and molecular fluxes are comparable to atomic fluxes. Thus, extra reaction channels are available, which may affect plasma kinetics, for instance the energy balance.

The measurement of molecular radiation was suggested as a diagnostic method for T_e being complementary to other diagnostic methods such as Langmuir probes or atomic spectroscopy, e.g. measurements of the Balmer to Paschen continuum. The basic approach is the measurement of the vibrational population in the excited state. In divertor plasmas it is reasonable to assume that the vibrational

population in the ground state is determined only by electron collisions. In technical plasmas heavy particle collisions and wall collisions are also important. Thus, the modified CR-model is applicable for predictions of ground state vibrational populations up to all 15 vibrational levels of hydrogen and the same number for deuterium. The population distributions are correlated with T_e , the higher T_e the lower is the vibrational population. The transfer of the population into the excited state gives directly an accessible measured quantity. In hydrogen discharges results of the method were compared with results from Langmuir probes and atomic spectroscopy, filling the gap between the limits of the two methods in detached divertor plasmas. In a next step, the method was checked for both isotopes simultaneously by investigating specially designed discharges. The method was shown to be sensitive and applicable for either isotope.

The role of hydrogen molecules in divertor plasmas was investigated in detail by combining the spectroscopic diagnostics with plasma edge calculations, i.e. B2-EIRENE including the CR-model. Of special interest was the question whether molecules assist plasma recombination or not. For this purpose, the rate for molecular assisted recombination was compared directly with the rate of three-body and radiative recombination in the detached divertor of ASDEX Upgrade. Rate coefficients for molecular assisted recombination depend strongly on the vibrational population of the molecules in their ground state. Therefore, the EIRENE code was extended to include seven vibrational states which are treated as metastable states in the code. The code was run for plasma parameters corresponding to discharges where many measured results are available. The agreement between measurements and calculations was reasonable only if vibrational population was included in the code and if the CR-model for molecular hydrogen was used. In the next step reaction channels were investigated in detail on the bases of the B2-EIRENE results which gave a deeper insight into the molecular processes at the plasma edge. As a result of this study the contribution of molecules to volume recombination was found to occur only in a thin plasma layer in front of the surface. This leads to an overall effect of approximately a few percent. Instead of greatly enhancing plasma recombination it was shown in further investigations that vibrationally excited molecules can lead to a re-attachment of the plasma. This may be due to the opening of additional reaction channels which influence the energy balance.

Plasma wall interaction is one of the main topics of concern in fusion devices. Since carbon is one of the favoured elements as wall material, the bombardment of hydrogen plasma particles on graphite surfaces was investigated in a number of experiments which cover a wide range of plasma parameters. Thus, model calculations describing the chemical erosion of carbon could be confirmed which then allows extrapolations to the next stage of fusion plant. In laboratory plasmas the chemical erosion of graphite at low temperatures and low ion energies was investigated by spectroscopic techniques. Special emphasis was given to the isotope effect between hydrogen and deuterium, in order to obtain possible scaling laws for tritium. In the low pressure plasma used for these experiments, the dominant particle flow is atomic, the ion flow being a factor of approximately

100 lower. Therefore chemically enhanced erosion, or the synergistic effect, is observed. Additionally, it has to be kept in mind that the dominant ion species in such plasmas is H_3^+ rather than H^+ . For a substrate temperature of 300 K and an ion energy of 5.6 eV no isotope effect occurs but still an erosion yield of 0.15% remains. With increasing temperature or ion energy erosion yields are higher for deuterium than for hydrogen, by up to a factor of a maximum of two. Comparisons with calculations carried out using the semi-empirical model of Roth show significant discrepancies at lowest temperatures and ion energies but the agreement becomes better as these parameters are increased. The reason for the deviation is partly the measured synergistic effect, which is not described explicitly in the model, and partly the use of fitted threshold energies in the code. The results presented here fill the gap in the data base for the semi-empirical model so that calculations will become more reliable. A detailed analysis of the spectroscopic measurements has shown that results from weight loss measurements and spectroscopy agree only if in the latter the radiation of both the CH band and the C_2 band is considered. This means that the formation of higher hydrocarbons has to be taken into account when determining erosion yields from spectroscopic measurements, because the CH radiation is related to methane and the C_2 radiation is related to higher hydrocarbons (C_2H_2). Currently, erosion yields in fusion experiments are determined from the relation of the carbon flux and the radiation of the CH band, using the D/XB ratio, i.e. dissociation events of methane per emitted photon. The C_2 radiation offers now a spectroscopic diagnostic tool for the determination of C_2H_2 formation in the plasma edge of fusion experiments.

Hydrocarbon chemistry in plasmas was studied by generating methane plasmas and using mainly emission spectroscopy to determine particle densities. In particular, dissociative dissociation channels contributing to the radiation of CH, C_2 , and C radicals were identified. The rate coefficients necessary for the analysis of measured radiation were compiled and the applicability of spectroscopic diagnostics was shown for a variety of examples. Silane plasmas were also investigated and the similarity of methane and silane plasmas was highlighted. The dilution of both gases in a plasma is between a factor of two and ten, indicating a high degree of dissociation of methane and silane. The dominant molecule in these plasmas is hydrogen which is separated out during the dissociation chain. The next most common species are the higher hydrocarbons or silanes which are produced preferentially at higher pressures because of the increase of heavy particle collisions. As a consequence, the dominant ion species originate from these higher hydrocarbons or silanes. Model calculations for particle densities were validated by the measurements, so that predictions for particle densities which are not accessible to diagnostics may be assumed to be reliable. Furthermore, such modeling allows us to study the influence of individual reactions on the plasma composition as well as to identify the processes important in forming selected species. The relationship between plasma diagnostics and the properties of plasma produced films will lead to better understanding of film growth. The spectroscopic diagnostics of methane and silane plasmas presented here contribute to this end. Additionally, comparison of hydrocarbons in methane plasmas with hydrocarbons due to

chemical erosion of surfaces in contact with hydrogen plasmas contributes to an improved understanding of hydrocarbon chemistry in erosion processes.

Plasmas of diatomic gases other than hydrogen were also investigated. Of special interest is the degree of dissociation in nitrogen and oxygen plasmas, since they have applications in plasma processing. Emission lines in the visible and VUV/UV spectral range suitable for the determination of atomic densities were identified and emission rate coefficients for the analysis of radiation were compiled. Furthermore, dissociative excitations as well as the opacity of resonance lines have to be taken into account in a manner similar to the hydrogen case. Comparing nitrogen, oxygen and hydrogen plasmas generated in the same discharge under almost equal conditions, oxygen plasmas have the highest degree of dissociation. Nitrogen, hydrogen and deuterium are closer together, their order determined by electron temperature and molecular particle pressure.

In summary, the investigations presented have illustrated that emission spectroscopy of atoms and molecules in plasmas is a powerful tool in plasma diagnostics. New diagnostic methods, developed and established in low pressure laboratory plasmas, were applied to the low temperature divertor plasmas of fusion experiments. Interest was focused on hydrogen and deuterium plasmas in both plasma processing and fusion experiments. Furthermore, plasma wall interaction of hydrogen with, mainly, carbon surfaces as well as methane plasmas were investigated. The diagnostic methods introduced here form the basis for further investigations; the results contribute to a deeper insight into the molecular dynamics of these plasmas.

References

- [ABH71] J.F.M. Aarts, C.I.M. Beenakker, and F.J. de Heer, *Radiation from CH_4 and C_2H_2 produced by electron impact*, Physica **53** (1971), 32–44.
- [ACK95] P. Awakowicz, G. Cirpan, and W. Kasper, *Automatic langmuir probe and energy-mass spectroscopy measurements in methane-hydrogen ECWR plasmas*, Proc. of XXII Int. Conf. on Phenomena in Ionized Gases (Hoboken, New Jersey), vol. 2, 1995, pp. 173–174.
- [AF89] O. Auciello and D.L. Flamm, *Plasma diagnostics, Vol. I: Discharge parameters and chemistry*, Academic Press, San Diego, 1989.
- [AGL00] L.W. Anderson, A.N. Goyette, and J.E. Lawler, *Advances in atomic, molecular and optical physics*, vol. 43, ch. Uses of High-Sensitivity White-Light Absorption Spectroscopy in Chemical Vapor Deposition and Plasma Processing, pp. 295–339, Academic Press, San Diego, 2000.
- [Beh90] K. Behringer, *Measurement of CH_4/CD_4 fluxes and of chemical carbon erosion from CH/CD band emission*, J. Nucl. Mater. **176&177** (1990), 606–610.
- [Beh91] K. Behringer, *Diagnostics and modelling of ECRH microwave discharges*, Plasma Phys. Contr. Fusion **33** (1991), 997–1028.
- [Beh98] K. Behringer, *Escape factors for line emission and population calculation*, Report IPP 10/11, IPP, Munich, 1998.
- [Beh00] K. Behringer, *Section: Experimental plasma physics division 4*, Annual report, IPP, 2000.
- [BF94] K. Behringer and U. Fantz, *Spectroscopic diagnostics of glow discharge plasmas with non-Maxwellian electron energy distributions*, J. Phys. D: Appl. Phys. **27** (1994), 2128–2135.
- [BF00] K. Behringer and U. Fantz, *The influence of opacity on hydrogen excited-state population and applications to low-temperature plasmas*, New J. Phys. **2** (2000), 23.1–23.19.

- [BMP⁺00] S. Brezinsek, Ph. Mertens, A. Pospieszczyk, G. Sergienko, and P.T. Greenland, *Molecules in the plasma edge of TEXTOR-94*, WHYPHE (Workshop on Hydrogen in the Plasma Edge), KFZ Jülich, IPP, 2000.
- [BOSS95] A.J.M. Buuron, D.K. Otorbaev, M.C.M. van de Sanden, and D.C. Schram, *A new absorption spectroscopy setup for the sensitive monitoring of atomic and molecular densities*, Rev. Sci. Instrum. **66** (1995), 968–974.
- [BPG⁺99] J.B. Boffard, G.A. Piech, M.F. Gehrke, L.W. Anderson, and C.C. Lin, *Measurement of electron-impact excitation cross section out of metastable levels of argon and comparison with ground-state excitation*, Phys. Rev. A **59** (1999), 2749–2763.
- [Bra87] B.J. Braams, *A multi-fluid code for simulation of the edge plasma in tokamaks*, Report EUR-FU IXII-80-87-68, NET, Comm. of the European Communities, 1987.
- [Bro61] S.C. Brown, *Basic data of plasma physics*, MIT, Cambridge, MA, 1961.
- [BS76] A. Burgess and H.P. Summers, *The recombination of level populations of ions-I*, Mon. Not. R. Astr. Soc. **174** (1976), 345–391.
- [BSD⁺89] K. Behringer, H.P. Summers, B. Denne, M. Forrest, and M. Stamp, *Spectroscopic determination of impurity influx from localized surfaces*, Plasma Phys. Contr. Fusion **31** (1989), 2059–2099.
- [CBSA99] D.P. Coster, K. Borrass, R. Schneider, and ASDEX Upgrade Team, *B2-EIRENE modelling of the density limit on ASDEX Upgrade*, J. Nucl. Mat. **266–269** (1999), 804–808.
- [CBSL98] J.E. Chilton, J.B. Boffard, R.S. Schappe, and C.C. Lin, *Measurement of electron-impact excitation into the $3p^5 4p$ levels of argon using Fourier-transform spectroscopy*, Phys. Rev. A **57** (1998), 267–277.
- [CC81] A. Chutjian and D.C. Cartwright, *Electron-impact excitation of electronic states in argon at incident energies between 16 and 100 eV*, Phys. Rev. A **23** (1981), 2178–2193.
- [CGL93] M. Capitelli, C. Gorse, and S. Longo, *Microwave discharges, fundamentals and applications*, C. M. Ferreira and M. Moisan ed., vol. Physics 302, NATO ASI Series B, 1993.
- [Cha87] P.J. Chantry, *A simple formula for diffusion calculations involving wall reflection and low density*, J. Appl. Phys. **62** (1987), 1141–1148.
- [Che74] F.F. Chen, *Introduction to plasma physics*, Plenum Press, New York and London, 1974.

- [CHRG84] H. Chatham, D. Hils, R. Robertson, and A. Gallagher, *Total and partial electron collisional ionization cross section for CH₄, C₂H₆, SiH₄ and Si₂H₆*, J. Chem Phys. **81** (1984), 1770–1777.
- [CJ95] R. Celiberto and R.K. Janev, *Analytic representation of electron impact excitation cross sections of vibrationally excited H₂ and D₂ molecules*, Report INDC(NDS)-333, IAEA, Vienna, 1995.
- [CLC⁺99] R. Celiberto, A. Laricchiuta, M. Capitelli, R.K. Janev, J. Wadhera, and D.E. Atems, *Cross section data for electron-impact inelastic processes of vibrationally excited hydrogen molecules and their isotopes*, Report INDC(NDS)-397, IAEA, Vienna, 1999.
- [CM71] A. Cornu and A. Massot, *Compilation of mass spectral data*, Heyden & Son Ltd., London, 1971.
- [CS00] H. Conrads and M. Schmidt, *Plasma generation and plasma sources*, Plasma Sources Sci. Technol. **9** (2000), 441–454.
- [CSN⁺97] D.P. Coster, R. Schneider, J. Neuhauser, H.-S. Bosch, R. Wunderlich, C. Fuchs, F. Mast, A. Kallenbach, R. Dux, G. Becker, ASDEX Upgrade Team, B.J. Braams, and D. Reiter, *B2-EIRENE modelling of ASDEX Upgrade*, J. Nucl. Mater. **241-243** (1997), 690–695.
- [DCG00] H.F. Döbele, U. Czarnetzki, and A. Goehlich, *Diagnostics of atoms by laser spectroscopic methods in plasmas and plasma-wall interaction studies (vacuum ultraviolet and two-photon techniques)*, Plasma Sources Sci. Technol. **9** (2000), 477–491.
- [DE73] H.W. Drawin and F. Emard, *Tables of reduced population coefficients for the levels of atomic helium*, Report EUR-CEA-FC-697, Association EURATOM-C.E.A., France, 1973.
- [DEK73] H.W. Drawin, F. Emard, and K. Katsonis, *Calculation of population densities of helium atoms in non-L.T.E. plasmas*, Z. Naturforsch. **28a** (1973), 1422–1431.
- [Dra69] H.W. Drawin, *Collisional-radiative ionization and recombination coefficients for quasi-stationary homogeneous hydrogen and hydrogenic plasmas*, Z. Naturforsch. **225** (1969), 470–482.
- [Dru30] M.J. Druyvesteyn, Physica **10** (1930), 61–70.
- [Fan98] U. Fantz, *Spectroscopic diagnostics and modelling of silane microwave plasmas*, Plasma. Phys. Control. Fusion **40** (1998), 1035–1056.
- [FBC⁺99] U. Fantz, K. Behringer, D. Coster, R. Schneider, D. Reiter, and ASDEX Upgrade Team, *Molecular enhanced recombination in the divertor of ASDEX Upgrade*, ECA Vol. **23J** (1999), 1549–1552.

- [FBG⁺99] U. Fantz, K. Behringer, J. Gafert, D. Coster, and ASDEX Upgrade Team, *Optical emission measurements of H_2 and D_2 molecules in the divertor region of ASDEX Upgrade*, J. Nucl. Mat. **266–269** (1999), 490–494.
- [FH98] U. Fantz and B. Heger, *Spectroscopic diagnostics of the vibrational population in the ground state of H_2 and D_2 molecules*, Plasma. Phys. Control. Fusion **40** (1998), 2023–2032.
- [FHB96] U. Fantz, B. Heger, and K. Behringer, *Besetzung der Vibrations- und Rotationszustände von H_2 und N_2 in Niederdruckplasmen*, Verhandl. DPG (VI), vol. 31, 1996, p. 775.
- [FHW01] U. Fantz, B. Heger, and D. Wunderlich, *Using the radiation of hydrogen molecules for electron temperature diagnostics of divertor plasmas*, Plasma. Phys. Control. Fusion **43** (2001), 907–918.
- [FL84] C.M. Ferreira and J. Loureiro, *Characteristics of high-frequency and direct-current argon discharges at low pressure*, J. Phys. D: Appl. Phys. **17** (1984), 1175–1188.
- [FL00] C.M. Ferreira and J. Loureiro, *Electron kinetics in atomic and molecular plasmas*, Plasma Sources Sci. Technol. **9** (2000), 528–540.
- [FMS88] T. Fujimoto, S. Miyachi, and K. Sawada, *New density diagnostic method based on emission line intensity ratio of neutral hydrogen in an ionizing phase plasma*, Nucl. Fusion **28** (1988), 1255–1263.
- [FP01] U. Fantz and H. Paulin, *Chemical erosion of carbon at low temperatures and low ion energies*, Phys. Scripta **T91** (2001), 43–46.
- [FRHC01] U. Fantz, D. Reiter, B. Heger, and D. Coster, *Hydrogen molecules in the divertor of ASDEX Upgrade*, J. Nucl. Mat. **290–293** (2001), 367–373.
- [FSB00] U. Fantz, B. Schalk, and K. Behringer, *Calculation and interpretation of the continuum radiation of hydrogen molecules*, New J. Phys. **2** (2000), 7.1–7.15.
- [FST89] T. Fujimoto, K. Sawada, and K. Takahata, *Ratio of Balmer line intensities resulting from dissociative excitation of molecular hydrogen in an ionizing plasma*, J. Appl. Phys. **66** (1989), 2315–2319.
- [Fuj79a] T. Fujimoto, *A collisional-radiative model for helium and its application to a discharge plasma*, J. Quant. Spectrosc. Radiat. Transfer **21** (1979), 439–455.
- [Fuj79b] T. Fujimoto, *Kinetics of ionization-recombination of a plasma and population density of excited ions. I. Equilibrium plasma*, J. Phys. Soc. Jpn. **47** (1979), 265–272.

- [Fuj79c] T. Fujimoto, *Kinetics of ionization–recombination of a plasma and population density of excited ions. II. Ionizing plasma*, J. Phys. Soc. Jpn. **47** (1979), 273–281.
- [Fuj95] T. Fujimoto, *private communication*, 1995.
- [GBC⁺99] J. Gafert, K. Behringer, D. Coster, C. Dorn, A. Kallenbach, R. Schneider, U. Schumacher, and ASDEX Upgrade Team, *Spectroscopic investigations of the dynamics of ions and neutrals in the ASDEX Upgrade divertor II*, J. Nucl. Mat. **266–269** (1999), 365–369.
- [GR96] P.T. Greenland and D. Reiter, *The rôle of molecular hydrogen in plasma recombination*, Report Jü-3258, IPP, KFA Jülich, 1996.
- [Gre01] P.T. Greenland, *Collisional–radiative models with molecules*, Proc. R. Soc. Lond. A **457** (2001), 1821–1839.
- [Gri64] H.R. Griem, *Plasma spectroscopy*, McGraw–Hill, New York, 1964.
- [Gri94] A. Grill, *Cold plasma in materials technology: From fundamentals to applications*, IEEE Press, New York, 1994.
- [GZS80] V.E. Golant, A.P. Zhilinsky, and I.E. Sakharov, *Fundamental of plasma physics*, John Wiley & Sons, New York, 1980.
- [HCB64] J.O. Hirschfelder, C.F. Curtiss, and R.B. Bird, *Molecular theory of gases and liquids*, Wiley, New York, 1964.
- [Heg98] B. Heger, *Spektroskopische Untersuchung der H₂- und D₂-Vibrationsbesetzung in ECR-Plasmen*, Diploma Thesis, University of Augsburg, 1998.
- [Heg02] B. Heger, *Untersuchung und Interpretation der Molekülstrahlung von Wasserstoff und Deuterium in Niederdruckplasmen*, PhD. Thesis, University of Augsburg, 2002.
- [Her50] G. Herzberg, *Molecular spectra and molecular structure I. Spectra of diatomic molecules*, Van Nostrand Reinhold, New York, 1950.
- [HFB00] B. Heger, U. Fantz, and K. Behringer, *Umverteilungsprozesse in H₂- und D₂-Niederdruckplasmen*, Verhandl. DPG (VI), vol. 35, 2000, p. 1022.
- [HFBA01] B. Heger, U. Fantz, K. Behringer, and ASDEX Upgrade Team, *Vibrational population of the ground state of H₂ and D₂ in the divertor of ASDEX Upgrade*, J. Nucl. Mater **290–293** (2001), 413–417.
- [HHKS92] F. J. De Heer, R. Hoekstra, A. E. Kingston, and H. P. Summers, *Excitation of neutral helium by electron impact*, Report JET-P(92)09, JET, Abingdon, 1992.

- [Hol47] T. Holstein, *Imprisonment of resonance radiation in gases*, Phys. Rev. **72** (1947), 1212–1233.
- [Hol51] T. Holstein, *Imprisonment of resonance radiation in gases.II*, Phys. Rev. **83** (1951), 1159–1168.
- [HSB⁺94] A. Horn, A. Schenk, J. Biener, B. Winter, C. Lutterloh, M. Wittman, and J. Küppers, *H atom impact induced chemical erosion reaction at C:H film surfaces*, Chem. Phys. Lett. **231** (1994), 193–198.
- [Hut87] I.H. Hutchinson, *Principles of plasma diagnostics*, Cambridge University Press, Cambridge, 1987.
- [ITE99] ITER, *ITER Physics Basis*, Nucl. Fus. **39** (1999), 2137–2638.
- [Jac98] W. Jacob, *Surface reactions during growth and erosion of hydrocarbon films*, Thin Solid Films **326** (1998), 1–42.
- [Jan92] G. Janzen, *Plasmatechnik: Grundlagen, Anwendungen, Diagnostik*, Hüthig, Heidelberg, 1992.
- [JH73] L.C. Johnson and E. Hinnov, *Ionization, recombination, and population of excited levels in hydrogen plasmas*, J. Quant. Spectrosc. Radiat. Transf. **13** (1973), 333–358.
- [JLEP87] R.K. Janev, W.D. Langer, J.K. Evans, and D.E. Post, *Elementary processes in hydrogen-helium plasmas*, Springer, Berlin, 1987.
- [Kas95] W. Kasper, *Automatic Langmuir probe measurements in triaxial-technology*, Proc of XXII Conference on Phenomena in Ionized Gases (Hoboken, New Jersey), vol. 2, 1995, pp. 171–172.
- [Kor93] U. Kortshagen, *A non-local kinetic model applied to microwave produced plasmas in cylindrical geometry*, J. Phys. D.: Appl. Phys. **26** (1993), 1691–1699.
- [Kov69] I. Kovács, *Rotational structure in the spectra of diatomic molecules*, ADAM Hilger Ltd., London, 1969.
- [KPSS97] S.I. Krashennnikov, A. Yu. Pigarov, T.K. Soboleva, and D.J. Sigmar, *Plasma-neutral gas interaction in a tokamak divertor: Effects of hydrogen molecules and plasma recombination*, J. Nucl. Mater. **241–243** (1997), 283–287.
- [KRMM96] R.J. Kee, F. M. Rupley, E.M. Miller, and J. A. Miller, *CHEMKIN III*, webpage <http://www.ca.sandia.gov/chemkin/>, Sandia National Laboratories, Sandia, 1996.
- [KT98] U. Kortshagen and L.D. Tsendin, *Electron kinetics and applications of glow discharges*, Plenum Press, New York, 1998.

- [KU00] H. Kempkens and J. Uhlenbusch, *Scattering diagnostics of low-temperature plasmas: Rayleigh scattering, Thomson scattering, CARS*, Plasma Sources Sci. Technol. **9** (2000), 492–506.
- [Lan24] I. Langmuir, Gen. Elec. Rev. **27** (1924), 449.
- [LH68] W. Lochte-Holtgreven, *Plasma diagnostics*, North-Holland Publishing, Amsterdam, 1968.
- [Lot67] W. Lotz, *An empirical formula for the electron-impact ionization cross-section*, Z. Physik **206** (1967), 205.
- [Lot00] A. Lotter, *Absorptionsmessungen an ECR-Plasmen im sichtbaren Spektralbereich*, Diploma Thesis, University of Augsburg, 2000.
- [LSAL92] R.B. Lockwood, F.A. Sharpton, L.W. Anderson, and C.C. Lin, *Cross sections for electron excitation out of the metastable levels of helium into the higher singlet levels*, Phys. Letters A **166** (1992), 357–360.
- [Mei00] S. Meir, *Spektroskopische Diagnostik im VUV/UV und sichtbaren Spektralbereich*, Diploma Thesis, University of Augsburg, 2000.
- [MH76] G.R. Möhlmann and F.J. de Heer, *Emission cross section of the H_2 ($3p^3\Pi_u - 2s^3\Sigma_g^+$) transition for electron impact on H_2* , Chem. Phys. Lett. **43** (1976), 240–244.
- [MHL77] G.R. Möhlmann, F.J. de Heer, and J. Los, *Emission cross section of Balmer- α , β , γ radiation for electrons (0 – 2000 eV) on H_2 and D_2* , Chem. Phys. **25** (1977), 103–116.
- [ML98] J. Marec and P. Leprince, *Recent trends and developments of microwave discharges*, J. Phys. IV France **8** (1998), Pr7–1.
- [Möl93] W. Möller, *Plasma and surface modeling of the deposition of hydrogenated carbon films from low-pressure methane plasmas*, Appl. Phys. A **56** (1993), 527–546.
- [MRDR01] L. Mechold, J. Röpcke, X. Duten, and A. Rousseau, *On the hydrocarbon chemistry in a H_2 surface wave discharge containing methane*, Plasma Sources Sci. Technol. **10** (2001), 52–60.
- [MSL26] H.M. Mott-Smith and I. Langmuir, *The theory of collectors in gaseous discharges*, Phys. Rev. **28** (1926), 727–763.
- [MTG72] W.T. Miles, R. Thompson, and A.E.S. Green, *Electron impact cross sections and energy deposition in molecular hydrogen*, J. Appl. Phys. **43** (1972), 678–686.

- [Mum72] M.J. Mumma, *Molecular branching-ratio method for intensity calibration of optical systems in the vacuum ultraviolet*, J. Opt. Soc. Am. **62** (1972), 1459–1466.
- [Ond00] T. Ondak, *Erweiterung und Anwendung des Programms HoBo zur Berechnung von Elektronenenergieverteilungsfunktionen in Niederdruckplasmen*, Zulassungsarbeit, University of Augsburg, 2000.
- [OSS95] D.K. Otorbaev, M.C.M. van de Sanden, and D.C. Schram, *Heterogeneous and homogeneous hydrogen kinetics in plasma chemistry*, Plasma Source Sci. Technol. **4** (1995), 292–301.
- [Pau00] H. Paulin, *Chemische Erosion von Kohlenstoff in H_2 und D_2 Plasmen*, PhD. Thesis, University of Augsburg, 2000.
- [PB86] D.E. Post and R. Behrisch, *Physics of plasma-wall interactions in controlled fusion*, vol. NATO ASI Series, Series B, v. 131, Plenum Press, New York, 1986.
- [Pec98] P. Pecher, *Quantitative determination of the particle fluxes emanating from methane ECR plasmas*, report IPP 9/118, IPP, Munich, 1998.
- [PLB96] J. Perrin, O. Leroy, and C. Bordage, *Cross-sections, rate constants and transport coefficients in silane plasma chemistry*, Contrib. Plasma Phys. **36** (1996), 3–49.
- [PMS⁺99] A. Pospieszczyk, Ph. Mertens, G. Sergienko, A. Huber, V. Philipps, D. Reiter, D. Rusbüldt, B. Schweer, E. Vietzke, and P.T. Greenland, *In situ measurement and modelling of hydrogen recycling and transport processes – the role of molecules*, J. Nucl. Mater. **266–268** (1999), 138–145.
- [PPE⁺97] V. Philipps, A. Pospieszczyk, H.G. Esser, U. Kögler, G. Mank, U. Samm, B. Schweer, J. von Seggern, B. Unterberg, E. Vietzke, F. Weschenfelder, P. Wienhold, J. Winter, and the TEXTOR Team, *Impurity release and deposition processes close to limiter surfaces in TEXTOR-94*, J. Nucl. Mater. **241–243** (1997), 105–117.
- [PSR⁺82] J. Perrin, J.P.M. Schmitt, G. de Rosny, B. Drevillon, J. Huc, and A. Lloret, *Dissociation cross section of silane and disilane by electron impact*, Chem. Phys. **73** (1982), 388–394.
- [Räu98] E. Räuchle, *Duo-plasmaline, a surface wave sustained linearly extended discharge*, J. Phys. IV France **8** (1998), PR7–99.
- [Rei92] D. Reiter, *Progress in two-dimensional plasma edge modelling*, J. Nucl. Mater. **196–198** (1992), 80–89.

- [Rei00] D. Reiter, *The data file AMJUEL: Additional atomic and molecular data for EIRENE*, Electronic File, KFA Jülich, May 2000.
- [RGR96] J. Roth and C. García-Rosales, *Analytic description of the chemical erosion of graphite by hydrogen ions*, Nucl. Fus. **36** (1996), 1647–1659.
- [RGR97] J. Roth and C. García-Rosales, *Corrigendum: Analytic description of the chemical erosion of graphite by hydrogen ions*, Nucl. Fus. **37** (1997), 897.
- [RMBB97] D. Reiter, Chr. May, M. Baelmans, and P. Börner, *Non-linear effects on neutral gas transport in divertors*, J. Nucl. Mater. **241–243** (1997), 342–348.
- [Rot95] J.R. Roth, *Industrial plasma engineering*, Institute of Physics Publishing, Bristol and Philadelphia, 1995.
- [Rot01] J. Roth, *Synopsis of erosion and redeposition*, Phys. Scripta **TIC 116** (2001), in print.
- [SBC⁺99] R. Schneider, H.-S. Bosch, D. Coster, J.C. Fuchs, G. Haas, A. Herrmann, M. Kaufmann, A. Kallenbach, J. Neuhauser, J. Schweinzer, U. Wenzel, and ASDEX Upgrade Team, *Role of divertor geometry on detachment in ASDEX Upgrade*, J. Nucl. Mat. **266–269** (1999), 175–181.
- [Sch93] U. Schumacher, *Fusionsforschung*, Wissenschaftliche Buchgesellschaft Darmstadt, Darmstadt, 1993.
- [Sch94] G. Schneider, *Modellierung eines ECR-Silanplasmas*, Diploma Thesis, University of Stuttgart, 1994.
- [Sch95] T. Schütte, *Laser-induzierte Fluoreszenzmessungen und Emissionsspektroskopie am ECR-Methanplasma*, PhD. Thesis, University of Stuttgart, 1995.
- [Sch00a] W. Schabert, *Modellierung eines detachten Divertorplasmas in ASDEX Upgrade mit dem Randschichtcode B2-EIRENE*, Praktikumsbericht, University of Augsburg, 2000.
- [Sch00b] K. Schmidtman, *Spektroskopische Untersuchung der Strahlungsrekombination im Divertor von ASDEX Upgrade*, Report IPP 10/15, IPP, Munich, 2000.
- [SEF93] K. Sawada, K. Eriguchi, and T. Fujimoto, *Hydrogen-atom spectroscopy of the ionizing plasma containing molecular hydrogen: Line intensities and ionization rate*, J. Appl. Phys **73** (1993), 8122–8125.

- [SF95] K. Sawada and T. Fujimoto, *Effective ionization and dissociation rate coefficients of molecular hydrogen in plasma*, J. Appl. Phys **78** (1995), 2913–2924.
- [SFAP01] P. Scheubert, U. Fantz, P. Awakowicz, and H. Paulin, *Experimental and theoretical characterization of an ICP source*, J. Appl. Phys. **90** (2001), 587–598.
- [Sha71] T.E. Sharp, *Potential-energy curves for molecular hydrogen and its ions*, Atomic Data (1971), 119–169.
- [She81] V.P. Shevelko, *Atoms and their spectroscopic properties*, Springer-Verlag, Berlin Heidelberg, 1981.
- [Sig00] Siglo, *Data Base*, <http://www.sni.net/siglo>, 2000.
- [SJB66] I.P. Shkarofsky, T.W. Johnston, and M.P. Bachynski, *The particle kinetics of plasma*, Addison-Wesley, Reading, MA, 1966.
- [Sob89] N.N. Sobolev, *Electron-excited molecules in nonequilibrium plasma*, Nova Science Publishers, New York, 1989.
- [SRZ⁺92] R. Schneider, D. Reiter, H.P. Zehrfeld, B. Braams, M. Baelmans, J. Geiger, H. Kastelewicz, J. Neuhauser, and R. Wunderlich, *B2-EIRENE simulation of ASDEX and ASDEX Upgrade scrape-off layer plasmas*, J. Nucl. Mater. **196-198** (1992), 810–815.
- [SS70] J.D. Swift and M.J.R. Schwar, *Electrical probes for plasma diagnostics*, Iliffe, London, 1970.
- [ST98] D.T. Stibbe and J. Tennyson, *Near-threshold electron impact dissociation of H₂ within the adiabatic nuclei approximation*, New J. Phys. **1** (1998), 2.1–2.9.
- [Sta00a] P.S. Stangeby, *The plasma boundary of magnetic fusion devices*, Institute of Physics Publishing, Bristol, 2000.
- [Sta00b] P. Starke, *Anwendung verschiedener Diagnostikmethoden an ECR-Plasmen: Mikrowelleninterferometrie, Langmuir-Sonde und optische Emissionsspektroskopie*, Diploma Thesis, University of Augsburg, 2000.
- [Sum99] H.P. Summers, *ADAS user manual version 2.1*, webpage <http://adas.phys.strath.ac.uk>, University of Strathclyde, Glasgow, 1999.
- [SVY81] I.I. Sobelman, L.A. Vainshtein, and E.A. Yukov, *Excitation of atoms and broadening of spectral lines*, Springer-Verlag, Berlin Heidelberg, 1981.

- [TIN⁺90] H. Tawara, J. Itikawa, H. Nishimura, H. Tanaka, and Y. Nakamura, *Collision data involving hydro-carbon molecules*, Report NIFS-DATA-6, NIFS, Nagoya, Japan, 1990.
- [TL29] L. Tonks and I. Langmuir, *A general theory of the plasma of an arc*, Phys. Rev. **34** (1929), 876–922.
- [TLJ99] A.P. Thorne, U. Litzén, and S. Johansson, *Spectrophysics: Principles and applications*, Springer-Verlag, Berlin Heidelberg, 1999.
- [TT82] H. Telle and U. Telle, *FCFRKR – A procedure to evaluate Franck-Condon type integrals for diatomic molecules*, Comput. Phys. Com. **28** (1982), 1–25.
- [Vin99] I.P. Vinogradov, *Development and applications of spectroscopic determinations of the electron energy distribution function in discharges*, Plasma Sources Sci. Technol. **8** (1999), 299–312.
- [Vlč89] J. Vlček, *A collisional-radiative model applicable to argon discharges over a wide range of conditions. I: Formulation and basic data*, J. Phys. D: Appl. Phys. **22** (1989), 623–631.
- [VP89] J. Vlček and V. Pelikan, *A collisional-radiative model applicable to argon discharges over a wide range of conditions. II: Application to low-pressure, hollow-cathode arc and low-pressure glow discharges*, J. Phys. D: Appl. Phys. **22** (1989), 632–643.
- [VWH99] E. Vietzke, M. Wada, and M. Hennes, *Reflection and absorption of deuterium atoms and molecules on graphite*, J. Nucl. Mater. **266–268** (1999), 324–329.
- [Wes87] J. Wesson, *Tokamaks*, Clarendon Press, Oxford, 1987.
- [WF01] D. Wunderlich and U. Fantz, *A collisional-radiative model for H₂ and H: Extensions and applications*, Report IPP 10/18, IPP, Garching, Germany, 2001.
- [ZB95] H. Zohm and H.J.de Blank, *Summer university of plasma physics*, Summarized Contributions, September 1995.

List of Symbols

α	degree of ionization
$\alpha(T_e)$	radiative recombination coefficient
$A_{i,k}$	transition probability from state i to state k
A_p	surface of a cylindrical electrode of probes
$\beta(T_e)$	three-body recombination coefficient
$B_{k,p}$	Einstein's transition probability for absorption
B_v	rotational constant of vibrational level v
c	velocity of light
D_k	diffusion coefficient of particle species k
D_n	diffusion coefficient of neutral particles
D_a	ambipolar diffusion coefficient
D, D_{eff}	(effective) rate coefficients for dissociation
ϵ_0	permittivity of free space
$\epsilon_{p,k}$	line emission coefficient
ϵ_ν	spectral emission coefficient
E	energy
$\langle E \rangle$	average kinetic energy
E_p	energy of level p
E_{thr}	threshold energy
E_{ion}	ionization energy
E_{el}	electrical field strength
f	oscillator strength (f-value)
$f(E)$	electron distribution function
$F(\mathbf{r}, \mathbf{v}, t)$	electron distribution function in the six-dimensional phase space \mathbf{r}, \mathbf{v}
Γ	particle flux
g_p	statistical weight of level p
I_ν	spectral intensity
h	Planck's constant
$I_{e,r}$	electron retarding current
$I_{e,s}$	electron saturation current
I_i	ion saturation current
j	electrical current density
j_k	gas flow of particle species k
J	rotational quantum number
$\kappa(\nu)$	absorption coefficient at frequency ν

$\kappa_{k,p}(\nu)$	spectral line absorption coefficient at frequency ν
k	Boltzmann's constant
λ	wavelength
$\Delta\lambda_D$	Doppler width
λ_k	mean free path of particle species k
Λ	diffusion length
$L_\lambda(\lambda)$	spectral radiance
l_α	extrapolation length
l_d	characteristic length of the plasma chamber
μ	atomic mass number
m_e	mass of neutral particles
m_n	electron mass
m_p	proton mass
$\dot{N}_{p,k}$	number of emitted photons per unit volume and time, line radiation
ν	frequency
ν_c	collision frequency
n	density
n_0	atomic or molecular density
n_1	population density in the ground state of an atom or molecule
n_e	electron density
n_i	ion density
n_n	neutral particle density
n_k	neutral particle density of species k
n_Z	particle density in the ionization stage Z
$n(p)$	population density in level p
Ω	solid angle
P_λ	spectral line profile
Q	quenching coefficient
$r_0(p)$	(reduced) population coefficient no 0
$r_1(p)$	(reduced) population coefficient no 1
$R_0(p)$	collisional-radiative coupling coefficient to the ion density
$R_1(p)$	collisional-radiative coupling coefficient to the ground state density
$R_{pq;kr}$	reaction rate coefficient from species p, q to species k, r
R^{3+r}	rate for three-body and radiative recombination of the hydrogen atom
R, H	cylinder with radius R and length H
R	reflection coefficient of atomic hydrogen on surfaces
$\sigma_{1,p}(E)$	excitation cross section from level 1 to level p
σ_{el}	electrical conductivity
s	sticking coefficient
S, S_{eff}	(effective) rate coefficient for ionization
S_ν	source function
$S_{Z,Z+1}(T_e)$	ionization rate coefficient from state Z to $Z + 1$
$\tau(\nu)$	optical thickness at frequency ν
$d\tau$	optical depth
τ_k	confinement time of neutral particle species k

τ_p	confinement time due to pumping gas flow
$\Theta_{p,k}$	escape factor
T	temperature
T_e	electron temperature
T_i	ion temperature
T_n, T_g	heavy particle temperature, gas temperature
T_{rot}	rotational temperature
T_s	substrate temperature
T_{vib}	vibrational temperature
u	kinetic energy expressed in volts $u = mv^2/(2e)$
U_{bias}	bias voltage of the substrate holder
ν_m	collision frequency of momentum transfer
v	particle velocity
v', v''	vibrational quantum number in the upper and lower electronic state
v_{th}	mean particle velocity
v_{de}, v_{de}	drift velocity of electrons, ions
V_{fl}	floating potential
V_p	probe potential
V_{pl}	plasma potential
ω	frequency of electromagnetic wave
ω_p^2	plasma frequency
$X_{1,p}^{exc}(T_e)$	rate coefficient for electron impact excitation from the ground state to level p
$X_{p,j}^{em}(T_e)$	emission rate coefficient
$X_{p,j}^{eff}(T_e)$	effective rate coefficient
X_q	quenching rate coefficient
Y	erosion yield
XB	effective emission rate coefficient
Z	nuclear charge

List of Tables

2.1	Compilation of radiative quantities	17
5.1	Atomic hydrogen fluxes in the ICP	101
5.2	Parameters of the ICP plasma used for measurements of erosion yields	139

List of Figures

2.1	Equilibriums: Corona – CR-model – LTE	10
2.2	Typical shapes of electron impact cross sections	12
2.3	Escape factors of Lyman lines	17
2.4	Dissociation cross sections for hydrocarbons and silanes	19
2.5	Electron impact ionization rate coefficients of various gases	23
2.6	DC glow discharge	29
2.7	ICP reactor	30
2.8	Duo-Plasmaline	31
2.9	ECR discharge	32
2.10	Poloidal cross section of the ASDEX Upgrade tokamak	34
2.11	LYRA divertor of ASDEX Upgrade with the lines of sight from divertor spectroscopy	36
3.1	Effective rate coefficients for the He-line at 728 nm	40
3.2	Excitation cross sections for argon $2p_1$ and $2p_2$ states	41
3.3	Emission rate coefficients for the argon lines at 696.5 and 750.4 nm	42
3.4	Correlation between the vibrational population of an excited and the ground state of N_2 and H_2	46
3.5	Spectrum of the N_2 band around 380 nm	47
3.6	Michelson setup for absorption measurements	49
3.7	Argon absorption spectrum around 810 nm	50
3.8	Microwave interferometer in Mach-Zehnder and Michelson configuration	52
3.9	The Langmuir probe system APS3	53
3.10	Current-voltage characteristic of a Langmuir probe	54
4.1	Demixing of gases in the ECR discharge	60
4.2	Gas and rotational temperatures determined from the radiation of the N_2 band around 380 nm	61
4.3	Radial profiles of n_e and $\langle E \rangle$ in the ICP discharge	62
4.4	Axial profiles of n_e and $\langle E \rangle$ in the ICP discharge	63
4.5	Electron density in the glow discharge	65
4.6	Spectroscopic determination of T_e in the glow discharge using different EEDFs	66
4.7	EEDF and $\langle E \rangle$ in pure helium ICP discharges	68

4.8	Calculated EEDFs in a He/Ar ICP	69
4.9	T_e in the ECR discharge using the radiation of Ar and He	70
4.10	Energy level diagram of helium	72
4.11	Energy level diagram of argon	73
4.12	Relative population densities of metastable and resonant levels in He and Ar	74
4.13	Opacity correction factors for two helium lines	75
4.14	Boltzmann-plot of helium	77
4.15	T_e derived from six helium lines using the CR-model	78
5.1	Energy level diagram of H_2 and H	80
5.2	Potential energy curves of H_2 , H_2^+ and H_2^-	81
5.3	Emission spectra of the Fulcher band ($d^3\Pi_u - a^3\Sigma_g^+$) of H_2 and D_2	82
5.4	Population processes of the $n = 3$ triplet state of H_2	86
5.5	Depopulation processes of singlet and triplet states of H_2	86
5.6	Emission rate coefficients of the H_α -line	87
5.7	Emission rate coefficient of the Fulcher radiation	88
5.8	Dissociation rate coefficients of H_2	90
5.9	Rate coefficients for dissociative attachment and ion conversion	90
5.10	Composition of ion densities in hydrogen plasmas	92
5.11	Emission rate coefficients of the first three Balmer lines of H and D	93
5.12	Opacity correction factors for three Balmer lines	94
5.13	Atomic hydrogen densities in a 10% H_2 (D_2)/He plasma	95
5.14	Balmer line ratios in H_2 (D_2)/He plasmas	97
5.15	δ determined from absolute line intensities and from line ratios	98
5.16	Atomic hydrogen densities above a surface	99
5.17	Densities of molecular hydrogen in a 10% H_2 /He ECR plasma	103
5.18	Zoom of the energy level diagram for the $n = 2$ and $n = 3$ triplet states of H_2	104
5.19	Intensity ratio of molecular bands.	104
5.20	Relative vibrational populations in the upper Fulcher state	106
5.21	Vibrational temperatures in the ECR discharge	107
5.22	$T_{rot}(X^1\Sigma_g^+)$ derived from the upper Fulcher state	108
5.23	Vibrational temperatures with and without introducing an additional surface into the plasma	109
5.24	Vibrational temperatures of H_2 in H_2 /He and CH_4 /He plasmas	110
5.25	Potential energy curves of three electronic states which contribute to the hydrogen continuum	111
5.26	Continuum spectra of H_2 and D_2 at 4 Pa in the ECR discharge	111
5.27	Electron temperatures derived from the continuum spectra and the He_{728} line	112
5.28	Fulcher spectrum and mass spectra in 50% H_2 /50% D_2 ECR discharges	114
5.29	Percentages of HD produced in H_2 / D_2 plasmas	114
5.30	Vibrational populations of H_2 , D_2 and HD	115

5.31	Ionization processes per emitted H_α photon	117
5.32	Balmer line ratios for various T_e and δ depending on n_e	118
5.33	Balmer line ratios calculated with different CR-models	119
5.34	Effective ionization and dissociation processes per emitted Fulcher photon	120
5.35	T_{rot} , T_{vib} and Γ_{H_2} in the divertor plasma	122
5.36	Calculated relative vibrational populations in the ground state of H_2 and D_2	124
5.37	Correlation between the ratio of vibrational populations in the upper Fulcher state and T_e	125
5.38	T_e in a hydrogen discharge determined by three diagnostic methods	126
5.39	T_e derived from molecular radiation in deuterium discharges in ASDEX Upgrade	128
5.40	Rate coefficients for MAR and MAD	130
5.41	Measured and calculated Fulcher photon fluxes and vibrational populations	131
5.42	Densities, T_e and rates for MAR, MAD, MAI and R^{3+r}	133
5.43	Outer target density profiles from B2-EIRENE calculations	134
5.44	Emission spectrum of the CD band around 431 nm	137
5.45	Particles of a hydrogen plasma bombarding a carbon surface	138
5.46	Mass spectra of hydrocarbons	140
5.47	Intensities of the CH(CD) band and the $CH_4(CD_4)$ signal depending on substrate temperature (EK98)	141
5.48	Intensity ratios of $C_2(H)/CH$ and $C_2(D)/CD$ depending on substrate temperature (EK98) and ion energy	142
5.49	Intensity ratios of $C_2(D)/C_2(H)$ and CD/CH depending on substrate temperature (EK98)	143
5.50	Erosion yields of graphite (EK98)	145
5.51	Graphite (EK98) temperature dependence of erosion yields at 8 eV ion energy	146
6.1	Dissociation and ionization channels of CH_4 and SiH_4	151
6.2	Emission rate coefficients for the CH and SiH band	152
6.3	Contribution of CH, CH_4 and C_2H_2 excitation to the CH emission as well as C_2 and C_2H_2 excitation to the C_2 emission	153
6.4	Composition of the C_2H_y group	154
6.5	T_e and particle densities in methane mixtures	155
6.6	T_e and particle densities in 5% SiH_4 /95% H_2 plasmas	157
6.7	T_e and particle densities in N_2/He and $N_2/H_2/He$ plasmas	159
6.8	T_e and particle densities in O_2/He plasmas	160
6.9	Comparison of dissociation degrees	161

Acknowledgments

I would like to thank Prof. Dr.-Ing. Kurt Behringer for giving me plenty of rope while carrying out this work and for the support in the calculation of opacity and the ADAS code.

I am very grateful to the students and PhD students of the Lehrstuhl für Experimentelle Plasmaphysik, Universität Augsburg, who have contributed with their work to the variety of results: Dipl.-Phys. Bernd Heger, Dr. rer. nat. Hermann Paulin, Dipl.-Phys. Stefan Meir, Dipl.-Phys. Patrick Starke, Dipl.-Phys. Anja Kottmair, Dipl.-Phys. Bernhard Schalk, Dipl.-Phys. Dirk Wunderlich, Dipl.-Phys. Andreas Lotter, Thomas Ondak, Markus Berger and Thomas Pütterich. Thank you!

I am grateful to the ASDEX Upgrade Team of the Max-Planck-Institut für Plasmaphysik, Garching, for providing the spectroscopic equipment and assistance during the measurements. In particular, I would like to mention the divertor spectroscopy group.

I would like to thank Prof. Dr. D. Reiter and Dr. P.T. Greenland from the Institut für Plasmaphysik, Jülich, for many fruitful discussions on molecules in divertors and CR-models for molecules.